AN ANISOTROPIC DAMAGE MODEL FOR ROCK

by

E. J. Sellers

Thesis submitted for the Degree of Doctor of Philosophy in the Faculty of Engineering

UNIVERSITY OF CAPE TOWN

Department of Civil Engineering

in association with

FRD/UCT Centre for Research in

Computational and Applied Mechanics

September 1994

Abstract

An anisotropic damage model is proposed for the constitutive description of microcracking processes in brittle rock under a general loading path. Experimental data and micromechanical models are reviewed to quantify the effect of microcracking on the material stiffness and the mechanisms of microcrack formation in brittle rocks under compression are discussed. The sliding crack concept is adopted as the micromechanical basis of the anisotropic damage model. Undamaged material is represented with a linear elastic constitutive equation. Damage initiation is defined by a Coulomb friction law, which excludes damage at low deviatoric stress levels. The formulation of the directional damage extends the arguments of continuum damage models for tension cracking to general, tension and compression, stress states. This is achieved by the definition of damage in a subdomain of the total strain and the characterisation of the directional microcracking by a fourth order tensor internal variable, the damaged secant stiffness of the 'crack' strain subdomain. Induced anisotropy results from the reduction of components of the initial stiffness tensor in the direction of the positive principal 'crack' strains.

Evolution of the damage magnitude is determined by the principle of maximum damage dissipation in terms of the undamaged energy norm of the positive part of the 'crack' strain tensor. Versatile evolution functions, based on the Weibull probability density function, are proposed for compression and extension damage modes. Unloading and reloading criteria are developed which are consistent with the sliding crack concept and introduce hysteretic behaviour. A numerical solution scheme is presented and the model is implemented in a nonlinear finite element program.

The material constants are determined in a straightforward procedure from standard rock mechanics test results. The physical interpretation of the material parameters is highlighted in a sensitivity study. Backpredictions of dilatancy, induced anisotropy and ultimate strengths of Witwatersrand Quartzite subjected to triaxial stress path tests show good agreement with experimental data.

The finite element analysis of mining simulation experiments in small Quartzite blocks verified the applicability of the model for a complex load path involving the sequential removal of elements. The extent and direction of damage, the predicted strains and the final excavated span are in good agreement with observations.

The model was applied to Indiana Limestone in diametral compression and three-point tests in a compression/tension stress field. A quasi-linear constitutive relation was required to account for stiffening of the highly porous material in compression. Predicted load - deformation response and damage energy release rates which compare well with experimental data.

A two-dimensional analysis of the Dinorwig power station cavern demonstrates the potential of the anisotropic damage model to predict the magnitude and direction of damage and the associated deformation in a full scale engineering problem involving different rock types, geological features and an excavation and construction sequence.

DECLARATION

I, Ewan James Sellers, declare that this thesis is essentially my own work and that it has not been submitted for a degree at any other university.

Signed by candidate

E.J. Sellers

September 1994

ACKNOWLEDGEMENTS

I would like to express my gratitude to the following:

My supervisor Dr F. Scheele, for his invaluable guidance, encouragement and patience during my research.

Professor J. B. Martin, for his encouragement and for organising financial support.

Mr T.H. Douglas, for interesting discussions and providing information about Dinorwig Power Station.

The Foundation for Research Development (FRD) and the Centre for Research in Computational and Applied Mechanics (CERECAM), for financial support.

The CSIR/Miningtek, formerly the Chamber of Mines Research Organisation, for permission to use experimental data.

My collegues at the Centre for Research in Computational and Applied Mechanics (CERECAM), especially Dr Greg Mitchell, for helpful discussions.

My family and friends for their continuous support and encouragement.

Table of Contents

1 Introduction **1**

2 Microcracks in Rocks - a Review **4**

2.1 Introduction and definitions 4

2.2 Initiation of microcracking during deviatoric loading 7

2.2.1 Microcrack initiation criteria 7

2.2.2 Microcrack direction 9

2.3 Evolution of microcracking 10

2.4 Failure of rock due to microcracking 13

2.5 Effect of microcracks on unloading and reloading behaviour 14

2.6 Experimental evidence for microcrack induced anisotropy 16

2.7 Conclusions 17

3 Micromechanical and Continuum Damage Models - a Review **19**

3.1 Introduction 19

3.2 Mechanisms of crack formation in rock 20

3.2.1 Microcracking in tension 20

3.2.2 Microcracking in compression 21

3.3 Constitutive formulation of micromechanical mechanisms 26

3.3.1 Randomly distributed tension cracks 26

3.3.2 'Aligned' penny-shaped tension cracks 27

3.3.3 Sliding cracks in compression 29

3.4 Phenomenological continuum damage models 32

3.4.1 Scalar damage models 32

3.4.2 Vector damage models 35

3.4.3 Second order tensor damage models 37

3.4.4 Fourth order tensor damage models 40

3.5 Conclusions 45

4 **Formulation of Anisotropic Damage Model** **48**

4.1 Introduction 48

4.2 Initial undamaged state 49

4.3 Damage initiation criteria 51

4.4 Anisotropic damage 54

4.5 Damage magnitude and direction 59

4.6 Damage evolution law 62

4.7 Un/reloading behaviour 64

4.8 Computational implementation 70

  4.8.1 Finite element solution procedure 70

  4.8.2 Corrector algorithm : Elastic and plastic strain update 71

  4.8.3 Corrector algorithm : Determination of loading state 72

  4.8.4 Evaluation of residual and damaged states 74

  4.8.5 Update of damaged stiffness and stress 75

4.9 Conclusions 77

5 **Parametric Studies of Damage Model** **79**

5.1 Introduction 79

5.2 Procedure for calibration of the anisotropic damage model 79

  5.2.1 Elastic constants and damage initiation parameters 80

  5.2.2 Parameters of the evolution law 81

5.3 Parametric study of evolution parameters 85

  5.3.1 Investigation of the effect of finite element discretization 85

  5.3.2 Size and shape parameter for triaxial compression 86

  5.3.3 Failure envelope in triaxial compression 91

  5.3.4 Size and shape parameters for reduced triaxial extension 92

5.4 Calibration of damage model for Witwatersrand Quartzite 95

5.5 Backprediction of conventional triaxial compression and reduced triaxial extension tests . . . 98

5.5.1 Dilatancy and induced anisotropy . . . 98

5.5.2 Ultimate strength . . . 99

5.6 Predictions of stress - strain response for specific load paths . . . 101

5.6.1 Un/reloading in triaxial compression and extension . . . 101

5.6.2 Uniaxial loading in plane strain . . . 103

5.7 Conclusions . . . 105

6 Modelling of Damage due to an Excavation in a Quartzite Block 107

6.1 Introduction . . . 107

6.2 Material parameters and finite element discretization . . . 108

6.3 Comparison of experimental and finite element results . . . 110

6.3.1 Principal strains . . . 110

6.3.2 Total damage magnitude and direction . . . 113

6.4 Conclusions . . . 117

7 Simulation of Damage in Experiments on Indiana Limestone 119

7.1 Introduction . . . 119

7.2 Modification of damage model for porous rock . . . 119

7.3 Experimental procedure and model calibration . . . 121

7.4 Modelling of experiments . . . 123

7.5 Results and discussion . . . 124

7.6 Conclusions . . . 127

8 Analysis of Cavern Excavation 129

8.1 Introduction . . . 129

8.2 Finite element model and parameters . . . 130

8.3 Prediction of damage and deformations due to sequential excavation . . . 134

8.4 Conclusions . . . 141

9 Conclusions **142**

10 References **146**

List of Tables

1 Summary of parameters of anisotropic damage model 80

2 Damage model parameters for Witwatersrand Quartzite 108

3 Material properties of Quartzite blocks 109

4 Damage model parameters for Indiana Limestone 122

5 Material parameters for Slate rockmass, Dolerite dyke and the dyke margins . . . 133

List of Figures

1 Schematic of stress - strain behaviour of rock during loading in triaxial compression (after Farmer, 1983) 6

2 Damage initiation and failure envelopes for rock a: in principal stress space (Brace, et al., 1966) b: in shear - confining stress space (Schock et al., 1973) . . 8

3 Increase of microcrack density with loading in triaxial compression (Tapponier and Brace, 1976) a: crack density increase with deviatoric stress b: idealisation of stages of crack growth 11

4 Increase of fracture density with nonlinear strain in triaxial extension (after Briggs and Vieler, 1984) 12

5 Development of inelastic volumetric strain during triaxial compression (Holcomb, 1981) 12

6 Changes in crack density calculated from ultrasonic velocity measurements during true triaxial compression (Sayers et al., 1990) 13

7 Stress versus volumetric strain for cyclic loading in uniaxial compression (after Scholz and Kranz, 1974) 14

8 Response of Westerly Granite to un/reloading cycles in triaxial compression (after Holcomb, 1981). a: stress history b: deviatoric stress - volumetric strain history c: deviatoric stress - travel time change history 15

9 Behaviour of Poisson's ratios with increasing deviatoric stress 16

10 Schematic of three modes of cracking in extension (Lawn and Wilshaw, 1975) . 21

11 Mechanisms for the introduction of axial cracks in triaxial compression (Brace et al., 1966) 22

12 Schematic diagrams of wing cracking a: in two-dimensional stress states (after Nemat-Nasser and Horii, 1982), and b: in three-dimensional stress states (after Dyskin et al., 1994) 24

13 Hyperbolic deadband region in stress space during back-sliding of frictional cracks (Kachanov, 1982) 30

14 Schematic diagram of the effect of damage on the stress - strain response in uniaxial tension 33

15 Mohr effective stress space with damage initiation criterion 51

16 Schematic of microcrack population under a: tensile stress state and b: compressive stress state 56

17 Influence of the 'shape' parameter β on the damage evolution law based on the Weibull probability distribution function 63

18 Influence of the 'size' parameter θ on the damage evolution law based on the Weibull probability distribution function 65

19 Schematic of stress - strain behaviour during loading and unloading in mode I . 66

20 Schematic of translation of undamaged domain in the effective stress space during loading and unloading in mode II 67

21 Schematic of stress - strain behaviour loading and unloading in mode II 70

22 Effect of load increment on the volumetric stress - deviatoric strain response of Quartzite 86

23 Effect of the 'size' parameter θ_{II} on the volumetric strain - deviatoric stress response in conventional triaxial compression 87

24 Effect of the 'size' parameter θ_{II} on the axial strain - radial strain response in conventional triaxial compression 88

25 Evolution of damage magnitude d_{II} with deviatoric stress a: influence of 'size' parameter θ_{II} and b: influence of 'shape' parameter β_{II} 89

26 Effect of the 'shape' parameter β_{II} on the volumetric strain - deviatoric stress response in conventional triaxial compression 89

27 Effect of the 'shape' parameter β_{II} on the axial strain - radial strain response in conventional triaxial compression 90

28 Failure envelopes calculated with different values of θ_{II} 91

29 Failure envelopes calculated with different values of β_{II} 92

30 Effect of the 'size' parameter θ_{I} on the volumetric strain - deviatoric stress response in reduced triaxial extension 93

31 Evolution of damage magnitude d_I with deviatoric stress a: influence of 'size' parameter θ_{II} and b: influence of 'shape' parameter β_{II} 93

32 Effect of the 'shape' parameter β_{I} on the volumetric strain - deviatoric stress response in reduced triaxial extension 94

33 Damage initiation and failure surfaces for Witwatersrand Quartzite 95

34 Evolution parameters θ_{II} and β_{II} with respect to confinement for Witwatersrand Quartzite 96

35 Comparison of backpredicted and experimental volumetric strain - deviatoric stress response in conventional triaxial compression 97

36 Comparison of the experimental and backpredicted axial strain - radial strain response in conventional triaxial compression 98

37 Comparison of backpredicted and experimental volumetric strain - deviatoric stress response in reduced triaxial extension 99

38 Comparison of the experimental and predicted axial strain - radial strain response in reduced triaxial extension 100

39 Predicted and experimental failure envelopes for conventional triaxial compression and reduced triaxial extension and selected load path predictions 101

40 Model simulation of un/reloading behaviour in conventional triaxial compression 102

41 Experimental (after Briggs, 1991) and predicted stress - strain behaviour in reduced triaxial extension 103

42 Stress - strain response on two-way loading, unconfined compression and unconfined tension, and on one-way tension loading 104

43 Prediction of stress - strain response in axisymmetric, unconfined compression and plane strain 105

44 Schematic of the block experiment with loading and boundary conditions for the finite element model 109

45 Displaced shape of the finite element mesh of the block and the loading platen . 110

46 Predictions and experimental data (Gay, 1976) of principal strains with aspect ratio of excavation at gauge position 1 111

47 Predictions and experimental data (Gay, 1976) of change of principal strains with excavation aspect ratio at gauge position 2 112

48 Predictions and experimental data (Gay, 1976) of change of dip angle of major principal strain with aspect ratio 113

49 Contours of total damage *d* for excavated spans of 25mm, 35mm, 45mm and 55mm 114

50 Vectors of positive 'crack' strain for excavated spans of a: 45mm and b: 55mm . 115

51 Typical sequence of fracturing in experiments (Gay, 1976) 116

52 Fracture map of the front and back faces of a Quartzite block (Gay, 1976) 117

53 Unconfined compression test results on Indiana Limestone (Scheele, 1993) and backpredictions using various initial moduli 121

54 Schematic of test specimens with mesh discretization of a: diametral compression test and b: three point test 123

55 Load - diametral strain relationships of experiments and predictions 124

56 Predicted contours of tangent bulk modulus at failure in diametral compression with quasi-linear damage model 125

57 Damage at failure a: contours of damage predicted with quasi-linear damage model and b: origins of acoustic events and crack pattern at failure (after Falls et al., 1989) 126

58 Increase of cumulative acoustic emission and total damage energy release rate with normalised load 126

59 Three-point loading tests a: damage contours within specimen prior to failure b: scanned photograph of a three-point test specimen at failure (Jaeger, 1967) . . . 127

60 Layout of underground caverns at Dinorwig Power Station (Douglas et al., 1984) 130

61 Cross-section of the trial enlargement showing the excavation sequence, the rock reinforcement and the extensometer positions (after Douglas et al., 1983) 130

62 Finite element mesh for Dinorwig cavern analysis 131

63 Finite element simulation of Dinorwig Slate (a) uniaxial stress - strain response (b) failure envelope 134

64 Damage contours at trial excavation steps a: stage 1, b: stage 2a, c: stage 2b, d: stage 3 135

65 Damage vectors after excavation a: stage 1 b: stage 3 136

66 Damage contours at various stages of excavation a: stage 6, b: stage 7, c: complete machine hall, d: main inlet valve gallery 137

67 Damage vectors after excavation of a: machine hall b: machine hall and valve gallery 138

68 Measurement of in-situ deformations at extensometers A1 and B1 140

69 Extensometer deformations predicted for the Dinorwig cavern analysis 140

List of Symbols

(Symbols may have two or more descriptions which are separated by a semicolon.)

Lowercase symbols

a	crack length
b	crack width
c	crack length; cross effect coefficient
$\bar{c}$	average crack length
d_{cI}	damage magnitude in mode I
d_{cII}	damage magnitude in mode II
f	yield surface
k	ratio of major to minor principal stress; additional compliance
m	crack geometry factor
n	number of cracks, material parameter
r, r_{cI}, r_{cII}, r_{cm}	radius of damage surface, in mode I, in mode II, in either mode
q	deviatoric stress
v	volumetric strain (compression positive)
$\bar{v}$	volume of representative region
v, v'	apex of elastic domain, translated apex
$\boldsymbol{b}$	vector of body forces
$\boldsymbol{f}$	vector of surface tractions
$\boldsymbol{i}$	second order identity tensor
$\mathbf{p}$	traction vector
$\boldsymbol{p}_i$	principal direction vector
$\boldsymbol{q}_n$	plastic internal variables
$\mathrm{s},\mathrm{s}^\star$	load bearing area, net load bearing area
$\boldsymbol{s},\boldsymbol{s}^+,\boldsymbol{s}^-$	deviatoric stress, positive part, negative part
$\boldsymbol{u}$	vector of nodal displacements

Uppercase symbols

A	material parameter
C'	deviatoric stress at start of dilatancy
C_1, C_2	material constants
C_{ij}	crack influence coefficients
D, D_t, D_c	damage, tensile damage , compressive damage
E, E_o, $\bar{E}$	Young's modulus , initial Young's modulus , effective Young's modulus
G, G_t, $\bar{G}$	shear modulus, tangent shear modulus, effective shear modulus
G, G_c,	crack extension force, characteristic value of crack extension force
$\hat{G}$,	damage surface in space of conjugate thermodynamic forces

$\hat{G}$, $\hat{G}_I$	damage surface in space of undamaged energy norm, in mode I
$\hat{G}_{II}$,$\hat{G}_m$	damage surface in space of undamaged energy norm in mode II,in either mode
H^+, H^-	damage evolution function in tension, in compression
H_{cI}, H_{cII}, H_{cm}	damage evolution function in mode I, in mode II, in either mode
I	extension mode of damage
II	compression mode of damage
K, K_t, $K_{t\max}$	bulk modulus, tangent bulk modulus, maximum tangent bulk modulus
K_I, K_{II}, K_{III}	stress intensity factors in fracture mode I, mode II, mode III
S, $S^\star$	load bearing area, net value of load bearing area
T	temperature
U	total energy
U_E	strain potential energy
W_L	energy of applied loads
$\boldsymbol{B}$	strain - displacement matrix
C_{ijkl}	stiffness tensor
$\boldsymbol{C}$	stiffness tensor
$\boldsymbol{C}_o$	initial stiffness tensor
$\boldsymbol{C}_c$	damaged subdomain secant stiffness tensor
$\boldsymbol{D}$	fourth order damage internal variable
$\boldsymbol{D}^i_j$	Jacobian matrix
$\boldsymbol{G}$	damage characteristic tensor
$\boldsymbol{I}$	fourth order identity tensor
$\boldsymbol{K}^i_j$	tangent stiffness matrix of element
$\boldsymbol{M}$	damage effect tensor (effective stress concept)
$\boldsymbol{M}_c$	damage effect tensor of damaged subdomain
$\mathbf{M}$	damage effect tensor (net stress concept)
$\boldsymbol{P}$	traction vector
$\mathbf{P}^+$	positive projection operator
$\mathbf{P}^-$	negative projection operator
$\boldsymbol{Q}$, $\boldsymbol{Q}^+$	rotation tensor, positive rotation tensor
$\boldsymbol{R}_I$, $\boldsymbol{R}_{II}$	tension response function, compression response function
$\boldsymbol{S}$	compliance tensor
$\bar{\boldsymbol{S}}$	self-consistent compliance tensor for single crack
$\bar{\boldsymbol{S}}^\star$	self-consistent compliance tensor for crack population
$\boldsymbol{V}$	crack direction vector
$-\boldsymbol{Y}$	thermodynamic conjugate force

Special symbols

$\cdot$	differential with respect to a time scale
$:$	inner product of two tensors
$\otimes$	outer product of two tensors

$^{-1}$	inverse of a matrix or tensor
∂	partial differentiation with respect to
d	differentiation with respect to
$\|\cdot\|$	norm of a tensor
$H[\,]$	Heaviside function
$< >$	MacCauley brackets

Greek symbols

α	angle of the normal to the plane of maximum shear
β	Weibull probability density function 'shape' parameter
$\beta_I, \beta_{II}, \beta_m$	'shape' parameter in mode I, in mode II, in either mode
$\beta_{0I}, \beta_{1I}, \beta_{0II}, \beta_{1II}$	'shape' constants in mode I, in mode II
β, β_{eff}	intrinsic compressibility; cleavage plane angle, effective compressibility
γ	free surface energy; permissible area; angle of flaw; angle of flaw; aspect ratio; weighting factor
$\gamma_{xy}, \gamma_{yz}, \gamma_{xz},$	engineering shear strains
δ_{ij}	Kroneker delta
ϵ	strain; crack density parameter
$\epsilon^e_{c\,(i)}$	principal value of crack strain
$\epsilon_a, \epsilon_{\|}$	axial strain
ϵ_{ca}	axial crack strain
ϵ_{cr}	radial crack strain
ϵ_h	strain at hydrostatic stress state
$\epsilon_r, \epsilon_{\perp}$	radial strain
ϵ_{Ra}	axial residual strain
ϵ_{Rr}	radial residual strain
η_1, η_2	material constants
θ_I, θ_{II}	'size' parameter in mode I, in mode II
$\theta_{0I}, \theta_{1I}, \theta_{0II}, \theta_{1II}$	'size' constants in mode I, in mode II
λ	interpolation factor; Lamé constant; maximum negative principal stress
$\dot{\lambda}$	flow parameter
μ	coefficient of friction; cumulative damage parameter; Lamé constant; "flow" parameter
μ_o	coefficient of friction
$\nu, \nu_t, \bar{\nu}$	Poisson's ratio, tangent Poisson's ratio, effective Poisson's ratio
ξ_c	scalar undamaged energy norm of 'crack' strain subdomain
ρ	density
φ	continuity
ψ	Helmholtz free energy
τ	equivalent tensile strain
$\bar{\tau}$	effective shear stress

$\bar{\tau}_0$	initial effective shear stress
σ	stress magnitude
σ_a	axial stress
σ_c	'crack' stress
σ_{ca}	axial 'crack' stress
σ_{cr}	radial 'crack' stress
σ_c^u	uniaxial compression stress
$\boldsymbol{\sigma}_d$	deviatoric stress
σ_n , $\bar{\sigma}_n$	normal stress, effective normal stress
σ_{nn}	normal component of far-field stress
σ_{nt}	shear component of far-field stress
σ_r	radial stress
$\bar{\sigma}_{Ra}$	residual axial stress
$\bar{\sigma}_{Rr}$	radial residual stress
σ_t	tensile stress
σ_t^u	uniaxial tensile stress
$\bar{\sigma}$	effective stress
$\bar{\sigma}_{max}, \bar{\sigma}_{min}$	maximum and minimum principal effective stress
$\bar{\sigma}_n$	effective normal stress, effective normal stress
Γ, Γ_{max}	damage initation surface, maximum of damage loading surface
Λ	unloading surface
Υ	damage mode surface
$\boldsymbol{\alpha}$	crack density tensor
$\boldsymbol{\beta}_i$	crack displacement vector
$\boldsymbol{\omega}$	cross effect coefficient
$\boldsymbol{\omega}_k^{\alpha}$	damage vectors
$\boldsymbol{\Omega}_k$	surface density of cavities
$\boldsymbol{\epsilon}$, $\boldsymbol{\epsilon}^+$,$\boldsymbol{\epsilon}^-$	strain tensor, positive part of strain tensor, negative part of strain tensor
$\boldsymbol{\epsilon}_c^e$	'crack' strain tensor
$\boldsymbol{\epsilon}_R^e$	residual strain tensor
$\boldsymbol{\epsilon}_o^e$	initial strain tensor
$\boldsymbol{\epsilon}^e$	elastic strain tensor
$\boldsymbol{\epsilon}^p$	plastic strain tensor
$\boldsymbol{\epsilon}^r$	inelastic damage strain tensor
$\boldsymbol{\nu}_i$	principal direction vector
$\boldsymbol{\sigma}$, $\boldsymbol{\sigma}^+$, $\boldsymbol{\sigma}^-$	stress tensor, positive part of stress tensor, negative part of stress tensor
$\bar{\boldsymbol{\sigma}}$	effective stress tensor
$\boldsymbol{\sigma}^*$	net stress tensor
$\boldsymbol{\sigma}_c$	'crack' stress tensor
$\boldsymbol{\sigma}_o$	initial stress tensor
$\boldsymbol{\sigma}_R$	residual stress tensor
$\bar{\boldsymbol{\sigma}}_R$	effective residual stress tensor

σ_p	projected stress tensor
$\bar{\sigma}_{trial}$	trial effective stress
σ_1, σ_2, σ_3	major principal stress, intermediate principal stress, minor principal stress
χ	damage internal variables

Superscripts

e	elastic
p	plastic
r	inelastic damage
i	iteration
u	uniaxial
$^{(n)}$	increment
$^{(n-1)}$	previous increment
$^{(n)(i)}$	current increment and current iteration
$^{(n)(i-1)}$	current increment and previous iteration
α	crack direction counter
$+$	positive part
$-$	negative part

Subscripts

a	axial
c	crack
ec	damaged elastic subdomain
ed	elastic, damaged
eR	residual elastic
i,j,k,l	tensor indices
m	mode I or mode II
n	normal
o	initial
pd	plastic, damaged
r	radial
trial	predicted value
t	tensile
x,y,z	material directions
I	in mode I
II	in mode II
R	residual

Chapter 1 Introduction

The South African mining industry continues to explore the possibilities of mining at depths of up to five kilometres. However, even at the current depths of 3000m to 4000m, the rock related accidents in the highly fractured rockmass continue to result in the loss of life and production. Ensuring the safety of mineworkers and the viability of extracting the gold bearing reef are problems which are currently of great importance. These issues can only be addressed once a good understanding of the behaviour of the rockmass surrounding the mine excavations is achieved. Assistance with this task is provided by the advancement of numerical analysis techniques which allow the modelling the processes of fracturing and the resulting deformations.

In any underground excavation, whether for mining or civil engineering purposes, a change of the in-situ stress state results in the formation of fractures around the opening. Stress concentrations in the rock can lead to local failures and rockfalls, if support is inadequate, and sudden rockbursts in seismically active areas. Fracturing is equivalent to a reduction of the stiffness of the rockmass and produces volumetric dilation. The fractured rock tends to expand into the excavated region. Such deformations are particularly significant in the deep gold mines where the sequential mining causes an extensive region of fracturing around the stope and the associated dilation eventually leads to complete closure of the excavation (Brummer, 1982).

The classical approach in rock engineering is to consider the rock as a linear elastic continuum and empirical failure criteria are applied to determine the ultimate strength of the rock. At present, the ability to predict the highly nonlinear material behaviour resulting from the fracture processes preceding failure is severely limited. Research into the behaviour of the rock under loading indicates that flaws and microcracks develop into macrocracks and fractures which in turn result in failure of the rock material. The major difficulty in describing these complex mechanisms is the development of suitable constitutive models which can capture the essential features of the overall behaviour without having to consider the contribution from each fracture in the rockmass.

The concepts of continuum damage mechanics were initially developed for modelling the progressive loss of stiffness and strength associated with the presence and development of microcracks in metals can, in principle, be extended to consider the behaviour of rock. In these models, the constitutive relations include a set of internal variables to describe the manner in which the microcrack distribution and density affects the material behaviour. The development of the loss in stiffness as a result of loading is quantified by evolution laws expressed in terms of internal variables (Krajcinovic, 1989). Application of damage models to the analysis of rock has been considered previously (e.g. Dragon, 1976; Resende, 1984), however, most models have assumed the fracturing to be isotropic and the influence of the directionality of the fracturing has been neglected. Damage formulations including the anisotropy induced into the material stiffness by directional cracking generally rely on tensile stress or positive strain based initiation criteria (e.g. Simo and Ju, 1987), which are characteristic of metals. These models cannot account for the fracturing in rock under the extension and compression loading conditions which are encountered in practice as a result of the excavation from a rockmass under a compressive in-situ stress state.

A continuum damage model for rock is proposed in this dissertation that seeks to address some of the shortcomings of previous formulations. The model is phenomenological in that evolution laws are required to describe the loss of stiffness associated with the growth of the microcracks. The objectives of this formulation are to produce a model that can predict the behaviour of rock under general loading with particular emphasis on

- initiation of microcracking for a wide range of stress states,
- evolution of the damage with loading,
- anisotropy of the stiffness induced by microcracking,
- material response during loading and unloading

for any loading path. A secondary objective is that the model formulation should allow implementation directly into a nonlinear finite element solution procedure to provide a relatively efficient computational tool. In addition, for practical application, the model should have parameters which require a minimum number of standard laboratory tests for calibration.

A brief review of the scattered information from laboratory experiments on rock is presented in Chapter 2. The emphasis is on introducing the essential features of the rock behaviour which should be incorporated into a constitutive model and on quantifying the relationship of the microfracturing and the stiffness of the rock. In Chapter 3, the micromechanical mechanisms which have been postulated for the formation of cracks in rock in tension and compression are reviewed. The concepts of continuum damage models are described in terms of one-dimensional models. Damage models for three-dimensional stress states are categorised according to the rank of the tensorial internal variables formulations and are discussed in terms of their ability to model the initiation, growth and induced anistropy resulting from microcracking.

The formulation of the anisotropic damage model is presented in Chapter 4. The choice of the internal variable to characterise the damage is based on the arguments of Ju (1987) for anisotropic damage in tension. The micromechanical concept of directional damage resulting from sliding of inclined, pre-exisiting flaws is incorporated into the constitutive relations for modelling of the initiation and growth of damage in compression and extension stress states. Evolution functions are proposed which can represent many possible situations of damage growth and have parameters with physical meaning. Unloading and reloading procedures are developed which are consistent with the sliding crack analogy. A computational scheme for finite element application is presented.

The usefulness of a constitutive law depends largely on the simplicity of the procedures for establishing the material constants. Calibration procedures based on standard laboratory tests are therefore developed in Chapter 5 and a sensitivity study investigates the predictions of dilatancy and induced anisotropy for a range of material constants.

The aniosotropic model has been developed especially for analyses of mining and tunnelling problems. However, quantitative information of the deformations and fracture patterns in the rockmass surrounding such excavations is scarce. Therefore, the analysis of an experiment simulating a mining excavation in small Quartzite blocks is described in Chapter 6. Fracture patterns and the strain history are available for comparison with the model predictions. Modelling of diametral compression tests on discs of Indiana Limestone is investigated in Chapter 7. Quantitative comparisons with load - deformation response and acoustic emission development provide a means of verifying the predictions for a weak, porous rock type. The proposed model is applied to a full size civil engineering problem in Chapter 8. The Dinorwig Hydroelectric power station in Wales, U.K., is analysed as an example of the sequential excavation of a cavern at low depths. Comparison of predicted displacements with in-situ extensometer measurements assists in verifying the choice of material parameters. The influence of the construction sequence, rock support and geological structures on the damage magnitude and direction are demonstrated. In Chapter 9, the research work is concluded with a summary and discussion. Recommendations for further developments are suggested.

Chapter 2 Microcracks in Rocks - a Review

2.1 Introduction and definitions

A microcrack is " an opening that occurs in rocks and has one or two dimensions much smaller than the third. For flat cracks, one dimension is much smaller than the other two and the width to length ratio, termed crack aspect ratio, must be less than 10^{-2} and is typically 10^{-3} to 10^{-5}. The length is ...of the order of 100 μm or less" (Simmons and Richter, 1976). The terms microcrack and microfracture are generally used synonymously (Kranz, 1983). When the openings are large enough to be visible (macroscopic), the terms crack and fracture apply.

The formation of microcracks in rock has been investigated by a number of researchers, mainly by observation of thin sections of rock under an optical microscope. Extensive reviews of the literature on microcrack formation, with emphasis on the shape, origin, kinematics, dynamics and statistics of the microcracking have been presented by Dengler (1976), Simmons and Richter (1976) and Kranz (1983). Their extensive conclusions will not be repeated here, and only those features of the formation of microcracks which are required for the development of the damage model will be highlighted in the following brief review.

There seems to be agreement on a common sequence of microcrack formation and evolution associated with the loading of rock specimens in compression (Brace et al., 1966; Bieniawski, 1967; Hallbauer et al., 1973; Tapponier and Brace, 1976; Farmer, 1983). Application of hydrostatic stress causes the closure of microcracks, as well as pores and voids contained within the rock. Thus, the average density of microcracks decreases with increasing confining pressure, and the aspect ratio of the cracks increases (Abdel-Gawad et al., 1987; Wong et al., 1989). The presence of pre-existing fractures significantly increases the amount of compaction once hydrostatic loading is applied (Simmons et al., 1974; Feves and Simmons, 1976). The volumetric compaction due to closure can vary in different directions, because pre-existing cracks aligned perpendicular to the direction of the loading tend to close whilst those in parallel remain open. As the voids close, the material becomes less compressible and the magnitude of the reduction in compressibility is proportional to the change in the initial porosity of the rock (Brace, 1965).

The behaviour of rock during the initial stage of compressive loading is therefore characterised by a nonlinear reduction in the volume which corresponds to an increase in the bulk modulus. Full closure of the pore space is seldom achieved and is in fact prevented by irregular crack boundaries, inclusions, and slight relative shear motions of the crack boundaries upon loading. In addition, new fractures may be formed by interactions between the cracks and the modification of the local stress distributions around grains by closure of existing cracks (Brace, 1965; Batzle et al., 1980).

Upon further loading, once the initial pore space is substantially reduced, there is a brief stage during which the stress - strain response of the specimen can be described as linear and elastic. At a specific stress level microcracks begin to form. After microcrack initiation, the material behaviour is characterised by volumetric dilatancy. Stress concentrations due to point and line contacts between grains cause local tensile stresses, resulting in the formation of extension microcracks in these tensile regions near grain boundaries. Similar cracking processes are observed emanating from intracrystalline cavities and at crack tips. Differences in the elastic properties of neighbouring grains cause extension cracks which split the grains of higher stiffness.

Microcrack formation in sedimentary rocks results from translations and rotations of the grains which cause cracking of grain boundaries and separation of grains. However, microcracking in crystalline rocks is due to a number of causes, namely the release of strain energy on cleavage planes, mis-alignment of anisotropic crystals, movement of dislocations within crystals and formation of kink bands in slender crystals depending on the particular combination of stress and temperature. In contrast, microcrack formation in clastic rock, for example Indiana Limestone, which consists of loosely cemented calcite grains, appears to occur mostly as a result of mechanical interaction between grains (Zheng, 1989). The observed splitting of grains is caused by the bending of beamlike grains orientated approximately perpendicular to the loading, by stress concentrations around pores and soft inclusions and is due to the higher stress concentrations at intergranular points of contact. Sliding along grain boundaries and slipping on weak crystal planes causes microcracks to grow along grain boundaries.

As more load is applied, the individual cracks grow in the direction of the maximum principal stress length and the microcrack population evolves as the number of cracks increases. Eventually, the frequency of microcrack events accellerates rapidly and the microcracks coalesce into crack arrays. At low confining pressures, the material is brittle and tends to form macroscopic fractures. At higher confinements relative displacements across the crack faces lead to the formation of shear planes. Finally, the crack arrays merge to become faults or macrocracks. The material can no longer be considered as a continuum; the stress - strain relationship exhibits strain softening as the shear resistance decreases and the deformation increases.

At very high confining pressures, the material exhibits true plastic behaviour due to slip within crystals leading to plastic flow. Also, apparent plasticity results from the crushing of grains and buckling of rock columns leading to failure described by slip plane formation and bulging (ductile flow). The rock becomes "ductile" and exhibits an overall volumetric decrease. This change of behaviour with increasing confinement is known as the brittle - ductile transition (Byerlee, 1968).

In uniaxial tension, the stress - strain response of the rock is initially linear. The Young's modulus is similar to that obtained in uniaxial compression (Hawkes et al., 1973). The modulus however, decreases with increasing axial loading. By 50% of the ultimate load the tangent Young's modulus is reduced to between a half and two thirds of the initial value. The Poisson's ratio also is initially very high, possibly even greater than 0.5, implying that volumetric reduction occurs during the initial stages of tensile loading. As the stress increases, the ratio reduces to a value in the order of 0.1 and remains constant. Unloading and reloading in tension causes no change in the Poisson's ratio. The radial strain decreases to zero on unloading, but the axial strain does not return to its initial value. This residual axial strain can be reversed by the

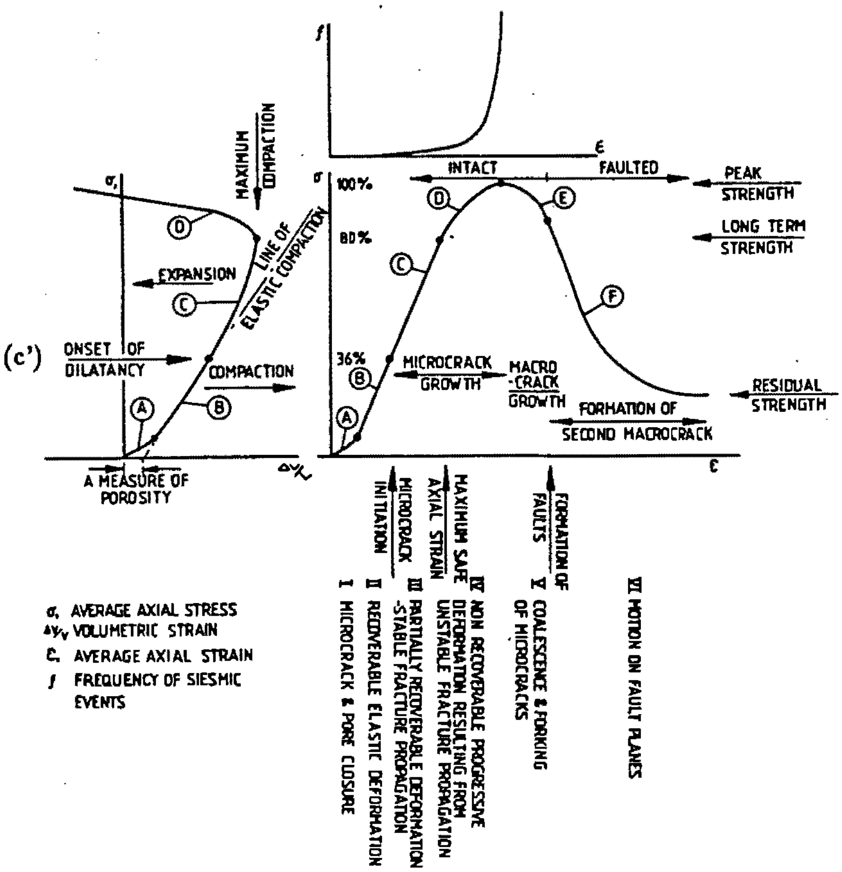

Figure 1: Schematic of stress - strain behaviour of rock during loading in triaxial compression (after Farmer, 1983)

application of compressive stress. The stress - strain behaviour is consistent with the growth of microcracks perpendicular to the axial tension.

During a conventional, reduced triaxial extension test the specimen is initially compressed by increasing the axial and radial stresses. The axial load is reduced so that the stress in the axial direction becomes the minor principal stress. The material response to the reduction of the axial stress is again initially linear elastic. As the deviatoric stress increases, microcracks develop and grow orthogonal to the axial direction. The dilation, resulting from the crack opening, causes nonlinearity of the axial strain with decreasing axial stress, and leads to ultimate failure of the rock specimen (Briggs, 1982, Briggs and Vieler, 1984).

The rather general, qualitative description of the rock deformation processes during loading will be substantiated by experimental data so that the the initiation of microcracks can be pinpointed, their direction determined, and the evolution of microcracking quantified in terms of the stress-strain relationship. This will be examined in the subsequent sections.

2.2 Initiation of microcracking during deviatoric loading

2.2.1 Microcrack initiation criteria

In most laboratory strength tests on rock specimens, it is difficult to detect the start of microcracking within the sample especially when the rock sample is completely encased in the test device. Thus, indirect methods must be applied to determine the start of microcracking for the purposes of developing an initiation criterion. A wide spectrum of methods, some with elaborate and complex methods, have been proposed based on the

- deviation from the linear volumetric strain - mean stress relationship (Brace et al., 1966),
- nonlinearity of the axial stress - radial strain response (Bieniawski, 1967),
- onset of nonlinearity in the axial stress - axial strain response in uniaxial and triaxial compression (Hallbauer et al., 1973; Taponnier and Brace, 1976),
- ratio of the radial strain (ϵ_r or $\epsilon_\perp$) to the axial strain (ϵ_a or $\epsilon_{||}$) (Scholz and Kozynski, 1979),
- tensile axial strain during reversed triaxial extension (Briggs and Vieler, 1984),
- onset of continued acoustic emission in the sample (Scholz, 1968; Holcomb and Costin, 1986),
- increase in the travel time of compression waves transmitted through the rock sample (Holcomb, 1981),
- observations of the increase in microcrack density from thin sections (Briggs and Vieler, 1984),
- decrease of the shear and compression wave velocities (Nur and Simmons, 1969; Gupta, 1973; Sayers et al., 1990),
- changes in electrical conductivity and permeability (Zoback and Byerlee, 1975).

Each technique has merits, and the selection of any particular method depends on the available test data. A complete and detailed discussion is considered to be beyond the scope of this dissertation.

Regardless of the technique with which microfracture initiation is measured, it is common practice to define an initiation surface in the stress space. In uniaxial and triaxial compression tests, the deviatoric stresses at which the volumetric strains deviate from the line of elastic compression, are the crack initiation stresses (denoted by C' in Figure 1) and define the onset of dilatancy (Brace et al., 1966). To provide a measure of the magnitude of C' in uniaxial compression and tension tests, the values for Bushveld Norite are found to be 35% and 95% of the ultimate

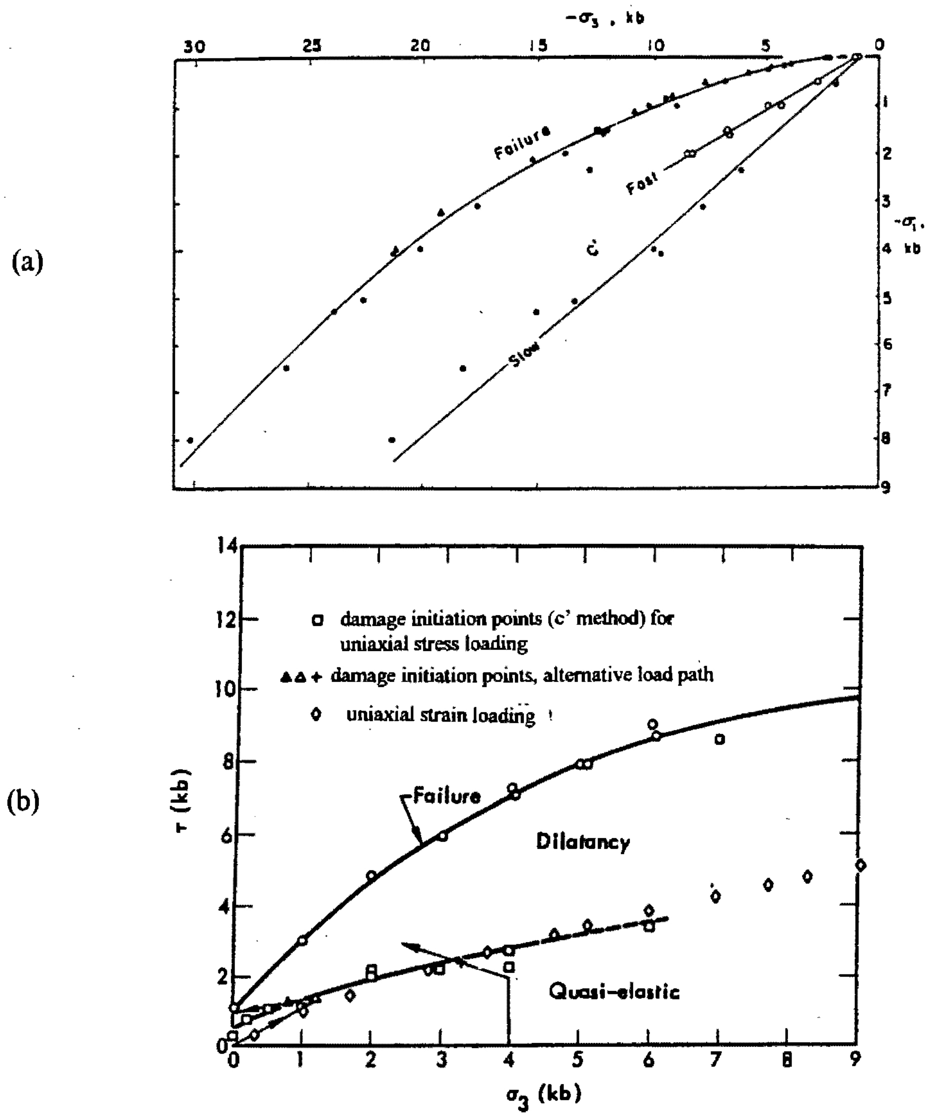

Figure 2: Damage initiation and failure envelopes for rock a: in principal stress space (Brace, et al., 1966) b: in shear - confining stress space (Schock et al., 1973)

strengths, respectively (Bieniawski, 1967). In triaxial compression the surface is a well defined boundary in principal stress space and is approximately parallel to the failure surface, as shown in Figure 2a. The accuracy with which the point C' can be determined is a subject of controversy, because it depends entirely on the precision of the stress - strain curves (e.g. Hadley, 1976; Holcomb, 1978 & 1981). Thus. the uncertainty in the stress level at which microcraking initiates can be in the order of 10% to 15% (Scholz, 1968). However, the evaluation of C' provides a means of identifying the initiation of microcracking from stress - strain data and enables the interpretation of trends in microcrack evolution (Hadley, 1976; Scholz and Kozynski, 1979).

The dilatancy envelope also exists in the shear stress - confining stress space (see Figure 2b) (Schock et al., 1973) and can also be represented by a linear relation between the deviatoric stress and the mean stress (Holcomb, 1981; Holcomb and Costin, 1986).

The dilatancy surface is independent of the loading path. This is demonstrated in an example in Figure 2b showing the results for two different load paths. Stress paths, in which the deviatoric stresses are low or the ratio k of the major to the minor principal stress remains below a critical value, do not result in microcracking (Bieniawski, 1967). A ratio of $k = 4$ has been determined for Witwatersrand Quartzite (Hallbauer et al., 1973).

Loading a sample in uniaxial strain produces no evidence of dilatancy, even if the stress state exceeds the dilatancy envelope (Schock et al., 1973). This can be attributed to the constraint of zero lateral strain. No failure was observed in these tests confirming a link between microcrack evolution and ultimate failure in brittle materials.

2.2.2 Microcrack direction

The microcracking is observed to initiate with a preferential orientation and will extend towards the direction of the maximum compressive stress. This directionality has been observed in sectioned samples by Hallbauer, et al. (1973), Kranz, (1979) and Dengler, (1976) amongst others. Other means of observation such as compression and shear wave velocity measurements (Nur and Simmons, 1969; Sayers et al., 1990), linear compressibility measurements (Bieniawski, 1967), and the increase in the apparent Poisson's ratio (e.g. Schock et al., 1973, Scholz and Kozynski, 1979) provide confirmation that directionality persists throughout the loading application.

The direction of the cracks is consistent for a variety of rock types and does not depend on the mechanism of initiation. Confirmation has been obtained for a number of igneous rocks types including Westerly Granite, Barre Granite, Granodiorite and Norite. (Brace, et al., 1966; Tapponier and Brace, 1976; Scholz and Kozynski, 1979; Kranz, 1979; Sayers, 1988b; Bieniawski, 1967). The same behaviour is exhibited in metamorphic rocks such as Witwatersrand Quartzite (Bieniawski, 1967; Hallbauer, et al., 1973) and sedimentary rocks such as Berea Sandstone, and Greywacke and Indiana Limestone (Sayers et al., 1990; Schock et al., 1973; Gupta, 1973; Zheng, 1989). Any pre-existing cracks will extend in the direction of compression (Feves and Simmons, 1976).

Most stress induced cracks are aligned within 10^o to 15^o of the uniaxial loading direction (Kranz, 1979). Under triaxial loading the angles of the microfractures appear to be distributed in a Gaussian distribution between 0^o and 30^o to the principal compressive stress. The average crack orientation was found to be 5^o off the loading direction with a standard deviation of 12^o. The alignment of cracks towards the principal compressive stress as the ultimate load is approached leads to a decrease in the mean and standard deviation of the distribution of crack directions (Kranz, 1983). In Indiana Limestone tested in triaxial compression, all cracks were within 15^o of the direction of maximum compression (Zheng, 1989). Cracks that were not initially aligned in this direction were observed to turn towards the maximum principal stress. The effect of the application of confining pressure is to reduce the ability of the cracks to extend and change direction. Thus, the distribution of microcrack orientations is determined by their direction at initiation. The microcrack angles therefore become more randomly distributed at higher confining pressures (Kranz, 1983; Zheng, 1989; Velde et al., 1993).

The above observations were mainly obtained from uniaxial compression and triaxial compression tests, but are valid for a wide range of other stress path tests. Microcracks in Quartzite under reduced triaxial extension loading are orientated in the direction of maximum compression (perpendicular to the sample axis) as the axial stress is reduced (Briggs and Vieler, 1984). In biaxial compression (plane stress) and multiaxial loading, the cracks grow toward the maximum compressive principal stress with the minor axes lying in a plane of the intermediate principal stress. Thus, the crack normals and the associated dilatancy occur in the direction of the minor principal stress (Mogi, 1967; Bieniawski, 1967; Gupta, 1973; Sayers et al., 1990).

The investigation of metal filled cracks in Indiana Limestone cylinders showed that cracks grow in a concentric manner under triaxial compression with normals directed towards the sample axis. Thus, the specimens retain the initial axial symmetry (Zheng, 1989). Loss of axial symmetry may occur during triaxial loading because of microcrack growth along preferential orientations, which are characterized by pre-existing fractures within the rock. A rock without an initial state of fracturing (e.g. Palisades Diabase) may contain a residual stress state in which case, the cracks will tend to grow in the direction of the maximum compressive residual stress (Scholz and Kozynski, 1979).

Another means of evaluating microcrack orientation is by determining the ratio of the shear wave velocity to the compression wave velocity in a particular direction (Gupta, 1973). Velocity measurements on a block of Indiana Limestone, loaded in approximately plane strain conditions suggests that fracturing extends towards the loading and that the direction of cracking is independent of the out-of-plane direction. The microcrack normals and the resulting dilatancy are in the direction of the minimum principal stress.

2.3 Evolution of microcracking

The loading of rock at stresses beyond the dilatancy envelope results in changes in the microcrack population (density) of the sample. The pre-existing cracks are found to extend and new cracks will form (Kranz, 1983). Thus, both the density and distribution of the microcracks changes as a result of loading. Observations of the change in cracking can only be made by studying sectioned samples, unloaded from specific load levels, under a petrographic or electron microscope. The method has the obvious disadvantages that a new sample is required to characterize each stress level, the crack count depends on the microscope magnification and changes may occur in the crack population during unloading and sectioning (Hallbauer et al. 1973). Indirect methods such as monitoring the dilatancy, the acoustic emission and the ultrasonic wave velocities provide information about changes to the sample during the course of testing. However, the relationship with the actual microcrack population must be obtained by an inverse analysis (Sayers et. al. 1988).

Quantitative evidence of the increase of crack densities and lengths during loading is scarce. Tapponier and Brace (1976) showed that the numbers of cracks in a triaxial test on Westerly Granite increase gradually after initiation, and more rapidly as the failure state is approached

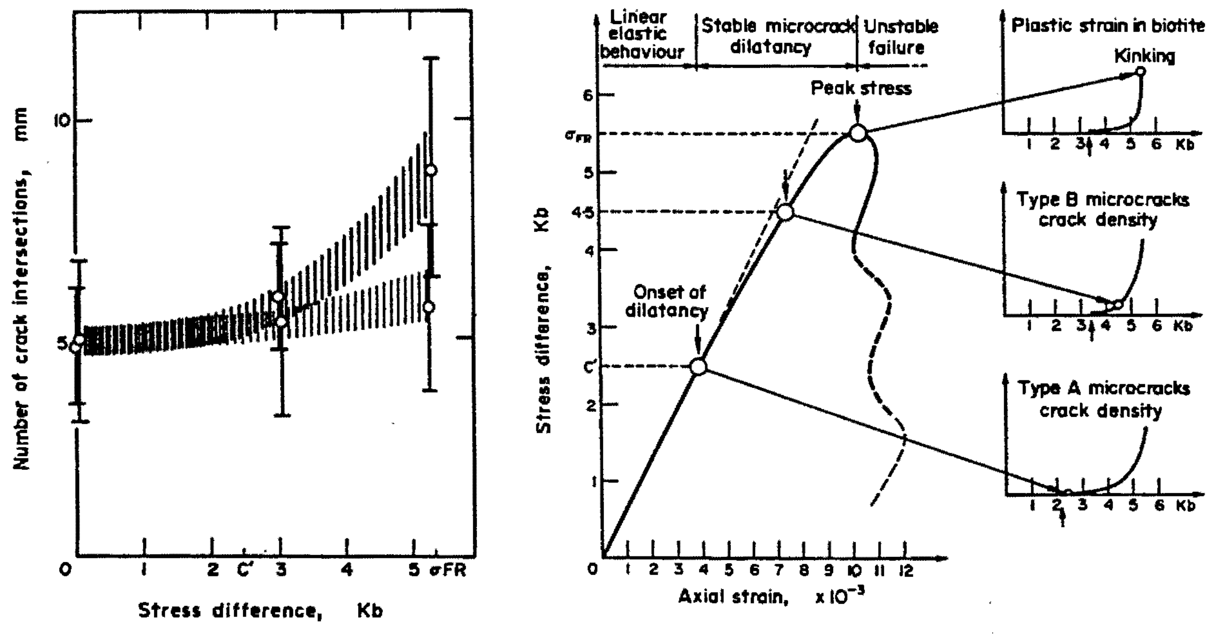

a) b)

Figure 3: Increase of microcrack density with loading in triaxial compression (Tapponier and Brace, 1976) a: crack density increase with deviatoric stress b: idealisation of stages of crack growth

(see Figure 3a). The steep increase in the ratio of crack numbers in the radial direction relative to the axial direction confirms that the cracks are mostly aligned in the direction of the axial (deviatoric) load. The inset diagrams, shown in Figure 3b, illustrate schematically the relative increases in intergranular (denoted as Type A microcracks) and transgranular (Type B microcracks) fracturing with increasing deviatoric load. The microcrack density at failure is lower as the confinement increases (Zheng, 1989).

Reduced triaxial extension tests on three types of Quartzite, performed by Briggs and Vieler (1984), showed a similar, continual increase in crack density with nonlinear strain (defined as the difference between the total strain and the projected linear elastic strain). At low deviatoric stress levels, microcracks seldom extend beyond one or two grain diameters and intersect the grain boundaries which provide energy barriers and absorb the excess energy. As the load increases, the microcracks become unstable and propagate across the grain boundaries. The graphs (Figure 4) of fracture density of intergranular (I.F.), intragranular (i.m.) and transgranular (T.F.) microcracks as a function of nonlinear axial strain suggest that the increases depend on the microstructure of the material. Thus, in rocks with a high quartz content, the quartz grains are mostly in contact leading to intra- and transgranular fracturing. In rocks with low quartz content, the fracturing tends to follow the weaker matrix material surrounding the grains and is consequently classifed as intergranular microcracking.

Quantitative information about microcrack density changes can be obtained by analysing the changes in the nonlinearity of the stress - strain behaviour. The increase in dilatancy (or acoustic

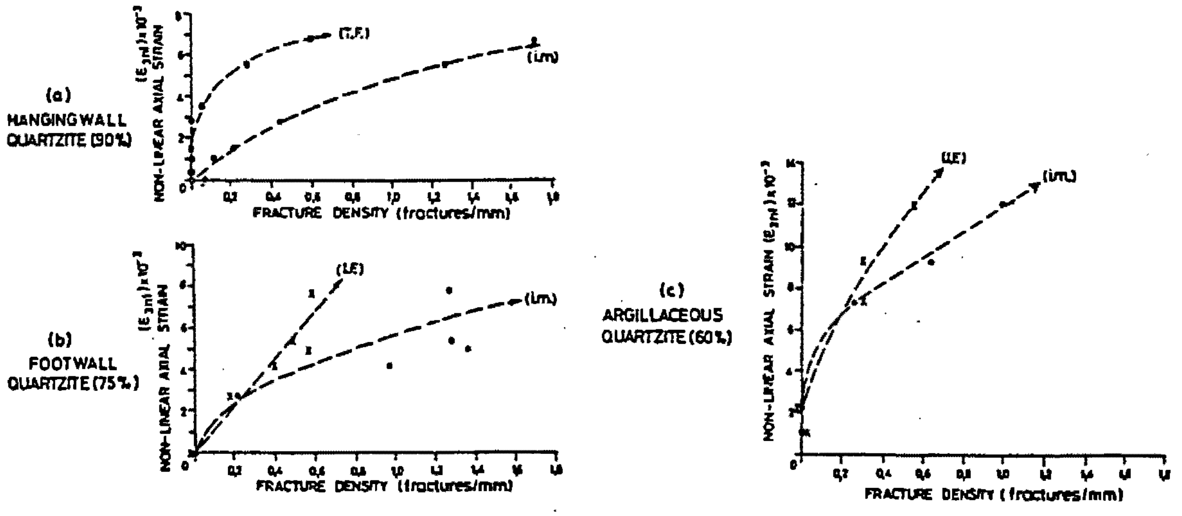

Figure 4: Increase of fracture density with nonlinear strain in triaxial extension (after Briggs and Vieler, 1984)

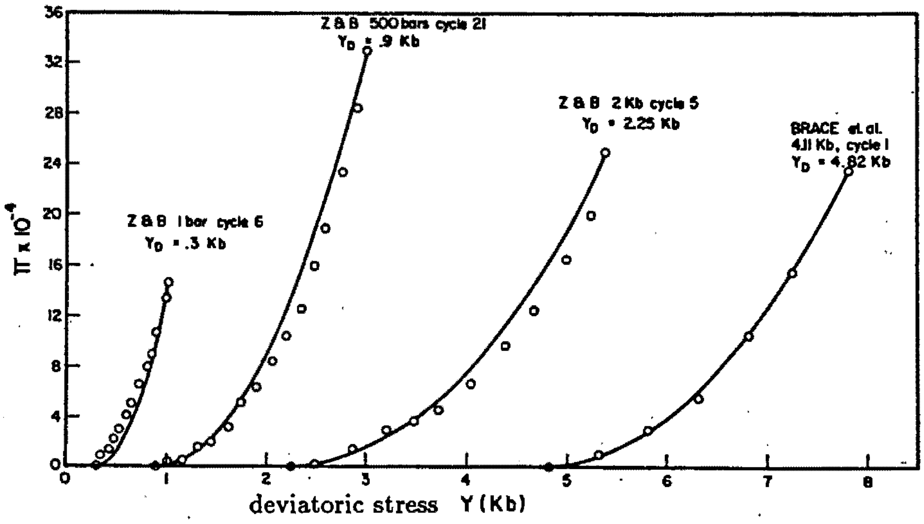

Figure 5: Development of inelastic volumetric strain during triaxial compression (Holcomb, 1981)

emission) with stress can be represented by a normal distribution probability density function up to 95% of the ultimate stress. Above this level, the microfracture events are no longer random and independent, and dilatancy increases more rapidly than the distribution function predicts (Scholz, 1968).

The growth of inelastic volumetric strain (dilatancy) with deviatoric stress of Westerly Granite in triaxial compression is shown in Figure 5 (Holcomb, 1981). The curves of inelastic volumetric strain exhibit the same continually increasing trend evident in the increase of fracture densities. In this case, the crack evolution is described by a Weibull probability function. The deviatoric stress at the onset of the inelastic volume change increases with the confinement which is con-

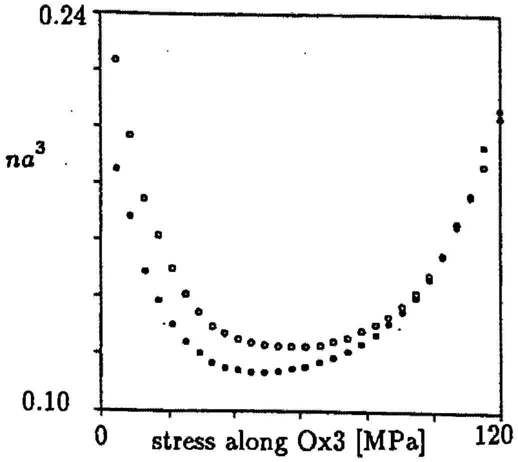

Figure 6: Changes in crack density calculated from ultrasonic velocity measurements during true triaxial compression (after Sayers et al., 1990)

sistent with the concept of a damage initation surface. Comparable results are observed in the data of Schock et al. (1973), Briggs (1982), Stavropoulou (1982) amongst many others.

Evolution of crack densities can also be inferred from ultrasonic compression and shear wave velocity measurements if assumptions are made with respect to the shape and distribution of the microcracks (Sayers, 1988). The density changes calculated for microcracking in Berea Sandstone under true triaxial compression are shown in Figure 6 (Sayers et al., 1990). Confinement of up to 4.1 MPa hydrostatic stress causes a decrease in the crack density parameter na^3. The density continues to decrease as the major principal stress is increased. The crack density reduces until the principal stress is about 40 MPa, and subsequently grows rapidly as the failure state is approached.

2.4 Failure of rock due to microcracking

The process of microcracking leading to failure of Witwatersrand Quartzite was studied in great detail by Hallbauer, et al. (1973). Initially, the microcracks are distributed randomly throughout the specimen. Upon loading, the microcracks concentrate along a plane that extends diagonally across the sample. As the load increases, the microcracks localise into a shear band that becomes visible on the macroscopic level. The macroscopic fracture appears to be a single surface, but is formed by shearing and buckling of columns of rock between the separate microcracks. The coalescence of microcracks into a macrocrack is termed en-echelon linking (Kranz, 1979b), and occurs at scales ranging from fractions of a millimetre (laboratory tests) (Bieniawski, 1967; Scholz, 1968; Velde et al., 1993 amongst others) to, in principle, hundreds of kilometres (crustal faults) (Lloyd and Knipe, 1992).

A similar process of microcrack coalesence near failure occurs in reduced triaxial extension tests (Briggs and Vieler, 1984). Linking of intragranular microcracks in high (70% to 90%) quartz content rocks led to failure surfaces that extend in the direction of the maximum compressive stress (i.e. perpendicular to the reducing axial stress). At lower quartz contents, coalescence of intergranular fractures became more predominant. The macrofracture then tends to follow the

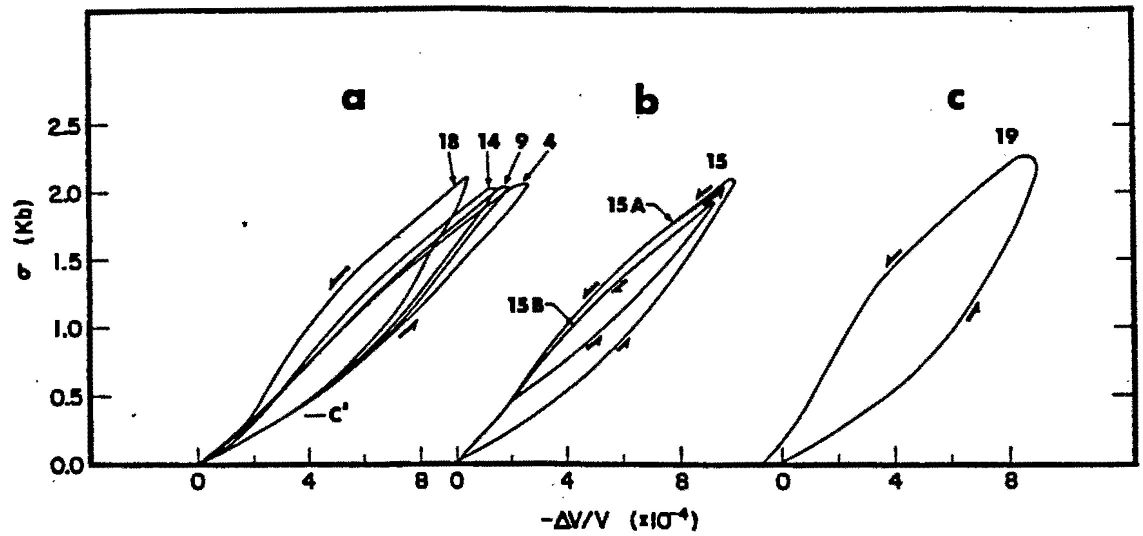

Figure 7: Stress versus volumetric strain for cyclic loading in uniaxial compression (after Scholz and Kranz, 1974)

grain boundary at an angle to the direction of maximum compression. Fracture planes obtained from the failure of rock in the Brazilian (splitting tensile) test show no transgranular and few grain boundary cracks (Dengler, 1976).

2.5 Effect of microcracks on unloading and reloading behaviour

At stress levels below failure, the application of cycles of loading and unloading to Westerly Granite in uniaxial conditions results in hysteresis in the stress - strain response as shown in Figure 7. During loading, the material behaviour is linear until the damage initiation stress C' is attained. The material dilates and becomes less stiff as the microcracking intensifies. Unloading initially occurs with a modulus which is similar to the initial modulus. As further unloading occurs, the stress - strain response becomes nonlinear and the dilatancy is recovered. On reloading, the material response is again characterised by the initial modulus. Dilatancy increases as the stress level approaches the previous maximum value forming closed hysteresis loops in the stress - strain behaviour. Dilatancy increases during every additional cycle and the stress - strain response continues to exhibit hysteresis. A similar change in dilatancy with the number of load cycles was found in cyclic uniaxial and cyclic triaxial tests by Zoback and Byerlee (1975), Hadley (1976). Hysteretic behaviour is observed in both, the radial and the axial directions. The radial strains are most sensitive to changes in the crack population because of the preferential alignment of microcracking towards the maximum principal stress (Scholz and Kozynski, 1979).

The response of Westerly granite to unloading and reloading cycles of varying amplitude shows that the rock retains a 'memory' of previous maximum applied stress states (Holcomb, 1981).

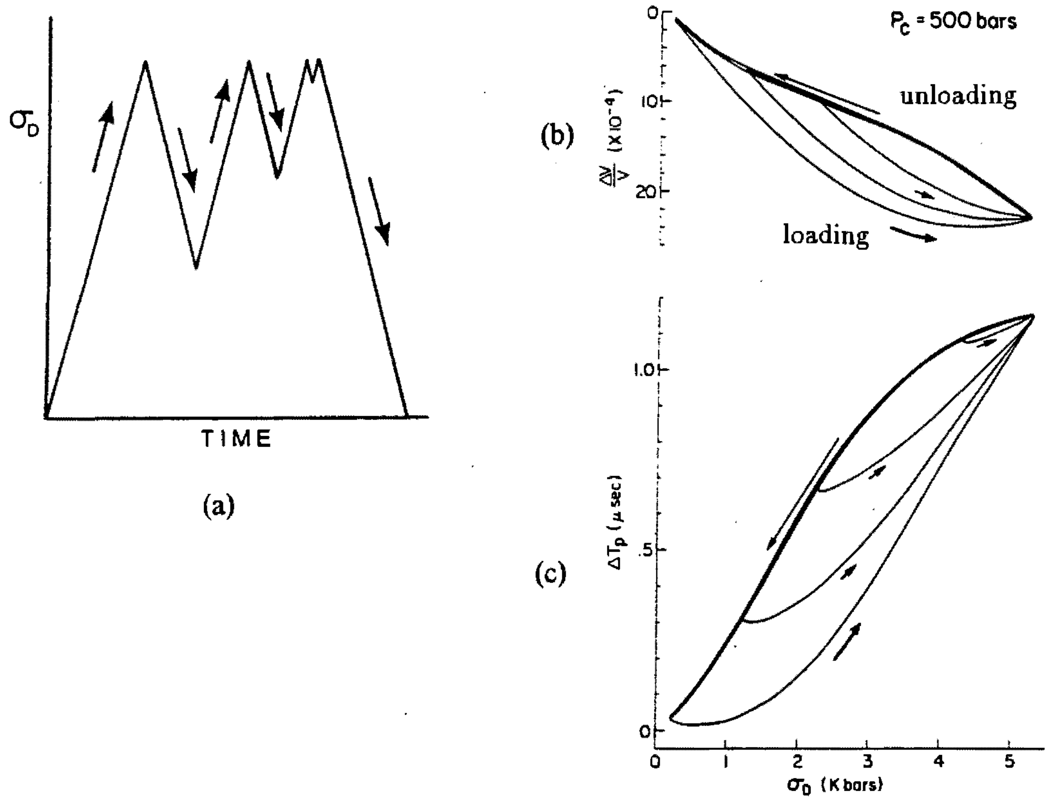

Figure 8: Response of Westerly Granite to un/reloading cycles in triaxial compression (after Holcomb, 1981). a: stress history b: deviatoric stress - volumetric strain history c: deviatoric stress - travel time change history

A typical sequence of material behaviour is shown in Figure 8. On loading, the rock exhibits dilatancy, which corresponds to an increase in the time for compression waves to travel through the sample. When the stress change over the cycle is small (e.g. the final cycle in Figure 8) the response appears to be almost elastic and the volumetric strain - deviatoric stress data for unloading and reloading are indistinguishable. The bulk modulus at unloading is of similar magnitude to the initial elastic bulk modulus. As the stress level is reduced, compression wave travel times decrease rapidly which suggests that increased closure of the stress induced cracks occurs. On reloading again, hysteresis loops are formed. Thus, the material exhibits abrupt changes in volumetric strain in reponse to a smooth decrease or increase in stress during each cycle.

Other stress histories applied to the rock demonstrate that the material appears to have a 'memory' of the previous two maxima and minima of the applied stress. The compression wave travel time will only increase once the previous maximum stress is exceeded and microcracks form. This lack of microcrack formation during un/reloading cycles can also be identified in acoustic emission testing and are attributed to the Kaiser effect (Holcomb and Costin, 1986).

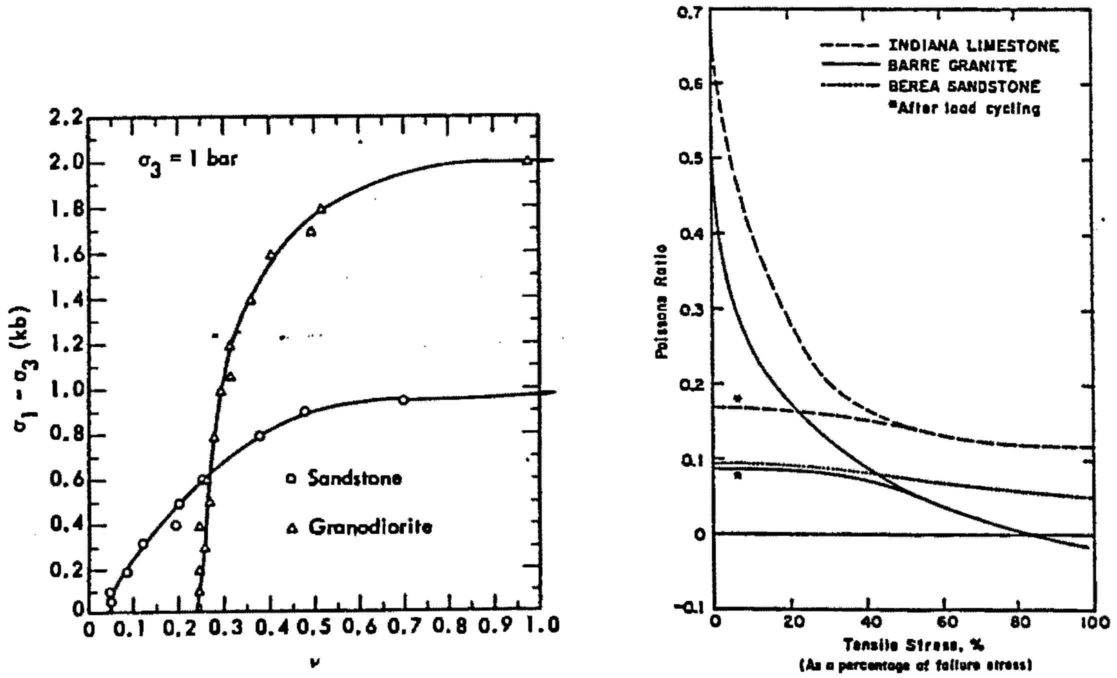

Figure 9: Behaviour of Poisson's ratios with increasing deviatoric stress
a: Change of effective Poisson's ratio in triaxial compression (Schock et al., 1973)
b: Change of tangent Poisson's ratio in uniaxial tension (Hawkes et al., 1973)

2.6 Experimental evidence for microcrack induced anisotropy

Continuum damage mechanics is based on the alteration of the elastic properites of a material as a result of microcracking. It is therefore important to obtain experimental confirmation of the evolution of the elastic properties, in terms of the Young's modulus and Poisson's ratio, with changes in the state of microcracking in the sample. The preferred orientation of fractures in the direction of the maximum compressive principal stress results in nonlinearities of the axial and radial components of strain arising at different stages of loading in a triaxial test. Therefore, a measure of the evolution of the microfracturing, in terms of the microcrack induced changes in the material stiffness, can be obtained by considering the effective Poisson's ratio which is defined as $\nu = \frac{-\epsilon_r}{\epsilon_a}$. The increase of the effective Poisson's ratio with deviatoric stress for Lance Sandstone and Granodiorite in triaxial compression (Schock et al., 1973) is shown in Figure 9a. Initially, the ratio remains constant at low deviatoric stress levels. The magnitude increases once microcracking initiates and approaches a limit value asymptotically with additional deviatoric loading.

An alternative measure to describe nonlinear behaviour is by defining a tangent Poisson's ratio $\nu_t = \frac{-d\epsilon_r}{d\epsilon_a}$ as the gradient of the radial strain - axial strain curve (Walsh, 1965). At the start of compressive loading, ν_t is equal to the elastic value and increases to a constant value at failure which is in excess of the theoretical maximum of 0.5 allowed in the theory of isotropic, linear elasticity (Hawkes et al., 1973).

In tension, a range of behaviour of the Poisson's ratio is observed for different rock types as shown in Figure 9b (Hawkes et al., 1973). Berea Sandstone shows a slight decrease from $\nu_t = 0.1$ at the start of loading to $\nu_t = 0.07$ at failure. This response does not change, even when subjected to two-way cyclic loading (from tension to compression stress states). Barre Granite and Indiana Limestone experience large changes in the tangent Poisson's ratio, as shown in Figure 9. The values for the Granite decrease from $\nu_t = 0.5$ to $\nu_t = 0.09$ and the ratio for the Limestone drops from 0.68 to 0.15. On subsequent load cycles, the values remained close to the lower limits. There is no explanation for this behaviour at this stage.

The most common method of investigating the variations in the elastic properties (stiffness) and measuring the anisotropy of the material is by ultrasonic velocity measurements. Nur and Simmons (1969) determined the Young's modulus and shear modulus parallel and perpendicular to the applied load in a diametral compression test. Both, the Young's moduli and the shear moduli were observed to increase with stress. The rate of increase reduced as the stress increased. The changes were most significant in the direction perpendicular to the loading. The Poisson's ratio was observed to increase slowly with stress.

Techniques for determining the elastic constants from ultrasonic velocity measurements are given by Sayers and Kachanov (1991) and Homand et al. (1993). Such procedures require assumptions about the effect of cracks on the elastic stiffness tensor. However, the predictions of the anisotropy may not reflect actual material behaviour (Sayers, 1993). These methods will not be discussed further since most of the experimental results available for calibration of the damage model consists of stress - strain data only.

2.7 Conclusions

The essential features of the stress - strain behaviour of rock which must be considered in a damage model formulation can be establised from the literature review. Initially, the rock is porous, locally heterogeneous, containing microcracks within the grains and the surrounding matrix material. The overall distribution of defects is usually random, permitting the assumption of initial isotropy, unless there is some existing fabric in which case the material exhibits elastic anisotropy.

Hydrostatic compression loading leads to nonlinear, isotropic volumetric compression due to closure of spherical pores and anisotropic compression on closure of pre-existing, oriented, cracks. At very high pressures, crushing of grains will cause isotropic, inelastic compaction.

Application of deviatoric stress at low confinements will firstly lead to closure of cracks perpendicular to loading direction and nonlinear stress - strain behaviour. When the deviatoric stress exceeds a crack intitiation threshold, intergranular and intragranular microcracking develops. This criterion is shown to exist in the stress space and the most convenient means of determining the surface is from observation of the onset of nonlinearity in the stress - strain relationship. However, the consideration of stress wave travel times or accumulated acoustic emission events may provide a more accurate assessment of the state of microcracking.

The microcracks extend in the direction of maximum compression and cause dilation in the direction of the most tensile principal stress. Quantitative description of the evolution of the microcrack density can be also be obtained from the ultrasonic wave travel times or accumulated acoustic emission. In triaxial tests, the development of nonlinearity in the axial strain - radial strain curve provides another indication of the microcrack growth.

The amount of microcracking will increase continually until interaction of closely spaced cracks lead to the formation of macroscopic fractures. The unstable growth of these fractures ultimately causes failure by rupturing of the rock.

There is experimental evidence that the microcracking induces anisotropic behaviour of the rock. Evaluation of the development of anisotropy of the stiffness is extremely difficult, and depends on the theoretical description of microcracking used to induce the presence of microcracks. Some of these theories will be discussed in the following chapter, in an attempt to identify the exact manner in which microcracks cause anisotropy.

Chapter 3 Micromechanical and Continuum Damage Models - a Review

3.1 Introduction

The observations of microcracking in experiments presented in Chapter 2 support the idea that the nonlinearities in the stress - strain response of rock under load are due to the opening and closing of pre-exisiting flaws in the material with subsequent formation and growth of populations of microcracks. Their orientation of the microcracks in a preferential direction leads to anisotropic behaviour. The data suggests that microcracking causes a loss of stiffness in the material.

A constitutive description of the magnitude of the stiffness loss and the induced anisotropy requires the theoretical investigation of the micromechanics, involved in the cracking processes, in order to relate the changes in the elastic properties of the material to the internal re-arrangements in the microstructure. The mechanisms causing the microcrack initiation must be identified for the particular material under consideration. In order to predict changes in the stress - strain response, the formulation of a model must also consider the growth and interactions of the defects. These processes may be included in the constitutive relation by micromechanical or phenomenological evolution laws.

In this chapter, a brief overview of the various damage formulations is provided. The first sections describe the micromechanics of crack initiation and growth under tensile and compressive stress states. In particular, mechanisms postulated for crack formation in brittle rock under compression are addressed. A selection of micromechanical models for the incorporation of the changes to the material stiffness (compliance) for selected crack arrangements are investigated in the second part.

Constitutive equations based on the continuum damage approach are discussed in the third section of this chapter. In these models, the effect of the microcracking on the material behaviour is represented by phenomenological internal variables. The internal variables are mathematical expressions which describe the changing state of the microstructure as it is deformed without direct association to the microcrack processes. This brief review of these models seeks to present the main points of some damage formulations in order to identify the necessary components of a continuum damage model and to determine the ability and potential of the models for representing the behaviour of rock in both compressive and tensile stress states. The principles of the damage concept are introduced. The generalisation of damage into three-dimensional stress and strain states and the introduction of induced anisotropy is discussed. The categorization of the various formulations in terms of the order of the tensor internal variables used to describe the damage may assist with the identification of the common features of the diverse constitutive models.

3.2 Mechanisms of crack formation in rock

3.2.1 Microcracking in tension

The analysis of tension cracks in brittle solids was formalised by Griffith in the years 1920 and 1924, laying the foundation for the development of linear elastic fracture mechanics. The theory of fracture mechanics for cracks in tension is well documented, and the following interpretations are in accordance with the textbook by Lawn and Wilshaw (1975). A crack with an elliptical cross section and of half length c is assumed to exist in a two dimensional body. When the semi-axes of the crack are equal, the crack is circular in plan (penny-shaped). Application of the concepts of reversible thermodynamics results in an expression for the total energy

$$U = (-W_L + U_E) + U_S, \tag{1}$$

which comprises contributions from the work due to the applied loads W_L, the strain potential energy U_E and the free surface energy of new crack surfaces U_S.

The Griffith energy-balance concept requires the minimisation of the total energy with respect to the crack length for equilibrium. Thus, the crack will extend when

$$\frac{dU}{dc} = \frac{d[(-W_L + U_E) + U_S]}{dc} = 0. \tag{2}$$

Expressions for each component of the energy under specific loading conditions can be derived for a linear elastic material characterised by the Youngs' modulus E and the Poisson's ratio ν. As an example, a crack in plane strain with a tensile stress σ_n applied normal to the direction of growth is considered here. The total energy is given by

$$U = -\sigma_n^2 \frac{\pi c^2(1-\nu^2)}{E} + 4c\gamma, \tag{3}$$

where γ is a material parameter - the free surface energy per unit area. The application of equation (2) results in an expression for the Griffith fracture criterion

$$\sigma_t = (\frac{2E\gamma}{\pi c})^{\frac{1}{2}} \tag{4}$$

which defines the magnitude of tensile stress σ_t, applied normal to the crack, which will cause crack propagation. Thus, when $\sigma_n = \sigma_t$, the crack becomes unstable and any additional stress will cause the crack to propagate without a limit. Linear elastic fracture mechanics generalises this approach to consider other loading configurations and modes of crack growth.

Three modes of crack growth are possible in tension. These are opening (mode I), sliding (mode II) and tearing (mode III) as shown schematically in Figure 10. The generalised crack extension force G, for a constant load, can be expressed as

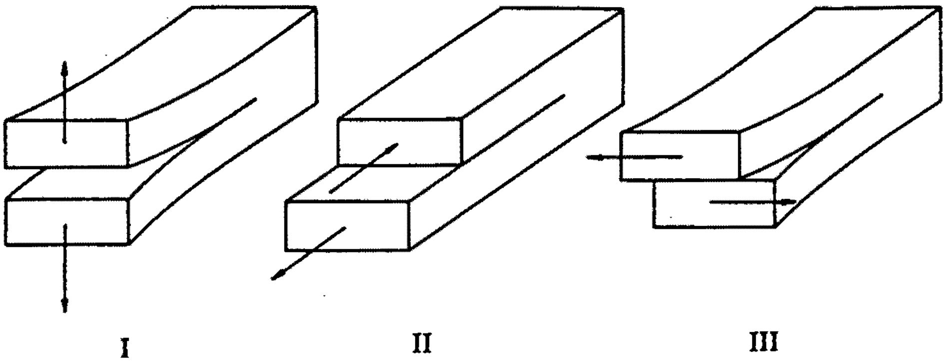

Figure 10: Schematic of three modes of cracking in extension (Lawn and Wilshaw, 1975)

$$G = -\left(\frac{\partial U_E}{\partial c}\right) = G_I(K_I) + G_{II}(K_{II}) + G_{III}(K_{III}), \tag{5}$$

which is the strain energy release rate per unit width of crack front. The crack extension force is often expressed as a function of the stress intensity factors K which depend on the crack boundary and loading conditions. The stress intensity functions are given as

$$K_I = m\sigma_{yy}(\pi c)^{\frac{1}{2}},\ K_{II} = m\sigma_{xy}(\pi c)^{\frac{1}{2}},\ K_{III} = m\sigma_{zy}(\pi c)^{\frac{1}{2}} \tag{6}$$

for a two-dimensional stress field, where m is a numerical modification factor to account for crack geometry, loading conditions and egde effects. Crack extension occurs when the strain energy release rate G attains a threshold value $G_c = 2\gamma$, which is characteristic of the material. The Griffith criterion can be generalised to three-dimensional stress states (Margolin, 1984).

3.2.2 Microcracking in compression

The application of compressive loading results in compaction and closure of pre-existing cracks (as described in Section 2.1). Walsh (1965 & 1980) investigated the measure of compressibility of an isotropic, porous medium containing randomly distributed cracks by considering the influence of pore geometry and concentration. Brace (1965) provided experimental confirmation of the findings. The effective compressibility β_{eff} of a porous medium is greater than the intrinsic compressibility β of the solid material. The effective compressibility of a porous medium containing penny-shaped cracks is given by

$$\beta_{\mathrm{eff}} = \beta\left(1 + \frac{16(1-\nu^2)\bar{c}^3}{9(1-2\nu)\bar{v}}\right), \tag{7}$$

where $\bar{c}$ is an average crack length, and $\bar{v}$ is the volume of a representative region. If the porosity of the material decreases, β_{eff} reduces to the intrinsic compressibility β of the solid material.

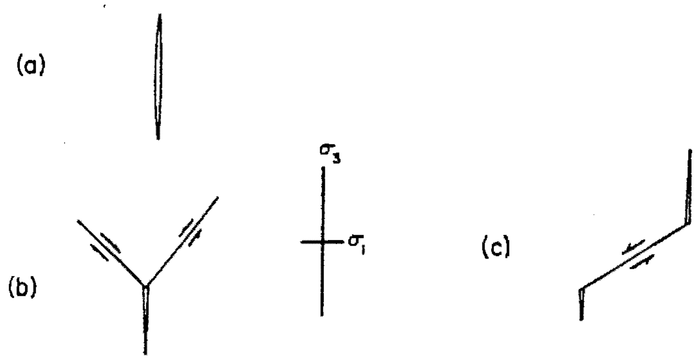

Figure 11: Mechanisms for the introduction of axial cracks in triaxial compression (Brace et al., 1966)

As compressibility is the inverse of the bulk modulus K, equation (7) implies that the material becomes stiffer as compressive load is applied. In a material containing ellipsoidal shaped cracks with a preferential orientation, the linear strain components making up the volume strain are affected differently by a mean pressure increase. If the cracks are rough, the changes in the effective compressibility due to void closure are resisted by the asperities on the crack surface. This results in a nonlinear relationship between the intrinsic compressibility and the effective compressibility (Walsh and Grosenbruch, 1979).

The formation of cracks in rock during deviatoric loading in compression, as detailed in Section 2.2.1, cannot be explained by the Griffith crack concept (Brace et al., 1966). Three mechanisms postulated for the formation of cracks in the direction of compression are shown in Figure 11. These mechanisms have been the subject of much research and debate and experimental results do not point to any one being dominant (Tapponier and Brace, 1976). The isolated crack is a penny-shaped crack which forms by opening of preferentially oriented grain boundaries or cleavage planes. In the second mechanism, the axial crack is initiated where three grain boundaries intersect. Crack growth results from the compressive load forcing the top grain into the boundary between the lower grains. The third occurs when the surfaces of inclined cracks, natural flaws, or pores slide relative to each other. The slip displacement results in the formation of axial cracks at the tips of the pre-exisiting flaw which propagate in the direction of the greatest principal compressive stress.

The hysteresis observed in the stress-strain response of rock under cyclic loading can be explained with the sliding crack model (Scholz and Kranz, 1974). On loading, frictional resistance prevents the inclined crack from sliding and the material remains elastic. Once the frictional resistance is exceeded, slip occurs on the inclined crack and tensile cracks extend from both ends of the sliding surface. The tensile cracks grow in the loading direction, causing dilatancy perpendicular to the loading. On unloading, the inclined crack remains fixed until the load level is reduced sufficiently to overcome the frictional stress in the reverse direction (back stress) and allow reverse sliding. As reverse sliding occurs, the tensile cracks close, reducing the dilatancy. Reloading results in a similar procedure, leading to hysteresis in the stress-strain response. Accumulation of dilatancy with cyclic loading can be attributed to wear along the sliding surfaces. Other experimenters (Zoback and Byerlee, 1975; Hadley, 1976; Holcomb and Stevens, 1980) have made use of this sequence of mechanisms to explain their experimental results.

The development of tensile cracks, termed wing cracks, at the edges of a sliding crack (flaw) in a two-dimensional, homogeneous, linear elastic material has been analysed extensively by Nemat-Nasser and Horii (1982), Horii and Nemat-Nasser (1986), Stief (1984) amongst others. The main features of the study will be reviewed in some detail since certain aspects are applied in the proposed damage model formulation (see Chapter 4). The stress intensity factors K_I and K_{II} relevant to the growth of the tensile cracks are determined in analytic form. Simplified, approximate expressions for the stress intensity functions are given by Horii and Nemat-Nasser (1986). The frictional resistance of the sliding flaw is considered to be a linear function of the stress σ_n acting normal to the flaw. Tensile crack growth occurs when the shear stress acting on the flaw equals the frictional resistance and K_I is equal to the opening mode fracture toughness K_c characteristic of the material.

To evaluate K_I and K_{II}, the pre-existing flaw of length $2c$ (at an angle γ to the principal compressive stress direction) and tension cracks of length l (at an angle θ to the flaw) are converted into a representative tensile crack of half-length l as shown in Figure 12. The representative crack is subjected to splitting forces which are equivalent to the driving shear stress on the flaw $\tau^\star$. The influence of the far-field stresses σ_1 and σ_2 is included in the expressions for the stress intensity factors which become

$$\begin{aligned} K_I &= 2c\tau^\star \sin\theta/\pi(l+0.27c)^{\frac{1}{2}} + (\pi l)^{\frac{1}{2}}\tfrac{1}{2}[\sigma_1+\sigma_2-(\sigma_1-\sigma_2)\cos 2(\theta-\gamma)] \\ K_{II} &= -2c\tau^\star \cos\theta/\pi(l+0.27c)^{\frac{1}{2}} + (\pi l)^{\frac{1}{2}}\tfrac{1}{2}(\sigma_1-\sigma_2)\sin 2(\theta-\gamma). \end{aligned} \tag{8}$$

The initial orientation of the wing cracks is calculated as the angle θ which maximises K_I. The result is $\theta = 72^o$ which appears to be independent of the angle of the sliding flaw.

The wing cracks are initially stable and cracks will grow only to a certain length. As the load increases, tensile cracks will extend from the smaller, less critical flaws. Eventually, at a sufficiently high density of wing cracking, the closely spaced microcracks grow together and the micro-columns between neighbouring wing cracks buckle, resulting in macroscopic faulting. This behaviour is observed in experiments on sheets of glass and resin and can also explain the processes of crack formation in brittle rocks (Nemat-Nasser and Horii, 1982).

An increase in confining (minor principal) stress decreases the length to which wing cracks will grow. Under relatively high confining stresses, shear failure occurs due to the formation of plastic zones parallel to the sliding flaw and the behaviour becomes ductile. The onset of the brittle - ductile transition depends on the orientation, the friction coefficient and the cohesion of the flaw. The presence of a slight lateral tensile stress (in the order of 4% of the axial compressive stress) alters the stability of the crack. The wing crack growth is initially stable, but will become unstable as the compressive load is increased resulting in propagation without the addition of

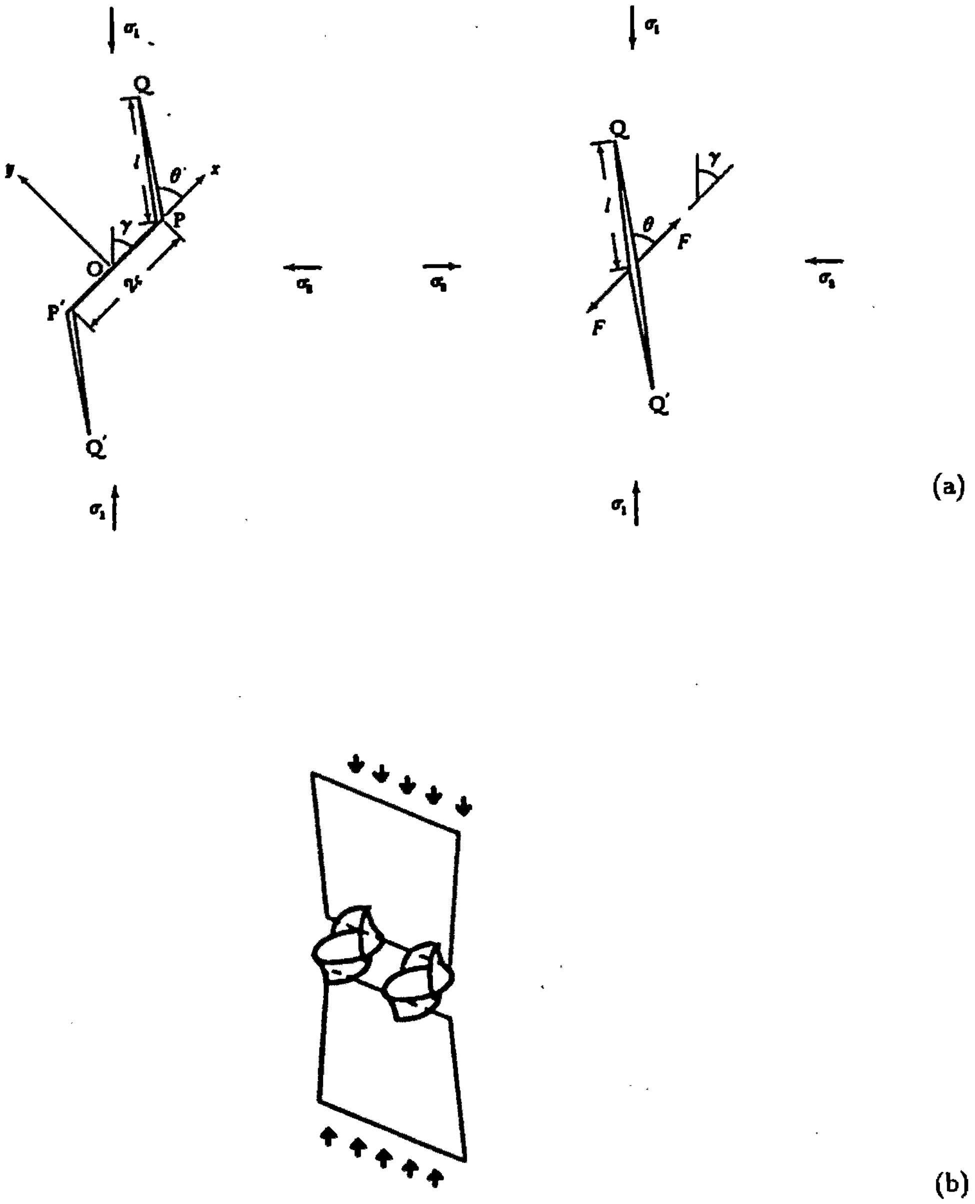

Figure 12: Schematic diagrams of wing cracking a: in two-dimensional stress states (after Nemat-Nasser and Horii, 1982), and b: in three-dimensional stress states (after Dyskin et al., 1994)

further loading.

Three-dimensional studies of wing crack formation due to compressive stresses were performed in plastic by Adams and Sines (1978). The initial penny-shaped flaw induces primary cracks which curve towards the direction of maximum compression. Secondary cracks, namely fish fin and petal cracks then initiate and extend in the loading direction. In resin, plexiglass or cementitious materials, large tensile cracks may grow in the direction of the maximum compressive stress when two initial flaws are aligned in the same plane, as shown in Figure 12b (Dyskin et al., 1994).

A similar formulation of wing (kinked) crack growth was developed by Stief (1984) who assumed that a friction law of the form

$$\tau = \sigma_{nt} \pm \mu \mid \sigma_{nn} \mid \tag{9}$$

controls the sliding processes along the surface. The stresses σ_{nt} and σ_{nn} are the shear and normal components of the far-field stresses, resolved along the flaw direction, and μ is the friction coefficient. A criterion for wing crack initiation is given which states that the deviatoric stress, required to cause crack initiation, is a linear function of the confining stress. The wing crack is initiated at an angle of about 70^o to the direction of the sliding crack and gradually grows towards the direction of the maximum compressive principal stress.

A population of sliding cracks can be represented by a mechanical analogue consisting of a block on a rough inclined plane, and restrained by an elastic spring in parallel with the plane (Holcomb, 1978). Sliding will take place when the force parallel to the place overcomes the shear resistance acting on the plane. If the load is reduced, the force in the spring will act to draw the block back up the plane, but only once the frictional resistance in the reverse direction has been overcome. For a constant crack aspect ratio, the dilatancy resulting from crack growth is proportional to the restoring force of the elastic spring. By considering a population of sliding flaws, having an assumed distribution of initial crack lengths and coefficients of friction, the deviatoric stress - volumetric strain relationship can be calculated for a particular loading and unloading sequence. The results compared qualitatively to inelastic volume measurements for triaxial tests on rock. An excessive amount of elastic volumetric behaviour is predicted during unloading, because elastic closure of wing crack on unloading was not modelled (Stevens and Holcomb, 1980).

An alternative to the sliding crack model, consisting of a population of 'Reversible Tensile Griffith Cracks' was proposed by Holcomb and Stevens (1980). The rock is assumed to contain a population of cracks which open as a result of tensile stress, and close when the stress is below some given magnitude. The population of cracks is specified by a distribution of opening and closing stresses and the dilatancy (inelastic volumetric strain) is proportional to the difference between the deviatoric stress and the stress at the onset of dilatancy. Tensile stresses caused by local inhomogeneities in the rock are assumed to cause crack opening. The hysteresis of the stress-strain response, and memory of previous stress states can be attributed to sequences of opening and closing in the crack population.

Dey and Wang (1981) analysed two other possible mechanisms for microcrack formation. In both models, a certain level of applied stress, a fraction of the ultimate load, is required before fracturing initiates. Microfracturing may occur either due to the mismatch of elastic properties between adjacent grains in the 'elastic inhomogeneity model' or at stress concentration points. In each model, the stress required for crack initiation is calculated to be a linear function of the confining stress.

3.3 Constitutive formulation of micromechanical mechanisms

3.3.1 Randomly distributed tension cracks

As mentioned earlier, the formation of microcracks in a material influences its stress - strain behaviour, and therefore its elastic properties. The elastic moduli of a cracked body in which elliptical shaped cracks are randomly distributed were obtained by Budiansky and O'Connell (1976) by application of the 'self-consistent method'. In this method, the calculation of the reduction in stiffness, or increase in compliance proceeds in such a way that "each individual inclusion sees itself as being a single crack embedded in an otherwise infinite and homogeneous body, but one which is characterised by the as yet unknown constants of the composite body" (Hoenig, 1979). Thus, the additional compliance due to the opening of cracks depends on the overall compliance of the material which is defined using an iterative procedure.

Budiansky and O'Connell (1976) calculate the crack influence by ascertaining the energy loss produced by a single elliptic crack under a general stress state in terms of shape and crack density parameters which depend on the Poisson's ratio, the crack size, its shape and direction. The energy loss for a random distribution of cracks is found by determining average values for the shape and crack parameters. Expressions for the effective (reduced) Young's and shear moduli ($\bar{E}$ and $\bar{G}$, respectively) resulting from the inclusion of elliptic cracks are then expressed in terms of a crack density parameter $\epsilon = \frac{2N}{\pi}\left\langle\frac{A^2}{P}\right\rangle$ related to the area A and perimeter P of the cracks, and the number N of cracks per unit volume. The initial isotropic compliance tensor, expressed in matrix form, relates the strain vector $\{\epsilon\}$ to the stress vector $\{\sigma\}$ by

$$\begin{Bmatrix} \epsilon_{xx} \\ \epsilon_{yy} \\ \epsilon_{zz} \\ \gamma_{yz} \\ \gamma_{zx} \\ \gamma_{xy} \end{Bmatrix} = [S] \begin{Bmatrix} \sigma_{xx} \\ \sigma_{yy} \\ \sigma_{zz} \\ \sigma_{yz} \\ \sigma_{zx} \\ \sigma_{xy} \end{Bmatrix} \quad \text{where} \quad S = \begin{bmatrix} \frac{1}{E} & -\frac{\nu}{E} & -\frac{\nu}{E} & 0 & 0 & 0 \\ -\frac{\nu}{E} & \frac{1}{E} & -\frac{\nu}{E} & 0 & 0 & 0 \\ -\frac{\nu}{E} & -\frac{\nu}{E} & \frac{1}{E} & 0 & 0 & 0 \\ 0 & 0 & 0 & \frac{1}{G} & 0 & 0 \\ 0 & 0 & 0 & 0 & \frac{1}{G} & 0 \\ 0 & 0 & 0 & 0 & 0 & \frac{1}{G} \end{bmatrix} \tag{10}$$

For long and narrow elliptic cracks of constant aspect ratio $b/a(b/a \ll 1)$ the relations between the effective and initial moduli, and the effective $\bar{\nu}$ and initial ν Poisson's ratio are given by

$$
\begin{aligned}
\frac{\bar{E}}{E} &= 1-\frac{16}{45}(1+\bar{\nu})(5-4\bar{\nu})\epsilon & (11)\\
\frac{\bar{G}}{G} &= 1-\frac{8}{45}(10-\bar{\nu}) & (12)\\
\epsilon &= \frac{45}{8}\frac{\nu-\bar{\nu}}{(1+\bar{\nu})[10\nu-\bar{\nu}(1+8\nu)]}. & (13)
\end{aligned}
$$

The equations can be solved simultaneously, given the initial elastic constants and the crack density parameter. As the crack density increases, the effective moduli decrease. For a crack density $\epsilon > \frac{9}{16}$, the effective moduli vanish altogether. This indicates that there is a critical density of cracking for which the material can retain its coherence.

3.3.2 'Aligned' penny-shaped tension cracks

Hoenig (1979) applied the self-consistent method to two situations of non-random cracks arrays. Firstly, the cracks are 'randomly distributed in planes, parallel to a given plane'. This situation results in planar transverse isotropy (PTI) of the compliance tensor. In this case two of the elastic constants are affected by the cracks in the material. If the given plane has its normal in the z-direction with respect to the global axes, the compliance is given by

$$
S = \begin{bmatrix}
\frac{1}{\bar{E}} & -\frac{\nu}{\bar{E}} & -\frac{\nu}{\bar{E}} & 0 & 0 & 0\\
-\frac{\nu}{\bar{E}} & \frac{1}{\bar{E}} & -\frac{\nu}{\bar{E}} & 0 & 0 & 0\\
-\frac{\nu}{\bar{E}} & -\frac{\nu}{\bar{E}} & \frac{1}{\bar{E}} & 0 & 0 & 0\\
0 & 0 & 0 & \frac{1}{\bar{G}} & 0 & 0\\
0 & 0 & 0 & 0 & \frac{1}{\bar{G}} & 0\\
0 & 0 & 0 & 0 & 0 & \frac{1}{\bar{G}}
\end{bmatrix} \tag{14}
$$

and the effective moduli are expressed as functions of the crack density parameter ϵ.

As an alternative arrangement. the normals to the cracks are assumed to be randomly distributed in a specified plane, giving rise to cylindrical transverse anisotropy (CTI) in which three of the independent constants are changed. The compliance matrix for crack normals distributed in a plane, with its normal in the z-direction with respect to the global axes, becomes

$$
S = \begin{bmatrix}
\frac{1}{\bar{E}} & -\frac{\bar{\nu}}{\bar{E}} & -\frac{\bar{\nu}}{\bar{E}} & 0 & 0 & 0\\
-\frac{1}{\bar{\nu}} & \frac{1}{\bar{E}} & -\frac{\bar{\nu}}{\bar{E}} & 0 & 0 & 0\\
-\frac{\bar{\nu}}{\bar{E}} & -\frac{\bar{\nu}}{\bar{E}} & \frac{1}{\bar{E}} & 0 & 0 & 0\\
0 & 0 & 0 & \frac{1}{\bar{G}} & 0 & 0\\
0 & 0 & 0 & 0 & \frac{1}{\bar{G}} & 0\\
0 & 0 & 0 & 0 & 0 & \frac{1}{G^*}
\end{bmatrix} \tag{15}
$$

where the values of $\bar{E}, \bar{\nu}, \bar{G}$ and G^* need to be determined by an iterative numerical procedure for a given crack density parameter. In both cases, the overall compliance always exhibits the form characteristic of transverse isotropy.

In a situation of a tensile crack introduced into an initially anisotropic medium (Hoenig, 1978; Ju and Lee, 1991) the additional compliance becomes fully anisotropic. The compliance then consists of the sum of the initial compliance $\boldsymbol{S}^{o'}$ and the additional compliance due to cracking in tension $\boldsymbol{S}^{\star\prime}$. The additional compliance for a single elliptical crack, of length a and aspect ratio γ, introduced into an anisotropic solid, of representative volume V, is given by

$$\boldsymbol{S}^{\star\prime} = \tfrac{4\pi a^3\gamma}{3V}\begin{bmatrix} 0 & 0 & 0 & 0 & 0 & 0 \\ 0 & 0 & 0 & 0 & 0 & 0 \\ 0 & 0 & C_{33}^{-1} & C_{32}^{-1} & C_{31}^{-1} & 0 \\ 0 & 0 & C_{23}^{-1} & C_{22}^{-1} & C_{21}^{-1} & 0 \\ 0 & 0 & C_{13}^{-1} & C_{12}^{-1} & C_{11}^{-1} & 0 \\ 0 & 0 & 0 & 0 & 0 & 0 \end{bmatrix} \qquad (16)$$

The components C_{ij}^{-1} are the coefficients of the crack influence matrix $\boldsymbol{C}^{-1}$ which relates the crack displacement magnitudes $\boldsymbol{\beta}_i$ to the applied stress state σ_i such that $\boldsymbol{\beta}_i = C_{ij}^{-1}\sigma_i$ (Hoenig, 1978). The overall compliance tensor is therefore also fully anisotropic.

The anistropy resulting from a predefined array of cracks can be described by a crack density tensor $\boldsymbol{\alpha}$ of second order (Kachanov, 1980) where

$$\boldsymbol{\alpha} = \frac{1}{V}\sum_k \sqrt{S_k}\int_{S_k(V)} n_k n_k dS_k \qquad (17)$$

and depends on the crack area S_k, the crack normals n_k , the number of cracks k in a representative volume element V of the material. In order to derive the compliance tensor, the elastic complementary energy f is expressed as an isotropic function of the invariants of the stress and crack density tensors, i.e. $f = f(\boldsymbol{\sigma}, \boldsymbol{\alpha})$. The degree of anisotropy that may be represented is determined by the choice of the order of terms involving the crack density tensor. Selection of terms which are linear in the crack density tensor is suggested to enable the evaluation of the material parameters. Thus. including only terms quadratic in stress and linear in $\boldsymbol{\alpha}$, the constitutive equation for the material becomes

$$\epsilon = \frac{\partial f}{\partial \sigma} = \frac{\partial}{\partial \sigma}\left[-\frac{\nu}{2E}(tr\sigma)^2 + \frac{1+\nu}{2E}(tr(\sigma\cdot\sigma)) + \eta_1 tr\sigma tr(\sigma\cdot\boldsymbol{\alpha}) + \eta_2 tr(\sigma\cdot\sigma\cdot\boldsymbol{\alpha})\right], \qquad (18)$$

which defines an orthotropic, linear elastic compliance with three different effective Young's moduli E_j. The effective shear moduli and Poisson's ratios are expressed as second order tensors G_{ij} and ν_{ij}, respectively. For $\boldsymbol{\alpha} = 0$ the free energy reduces to the isotropic elastic potential.

The change in the stiffness tensor resulting from the inclusion of arrays of microcracks can be obtained with a complementary procedure (Talrega, 1985) considering the Helmholtz strain energy ψ. The crack arrays are described by a set of vectors $V^{(\alpha)}$. The strain energy is expressed as a second order polynomial function of the strain tensor and the crack vectors and thus, the stress can be calculated as

$$\sigma = \rho(\frac{\partial\psi(\epsilon, V^{(\alpha)})}{\partial\epsilon}) \equiv (C^{o}_{ijkl} + C^{1}_{ijkl})\epsilon_{ij}. \tag{19}$$

The anisotropic stiffness tensor C^{1}_{ijkl} resulting from the cracks can be calculated for a variety of crack patterns. In a composite material, the crack patterns are predefined by the structure of the material, thus preserving the initial anisotropy (transverse or orthotropic) of the stiffness tensor.

The previously mentioned models have not considered the evolution of the microcracks with load. A 'process' model for the constitutive description of the evolution of a population of tensile cracks in concrete due to mode I crack growth was proposed by Sumerac and Krajcinovic (1987). The additional compliance due to cracking is again calculated with the self-consistent method (Hoenig, 1979; Horii and Nemat-Nasser, 1983). The crack population is represented by a distribution of initial lengths and orientations and microcrack growth occurs when the stress intensity factor K_I for any crack reaches a critical value K_c, the stress intensity factor characteristic of the material. The initial crack of length a is assumed to extend instantaneously to a length D, equal to a length defined by a unit cell or material grain which acts as an energy barrier. Complete failure of the material occurs as a result of a 'run-away' crack when K_I for any crack of length D exceeds K_{Ic}. Thus, the constitutive response in tension is characterised by nonlinear stress - strain behaviour while microcracks extend from lengths a to D, which end with an abrupt and complete loss of strength at failure when the first 'run-away' crack propagates.

3.3.3 Sliding cracks in compression

Initial studies of cracks in compression only considered the changes in elastic properties due to closure and sliding of pre-existing tensile cracks (Walsh, 1965; Horii and Nemat Nasser, 1983), as described in Section 3.2.2. However, the frictional sliding introduces a coupling between the volumetric and the shear behaviour and results in induced anisotropy of the compliance tensor. The anisotropy is introduced as additions to certain components of the compliance tensor. The identification and the magnitude of these additional components depends on the stress state and the load path.

Materials containing a population of sliding cracks were investigated by Kachanov (1982). Sliding is governed by a Coulomb friction law. It initiates on the surface with the most favourable direction which was found to be $\phi = \frac{1}{2}arctan\mu^{-1}$, where μ is the friction coefficient. As the stress state increases, cracks at other angles become active and start to slide. The total inelastic strain is evaluated as the sum of contributions of the strains from each sliding (active) crack. The re-

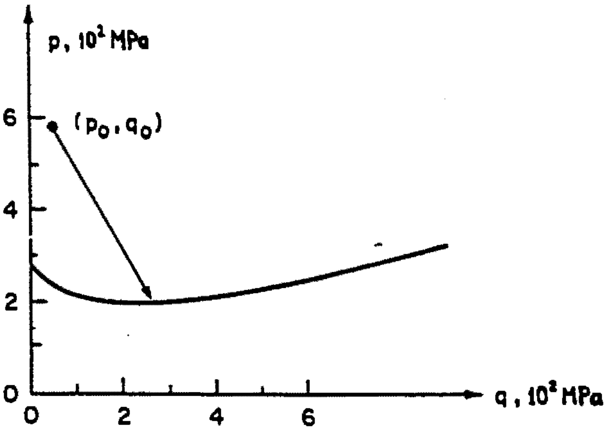

Figure 13: Hyperbolic deadband region in stress space during back-sliding of frictional cracks (Kachanov, 1982)

sulting incremental compliance tensor for conventional triaxial compression exhibits cylindrical transverse isotropy. Thus, for axial loading (in the σ_{33} direction), the symmetry conditions are

$$\begin{aligned} &S_{2222} = S_{1111}, \quad S_{1122} = S_{2211}, \quad S_{2233} = S_{1133}, \quad S_{1313} = S_{2323} \\ \text{and} \quad &S_{1212} = \tfrac{1}{2}(S_{1111} - S_{2211}), \quad S_{3311} = -(S_{1111} + S_{2211}), \quad S_{3333} = -2(S_{1133}). \end{aligned} \tag{20}$$

For a general loading path, the total compliance will become fully anisotropic.

Initiation of wing cracks (crack branching) is determined when the stress intensity factor at the edges of the sliding flaw reaches the fracture toughness (Kachanov, 1982), as described in Section 3.2.2. Explicit relations are given for the strain due to each wing crack, and constitutive relations are obtained by integrating these over the entire crack population. However, the observed dilatancy is underestimated by this formulation and modifications need to be included to consider opening due to asperities on the sliding cracks.

Upon unloading, the frictional resistance on the sliding cracks prevents back-sliding. The 'deadband' region, observed in experiments, identifies the stress interval during which the frictional resistance force changes direction and the onset of back-sliding can be described by a hyperbola in the p-q plane (see Figure 13).

Alternative constitutive relations for materials containing flaws and wingcracks can be obtained by simulating the three-dimensional microcracks as a distribution of effective, penny-shaped, cracks embedded in an isotropic, homogeneous medium (Fanella and Krajcinovic, 1988; Nemat-Nasser and Obata, 1988). The constititutive relations are produced by determining an expression for the strain as a function of the contributions from the initial elastic compliance, the sliding on cracks due to the far-field stresses, the increase in length of the sliding flaws and the opening of wing cracks. In this way, complex situations of crack growth can be modelled for an initial distribution of flaws. Sliding on flaws with or without growth, including wing crack extension are considered for loading in compression. During unloading, flaws may grow without sliding, slide in reverse without closing wingcracks, or back-slide with wingcrack closure. Numerical simulations of a number of triaxial stress paths exhibit trends which are qualitatively similar to the expected material behaviour.

A material containing cracks, and acted on by a sequence of loading in compression, has a fully anisotropic compliance tensor (Lee and Ju, 1991). Anisotropy is induced into the compliance tensor by opening, closing or sliding of the cracks. The sliding cracks may in turn initiate wing cracks at an angle to the initial flaw direction, which introduces additional components into the overall compliance tensor. For any stage of loading, the global compliance is expressed as

$$\bar{S} = \bar{S}^{\star 0} + \bar{S}^{\star sm} + \bar{S}^{\star um} + \bar{S}^{\star sII} + \bar{S}^{\star uII} + \bar{S}^{\star k} + \bar{S}^{\star n}, \tag{21}$$

where the superscript ^{0} denotes the initial compliance. The induced anisotropy results from the growth of :

open, stable cracks ($\bar{S}^{\star sm}$),
open, unstable cracks ($\bar{S}^{\star um}$),
closed, stable, sliding cracks ($\bar{S}^{\star sII}$),
closed, unstable, sliding cracks ($\bar{S}^{\star uII}$),
kinked (wing) cracks ($\bar{S}^{\star k}$),
nucleation of new cracks ($\bar{S}^{\star n}$).

The contribution from a single kinked (wing) crack $S^{\star k}$ has components due to the differential loading and to the confining stress acting normal to the wing crack i.e.

$$S^{\star k} = S_p^{\star k} + S_c^{\star k}. \tag{22}$$

The compliance component $\bar{S}^{\star n}$ results from the nucleation of new cracks and it includes contributions from nucleaction due to stable sliding, unstable sliding, and crack kinking. The overall compliance is calculated by integrating the additional compliance tensors from every active crack direction, and is a fully anisotropic, non-symmetric fourth order tensor.

The self-consistent method used to define the change in the compliance due to the inclusion of additional microcracks becomes invalid at high crack concentrations. Once the crack density has increased sufficiently, the cracks begin to interact and intersect and the effects of interaction between arrays of kinked cracks must be included in the constitutive relations as additional components of the compliance tensor (Kemeny and Cook, 1987; Ju, 1990).

3.4 Phenomenological continuum damage models

3.4.1 Scalar damage models

The development of phenomenological damage models arose from the concept that the growth of microcracks perpendicular to the direction of tensile loading can be expressed in terms of the loss of continuity of the material (Kachanov, 1958). Kachanov proposed a scalar internal variable φ to represent the continuity such that $\varphi = 1$ implied a material without any flaws or cracks, and $\varphi = 0$ represented the complete destruction of the ability of the material to sustain load. The magnitude of φ therefore describes the absence of imperfections in the material. An alternative concept, introduced by Rabotnov (1969) is to define the damage as the void area density $D = 1 - \varphi$. The damage parameter D therefore ranges from 0 to 1 as the continuity decreases, and characterises the evolution of the imperfections in the material. Damage evolution is described by an evolution law. For creep damage, Kachanov (1987) suggests a time dependent power law function of the stress σ such that

$$\frac{d\varphi}{dt} = -A(\frac{\sigma}{\varphi})^n, \tag{23}$$

where A and n are material parameters. The opening of voids within the material implies that there is a loss of the load carrying area and stress is only transferred by the continuous part of the material (Rabotnov, 1969). An 'effective stress principle' is defined which states that the stress $\bar{\sigma}$ in the solid part of the material is higher than the true (Cauchy) stress σ and can be expressed as $\bar{\sigma} = \sigma/\varphi$ or alternatively $\bar{\sigma} = (1 - D)\sigma$.

The effective stress is sometimes referred to as the net stress. To clearly distinguish between these two terms, the following convention is applied here :

- *the net stress* refers to the increase in stress within a sample due to the reduction in load bearing area (from the original area S to the current area $S^\star$) as a result of void growth. The net stress $\sigma^\star = \sigma S/S^\star = \sigma/(1 - \Omega)$.
- *the effective stress* is related directly to the true stress by the damage parameter. The effective stress $\bar{\sigma} = \sigma/(1-D)$. Direct specification of the evolution of the damage parameter D allows the consideration of the effect of local stress concentrations, interaction between defects, as well as void growth, on the material stiffness.

In the one-dimensional case, the definitions of damage in terms of D or Ω lead to equivalent damage models, the distinguishing feature of any model being the evolution law. These concepts have been extensively applied to model the creep behaviour of metals in tension (Chaboche, 1988; Hult, 1987; Kachanov, 1986; Lemaitre, 1984, 1985 & 1987, Lemaitre and Chaboche, 1990).

The effective stress principal must be supplemented by a principle of strain equivalence to derive a constitutive relation. This principle is expressed as : "any strain constitutive equation for a

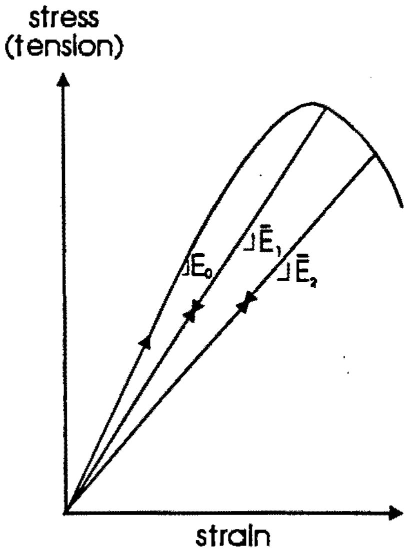

Figure 14: Schematic diagram of the effect of damage on the stress - strain response in uniaxial tension

damaged material ($D \neq 0$) is derived from the same potentials as for a virgin material ($D = 0$) except that all the stress variables are replaced by effective stresses" (Lemaitre, 1987). In one-dimensional applications, the elastic strain is defined as

$$\epsilon^e = \frac{\bar{\sigma}}{E_o} = \frac{\sigma}{E_o(1-D)} \tag{24}$$

for a material with an initial Young's modulus E_o. Damage evolution is defined by specifying the change of D during loading. An equivalent expression can be found by noting that the damage modifies the Young's modulus and thus, the constitutive relation is given by

$$\sigma = \bar{E}\epsilon^e, \quad \text{where} \quad \bar{E} = E_o(1-D). \tag{25}$$

The evolution of the damage can either be expressed through the parameter D or by directly specifying the effective modulus $\bar{E}$ (Lemaitre and Chaboche, 1990). As the damage evolves, the effective modulus decreases resulting in nonlinear stress - strain response, as shown schematically for uniaxial tension in Figure 14. The material unloads with the effective modulus and no permanent strain occurs during brittle damage. Physical interpretation of the damage concept is possible by considering a fibre bundle containing fibres with a non-uniform distribution of tensile strengths. As tensile load is applied, the individual fibres break in sequence and reduce the stiffness of the bundle (Krajcinovic, 1989; Breyesse, 1990).

The concepts of damage developed in the uniaxial situation can be generalised to three-dimensional stress and strain states (Chaboche, 1984; Simo and Ju, 1987; Lemaitre, 1985; Lemaitre and Chaboche, 1990). The constitutive relation of equation (24) becomes

$$\sigma = (1 - D)C_o\epsilon, \tag{26}$$

where the scalar damage parameter D modifies all components of the initial stiffness tensor C_o. The resulting model is isotropic, because the symmetry characteristics of the initial stiffness tensor are not altered by the damage (Ju, 1990).

The description of damage in brittle rock requires that the three-dimensional constitutive relations are divided into deviatoric and volumetric parts (Resende, 1984, Resende and Martin, 1984 & 1988). A scalar internal damage variable λ defines the degradation in the shear modulus. Thus, the secant shear modulus G reduces from the initial value G_o to zero as the damage parameter λ approaches unity. The situation of $\lambda = 1$ implies that the material can no longer sustain any shear stress. Failure, in the sense of rupture, occurs when a peak stress is attained, at some intermediate value of damage. Damage evolution is defined using rational functions of the deviatoric and the volumetric strain invariants and the mean stress. The stiffness decreases equally in all directions and no directional effect is experienced as the crack forms.

Dilatancy is introduced by expressing the elastic volumetric strain as a nonlinear function of the mean stress, the damage parameter λ, the damage rate $\dot{\lambda}$, the shear strain e and the shear strain rate $\dot{e}$. Damage couples the shear and volumetric strains and is decomposed into a shear component and a hydrostatic tension component. The shear damage is activated whenever the deviatoric strain invariant increases. Tension damage only occurs for a state of tensile mean stress, resulting in the identification of seven distinct modes of material behaviour. Comparison of model predictions with triaxial tests on Norite rock suggests that the dilatancy is modelled well, however, the anisotropic increase of the effective (tangent) poisson's ratio resulting from the opening of orientated cracks cannot be modelled.

Lubliner et al. (1989) considered two other types of damage behaviour namely the 'plastic' degradation of the cohesion of the material and the degradation of the elastic stiffness. The reduction of the elastic stiffness is achieved by expressing the stiffness as a function of a set of elastic and plastic damage variables. Scalar, elastic damage variables cause an isotropic reduction in the bulk and shear moduli according to evolution laws which are exponential functions of the volumetric and octahedral strains, respectively. Plastic degradation is defined as the reduction of the current stiffness proportional to the loss of cohesion during softening and increases as a function of the accumulated plastic work. Macroscopic cracking and the onset of localised failure modes is determined by post processing the converged results after each load step.

In concrete, the tension and compression strengths are significantly different. In a unilateral damage model, independent behaviour is defined for tensile and compressive states of stress (Lemaitre, 1987; Mazars and Pijaudier-Cabot, 1989; Chaboche, 1992). The stress tensor is decomposed into positive σ_+ and negative parts σ_- such that

$$\boldsymbol{\sigma}_+ = \begin{bmatrix} <\sigma_1> & 0 & 0 \\ 0 & <\sigma_2> & 0 \\ 0 & 0 & <\sigma_3> \end{bmatrix}, \quad \boldsymbol{\sigma}_- = -\begin{bmatrix} <-\sigma_1> & 0 & 0 \\ 0 & <-\sigma_2> & 0 \\ 0 & 0 & <-\sigma_3> \end{bmatrix}, \quad (27)$$

where the MacCauley bracket is defined as $< x >= x$ if $x \geq 0$, and $< x >= 0$ if $x < 0$. Then the constitutive relation becomes

$$\boldsymbol{\epsilon} = \frac{1}{E(1-D_t)}[(1+\nu)\boldsymbol{\sigma}_+ - \nu(tr\,\boldsymbol{\sigma})_+\boldsymbol{i}] + \frac{1}{E(1-D_c)}[(1+\nu)\boldsymbol{\sigma}_- - \nu(tr\,\boldsymbol{\sigma})_-\boldsymbol{i}], \quad (28)$$

where D_t and D_c are the tensile and compressive damage magnitudes, respectively and $\boldsymbol{i}$ is the second order identity tensor and tr denotes the trace of the tensor. The damage evolution is specified by independent functions for tension and compression.

3.4.2 Vector damage models

The concept of a vector damage model is a logical extension of the scalar damage models to be able to incorporate directionality of the microfracturing. The models are based on the assumption that a penny-shaped microfracture can be represented by a vector in the direction normal to the crack, the length of which is proportional to the crack area. A set of vectors defines the total damage, each vector corresponding to the void density in a particular plane of cracking (Davison and Stevens, 1972; Krajcinovic and Fonseka, 1981). The constitutive equation is obtained by expressing the Helmholtz free energy ψ of the material as a polynomial function of the strain tensor $\boldsymbol{\epsilon}$ and the damage vectors $\boldsymbol{\omega}$ using the theory of invariants. Thus,

$$\psi = \frac{1}{2}\epsilon_{ij}C_{ijkl}\epsilon_{kl} + c_1\omega_k^\alpha\epsilon_{kl}\omega_l^\beta\epsilon_{mm} + c_2\omega_k^\alpha\epsilon_{kl}\epsilon_{lm}\omega_m^\beta \quad (29)$$

for damage fields $\alpha, \beta = 1, 2\ldots$ with the material constants c_1 and c_2. The stiffness of the damaged material is given by

$$\frac{\partial^2\psi(\boldsymbol{\epsilon},\boldsymbol{\omega})}{\partial\boldsymbol{\epsilon}^2} \equiv C_{ijkl} = C_{ijkl}^0 + \sum_\alpha\sum_\beta[c_1(\delta_{ij}\omega_k^\alpha\omega_l^\beta + \delta_{kl}\omega_i^\alpha\omega_j^\beta) + c_2(\delta_{ik}\omega_j^\alpha\omega_l^\beta + \delta_{jl}\omega_i^\alpha\omega_k^\beta)], \quad (30)$$

in which only those crack directions corresponding to a positive (tensile) strain ϵ_a are considered, δ_{ij} being the Kroneker delta. Then,

$$\boldsymbol{\omega} \begin{array}{ll} \neq 0 & \text{if } \epsilon_a = \boldsymbol{\omega}\cdot\boldsymbol{\epsilon}\cdot\boldsymbol{\omega} > 0 \\ = 0 & \text{if } \epsilon_a < 0 \end{array} . \quad (31)$$

The formulation consists of a superposition of a number of transversely isotropic stiffness matrices, rendering the material orthotropic. For example, in the case of microcracking under uniaxial tension (in the σ_{11} direction) the damage occurs in one direction ($\alpha = \beta = 1$) and the stiffness matrix becomes

$$C = Ek \begin{bmatrix} 1+(C_1+C_2)\omega^1 & \bar{\nu}+\frac{1}{2}C_1\omega^1 & \bar{\nu}+\frac{1}{2}C_1\omega^1 \\ \bar{\nu}+\frac{1}{2}C_1\omega^1 & 1 & \bar{\nu} \\ \bar{\nu}+\frac{1}{2}C_1\omega^1 & \bar{\nu} & 1 \end{bmatrix} \tag{32}$$

with $k = \frac{1-\nu}{(1+\nu)(1-2\nu)}$, $\bar{\nu} = \frac{\nu}{1-\nu}$ and c_1 and c_2 are the material constants.

For uniaxial compression in the σ_{33} direction, two sets of microcracks occur in the directions of the positive radial strains ϵ_{11} and ϵ_{22}. The stiffness is then

$$C = Ek \begin{bmatrix} 1+(C_1+C_2)\omega^\alpha & \bar{\nu}+\frac{1}{2}C_1(\omega^\alpha+\omega^\beta) & \bar{\nu}+\frac{1}{2}C_1\omega^\alpha \\ \bar{\nu}+\frac{1}{2}C_1(\omega^\alpha+\omega^\beta) & 1+(C_1+C_2)\omega^\beta & \bar{\nu}+\frac{1}{2}C_1\omega^\beta \\ \bar{\nu}+\frac{1}{2}C_1\omega^\alpha & \bar{\nu}+\frac{1}{2}C_1\omega^\beta & 1 \end{bmatrix}. \tag{33}$$

The initiation of damage is defined by a set of surfaces in the strain space, each corresponding to a possible crack direction. The damage initiation criterion consists of a hyperbolic function of the strains normal and tangential to the crack. The damage increment is assumed to occur normal to the active (representing a critical state of strain) damage surface, analogous to associated flow in the theory of plasticity. An evolution law specifies the relationship between the strain and the damage magnitude for each damage vector. The shape of the damage surface changes if new crack directions are activated during loading. Damage induced by previous stress paths influences the stress - strain relationship and the ultimate strength. Thus, the formulation is path dependent.

Singh and Digby (1989) proposed a modification of the phenomenological model by Krajcinovic and Fonseka (1981) by expressing the damage surface as a quadratic function of the normal and shear strains. Damage is defined by a number of vectors, each representing a set of equal sized, penny-shaped cracks in a particular direction. The effective damage on a plane is considered to be the sum of the projections of the damage vectors onto a specified plane. The additional compliance tensor resulting from the effective damage is evaluated using the self-consistent method by Horii and Nemat-Nasser (1983).

Analysis of the thermodynamics of the damage process by Krajcinovic (1983 & 1985) showed that the damage evolution must be expressed in terms of the conjugate thermodynamic forces instead of being formulated directly in the strain space. In vector damage models, the conjugate forces represent the energy release rates in each crack direction and are derived directly from the free energy potential. Application of this concept leads to the formulation of the damage surface as a set of hyperplanes in the n-dimensional conjugate force space, where n is the number of pre-defined crack orientations (Ilankamban and Krajcinovic, 1987). The increment of damage in a particular direction is normal to the corresponding hyperplane. The interaction between damage directions is neglected. The model is able to simulate the evolution of both, the pattern and the density of the microcracking in Quartzite and Norite in uniaxial and triaxial compression assuming an initially uniformly distributed crack arrangement.

Krajcinovic (1985) stated that in vector damage models, the magnitude of the damage depends on whether the stress is tensile or compressive. Therefore, only the microcrack distribution properly represents the history and the current state of the material and should be selected as the internal variable instead of the damage magnitude. There is considerable controversy regarding the ability of vector damage models to represent the opening and closing of microcracks under mixed tension and compression stress states (Chaboche, 1992). A vector damage model developed by Andrieux et al. in 1986 which excludes the possibility of stress discontinuities during loading from tension to compression was shown to introduce other problems, because it does not properly represent the change in compliance due to aligned cracks as derived in the analytical solution by Hoenig (1979) (Chaboche, 1992) (see also Chapter 2). Vector damage model can, however, be formulated to distinguish between damage growth due to crack opening under tension and due to crack growth by sliding under compression (Gambarotta et al., 1993).

The discussed vector damage models consider only homogeneous materials with prescribed initial flaw distributions. Heterogeneous materials such as concrete were addressed by Ortiz and Popov (1982b). Different constitutive relations are developed for the mortar and aggregate phases. The two phases are combined in proportion to the relative volume of each phase using the theory of mixtures (Ortiz and Popov, 1982a). The combination of the isotropic, elastic model for the aggregate phase and the vector model for the tension damage in the mortar results in a material which is orthotropic. In compression, interaction between the two phases results in tensile stresses in the mortar which, in turn, cause damage to occur.

The vector damage representations implicitly assume that the shape of the microfracturing has little effect on the material response. Irregular shaped cracks can only be represented by the projection onto a plane in the average direction of the crack. Thus, the dilatancy normal to the crack due to the crack opening is neglected (Krajcinovic, 1984). As a further complication, the microcracks are actually distributed throughout the material and Krajcinovic (1985) showed that there must be some means of averaging of the damage in a particular plane. One method is to determine the damage variable corresponding to a particular direction as the ratio of the weighted average of the void area with respect to the area of a representative material element. The weighting function is defined such that only flaws within a specified characteristic length of the damage plane are considered. The constitutive description of the material therefore depends on the state of damage apart from the point under consideration.

3.4.3 Second order tensor damage models

An improved, three-dimensional representation of the microcracking can be obtained with second order tensor damage models. Most of these models are based on a generalisation of the net stress concept (Murakami and Ohno, 1981; Murakami, 1987 & 1988; Kawamoto et al., 1988; Swoboda, 1990; Swoboda et al., 1990; Chaboche, 1992). The reduction in the net load bearing area, defined by a vector $\mathbf{s}^\star$, from the the original area, represented by $\mathbf{s}$, is characterised by the second order damage tensor Ω in a linear relationship

$$\mathbf{s}^\star = [\boldsymbol{i} - \boldsymbol{\Omega}]\mathbf{s}, \tag{34}$$

where $\boldsymbol{i}$ is the second order identity tensor. Assuming that the traction vector $\mathbf{p}$ on the plane of damage is equal in the damaged and undamaged configurations, i.e.

$$\mathbf{p} = \boldsymbol{\sigma} \cdot \mathbf{s} = \boldsymbol{\sigma}^\star \cdot \mathbf{s}^\star, \tag{35}$$

the net stress $\boldsymbol{\sigma}^\star$ is related to the Cauchy stress $\boldsymbol{\sigma}$ by

$$\boldsymbol{\sigma}^\star = [\boldsymbol{i} - \boldsymbol{\Omega}]^{-1} \cdot \boldsymbol{\sigma}. \tag{36}$$

The exact definition of the damage tensor $\boldsymbol{\Omega}$, and the manner in which the evolution law is defined, is the major difference in the various formulations, some of which are discussed below.

The damage tensor can be expressed as

$$\boldsymbol{\Omega} = \sum_{j=1}^{3} \Omega_j \boldsymbol{v}_j \otimes \boldsymbol{v}_j \tag{37}$$

in terms of the surface density of cavities Ω_j in the principal directions $\boldsymbol{v}_j$ (Murakami and Ohno, 1981). Additional strains resulting from damage are determined from the hypothesis of strain equivalence by replacing the Cauchy stress tensor in the elastic constitutive relations with the symmetric part of the net stress tensor. The symmetric part of the net stress is assumed to be

$$\boldsymbol{\sigma}_s^\star = \tfrac{1}{2}(\boldsymbol{\sigma} \cdot [\boldsymbol{i} - \boldsymbol{\Omega}]^{-1} + [\boldsymbol{i} - \boldsymbol{\Omega}]^{-1} \cdot \boldsymbol{\sigma}). \tag{38}$$

For damage of rock and concrete, the positive and negative parts of the stress tensor are independently made symmetric (Murakami, 1988). An alternative expression given as

$$\boldsymbol{\sigma}_s^\star = ([\boldsymbol{i} - \boldsymbol{\Omega}]^{-\frac{1}{2}} \cdot \boldsymbol{\sigma}[\boldsymbol{i} - \boldsymbol{\Omega}]^{-\frac{1}{2}}). \tag{39}$$

can also be used to obtain a symmetric net stress (Chaboche, 1992). The method by which the net stress is made symmetric can cause subtle differences in the material behaviour and, in particular, affects the principal stress magnitude and directions, the damaged elastic moduli, and the failure criterion (Zhang et al., 1990).

The damage tensor for a set of N cracks in rock can be expressed as

$$\Omega_{\text{total}} = \sum_{k=1}^{N} \omega_k \boldsymbol{n}_k \otimes \boldsymbol{n}_k, \tag{40}$$

where ω_k is the crack density on the plane with the orientation vector $\boldsymbol{n}$. Inclusion of the net stress tensor into the principle of virtual work for the material results in a finite element formulation in which the material constitutive behaviour remains isotropic elastic. The difference between the net and Cauchy stresses is applied as a set of additional nodal loads (Swoboda, 1990; Swoboda et al., 1990) Evolution of the damage tensor as a result of ductile, plastic creep is included by relating the damage increment to the evolution of the plastic strain (Swoboda and Beichuan, 1991). The damage is anisotropic and propagates in the direction of the maximum principal compressive stress.

Stress induced damage in rock under uniaxial compression is modelled by expressing the stiffness tensor as a function of two second order damage tensors. The tensors express the contributions to damage from the normal and shear components of the strain acting on the plane of cracking. Damage growth is determined by an anisotropic hardening damage potential in the space of the conjugate thermodynamic force (Stumvoll et al., 1991). The angle of the crack planes and the confining pressure have a strong influence on the material response in biaxial compression (Swoboda and Ito, 1993).

A mixture of the net stress and effective stress concepts was proposed by Costin(1983) for damage modelling of rock. Isolated penny-shaped microcracks require tensile stresses for growth. The problem of the growth of cracks in a continuum subjected to a compressive stress state is approached by assuming that tensile stresses arise from contacts between irregular grain boundaries in rock. The microcracks are assumed to be driven by local tensile stress fields, acting in the same direction, and are proportional in magnitude to the applied principal deviatoric stresses. Damage is modelled by reducing the Young's moduli in three principal directions as a function of the principal deviatoric stresses. Dilation, resulting from the opening of the microcracks, is included as a contribution to each principal strain in proportion to the local tensile stresses in the corresponding direction.

A damage surface similar to the Mohr-Coulomb failure surface is derived by assuming that the growth of a set of microcracks can be modelled by the evolution of a single crack. The damage criterion is developed using concepts form linear elastic fracture mechanics for penny-shaped cracks, combining a positive stress intensity factor for crack growth due to the deviatoric stresses, a negative stress intensity factor for crack closure resulting from the overall state of hydrostatic compression, a stress orientation function, and a memory function that remembers the maximum crack size. A constitutive relation is derived by expressing the Young's modulus in terms of a damage internal variable that expresses the current crack density as a proportion of the critical crack density parameter. The model tends to overestimate the volumetric compression observed in uniaxial and triaxial tests on Westerly Granite.

A plasticity formulation was used as a basis of models for stress induced damage in rock (Dragon,

1976) and for creep damage (Dragon and Mroz, 1979). The damage is quantified by a second order tensorial internal variable that defines the magnitude and direction of cracking. The damage variable ϕ_{ij} is therefore a phenomenological equivalent of the average crack density tensor $\boldsymbol{\alpha}$, presented by Kachanov (1980) (see Section 3.3.2). The direction of damage is defined from observations that cracking is related to the increments of the positive principal deviatoric stress. A surface defining the onset of cracking is assumed to exist in stress space. Damage occurs in compression, once the stress state exceeds the damage surface and a positive increment of a non-negative principal deviator stress occurs. In tension, the positive, principal values of the total stress tensor define the damage direction.

The change in the damage tensor is defined by a further potential, which incorporates the effect of the stress state in inhibiting or accelerating the damage evolution. The constitutive relations are developed from a potential function of the stress as well as the damage variable. The material is assumed to be isotropic, and evolution laws are porposed for the change in the shear and bulk moduli as a function of a 'crack intensity' parameter. The evolution of dilatancy and the failure envelope predicted by the model are similar to experimental results obtained for concrete.

3.4.4 Fourth order tensor damage models

The expression for the relationship between the net stress $\boldsymbol{\sigma}^{\star}$ and the Cauchy stress $\boldsymbol{\sigma}$, presented in equation (36), can be generalised as

$$\boldsymbol{\sigma}^{\star} = [\mathrm{M}(\boldsymbol{D})]\boldsymbol{\sigma} \tag{41}$$

and the fourth order 'damage effect' tensor $\mathrm{M}(\boldsymbol{D})$ can be specified directly in terms of the relative loss of area in the principal directions of damage D_i. The equivalent strain principal is replaced by a hypothesis of equivalent elastic strain energy to obtain the net elastic stiffness

$$\boldsymbol{C}^{\star} = \mathrm{M}^{-1}\boldsymbol{C}_o(\mathrm{M}^{-1})^T \tag{42}$$

which is a symmetric fourth order tensor (Chow and Wang, 1987; Chow and Lu, 1989).

Evolution of the damage can be described by the thermodynamic force conjugate to the damage tensor $\boldsymbol{D}$ which is the fourth order, elastic strain energy release rate tensor $-\boldsymbol{Y}$. The tensor $\boldsymbol{Y}$ is analogous to the strain energy release rate G in linear elastic fracture mechanics presented in Section 3.2.1. A damage dissipation potential is required in the space of $-\boldsymbol{Y}$ to define the evolution of the fourth order damage tensor. For creep damage of metals in tension, a damage characteristic tensor $\boldsymbol{J}$ is used to reduce the damage potential to a function of scalar variables (Chow and Lu, 1989).

A similar concept is applied by Valliappan et al., (1990) and Zhang et al., (1990) to include the damage due to sets of pre-existing cracks in rocks into a finite element analysis. Quantification of the damage variables is performed by a statistical estimate of the loss of area, based on a probabilistic analysis of the cracks (Zhang and Valliappan, 1990a & b). An evolution law is not specified for the damage variables, and therefore the formulation cannot be strictly considered as a damage model in terms of the definitions suggested by Krajcinovic (1989).

The above-mentioned fourth order models are generalisations of the net stress concept. Other fourth order models can be derived by extending the effective stress principle to three-dimensional stress states. In these models, the stiffness tensor is directly modified by the damage.

Generalisation of a fibre bundle model (Dougill and Rida, 1980) results in the description of the damage initiation by a set of linear loading functions in the strain space. Each potential direction of fracturing is defined by a loading function. The functions expand as a result of energy dissipated during progressive fracturing, analogous to the theory of isotropic hardening in the strain based theory of plasticity. Individual components of the stiffness tensor which are changed by the damage are identified by a fourth order direction tensor comprising the tensor product of the normal of the current fracture surface with itself. The magnitude of the change in the damage is related to dissipation potentials, which are different for extension and compression.

Another way of directly expressing the effective stiffness tensor $\boldsymbol{C}$ in terms of a fourth order damage tensor $\boldsymbol{D}$ is in a linear relationship with the initial stiffness $\boldsymbol{C}_o$. Then

$$\boldsymbol{C} = (\boldsymbol{I} - \boldsymbol{D})\boldsymbol{C}_o, \tag{43}$$

and the evolution of damage is defined in terms of changes to $\dot{\boldsymbol{D}}$ (Chaboche, 1984; Lemaitre and Chaboche, 1990). The Cauchy stress is now related to the effective stress by

$$\sigma = \boldsymbol{M}\bar{\sigma}. \tag{44}$$

where $\boldsymbol{M}$ is a damage effect tensor (different to $\mathbf{M}$ in equation (41). The direction of the damage is defined to be a linear combination of isotropic damage and damage due to a particular pattern of cracking, defined by a fourth order 'damage characteristic tensor' $\boldsymbol{G}$. The increment in damage comprises a scalar magnitude parameter D and the fourth order direction tensor $\boldsymbol{Q}$. Thus, the change in the damage tensor is

$$\dot{\boldsymbol{D}} = \boldsymbol{Q}\dot{D} = [\gamma \boldsymbol{I} + (1-\gamma)\boldsymbol{G}]\dot{D}, \tag{45}$$

where the parameter γ is a weighting factor and $\boldsymbol{I}$ is the fourth order identity tensor. The tensor $\boldsymbol{G}$ is be defined for specific crack patterns.

A phenomenological damage theory was proposed specifically for concrete by Ortiz (1985), to account for material behaviour due to the influence of aggregate - mortar interaction. The aggregate and mortar are considered as two separate phases similar to the earlier, vector damage model for concrete (Ortiz and Popov 1982 a &b). The model aimed to predict the different damage evolution rates and ultimate strengths in tension and compression, induced anisotropy, dilatancy, postfailure softening, including the effect of confining pressure and hysteresis during un/reloading cycles. The internal variable is the additional compliance S^c resulting from the opening of cracks. The total compliance tensor can be expressed as the sum of the initial S^o and additional (damaged) S^c components e.g.

$$S = S^o + S^c. \tag{46}$$

Tensile damage is assumed to result from the loss of load bearing area, normal to a crack, due to crack growth. Compression damage is due to loss of area in "the average plane of the crack" that occurs as a result of the "tortuous path" followed by compressive cracks (Ortiz, 1985). The strain associated with tension crack opening is assumed to always have positive eigenvalues. This produces a unilateral constraint such that the material remains undamaged when the cracks are not active (open). In the model, this constraint is enforced by ensuring that the tensile damage strain is related to the positive part of the stress tensor σ^+. Compression damage depends on the negative part of the stress tensor σ^-. Thus, the total strain

$$\epsilon = S^o : \sigma + \mathbf{P}^+(S^c : \sigma^+) + \mathbf{P}^-(S^c : \sigma^-). \tag{47}$$

The projection operators $\mathbf{P}^+$ and $\mathbf{P}^-$ are determined from the expressions

$$(\mathbf{P}^+ : \epsilon)_{ij} = \sum_{\alpha=1}^{3} < \epsilon^\alpha > d_i^\alpha d_j^\alpha \quad \text{and} \quad \mathbf{P}^- = I - \mathbf{P}^+ \tag{48}$$

in terms of the eigenvalues ϵ^α and eigenvectors d^α of the strain tensor.

The Gibb's free energy can then be expressed in terms of the separate parts of the stress. The dissipation potential associated with the Gibb's free energy becomes a thermodynamic flow potential which defines the damage initiation surface. The direction of damage is related to the gradient of the damage surface by fourth order tensor response functions $\boldsymbol{R}_I(\sigma)$ for tension, and $\boldsymbol{R}_{II}(\sigma)$ for compression, respectively. The magnitude of the additional compliance in tension is defined by a cumulative damage parameter μ which is always positive and increasing. The magnitude of the damage in compression is a fraction of the tensile damage, determined by the cross effect coefficient c.

The increment in the compliance tensor due to damage becomes

$$\dot{S}^c = \dot{\mu}\boldsymbol{R}_I(\sigma) + c\dot{\mu}\boldsymbol{R}_{II}(\sigma) = \dot{\mu}\frac{\sigma^+ \otimes \sigma^+}{\sigma^+ : \sigma^+} + \dot{\mu}c\frac{\sigma^- \otimes \sigma^-}{\sigma^- : \sigma^-}. \tag{49}$$

This is analogous to the assumption of associated flow in the theory of plasticity. The magnitude of μ is determined from an empirical expression obtained from an uniaxial tension test.

Aggregate is modelled by a Drucker-Prager elastic-perfectly plastic model, and the combination of the mortar and aggregate is achieved by assuming that an arbitrary small volume includes both phases. The strain in each phase is assumed to be equal and thus, different phase stresses occur in the mortar and the aggregate to equilibrate the applied stress. The damage is therefore driven by the stresses in the mortar phase.

The damage model by Yasdani and Schreyer (1988) is based on that of Ortiz (1985), but is concerned mainly with the compressive stress environment. The model neglects the two phase approach and instead includes a more complicated partition of the strain tensor into elastic, recoverable and inelastic damage. Damage under hydrostatic compression is prevented by expressing the response function in compression in terms of the cross product of a modified negative stress tensor

$$\tilde{\boldsymbol{\sigma}} = (\boldsymbol{\sigma}^- - \lambda \boldsymbol{i}). \tag{50}$$

The maximum eigenvector of the negative stress tensor λ is subtracted from each negative eigenvalue to ensure that no damage occurs in the direction of λ. In this way, damage will only occur for non-hydrostatic compression paths. There is no initial damage threshold, and the damage occurs immediately once the stress changes from hydrostatic compression. In a triaxial compression test, only the axial strain is affected by damage, and so an additional response function is included to cause damage in the lateral direction. This results in an increase in the Poisson's ratio as the damage evolves. The contributions to the compliance resulting from tension and compression damage are expressed as

$$\dot{\boldsymbol{S}}_I^c = \dot{k}\frac{\boldsymbol{\sigma}^+ \otimes \boldsymbol{\sigma}^+}{\boldsymbol{\sigma}^+ : \boldsymbol{\sigma}^+} \qquad \text{and} \qquad \dot{\boldsymbol{S}}_{II}^c = \dot{k}\omega\frac{\tilde{\boldsymbol{\sigma}} \otimes \tilde{\boldsymbol{\sigma}}}{\tilde{\boldsymbol{\sigma}} : \tilde{\boldsymbol{\sigma}}} + \omega\alpha H(-\lambda)(\mu \boldsymbol{I} - \boldsymbol{i} \otimes \boldsymbol{i}), \tag{51}$$

respectively. The parameter ω is the cross effect coefficient, α is the lateral pressure parameter, μ is a material parameter and $\boldsymbol{i}$ and $\boldsymbol{I}$ are the second order and fourth order identity tensors, respectively. The magnitude of the increment in the additional compliance $\dot{k}$ is determined by the same empirical expression for the additional compliance in uniaxial tension $\dot{\mu}$ from the Ortiz (1985) model. Inelastic strain $\boldsymbol{\epsilon}^r$ representing microcracks which do not close fully, is included as a function of the deviatoric part $\boldsymbol{s}$ of the negative stress tensor $\boldsymbol{\sigma}^-$, and evolves differently for the negative and positive parts $\boldsymbol{s}^-$ and $\boldsymbol{s}^+$. Thus,

$$\dot{\boldsymbol{\epsilon}}^r(k) = \dot{k}\omega \boldsymbol{s}^- + \dot{k}\omega\beta \boldsymbol{s}^+, \tag{52}$$

where β is a material constant. Ductile behaviour at higher confining pressures is modelled by an independent, isotropic hardening plasticity model with a von Mises yield surface (Yasdani and Schreyer, 1990). The damage and plasticity surfaces exist simultaneously in stress space, and the mode of behaviour is determined by whether the damage criterion or the yield surface is attained first.

Damage in the lateral direction during tensile loading is included by Yasdani (1993). In addition, the cross effect coefficient ω is removed, and a distinction between the compressive and tensile damage is made by applying independent evolution functions for the additional compliance.

A strain based model for tension damage, in which the stiffness tensor is the internal variable, was developed from similar principles by Simo and Ju (1987). Damage is considered to be either ductile (isotropic) or brittle (anisotropic). For isotropic damage, the magnitude of the damage is related to the evolution of the equivalent energy norm of the strain tensor. In the case of brittle damage, only the positive part of the strain tensor is considered in the energy norm.

The free energy is defined in terms of the total strain, and is divided into elastic, plastic and dissipative parts. Introduction of the 'principle of maximum damage dissipation' allows the definition of the direction and magnitude of the damage tensors in terms of a damage criterion in the space of the conjugate thermodynamic force. The conjugate force is a fourth order tensor determined by the cross product of the positive projections of the current strain tensor. The description of the evolution of damage is simplified by expressing the damage criterion in terms of a scalar function of the positive strain tensor, the equivalent tensile strain τ. The magnitude of the damage accumulation then depends on the increase in τ. Anisotropy of the stiffness arises from the modification of selected components of the initial stiffness tensor. The components for a particular strain state are identified by the operation of the fourth order, positive projection tensor on the initial stiffness tensor. Thus, the reduction in stiffness is given by

$$\dot{\boldsymbol{C}} = -\dot{\tau} H \mathbf{P}^{+} : \boldsymbol{C}_o : \mathbf{P}^{+} \tag{53}$$

where H represents the damage accumulation function, and the postitive projection operator $\mathbf{P}^{+}$ is defined in terms of the eigenvalues ϵ_i^e of the strain tensor as

$$\mathbf{P}^{+}{}_{ijkl} = Q^{+}_{ia} Q^{+}_{jb} Q_{ka} Q_{lb} \quad \text{with} \quad \boldsymbol{Q}^{+} \equiv \sum_{i=1}^{3} H[\epsilon_i^e](\boldsymbol{p}_i \otimes \boldsymbol{p}_i) \quad \text{and} \quad \boldsymbol{Q} \equiv \sum_{i=1}^{3} (\boldsymbol{p}_i \otimes \boldsymbol{p}_i), \tag{54}$$

where the Heaviside function $H[\epsilon_i^e]$ selects only the positive eigenvalues corresponding to the principal directions $\boldsymbol{p}_i$.

The strain based formulation was extended by Ju (1989) who redefined the free energy to only depend on the elastic part of the strain tensor and the plastic internal variables. This is consistent with the split of strain into elastic and plastic components in conventional plasticity models, and allows for elastic-plastic coupling of the damage.

The effective stress principle is generalised to relate the effective stress tensor to the nominal stress by a linear transformation. The hypothesis of strain equivalence is shown to result in a one to one relationship between the damage tensor and the secant stiffness. Thus, the secant stiffness itself is taken as the internal variable.

The elastic and plastic properties are coupled by the introduction of the stiffness tensor, the internal variable, in both, the elastic and the plastic parts of the free energy. The plastic behaviour is formulated in the effective stress space, resulting in an elastic-plastic coupling. Thus, elastic degradation induces degradation in the plastic yield stresses. The effective stress principle allows for independent consideration of the plastic and damage material response. The plasticity is formulated in the effective stress space, allowing the application of standard return algorithms for the numerical integration procedure.

The magnitude of the damage is represented by the undamaged energy norm ξ^+ of the positive part of the strain tensor. The components of the stiffness tensor that are affected by the damage are defined by an operation of the fourth order positive projection tensor on the initial stiffness tensor as

$$\dot{C}^{c+} = \xi^+ H^+ \mathbf{P}^+ : C^o : \mathbf{P}^+ \quad \text{and} \quad \dot{C}^{c-} = \xi^- H^- \mathbf{P}^- : C^o : \mathbf{P}^- . \tag{55}$$

This formulation considers the change in stiffness which has the advantage of being more stable than the compliance based models when implemented in a finite element scheme. The projections of the stiffness tensor based on the positive and negative parts of the strain are similar to those of Ortiz (1985), however, as pointed out by (Ju, 1989), the effects on the damage directions are quite different.

The generalisation of the principle of effective stress leads to a linear relationship between the effective stress and the Cauchy stress, as expressed in equations (41) and (44). This places excessively restrictive constraints on the damage and prevents a proper description of three dimensional damage evolution (Baste and Audoin, 1991).

To overcome these restrictions, the internal variable is defined directly equivalent to the difference between the initial and the total stiffness tensors (Baste and Audoin, 1991). The internal variable is included in the free energy potential and the damage growth is then defined in terms of the conjugate thermodynamic force. Depending on the load path, the induced anisotropic damage may either retain the original elastic symmetry, cause the symmetry axes to rotate, or change the symmetry characteristics. The only thermodynamic restriction to the change in stiffness during uniaxial tension loading is that the stiffness component in the loading direction must decrease. No restrictions exist for the change in other components of the stiffness tensor. Twenty one constants need to be defined for the complete definition of the evolution of the damage tensor. This is, in principle, experimentally possible, but requires many, complex laboratory tests (Baste et al., 1992).

3.5 Conclusions

The analysis of brittle materials containing flaws loaded in tension, is well established. Crack grow perpendicular to the tensile loading and criteria for crack initiation and growth can be determined from standard procedures of linear elastic fracture mechanics. The material becomes more compliant (less stiff) due to the crack opening. The additional components of the compliance tensor can be evaluated by the self-consistent method. Random cracks cause an isotropic increase in compliance. Cracks in parallel result in transverse isotropy and sets or arrays of cracks lead to orthotropy or fully anisotropic behaviour.

The shape and direction of isolated tensile cracks can be represented as vector or tensor quantities and can be introduced into a linear elastic constitutive equation by expanding the elastic free energy as a polynomial function of the crack tensor.

In compression, alternative mechanisms must be postulated for the development of microcracks towards the loading direction (defined by the maximim principal compression stress). Models, which have been proposed, include the opening of grain boundaries, grain interactions and local tensile stress distributions. The sliding flaw mechanism, in which relative movement of the surface of flaws, inclined to the loading direction, causes wing cracks to form and grow towards the load, can explain much of the observed stress-strain response of rock during loading and unloading.

Initiation and growth of the sliding flaws and the wing cracks can be determined by means of linear fracture mechanics. However, the introduction of this type of crack mechanism into constitutive laws require the consideration of many complex interactions between the sliding flaws and the wing cracks. In general, the compliance of a material containing a population of these cracks is fully anisotropic and nonsymmetric.

Damage models consider the overall effect of the opening of voids on the stiffness. Phenomenological evolution laws need to be defined for a specific type of damage. The void area reduces the load bearing area in the material and the effective stresses in the undamaged material increase as the damage evolves. Constitutive equations can be derived with the principle of strain equivalence by substitution of the effective (or net) stress for the Cauchy stress in the elastic constitutive equation. Scalar damage models result in an isotropic distribution of damage with no directional effect from the microcracking. Models for isotropic damage in rock suggest that the volumetric and shear components of the behaviour must be considered independently. The dilatancy which is observed in rock under loading must be introduced by expressing the volumetric strain as a function of the damage. The difference in tensile and compressive strengths can be incorporated with a decomposition of the stress tensor into positive and negative parts and defining separate evolution laws for tension and compression.

Vector damage models express the damage in terms of the magnitude and direction of anequivalent crack. The damage vectors are incorporated into the free energy and damage evolution is properly described by a damage potential in the space of the thermodynamic force conjugate to the internal variable. The effect of the shape of the cracks and the distribution of the crack vectors in the material is neglected and no dilatancy is produced normal to the crack. Discontinuities in the material behaviour can occur during two-way loading.

In general, the extension of the net stress concept to three-dimensional stress states is acheived with second order damage models. The reduction in load bearing area due to damage leads to an unsymmetric net stress and strain tensor which require amendments to standard numerical schemes. If the symmetric part of the net stress is applied, then the material response strongly depends on the method of symmetrization. In some models, the induced anisotropy of the damage due to the preferred orientation of microcracks can be related to the deviatoric stress tensor.

The majority of fourth order tensor damage models consider the compliance or stiffness tensor to represent the damage history. The evaluation of evolution laws for all components of the fourth order internal variable is impractical, and most models consider the damage magnitude and direction separately. The direction is either predefined by a 'damage characteristic' tensor, or else is determined in terms of the postitive and negative parts of the stress or strain tensor. The selection of the decomposition of the stress or strain tensor becomes crucial in the correct description of the damage. The magnitude of damage is a scalar and the evolution laws are developed independently. The damage evolution is specified terms of the additional compliance, or as an equivalent strain or energy norm. The models are based on the micromechanical models for tensile cracks and modifications are required to incorporate compression damage. Implementation of the strain based formulations in finite element solution procedures is straightforward and these models will therefore be developed further in order to describe the growth of damage in rock.

Chapter 4 Formulation of Anisotropic Damage Model

4.1 Introduction

The assumption of isotropic damage is often sufficient to predict the failure of metal due to creep under tensile loading. Such damage models are relatively simple due to the fact that the damage variable is a scalar. Consideration of the experimental evidence, as reviewed in Chapter 2, suggests that in rock mechanics problems, the directionality of the microfracturing has a considerable influence on the stress - strain response. Micromechanical theories (see Chapter 3) emphasise that the opening of cracks in preferential directions induces anisotropy in the material stiffness. Thus, the introduction of induced anisotropy into continuum damage models is required for rock and can be achieved by representing the damage with internal variables of tensorial nature. Unfortunately, the physical clarity of the scalar damage models is lost.

The proposed anisotropic model is based on a fourth-order tensor internal variable characterisation of the material mechanical responses. Damage is incorporated by modification of the components of the stiffness tensor, and thus the formulation is perfectly suited for implementation into a finite element scheme. To provide some transparency the damage model incorporates the ideas of vector damage models in the sense of separating the description of damage into the direction of microcracking and the magnitude of the stiffness loss. The evolution of damage is formulated in a phenomenological framework, however, its theoretical concept is firmly tied into micromechanical considerations.

The microcracking mechanisms, described in Section 3.2.2, in which flaws, oriented at an angle to the major principal compressive stress, slide when the frictional resistance of their surfaces is exceeded and nucleate wing cracks in the loading direction, play an essential part in the formulation of the proposed model. Wing crack formation introduces anisotropy in terms of directionality and dilatancy, both of which are, in principle, addressed in the phenomenological tensile damage theory by Ju (1989). The proposed model extends these concepts to a general compression/extension stress state in accordance with the micromechanical derivations.

A detailed description of the formulation of the anisotropic damage model with particular emphasis on the presentation of the various phases of loading and unloading follows. The procedure for implementation in finite element program with a Newton-Raphson nonlinear solution scheme is presented in the second part of this chapter.

4.2 Initial undamaged state

The material is initially considered to be a hyperelastic material containing randomly oriented flaws. The total strain is split into an elastic ϵ^e and a plastic part ϵ^p as

$$\epsilon = \epsilon^e + \epsilon^p. \tag{56}$$

The material behaviour is assumed to be characterised in accordance with the theory of thermodynamic processes with internal variables (Coleman and Gurtin, 1967; Mroz, 1973; Martin, 1976; Germain et al., 1983; Lubliner, 1990 amongst others). The material response is assumed to be isothermal, and governed by the Helmholtz free energy

$$\psi = \psi(\epsilon, T, q_n, \chi_m), \tag{57}$$

which, in general, depends on the strain ϵ, the temperature T, and n plastic internal variables q and m damage internal variables χ, respectively. The tensor valued internal variables allow a phenomenological representation of internal structural rearrangements within the material and can theoretically be measured, but not directly controlled. The plastic internal variables represent the effect of slip dislocations during ductile flow whereas the damage internal variables describe the opening of microcracks resulting from brittle fracture processes. The choice of the appropriate internal variables to represent the effect of microfracturing in the material is the central problem in the development of any continuum damage model (Krajcinovic, 1987 & 1989; Lemaitre, 1990; Murakami, 1987; Onat and Leckie, 1988). In this formulation, the arguments of Ju (1989) in this regard will be followed, modified and extended.

In the effective stress principle, the stress in the undamaged material is termed the effective stress $\bar{\sigma}$ and is related to the Cauchy, or applied, stress σ on the material element by means of a fourth order transformation tensor M such that

$$\sigma = M\bar{\sigma} \tag{58}$$

(see also equation 44 in Section 3.4.4). Introducing a fourth order tensor damage internal variable D, the constitutive relation can be expressed as

$$\sigma = (I - D)\bar{\sigma} = (I - D)C_o\epsilon = C\epsilon, \tag{59}$$

in which the current (damaged) secant stiffness C is linearly related to the initial undamaged stiffness C_o. The damaged secant stiffness is assumed to be the internal variable since there is a one to one correspondence between the damage tensor D and the stiffness C. With the assumption that the elastic and plastic parts of the free energy are separable, the Helmholtz free energy of the undamaged material has the form

$$\psi(\boldsymbol{\epsilon}^e, \boldsymbol{q}, \boldsymbol{C}) \equiv \psi_{ed}(\boldsymbol{\epsilon}^e, \boldsymbol{C}) + \psi_{pd}(\boldsymbol{q}, \boldsymbol{C}), \tag{60}$$

where the elastic part $\psi_{ed}(\boldsymbol{\epsilon}^e, \boldsymbol{C})$ and the plastic part $\psi_{pd}(\boldsymbol{q}, \boldsymbol{C})$ of the free energy are functions of the stiffness tensor $\boldsymbol{C}$. The inclusion of the current secant stiffness into the plastic free energy allows the consideration of coupled elastic-plastic damage, such that plastic deformation will contribute to the damage formation.

In principle, any hyperelastic constitutive relation may be included in the damage formulation to describe the undamaged material. For simplicity, brittle rock is assumed to be a linear elastic material before microcracking initiates. The elastic strain (potential) energy per unit volume can therefore be expressed as a quadratic function of the elastic strains (Love, 1937). For geotechnical problems in which an initial stress $\boldsymbol{\sigma}_o$ is associated with the initial state of zero strain, the undamaged material has the free energy

$$\psi(\boldsymbol{\epsilon}^e, \boldsymbol{q}, \boldsymbol{C}) = \boldsymbol{\sigma}_{o(ij)}\epsilon^e_{kl} + C_{o(ijkl)}\epsilon^e_{ij}\epsilon^e_{kl} + \psi_{pd}(\boldsymbol{q}, \boldsymbol{C}). \tag{61}$$

A material with a completely anisotropic initial stiffness has 21 independent components of the stiffness tensor. In this formulation, the assumption of initial elastic isotropy will be made, which reduces the independent constants to the two Lamé coefficients λ and μ. The initial stiffness tensor is then expressed as

$$\boldsymbol{C}_o \equiv C_{o(ijkl)} = \lambda\delta_{ij}\delta_{kl} + \mu(\delta_{ik}\delta_{jl} + \delta_{il}\delta_{jk}) \tag{62}$$

and the stress is determined following the conventional procedure (Malvern, 1969) as

$$\boldsymbol{\sigma} = \frac{\partial\psi}{\partial\boldsymbol{\epsilon}^e} = \boldsymbol{\sigma}_o + \boldsymbol{C}_o\boldsymbol{\epsilon}^e \equiv \boldsymbol{\sigma}_{o(ij)} + \lambda\delta_{ij}\epsilon_{kk} + 2\mu\epsilon_{ij}. \tag{63}$$

The constant μ corresponds to the shear modulus G of the material and the bulk modulus can be obtained in terms of the Lamé coefficients as

$$K = \lambda + \frac{2\mu}{3} = \lambda + \frac{2G}{3}. \tag{64}$$

The stress is then

$$\boldsymbol{\sigma} = \boldsymbol{\sigma}_o + (K - \frac{2}{3}G)\delta_{ij}\epsilon_{kk} + 2G\epsilon_{ij}. \tag{65}$$

The elastic constants are related to the initial Young's modulus E_o and Poisson's ratio ν in the expressions

$$E_o = \frac{9GK}{3K + G} \quad \text{and} \quad \nu = \frac{3K - 2G}{2(3K + G)}, \tag{66}$$

respectively.

The material is assumed to remain elastic until the damage initiates. The criterion for damage initiation is closely connected to the choice of the damage internal variable and will be examined in the following section.

4.3 Damage initiation criteria

In most continuum damage models, the damage initiation criterion is determined in terms of the thermodynamic force conjugate to the damage internal variable (Krajcinovic, 1987; Lemaitre, 1990, amongst others) as

$$Y_m = \frac{\partial \psi}{\partial \chi_m}. \tag{67}$$

This approach assumes that the microcrack initiation and evolution is caused by the same processes. However, as described in Section 3.2.2, a common feature of all micromechanical models for microcrack growth in compression is the existence of some mechanisms acting within the rock which eventually result in the initiation of the directional microcracking. This leads to a requirement that a threshold stress state must be exceeded prior to microcrack formation. For example, in the sliding crack concept this threshold corresponds to the shear resistance of the flaw surface at wing crack initiation (Nemat-Nasser and Horii, 1982). The stress required to initiate the fracture due to a point contact, or elastic inhomogeneities (Dey and Wang, 1981), or local tensile stresses (Holcomb, 1981) can also be considered as an equivalent threshold for the initiation of damage.

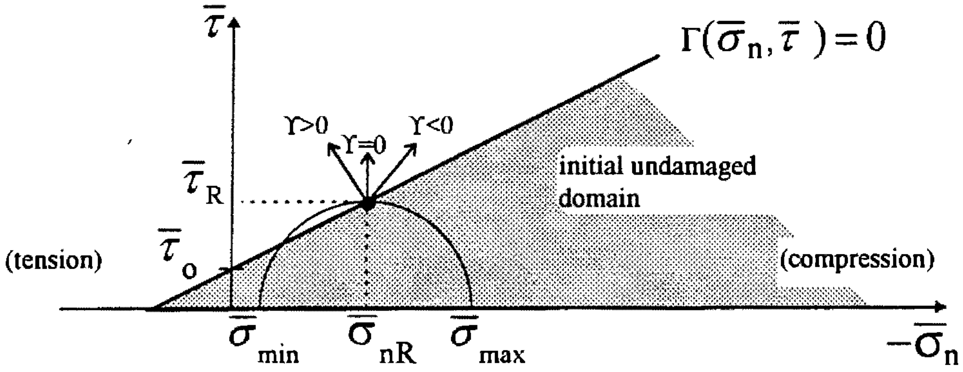

Figure 15: Mohr effective stress space with damage initiation criterion

The proposed damage model is a phenomenological formulation, and there is no need to specify the exact mechanism which activates the initiation of the directional microcracking. However, a convenient interpretation of the processes involved is provided by the sliding flaw concept, with flaws assumed to be distributed throughout the material. In a micromechanical model, it is necessary to determine the damage initiation by the consideration of the stress states existing in all possible flaw directions (Wiebols and Cook, 1973; Kachanov, 1982; Fanella and Krajcinovic, 1988; Nemat-Nasser and Obata, 1988) to evaluate which crack slides first. Here, the threshold of flaw sliding is defined, for convenience, in terms of the shear resistance on a plane of sliding at a point within the material. Thus, consideration of the stress state on each pre-exisiting flaw within the material is not required. The magnitude of the shear resistance at damage initiation is expressed as a linear function of the normal stress acting on the plane in a Mohr-Coulomb friction law (Jaeger and Cook, 1979). However, the magnitude of the shear resistance at damage initiation will be significantly less than the ultimate shear resistance that would be predicted if the Mohr-Coulomb law is applied as a failure criterion. Therefore, the significance of the tension cut-off condition, commonly applied to the failure criterion, is reduced and has not been included in the initiation criterion.

The development of anisotropic damage corresponds to the growth of the wing cracks in a preferential direction. The anisotropy induced by the relative sliding of the flaw surfaces, which is included in the micromechanical models (described in Section 3.3.3), is not considered in this formulation. Therefore, the mechanism causing the initiation of microcracking in a preferential direction (e.g. sliding on flaws) does not cause any damage and is part of the undamaged material behaviour. From the principle of effective stress, the undamaged material response is determined by the effective stress state. The anisotropic damage initiation criterion is expressed in terms of the Mohr-Coulomb friction law, represented by a surface in the effective stress space. After initiation of damage, the effective stress will increase further as a result of the damage. This, in turn, leads to additional damage and a progressive process of anisotropic damage growth is started.

Thus, the damage initiation criterion can be expressed as a straight line

$$\Gamma(\bar{\sigma}) \equiv \bar{\tau} - \mu_o \bar{\sigma}_n - \bar{\tau}_o = 0 \tag{68}$$

in the Mohr effective stress space, where μ_o is the coefficient of friction and $\bar{\tau}_o$ is the effective shear resistance, as shown in Figure 15. Tensile stresses are considered positive. The maximum effective shear stress $\bar{\tau}$ and effective normal stress $\bar{\sigma}_n$ acting on the plane of sliding are given by

$$\bar{\tau} = 0.5 * \sqrt{(\bar{\sigma}_{max} - \bar{\sigma}_{min})^2} \quad \text{and} \quad \bar{\sigma}_n = 0.5 * (\bar{\sigma}_{max} + \bar{\sigma}_{min}), \tag{69}$$

respectively. The terms $\bar{\sigma}_{max}$ and $\bar{\sigma}_{min}$ represent the maximum compressive and the minimum compressive (most tensile) principal effective stresses. The normal to the plane of sliding occurs at an angle $\alpha = (\pi/4) + \sin^{-1}\mu_o$ to the direction of $\bar{\sigma}_{max}$ (Jaeger and Cook, 1979). For three-dimensional and axisymmetric stress states, all three principal stress directions need to be considered to identify the direction of the sliding plane. In plane strain conditions, consideration of only the in-plane principal stresses results in the constraint that the damage is independent of the out-of-plane direction.

Anisotropic damage commences when $\Gamma(\bar{\sigma}_n, \bar{\tau}) > 0$ and the flaws would be in the process of sliding (without affecting the undamaged material response) whenever $\Gamma > 0$. The elastic strains corresponding the material behaviour up to the point of sliding ($\Gamma \leq 0$) define the reference state of strain denoted as the residual elastic strain, $\boldsymbol{\epsilon}_R^e$. The directional microfracture growth (anisotropic damage) is then related to the difference between the total strain state and the reference state, in analogy to the residual elastic strain concept (Friedman and Logan, 1970; Friedman, 1972). Thus, the novel feature of this initiation concept is that the anisotropic damage occurs in a subdomain, the 'crack' strain $\boldsymbol{\epsilon}_c^e$, of the elastic strain, which is expressed as

$$\boldsymbol{\epsilon}_c^e = \boldsymbol{\epsilon}^e - \boldsymbol{\epsilon}_R^e. \tag{70}$$

The damage directions can then be identified for any loading path without the complications of considering different partitions of the stress or strain tensors for loading in compression and tension stress states, as required in previous damage formulations (see Section 3.4). In addition, damage will not occur for load paths in hydrostatic compression, or at low levels of deviatoric stress, in agreement with the experimental observations, as reviewed in Section 4.3.

Uniqueness of the 'crack' strain must be ensured so that a monotonic increase in 'crack' strain will be reflected as a corresponding increase in damage. This is achieved by providing an evolution law for the residual strains in such a way that once damage has initiated ($\Gamma > 0$), the residual elastic strain is fixed and the change in the 'crack' strain is identical to the elastic strain increment, thus,

$$\dot{\boldsymbol{\epsilon}}_R^e = 0 \quad \text{and } \dot{\boldsymbol{\epsilon}}_c^e = \dot{\boldsymbol{\epsilon}}^e \quad \text{when} \quad \Gamma > 0. \tag{71}$$

Damage will not occur when the flaws are locked (not sliding) in accordance with the sliding crack analogue. Then, the residual and 'crack' strain increments are

$$\dot{\boldsymbol{\epsilon}}_R^e = \dot{\boldsymbol{\epsilon}}^e \quad \text{and} \quad \dot{\boldsymbol{\epsilon}}_c^e = 0 \quad \text{when} \quad \Gamma \leq 0. \tag{72}$$

As mentioned before, the residual strain state is associated with the sliding flaws in the undamaged material. The residual strains correspond to residual stresses. These are effective stresses and can be determined using the initial elastic modulus $\boldsymbol{C}_o$ as

$$\boldsymbol{\sigma}_R \equiv \bar{\boldsymbol{\sigma}}_R = \boldsymbol{\sigma}_o + \boldsymbol{C}_o \boldsymbol{\epsilon}_R^e. \tag{73}$$

The residual shear and residual normal effective stresses on the plane of maximum shear are given by

$$\begin{aligned} \bar{\tau}_R &= 0.5 * \sqrt{(\bar{\sigma}_{R\,max} - \bar{\sigma}_{R\,min})^2} \quad \text{and} && (74) \\ \bar{\sigma}_{nR} &= 0.5 * (\bar{\sigma}_{R\,min} + \bar{\sigma}_{R\,min}), && (75) \end{aligned}$$

which correspond to the stress state at damage initiation (point $(\bar{\sigma}_{nR}, \bar{\tau}_R)$ in Figure 15).

Two distinct types of microcrack evolution can be identified, depending largely on whether the applied stress state is in tension or compression (similar to the approach by Nemat-Nasser and Horii, 1982). As mentioned in Section 3.2.2, stable fracture growth is associated with an overall compressive stress state and implies that a fracture grows to a finite length and will only propagate further when additional loading is applied.

Alternatively, unstable fracture propagation occurs in the presence of tensile stresses, and implies that once the fracture has initiated, no further addition of loading is needed to ensure propagation, unless the crack encounters some energy barrier that prevents crack growth. As expressed in Sections 2.3 and 3.3.2, experimental observations (Briggs and Vieler, 1984) and micromechanical models (Sumerac and Krajcinovic, 1987) suggest that the damage process in rock is never completely unstable since the grain boundaries provide energy barriers to microcrack growth. The evolution will, however, proceed more rapidly if the confining stress is decreasing or even becomes tensile (Nemat-Nasser and Horii, 1982).

Two distinct damage modes are defined in the proposed damage initiation formulation corresponding to the unstable and stable evolution processes, each provided with its own evolution law. Since the model is strain based, and the calculation of the applied stress depends on the damage, the differentiation of these modes in terms of the confining stress acting on the flaw would introduce an iterative scheme into the numerical solution procedure. The alternative is an identification based on the effective normal stress on the sliding flaw, which is known.

The anisotropic damage is defined in the 'crack' strain subdomain, and therefore the damage evolution is also determined by the difference between the effective normal stress $\bar{\sigma}$ and the residual effective stress $\bar{\sigma}_{nR}$. This definition permits damage evolution under both, compression and extension stress paths and removes the discontinuity in damage evolution during the transition from compressive to tensile stress states evident in previous damage models (e.g Ju, 1987). The two modes are the 'unstable' mode I (extension) corresponding to an increase of the effective normal stress $\bar{\sigma}_n$ and the 'stable' mode II that occurs when the effective normal stress $\bar{\sigma}_n$ decreases (note, tension is defined as positive). The terms mode I and mode II were chosen because the respective mechanisms of microcrack initiation on a microscopic level are similar to the processes described at a macroscopic level in linear elastic fracture mechanics. The distinction between the modes is defined by an effective stress surface

$$\Upsilon = \bar{\sigma}_n - \bar{\sigma}_{nR}, \quad \text{where} \quad \begin{array}{l} \Upsilon > 0 \ \text{for mode I} \\ \Upsilon \leq 0 \ \text{for mode II.} \end{array} \tag{76}$$

Damage is assumed to be governed by the same mode as assigned when the damage initiated. If the effective stress state returns into the initial undamaged domain and the material is subsequently reloaded, a new damage mode will be assigned once the damage initiation criterion is exceeded.

4.4 Anisotropic damage

Once the damage initiates ($\Gamma > 0$) the formation of directional microcracking and therefore anisotropic damage begins. The determination of the damage direction is the most important part of the formulation. In the formulation of the continuum damage model, the stress and strain states and material stiffness are known. There is no other information such as the initial distribution of flaws to prescribe the damage direction. A number of methods have been postulated for relating the damage direction to the stress tensor or the strain tensor, as described in Section 3.4.4. These models consider the microcracks to be idealised as tensile cracks, and therefore their concept for the prediction of the damage direction cannot be applied directly in this formulation, in which the directional microcracking is assumed to be represented by the sliding flaw analogy. The methods applied in previous models do, however, provide a basis for the proposed implementation and need to be analysed in detail.

Initially, Ortiz (1985) proposed that the strains, resulting from the opening of the microcracks during the application of tensile stress, should have positive eigenvalues. In compression, any microcracks that have formed due to previous tensile stress states are assumed to be closed and the microcracking would develop in the 'average plane of the loading' and be described by the negative eigenvalues of the strain tensor. Since the Ortiz (1985) damage model is a stress based formulation these requirements are expressed in terms of the principal stresses so that tensile damage occurs in the direction of positive principal stresses and compression damage is oriented accordingly in the direction of negative principal stresses.

Consideration of the damage model under a number of standard loading paths demonstrates that these assumptions are not appropriate for rock behaviour. For instance, in uniaxial compression damage is predicted in the axial direction only and is a specified fraction of the magnitude of the uniaxial tension damage. In a conventional triaxial compression test, all principal stresses are negative and so damage is predicted in all directions, during both the hydrostatic and the deviatoric loading stages. However, such behaviour is not in agreement with the damage initiation surface exhibited in experiments on rock, described in Chapter 2.

The modified approach by Yazdani and Schreyer (1988 & 1990) excluded damage during hydrostatic compression, however, damage initiation still occurs simultaneously with the application of deviatoric load. The damage only occurs in the axial direction with the results that the increase of the tangent Poissons' ratio with loading is not predicted. The effect of damage in the lateral direction during uniaxial compression was introduced by Yazdani (1993).

Subsequently, Simo and Ju (1987) and Ju (1989) applied the ideas of Ortiz (1985) in a strain based formulation, which allows the constraint of positive damage strains for tension, and negative strains for compression to be enforced directly. Thus, tensile and compressive damage components occur in the direction of the tensile and compressive principal strains, respectively. However, a damage initiation surface is predicted which does not properly reflect experimental observations. In particular, in triaxial compression, the existence of three compressive principal strains during hydrostatic compression will produce damage, once the damage surface is exceeded (Sellers and Scheele, 1993). This damage results in a reduction of the material stiffness in contrast to experimental evidence that hydrostatic compression leads to stiffening of the material (Brace, 1965). During deviatoric loading at low confinements, damage occurs in the radial direction as expected. At higher confinements, and in other tests, such as reduced triaxial extension, the damage caused during hydrostatic compression results in a stress - strain response which is not in agreement with the experimental trends.

Thus, the selection of the damage direction on the basis of the principal values of the total stress tensor or total strain tensor is problematic. This can be demonstrated by consideration of uniaxial tension and compression loading situations, shown schematically in Figure 16. Experiments (Briggs, 1982) and classical fracture mechanics studies (Griffith, 1920) suggest that, in tension, microfractures tend to grow perpendicular to the direction of loading. The significant damage, measured either in terms of a loss in load bearing area orthogonal to the loading or as a decrease in stiffness, occurs in the direction of the loading. This is depicted in Figure 16a.

In compression, however, the microfractures generally grow towards the direction of loading (see Section 2.2.2). The significant contribution to the damage occurs orthogonal to the loading, as shown schematically in Figure 16b. Negative strains only occur in the loading direction, and therefore the determination of the damage in the direction of the negative principal strains addresses only a small amount of damage resulting from the crack opening. The main component of the damage which occurs perpendicular to the loading is not considered.

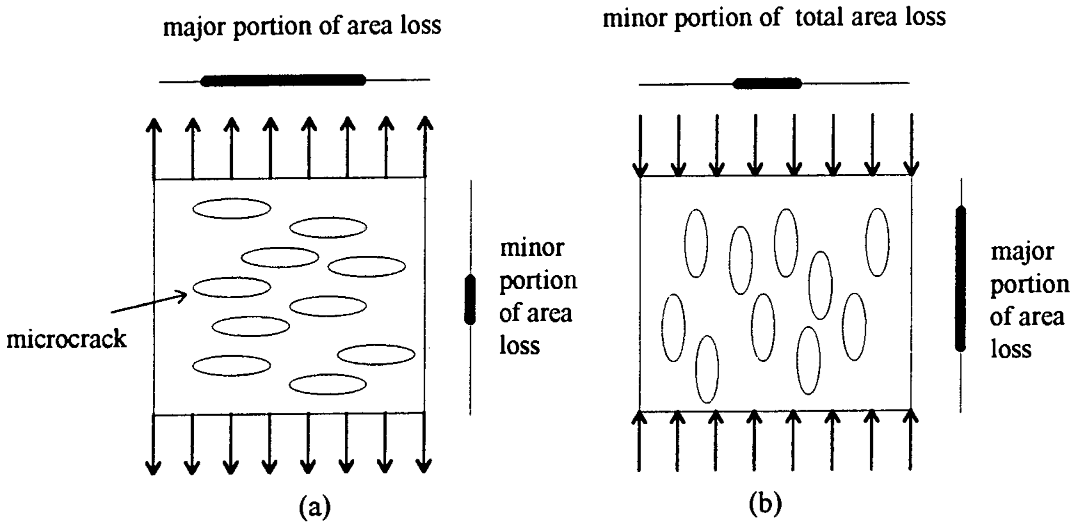

Figure 16: Schematic of microcrack population under a: tensile stress state and b: compressive stress state

In order to improve the modelling of the damage initiation and directionality for all stress states, the basis of the formulation is that two distinct types of processes govern the material behaviour. The first type encompasses the processes leading to microcrack initiation as discussed in Section 4.3. The second type of behaviour is characterised by the development of anisotropic damage and follows once the initiation criterion is attained. The damage magnitude and directions are then controlled by the difference between the total elastic strain and the strain that existed at the onset of damage.

The effect of microcrocracking on the material stiffness can be modelled by making the assumption that anisotropic damage occurs whenever the principal strains of the subdomain ϵ_c^e of the elastic strain tensor are positive. Then, extending the arguments of Ortiz (1985) to tensile as well as compressive stress states, the direction and magnitude of the damage can be related to the positive eigenvalues of the 'crack' strain $\boldsymbol{\epsilon}^e_c$. The anisotropic damage model is therefore equivalent to the micromechanical models, discussed in Section 3.3.3, in which wing cracks, produced by sliding on flaws, are represented by equivalent tensile cracks.

The free energy of the anisotropic damaged material, reflecting the internal structural rearrangements, is consequently a function of $\boldsymbol{\epsilon}^e_c$ which is now a more restricted strain subdomain. The formulation allows for coupled elastic - plastic damage by the inclusion of the damage internal variable in both, the elastic and plastic parts of the free energy. In the initial stages of the model development the inclusion of coupling of the elastic and the plastic parts with damage was envisaged, but was eventually abandoned due to a lack of experimental data.

From equation (60), the free energy becomes

$$\psi(\boldsymbol{\epsilon}^e, \boldsymbol{q}, \boldsymbol{C}) \equiv \psi_{ed}(\boldsymbol{\epsilon}^e, \boldsymbol{C}) + \psi_{pd}(\boldsymbol{q}). \tag{77}$$

The plastic part of the constitutive equations can be derived from an appropriate choice of the plastic component of the free energy $\psi_{pd}(\boldsymbol{q})$ (Germain et al., 1983). Conventional yield surfaces (Martin, 1976; Desai and Siriwardane, 1984; Lubliner, 1990) are applied, but are expressed in terms of the effective stresses. Including a plasticity theory with internal variables q_n, defined by a hardening function, the yield condition becomes

$$f(\bar{\sigma}, q_n) \leq 0, \tag{78}$$

the associated flow rule for the plastic strain rate, and the plastic internal variables are given by

$$\dot{\boldsymbol{\epsilon}}^p = \dot{\lambda}\frac{\partial f}{\partial \bar{\boldsymbol{\sigma}}} \quad \text{and} \quad \dot{\boldsymbol{q}} = \dot{\lambda}\boldsymbol{h}, \tag{79}$$

respectively, where $\boldsymbol{h}$ is the hardening function.

Considering only completely brittle rock behaviour, the free energy of the whole material can be expressed as

$$\psi(\boldsymbol{\epsilon}^e, \boldsymbol{q}, \boldsymbol{C}) \equiv \psi_{eR}(\boldsymbol{\epsilon}^e_R, \boldsymbol{C}_o) + \psi_{ec}(\boldsymbol{\epsilon}^e_c, \boldsymbol{C}_c) = \frac{1}{2}\boldsymbol{\epsilon}^e_R : \boldsymbol{C}_o : \boldsymbol{\epsilon}^e_R + \frac{1}{2}\boldsymbol{\epsilon}^e_c : \boldsymbol{C}_c : \boldsymbol{\epsilon}^e_c, \tag{80}$$

where $\boldsymbol{C}_c$ is the current secant stiffness tensor of the damaged portion of the material, which is taken to be the internal variable. The uniqueness of the cracking strain is ensured by requiring that $\boldsymbol{\epsilon}^e_R$ remains constant during damage. Thus, the processes of damage initiation and damage development are independent. Following the standard methods of thermodynamics with internal variables (Coleman and Gurtin, 1967; Martin, 1976; Lubliner, 1990), the constitutive relation for the elastic anisotropic damaged subdomain of the material is expressed as

$$\boldsymbol{\sigma}_c = \frac{\partial \psi_{ec}}{\partial \boldsymbol{\epsilon}_c^e} = \boldsymbol{C}_c : \boldsymbol{\epsilon}_c^e. \tag{81}$$

The Clausius - Duhem inequality requires that

$$-\dot{\psi} + \boldsymbol{\sigma} : \dot{\boldsymbol{\epsilon}} \geq 0 \tag{82}$$

and therefore, in this case

$$-(\boldsymbol{\sigma}_o\dot{\boldsymbol{\epsilon}} + (\boldsymbol{C}_o : \boldsymbol{\epsilon}_R^e)\frac{\partial \boldsymbol{\epsilon}_R^e}{\partial \boldsymbol{\epsilon}^e}\frac{\partial \boldsymbol{\epsilon}^e}{\partial \boldsymbol{\epsilon}}\dot{\boldsymbol{\epsilon}} + \frac{1}{2}\boldsymbol{\epsilon}_R^e : \dot{\boldsymbol{C}}_o : \boldsymbol{\epsilon}_R^e + (\boldsymbol{C}_c : \boldsymbol{\epsilon}_c^e)\frac{\partial \boldsymbol{\epsilon}_c^e}{\partial \boldsymbol{\epsilon}^e}\frac{\partial \boldsymbol{\epsilon}^e}{\partial \boldsymbol{\epsilon}}\dot{\boldsymbol{\epsilon}} + \frac{1}{2}\boldsymbol{\epsilon}_c^e : \dot{\boldsymbol{C}}_c : \boldsymbol{\epsilon}_c^e) + \boldsymbol{\sigma} : \dot{\boldsymbol{\epsilon}} \geq 0 \tag{83}$$

and so for an arbitrary strain rate, this can be written as

$$\boldsymbol{\sigma} = \boldsymbol{\sigma}_o + (\boldsymbol{C}_o : \boldsymbol{\epsilon}_R^e)\frac{\partial \boldsymbol{\epsilon}_R^e}{\partial \boldsymbol{\epsilon}^e}\frac{\partial \boldsymbol{\epsilon}^e}{\partial \boldsymbol{\epsilon}} + (\boldsymbol{C}_c : \boldsymbol{\epsilon}_c^e)\frac{\partial \boldsymbol{\epsilon}_c^e}{\partial \boldsymbol{\epsilon}^e}\frac{\partial \boldsymbol{\epsilon}^e}{\partial \boldsymbol{\epsilon}}. \tag{84}$$

Following the procedures for evaluating the residual and 'crack' strain subdomains as expressed in equations (72) and (71), the complete constitutive relation for loading with damage occurring is

$$\boldsymbol{\sigma} = \boldsymbol{\sigma}_o + \boldsymbol{C}_o : \boldsymbol{\epsilon}_R^e + \boldsymbol{C}_c : \boldsymbol{\epsilon}_c^e = \boldsymbol{\sigma}_o + \boldsymbol{\sigma}_R + \boldsymbol{\sigma}_c. \tag{85}$$

Including the elastic strain $\boldsymbol{\epsilon}^e = \boldsymbol{\epsilon}_R^e + \boldsymbol{\epsilon}_c^e$, this equation is transformed into

$$\boldsymbol{\sigma} = \boldsymbol{\sigma}_o + \boldsymbol{C}_o : \boldsymbol{\epsilon}^e - (\boldsymbol{C}_o - \boldsymbol{C}_c) : \boldsymbol{\epsilon}_c^e. \tag{86}$$

The constitutive equations for unloading and reloading follow from similar arguments (see Section 4.7 below). The effective stress is calculated in the conventional manner as

$$\bar{\boldsymbol{\sigma}} = \boldsymbol{\sigma}_o + \boldsymbol{C}_o : \boldsymbol{\epsilon}^e, \tag{87}$$

however, there is no longer a linear relation between the Cauchy and effective stresses. This is in accordance with the micromechanics of the damage (Baste and Audion, 1991), as detailed in Section 3.4.4. Thus, from equation (86) the stress can be expressed as

$$\boldsymbol{\sigma} = \bar{\boldsymbol{\sigma}} - (\boldsymbol{C}_o - \boldsymbol{C}_c) : \boldsymbol{\epsilon}_c^e = \bar{\boldsymbol{\sigma}} - (\boldsymbol{I} - \boldsymbol{D}_c)\boldsymbol{C}_o : \boldsymbol{\epsilon}_c^e = \bar{\boldsymbol{\sigma}} - \boldsymbol{M}_c\boldsymbol{C}_o : \boldsymbol{\epsilon}_c^e, \tag{88}$$

where $\boldsymbol{M}_c$ is the damage effect tensor in the damaged subdomain. The effective stress $\bar{\boldsymbol{\sigma}}$ which is acting on the undamaged part of the material (containing flaws) is therefore greater than the Cauchy stress $\boldsymbol{\sigma}$ acting on the whole material element. As the loading increases, the effective stress will increase and the Cauchy stress will reduce. The reduction in the Cauchy stress will eventually lead to failure of the material.

Development of induced anisotropy in the material is obtained by providing an evolution law for the internal variable $\boldsymbol{C}_c$ in terms of its conjugate thermodynamic force. Following thermodynamic considerations, the dissipation inequality can be obtained from the Clausius - Duhem inequality expressed in equation (83) and is given by

$$\frac{1}{2}\boldsymbol{\epsilon}^e_R : \dot{\boldsymbol{C}}_o : \boldsymbol{\epsilon}^e_R + \frac{1}{2}\boldsymbol{\epsilon}^e_c : \dot{\boldsymbol{C}}_c : \boldsymbol{\epsilon}^e_c \geq 0. \tag{89}$$

For initially linear elastic material, $\dot{\boldsymbol{C}}_o = 0$ allows the identification of the thermodynamic force $-\boldsymbol{Y}$, conjugate to the internal variable $\boldsymbol{C}_c$, as the variation of the Helmholtz free energy (in equation (80)) with respect to the internal variable. Thus,

$$-\boldsymbol{Y} \equiv \frac{\partial \psi}{\partial \boldsymbol{C}_c} = \frac{1}{2}\boldsymbol{\epsilon}^e_c \otimes \boldsymbol{\epsilon}^e_c, \tag{90}$$

which is a fourth order tensor and physically defines the anisotropic damage energy release rate.

4.5 Damage magnitude and direction

The damage direction and growth is properly described by a damage dissipation surface, expressed in terms of the thermodynamic force $-\boldsymbol{Y}$ (Krajcinovic, 1989; Simo and Ju, 1987; Ju, 1989). This damage surface is expressed as

$$g \equiv \hat{G}(-\boldsymbol{Y}) - r \leq 0, \tag{91}$$

where r describes the current "radius" of the damage surface. The damage evolution is now characterised by the principle of maximum damage dissipation. Thus, the change in the damage, measured by the change in the internal variable $\boldsymbol{C}_c$, is given by

$$\dot{\boldsymbol{C}}_c = -\dot{\mu}\frac{\partial g}{\partial(-\boldsymbol{Y})}, \quad \dot{\mu} \geq 0, \quad g \leq 0, \quad \dot{\mu} g \equiv 0, \tag{92}$$

which are the Kuhn-Tucker conditions for the principle of maximum damage energy dissipation (Ju, 1989) and $\dot{\mu}$ is a 'flow' parameter. The damage surface g is a function of the damage energy release rate $-\boldsymbol{Y}$ which is a fourth order tensor. The specification of this surface requires the consideration of 81 potentially independent components of $-\boldsymbol{Y}$. Since the evolution of these components would have to be calibrated based on a complex testing program (as in Baste, et al., 1992) which, even if all components can be associated with some physical meaning, would demand an experimental effort that is unrealistic in practice.

The need to specify these evolution laws can be avoided by assuming that the change in stiffness can be expressed by uncoupling the components associated with the damage magnitude from those associated with the damage direction (Ju, 1989). Then, equation (92) is rewritten as

$$\dot{\boldsymbol{C}}_c = -\dot{\mu}\frac{\partial g}{\partial \xi_c}\frac{\partial \xi_c}{\partial(-\boldsymbol{Y})} \tag{93}$$

allowing the damage surface g to be expressed in terms of a scalar, undamaged energy norm ξ_c, and the damage evolution by an evolution function for $\frac{\partial g}{\partial \xi_c}$. The fourth order 'direction' tensor $\frac{\partial \xi_c}{\partial(-\boldsymbol{Y})}$ selects the components of the initial stiffness tensor $\boldsymbol{C}_o$ which are modified by the anisotropic damage and thus, permits the identification of the damage 'direction'. These components are subsequently scaled by the damage magnitude and subtracted from the initial stiffness tensor to form the anisotropic, damaged stiffness tensor $\boldsymbol{C}_c$.

The positive eigenvalues of the 'crack' strain subdomain $\boldsymbol{\epsilon}^e_c$ represent the opening of microcracks, normal to the direction of growth. The scalar, undamaged energy norm of the positive part of $\boldsymbol{\epsilon}^e_c$ is chosen to represent the magnitude of the damage such that

$$\xi_c = \frac{1}{2}\mathbf{P}^+\boldsymbol{\epsilon}^e_c : \boldsymbol{C}_o : \mathbf{P}^+\boldsymbol{\epsilon}^e_c. \tag{94}$$

The operator $\mathbf{P}^+$ is the fourth order positive projection operator which determines the positive part of the current 'crack' strain, denoted by

$$\boldsymbol{\epsilon}^{e+}_c = \mathbf{P}^+ : \boldsymbol{\epsilon}^e_c. \tag{95}$$

The anisotropy of the stiffness tensor due to the directionality of the damage can be calculated from $\frac{\partial \xi_c}{\partial(-\boldsymbol{Y})}$ as

$$\frac{\partial \xi_c}{\partial(-\boldsymbol{Y})} \equiv \mathbf{P}^+ : \boldsymbol{C}_o : \mathbf{P}^+. \tag{96}$$

The function of the $\mathbf{P}^+$ operator is to rotate the 'crack' strain tensor into the principal directions, extract the positive eigenvalues, and rotate the tensor back to the global coordinate system. In this formulation the positive projection operator $\mathbf{P}^+$ is defined as

$$\begin{aligned} \mathbf{P}^+{}_{ijkl} &= Q^+_{ia}Q^+_{jb}Q_{ka}Q_{lb}, && (97)\\ \text{with}\quad \boldsymbol{Q}^+ &\equiv \sum_{i=1}^{3} H[\epsilon^e_{ci}](\boldsymbol{p}_i \otimes \boldsymbol{p}_i) && (98)\\ \text{and}\ \boldsymbol{Q} &\equiv \sum_{i=1}^{3}(\boldsymbol{p}_i \otimes \boldsymbol{p}_i), && (99)\end{aligned}$$

where ϵ_{ci}^{e} and $\boldsymbol{p}_i$ are the eigenvalues and eigenvectors of $\boldsymbol{\epsilon}_c^e$, respectively. $H[\epsilon_{ci}^{e}]$ is the Heaviside ramp function of the eigenvalues ϵ_{ci}^{e} of the 'crack' strain subdomain and is defined as

$$H[\epsilon_{ci}^{e}] = \begin{cases} 0 & \text{if} \quad \epsilon_{ci}^{e} > 0 \\ 1 & \text{if} \quad \epsilon_{ci}^{e} \leq 0. \end{cases} \tag{100}$$

This expression for the positive projection operator is analogous to the operator defined for the total strain tensor by Simo and Ju (1987) (see equation (55)) , but considering only the positive eigenvalues of the crack strain subdomain $\boldsymbol{\epsilon}_c^e$.

The key component of this damage theory is that damage induced anisotropy will be defined only for 'crack' strains $\boldsymbol{\epsilon}_c^e = \boldsymbol{\epsilon}^e - \boldsymbol{\epsilon}_R^e$. Then, since $\boldsymbol{\epsilon}_R^e$ is defined by the initial damage surface Γ, all stress states for which $\Gamma < 0$ will produce no damage. The damage is assumed to grow in one of the two modes depending on whether the cracking strain $\boldsymbol{\epsilon}_c^e$ occurs in the loading direction (mode I), or orthogonal to the loading (mode II) as discussed in Section 4.3.

The experimental observations, discussed in Section 2.3, suggest that the damage evolution depends on the confining pressure. Two damage surfaces, corresponding to equation (93), are a function of the undamaged energy norm ξ_c and the confinement ζ and are expressed as

$$g(\xi_c, \zeta)_m \equiv \hat{G}_m(\xi_c, \zeta) - r_{cm} = 0, \tag{101}$$

with m = I or II indicating mode I or mode II, and r_{cm} being the current "radius" of the damage surface for the respective mode. In this model, the damage threshold is defined in terms of the effective stress surface Γ and damage must initate whenever $\Gamma \geq 0$. The quantities r_{cm} are therefore initially equal to zero. The radius of the damage surface will increase during damage and thus, the change in r_{cm} is given by

$$\dot{r}_{cm} \equiv \dot{\mu}\frac{\partial \hat{G}_m}{\partial \xi_c} = \dot{\mu}\tilde{H}_{cm}. \tag{102}$$

Isotropic hardening rules for the respective modes are given by identifying the 'flow' parameter $\dot{\mu}$ (in equation (93)) with $\dot{\xi}_c$. Then,

$$\dot{r}_{cm} = \dot{\xi}_c\tilde{H}_{cm}. \tag{103}$$

The damage evolution functions $\tilde{H}_{cm}$ are specified directly, and may be different for each mode, as will be discussed in the following section.

The change in the internal variable is given by

$$\dot{\boldsymbol{C}}_c = -(\dot{\xi}_{cm}\tilde{H}_{cm})\mathbf{P}^+ : \boldsymbol{C}_0 : \mathbf{P}^+ = \dot{d}_{cm}\mathbf{P}^+ : \boldsymbol{C}_0 : \mathbf{P}^+, \tag{104}$$

where $\dot{d}_{cm}$ is the change in the damage magnitude. The evolution law $\tilde{H}_{cm}$ is defined so that the damage magnitude d_{cm} will range from 0 to 1 as the damage progresses. This implies that, although the internal variable is a fourth order tensor, the damage direction is defined by the principal directions of the positive eigenvalues of ϵ_c^e and the transformation into the material coordinate system is determined by the positive projection operator. For uniaxial tension, the projection of the stiffness tensor can be shown to be a close approximation of the analytical solution for the stiffness of an isotropic elastic medium containing aligned penny-shaped cracks perpendicular to the loading (Sellers and Scheele, 1993).

The integration of the damaged stiffness in a previous model (Ju, 1989), which considered damage in terms of the total stiffness $\boldsymbol{C}$, as

$$\boldsymbol{C} = \boldsymbol{C}_o - \mathbf{P}^+ : (\int_0^t (-\dot{\boldsymbol{C}})dt) : \mathbf{P}^+ \tag{105}$$

enforced the unilateral constraint that cracks opened under tension loading will be closed under the application of a compressive stress (Ju, 1989). In the proposed formulation, the opening and closing of the microcracks will be considered as being analogous to the sliding crack concept. The internal variable can be integrated directly,

$$\boldsymbol{C}_c = \boldsymbol{C}_o - (\int_0^t (-\dot{\boldsymbol{C}}_c)dt). \tag{106}$$

The updated damaged stiffness can be included in equation (85) and the Cauchy stress is given by

$$\boldsymbol{\sigma} = \boldsymbol{\sigma}_o + \boldsymbol{C}_o : \boldsymbol{\epsilon}_R^e + (\boldsymbol{C}_o - (\int_0^t (-\dot{\boldsymbol{C}}_c)dt)) : \boldsymbol{\epsilon}_c^e = \boldsymbol{\sigma}_o + \boldsymbol{\sigma}_R + \boldsymbol{\sigma}_c. \tag{107}$$

which forms the complete constitutive equation for loading with damage.

4.6 Damage evolution law

The evolution of damage can be quantified by providing a phenomenological expression for $\tilde{H}_{cm}$. A versatile damage evolution function is proposed here to allow the description of a variety of damage evolution processes. The function is based on the Weibull probability density function (Nelson, 1982) and its parameters can be identified to have physical meaning. The Weibull probability density function is expressed as

$$f(y) = \frac{\beta}{\theta^\beta} y^{(\beta-1)} \exp[-(\frac{y}{\theta})^\beta]. \tag{108}$$

By varying the parameter β, the function can accommodate a wide variety of shapes (Nelson, 1982). The scale parameter θ is known as the 'charateristic life' and determines the spread of the

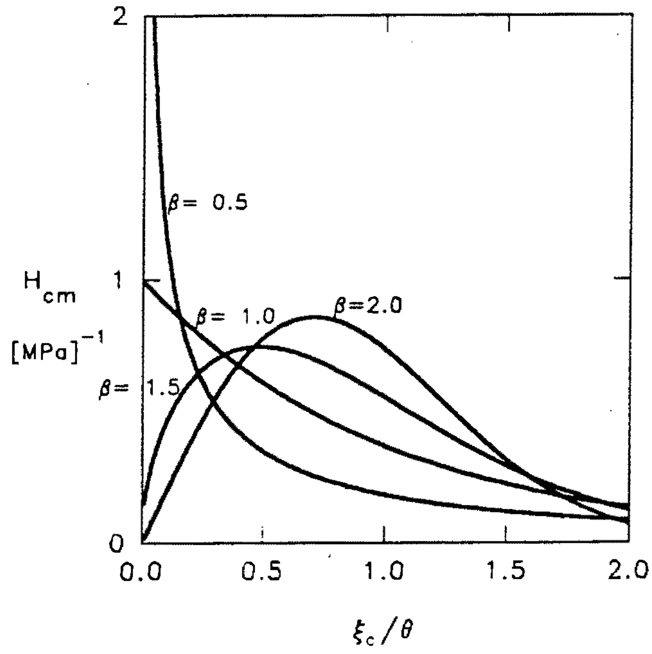

Figure 17: Influence of the 'shape' parameter β on the damage evolution law based on the Weibull probability distribution function

curve in terms of the parameter y. Associating the damage energy norm ξ_c with the parameter y and the change of damage $\dot{d}_{cm}$ with $f(y)$, the damage evolution functions can be expressed as

$$\tilde{H}_{cm} = \frac{d\hat{G}^d_m}{d\xi_c} = \frac{\beta_m}{\theta_m}\left[\frac{\xi_c}{\theta_m}\right]^{(\beta_m-1)} \exp\left[-(\frac{\xi_c}{\theta_m})^{\beta_m}\right] \tag{109}$$

where β_m is a 'shape' parameter, and θ_m is a positive 'scale' parameter. The parameter θ_m has the same dimensions as the undamaged energy norm ξ_c. The 'shape' parameter β_m is dimensionless and defines the rate at which the damage accumulates. Some selected shape of the evolution curves, as a function of the ratio ξ_c/θ_m for a range of values of β_m are shown in Figure 17. Two typical damage accumulation processes are possible. For $\beta_m \leq 1$ the value of $\tilde{H}_{cm}$ (rate of damage accumulation) decreases continually. If $\beta_m > 1$, a rapid increase of the accumulation of damage is experienced in the initial stages which reaches a maximum and then gradually decreases with and increase in ξ_c (which is equivalent to an increase in loading).

The parameter θ_m has the effect of changing the range of values of ξ_c over which the damage d_{cm} accumulates. Since ξ_c is related to the 'crack' strains ϵ^e_c, θ_m defines the amount of loading that is required for damage to develop. Thus, lower values of θ_m results in rapid damage accumulation with loading as experienced in very brittle behaviour. As θ_m is increased, a wider range of loading is involved in the damage process, as shown in Figure 18.

Based on experimental observations (for example Zheng, 1989), it is expected that the rate of damage evolution decreases with an increase in confining pressure. Thus, the confinement must be introduced into the evolution function. To allow for a wide range of realistic damage development in a material under any loading path, the 'scale' parameter θ_m is selected as a linear function of the confinement ζ that

$$\theta_m = \theta_{0m} + \theta_{1m}\zeta \tag{110}$$

with an initial value θ_{0m} and gradient θ_{1m}. The 'shape' of the damage evolution function is defined in a similar fashion as

$$\beta_m = \beta_{0m} + \beta_{1m}\zeta \tag{111}$$

with an initial value β_{0m} and gradient β_{1m}. The confinement ζ may be calculated in a number of ways. It could be a function of either the effective stress $\bar{\sigma}$, which is known at the commencement of the constitutive calculation, or the applied stress σ which is not known explicitly.

In mode II (compression), the confinement ζ is selected to be the magnitude of the projection of the applied stress in the direction of the positive 'crack' strains, (orthogonal to the direction of microcrack growth) and is accordingly calculated by

$$\zeta = \left|\left|\mathbf{P}^+ : \boldsymbol{\sigma}\right|\right| \equiv \frac{1}{2}(\sigma^+_{pij}\sigma^+_{pij})^{\frac{1}{2}} \text{ with } \mathbf{P}^+ = \mathbf{P}^+(\epsilon^e_c). \tag{112}$$

Thus, ζ is a normalised value of the stress σ^+_p acting in the direction of the positive eigenvalues of the damage strain subdomain ϵ^e_c and is in general not equal to the positive projection of the stress tensor $\boldsymbol{\sigma}^+$ i.e. $\mathbf{P}^+(\epsilon^e_c) \neq \mathbf{P}^+(\boldsymbol{\sigma})$. The physical meaning of this particular choice for ζ can been seen by examining the stress and strain states in the conventional triaxial compression test. In this case ζ is equal to the applied confining pressure of the sample, which remains constant throughout the test, thus facilitating the calibration of the evolution laws with respect to ζ.

In mode I, the damage is in extension and the loading stress is normal to the crack plane. Compressive stress in the plane of the crack has a stabilising effect on the growth of microcracks in extension. The confinement ζ therefore acts in the direction orthogonal to the positive eigenvalues of ϵ^e_c and is expressed as

$$\zeta = \left|\left|\mathbf{P}^- : \boldsymbol{\sigma}\right|\right| \equiv \frac{1}{2}(\sigma^-_{pij}\sigma^-_{pij})^{\frac{1}{2}} \quad \text{with } \mathbf{P}^- = \mathbf{P}^-(\epsilon^e_c) = I - \mathbf{P}^+(\epsilon^e_c). \tag{113}$$

For a higher value of ζ, the damage evolution function H_{cm} depends on a wider range of values of undamaged energy norm ξ_c.

4.7 Un/reloading behaviour

The essential concept of damage modelling is that the opening of microcracks within the material due to loading is reflected as a reduction the stiffness of the material. The stress - strain response during unloading is controlled by the damaged stiffness as shown schematically in Figure 14. In the proposed model, damage is only associated with a subdomain of the material behaviour

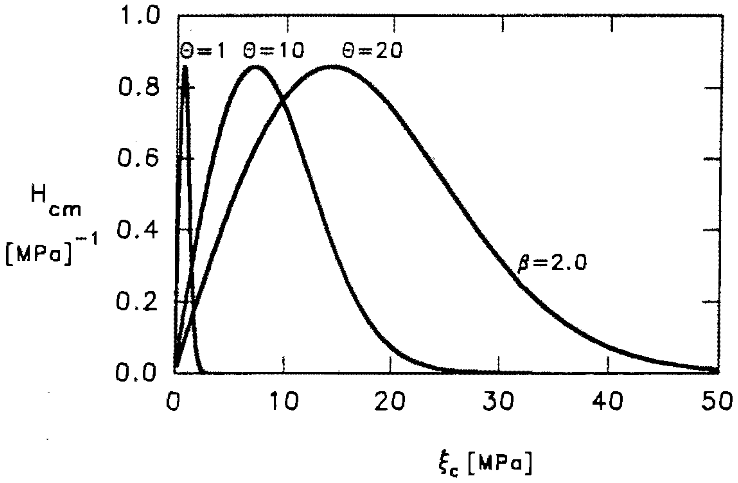

Figure 18: Influence of the 'size' parameter θ on the damage evolution law based on the Weibull probability distribution function

defined by the 'crack' strain ϵ^e_c. Thus, as mentioned in Section 4.3, a model for a sequence of unloading and reloading must consider the behaviour of both, the undamaged and the damaged parts of the material. The analogy of the inclined flaw, which slides and subsequently generates wing cracks, has been applied to develop the criteria for damage initiation and growth in loading. It will now be extended to incorporate the unloading and reloading behaviour.

During loading, the shear resistance on an inclined flaw surface must be exceeded before wing cracks form at the edges of the flaw, and grow in the direction of the maximum compressive principal stress. The undamaged material response is determined by the effective stresses. The damage initiation criterion delimits the initial undamaged domain in the effective stress space as shown in Figure 15. The damage initiation surface $\Gamma(\bar{\sigma})$ now also defines the loading/unloading criterion. The unloading material response, analogous to the closure of the wing cracks, can occur in two possible ways, depending on the change of the effective normal stress on the flaw.

Firstly, in mode I, the applied load is defined by the highest tensile principal stress. The material is in extension, and the wing cracks extend perpendicular to the loading direction. On reversal of the load (unloading), the wing cracks close as the applied stress becomes less tensile. Once the effective stress state returns to the initial undamaged domain, it is assumed that the wing cracks are completely closed and the material returns to an essentially undamaged state. Further unloading occurs with the material behaviour being characterised by a linear elastic constitutive model. Thus, the unloading criteria for updating the residual and 'crack' strains can be expressed as

$$\begin{aligned} &\dot{\epsilon}^e_c = \dot{\epsilon}^e, \quad \dot{\epsilon}^e_R = 0, \quad \text{for} \quad 0 < \Gamma < \Gamma_{max} \qquad \text{and} \\ &\dot{\epsilon}^e_c = 0, \quad \dot{\epsilon}^e_R = \dot{\epsilon}^e \quad \text{for} \quad \Gamma \leq 0 \end{aligned} \tag{114}$$

and the stress is updated according to the constitutive equation (107). The microcracks, represented by the mode I damage, resulting from the application of tension loading are closed once

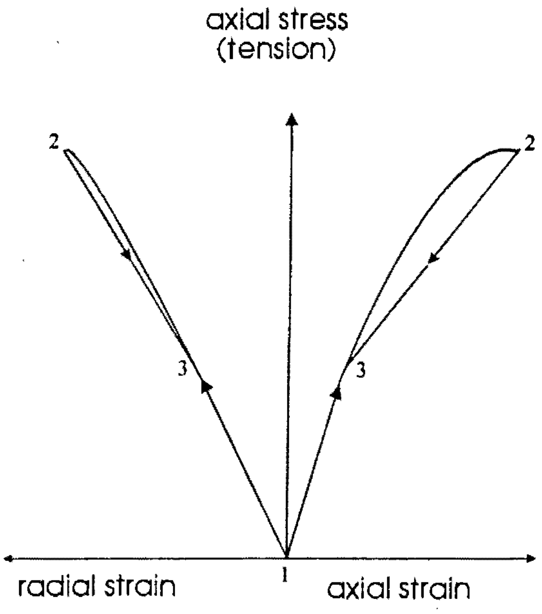

Figure 19: Schematic of stress - strain behaviour during loading and unloading in mode I

the load is removed. Subsequent compressive loading in the same direction will occur with the elastic material response, until compression damage (mode II) forms, orthogonal to the loading. This unilateral constraint on the damage growth in the specific loading case of tension - compression loading (as described in Section 4.5) is therefore directly included in the formulation of the unloading/reloading behaviour.

On reloading the material is described with the initial linear elastic characteristics until the damage surface is reached in the effective stress space, and if exceeded, continues to respond with the damaged material stiffness. The complete sequence of loading, unloading and reloading in terms of the stress - axial/radial strain response of a uniaxial tension test is depicted schematically by the series of points 1-2-3-1-3-2 as shown in Figure 19.

Secondly, in mode II, as the applied load becomes more compressive, the wing cracks grow in the direction of the maximum compressive principal stress. Upon unloading, closure of the wing cracks does not occur directly. The sliding flaw mechanism which caused the growth of the wing cracks must now, in turn, control the closure of the cracks. The resistance of the flaw surface must be overcome prior to closure of the wing cracks and thus, a 'deadband' region (Kachanov, 1982) occurs in the effective stress space during which the material behaves with the initial stress - strain response. The surfaces of the inclined flaws only start to slide relative to each other after continued unloading, leading to closure of the wing cracks. At this stage, the sliding and wing crack closure occur simultaneously, and the material behaviour is characterized by the damaged stiffness.

To accommodate the resistance of the sliding flaw in the constitutive equation, the rock behaviour is modelled as being undamaged immediately upon unloading. This response can be incorporated by an expansion or a translation of the initial undamaged domain during loading. Assuming that the loading, which causes damage, does not change the frictional resistance of

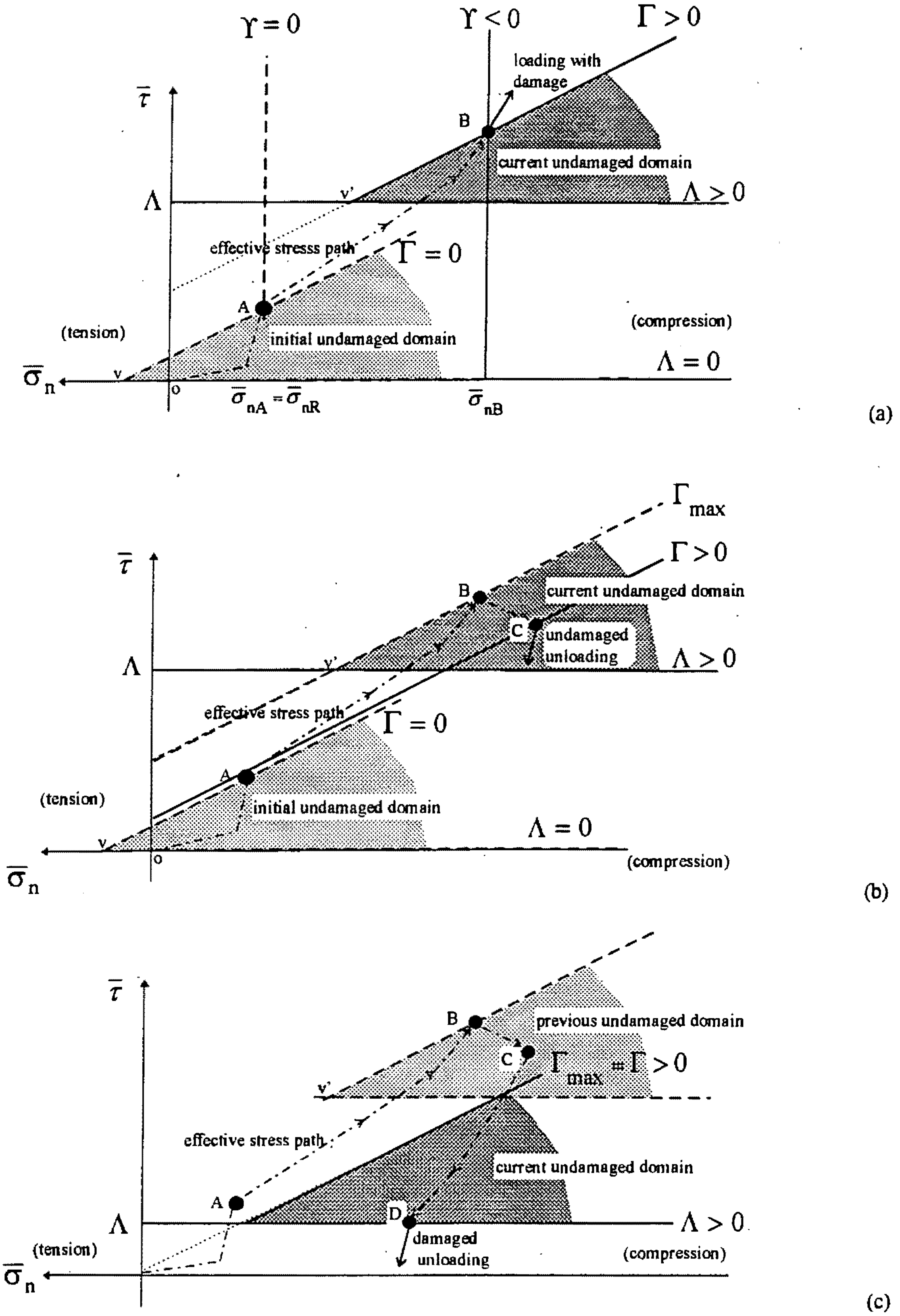

Figure 20: Schematic of translation of undamaged domain in the effective stress space during loading and unloading in mode II

sliding surfaces through wear, the undamaged domain must remain the same size and shape in the effective stress space as the initial undamaged domain and cannot therefore expand. Thus, the undamaged domain must translate in the effective stress space. In Figure 20a the initial undamaged domain (which is essentially the same as in Figure 15) is shown with a translated undamaged domain.

A further surface is, however, required to distinguish between elastic (undamaged) unloading with flaws not in the process of sliding and damaged unloading when sliding occurs. The unloading surface, denoted by Λ, delimits the lower boundary of the undamaged domain in the effective stress space and is defined by a constant effective shear stress

$$\Lambda = \bar{\tau}. \tag{115}$$

This is equivalent to the hyperbolic surface after Kachanov (1982) shown in Figure 13.

The definitions and criteria for the loading and unloading stages are best expressed by considering an example for the effective stress path $\bar{\sigma}_O \rightarrow \bar{\sigma}_A \rightarrow \bar{\sigma}_B \rightarrow \bar{\sigma}_C \rightarrow \bar{\sigma}_D$ as shown in Figures 20a, b and c. The initial loading from the origin to $\bar{\sigma}_A$ is within the undamaged domain. When the effective stresses reach the point A, the loading criterion is $\Gamma(\bar{\sigma}) = 0$ and damage initiates. The residual effective stress and strain are determined from the applied stress at damage initiation (i.e. $\bar{\sigma}_R = \bar{\sigma}_A$ and $\epsilon^e_R = \epsilon^e{}_A$). The damage surface $g(\xi_c, \zeta)$ (see also equation (101)) determines the damage evolution, as detailed in sections 4.5 and 4.6. The initial radii r_{cm} are zero and damage initiates immediately.

Damage progresses as the load increases. The mode of damage is determined by Υ as expressed in equation (76). For the given loading path damage occurs in mode II ($\Upsilon \leq 0$). Loading with damage changes both, the shear and the normal components of the effective stress. Geometric considerations show that, for the undamaged domain to remain constant in size, the change in the unloading surface Λ must consist of a component from the change in the loading criterion $\dot{\Gamma}$ as well as the projection of the increment in the effective normal stress $\dot{\bar{\sigma}}$ onto the effective shear stress axis. Thus, for any loading path in mode II, this change can be expressed as

$$\Lambda = \Gamma + \mu_o(\bar{\sigma}_n - \bar{\sigma}_{nR}), \tag{116}$$

where μ_o is a material parameter. For example, in Figure 20a, the location of the updated unloading surface becomes

$$\Lambda = \Gamma_B + \mu_o(\bar{\sigma}_{nB} - \bar{\sigma}_{nR}). \tag{117}$$

The distance from the apex of the undamaged domain to the stress point remains constant i.e. $vA = v'B$. For the point B in Figure 20a, the Cauchy stress is calculated from the constitutive equation (107) as

$$\boldsymbol{\sigma}_B = \boldsymbol{\sigma}_o + \boldsymbol{C}_o : \boldsymbol{\epsilon}^e_R + \boldsymbol{C}_c : (\boldsymbol{\epsilon}^e{}_B - \boldsymbol{\epsilon}^e_R) = \boldsymbol{\sigma}_o + \boldsymbol{C}_o : \boldsymbol{\epsilon}^e_R + \boldsymbol{C}_c : (\boldsymbol{\epsilon}^e_{cB}). \tag{118}$$

Unloading occurs when $\Gamma < \Gamma_{max}$, the effective stress state enters the undamaged domain and the path proceeds to point C in Figure 20b. The stress-strain response is controlled by the undamaged material behaviour and therefore the residual stress and strain state change. The increment in the residual strain is equal to the elastic strain increment and the residual shear and normal effective stresses are updated. The unloading surface and the maximum of the loading surface remain constant, the unloading conditions are given by

$$\begin{array}{llllll} \dot{\boldsymbol{\epsilon}}^e_R = \dot{\boldsymbol{\epsilon}}^e, & \dot{\boldsymbol{\epsilon}}^e_c = 0, & \text{for} & \Gamma < \Gamma_{max} & \text{and} & \bar{\tau} > \Lambda > 0 \\ \text{with} & \dot{\Gamma}_{max} = 0 & \text{and} & \dot{\Lambda} = 0. & & \end{array} \tag{119}$$

The Cauchy stress at point C is calculated as

$$\boldsymbol{\sigma}_C = \boldsymbol{\sigma}_o + \boldsymbol{C}_o : (\boldsymbol{\epsilon}^e_R + (\boldsymbol{\epsilon}^e{}_C - \boldsymbol{\epsilon}^e{}_B)) + \boldsymbol{C}_c : (\boldsymbol{\epsilon}^e_{cB}). \tag{120}$$

On reloading, for example from point C to point B in Figure 20b, the undamaged domain remains at the same location and the stress-strain response would be elastic. This behaviour would correspond to the material response observed in cyclic triaxial compression tests (Holcomb, 1981) (see also Figure 8 in Section 2.5).

Once the effective shear stress decreases below the unloading surface ($\bar{\tau} - \Lambda < 0$), the residual stress and strain remain unchanged. A typical effective stress state is shown at point D in Figure 20c. The 'crack' strain subdomain is updated and the material response is calculated with the damaged stiffness. The undamaged domain follows the stress path in the effective stress space and point D being fixed on the unloading surface. The unloading conditions now become

$$\begin{array}{llllll} \dot{\boldsymbol{\epsilon}}^e_R = 0, & \dot{\boldsymbol{\epsilon}}^e_c = \dot{\boldsymbol{\epsilon}}^e, & \text{for} & \Gamma < \Gamma_{max} & \text{and} & \bar{\tau} \leq \Lambda \\ \text{then} & \dot{\Gamma}_{max} = \dot{\bar{\tau}}_n & \text{and} & \dot{\Lambda} = \dot{\bar{\tau}}_n. & & \end{array} \tag{121}$$

Reloading from this state will be elastic as the effective stress enters the undamaged domain. The behaviour is described by the same conditions as for point C. A further increase in the stress state will cause the loading surface Γ to exceed the maximum value Γ_{max}. The reloading is controlled by the damage processes as detailed in Section 4.5. However, the radius of the damage surface r_{cII} will have expanded due to the previous damage loading. The damage surface at $\Gamma = \Gamma_{max}$ is

$$g(\xi_c, \zeta)_{II} \equiv \hat{G}_{II}(\xi_c, \zeta) = r_{cII}. \tag{122}$$

Reloading will occur with the damaged modulus until the new value of $\hat{G}_{II}(\xi_c, \zeta)$ exceeds the previous damage surface radius r_{cII}. Damage will then occur as loading continues.

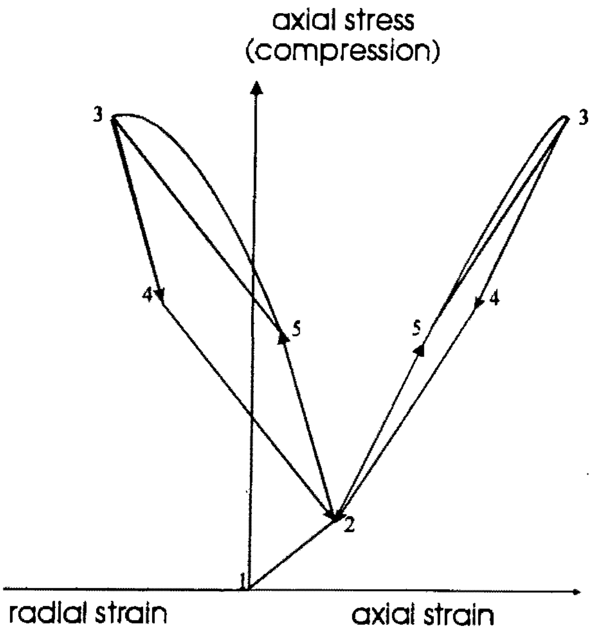

Figure 21: Schematic of stress - strain behaviour loading and unloading in mode II

The stress-strain response associated with such a sequence of loading is shown in the schematic of Figure 21 for a triaxial compression stress path. The sample is loaded in hydrostatic compression (1-2) followed by a deviatoric stress application (2-3). As the deviatoric stress is removed, the response is described by undamaged (3-4) and then damaged unloading (4-2). Removal and re-application of the hydrostatic stress is elastic (2-1-2). Increase of the deviatoric stress results in elastic response (2-5) followed by reloading with a damaged stiffness (5-3). Damage will proceed once the previous maximum stress state (3) is exceeded.

4.8 Computational implementation

4.8.1 Finite element solution procedure

The anisotropic damage model is a strain based formulation and therefore suited for implementation into a standard, displacement based, nonlinear finite element scheme for the purposes of solving geotechnical engineering problems. The Newton-Raphson iterative procedure is applied for the solution of the nonlinear analysis.

The virtual work of a body of volume V subjected to surface tractions $\boldsymbol{f}$ on an area S and body force $\boldsymbol{b}$, is given by the 'Principle of Virtual Work', stated (Owen and Hinton, 1980; Mitchell, 1990) as

$$F(\boldsymbol{u}, \delta\boldsymbol{u}) = \int_V \sigma\delta\epsilon dV - \int_S \boldsymbol{f}\delta\boldsymbol{u} dS + \boldsymbol{b}\delta\boldsymbol{u} dV \tag{123}$$

where $\delta\epsilon$ and $\delta\boldsymbol{u}$ are virtual strains and nodal displacements, respectively. The expression is linearised by expansion in Taylor series form, and neglecting the higher order terms gives

$$F(\boldsymbol{u} + d\boldsymbol{u}, \delta\boldsymbol{u}) = F(\boldsymbol{u}, \delta\boldsymbol{u}) + \frac{dF}{d\boldsymbol{u}} d\boldsymbol{u}. \tag{124}$$

By setting $F(\boldsymbol{u} + d\boldsymbol{u}, \delta\boldsymbol{u})$ to zero, an iterative scheme can be defined for each load increment j and iteration i as

$$F_j^i + \frac{dF}{d\boldsymbol{u}}\|_j^i d\boldsymbol{u}_j^i = 0, \tag{125}$$

analogous to the standard Newton-Raphson iterative procedure.

Introducing the strain - displacement relation $\boldsymbol{\epsilon} = \boldsymbol{B}\boldsymbol{u}$, equation (125) becomes

$$\int_V \boldsymbol{B}^T \boldsymbol{D}_j^i \boldsymbol{B} dV \, d\boldsymbol{u}_j^i = - \int_V \boldsymbol{B}^T \boldsymbol{\sigma}_j^i dV + \int_S \boldsymbol{f}_j dS + \int_V \boldsymbol{b}_j dV \tag{126}$$

where $\boldsymbol{D}_j^i = \frac{d\boldsymbol{\sigma}}{d\boldsymbol{\epsilon}}|_j^i$ is the Jacobian, or tangent modulus. Equation (126) can be expressed in terms of the global stiffness matrix $\boldsymbol{K}_j^i$, and the residual load vector $\boldsymbol{r}_j^i$ as

$$\boldsymbol{K}_j^i d\boldsymbol{u}_j^i = \boldsymbol{r}_j^i, \tag{127}$$

which is the standard form of the incremental solution procedure. The solution of this equation requires two steps for each iteration. Firstly, the displacement increment is predicted using an estimate for the tangent modulus. The total strain calculated from the displacement, considering a small strain - displacement relationship. Secondly, the stress and internal variables are updated in a corrector step. If the tangent modulus $\boldsymbol{D}_j^i$ is calculated in a manner consistent with the integration of the constitutive equation, quadratic convergence is assured.

The anisotropic damage model is a secant formulation and so the initial stiffness approach is applied in the incremental finite element solution procedure. Therefore, the displacement update is predicted using the initial elastic stiffness matrix in the expression for the tangent modulus, i.e. $\boldsymbol{D}_j^i = \boldsymbol{D}_o^o$. The corrector algorithm for an iteration n, using the Euler backward (fully implicit) integration of the constitutive relation is summarised in the subsequent sections.

4.8.2 Corrector algorithm : Elastic and plastic strain update

The strains are updated by adding the current strain increment to the previous value of strain. Then, for perfectly brittle materials,

$$\boldsymbol{\epsilon}^{(n)} = \boldsymbol{\epsilon}^{(n-1)} + \Delta\boldsymbol{\epsilon}^{(n)} \quad \text{and} \quad \boldsymbol{\epsilon}^{e(n)} = \boldsymbol{\epsilon}^{(n)}. \tag{128}$$

If the undamaged material is considered to have elastic-plastic constitutive behaviour, the trial values for the plastic strain $\boldsymbol{\epsilon}^p$ and internal variables $\boldsymbol{q}$ are found as

$$\epsilon^{p}_{trial}{}^{(n)} = \epsilon^{p(n-1)}, \quad q^{(n)} = q^{(n-1)} \tag{129}$$

and the trial elastic strains can be calculated as

$$\epsilon^{e}_{trial}{}^{(n)} = \epsilon^{(n)} - \epsilon^{p}_{trial}{}^{(n)} = \epsilon^{(n-1)} + \Delta\epsilon^{(n)} - \epsilon^{p}_{trial}{}^{(n)}. \tag{130}$$

If the material has a plastic component of the free energy, the predicted values of the effective stresses are

$$\bar{\sigma}_{trial}{}^{(n)} = \sigma_o + C_o : \epsilon^{e}_{trial}{}^{(n)} \tag{131}$$

and the yield criterion $f(\bar{\sigma}, q) = 0$ is applied. If the yield criterion is exceeded, then the effective stresses are updated using a standard corrector algorithm (e.g. Ortiz and Martin, 1988) to obtain $\bar{\sigma}^{(n)}, q^{(n)}$, and $\epsilon^{p(n)}$ in such a way that

$$f(\bar{\sigma}, q) \leq 0, \quad \dot{\lambda} \geq 0, \quad \text{and} \quad \dot{\lambda} f(\bar{\sigma}, q) = 0. \tag{132}$$

In this case, the elastic strains are updated by calculating

$$\epsilon^{e(n)} = \epsilon^{(n)} - \epsilon^{p(n)}. \tag{133}$$

4.8.3 Corrector algorithm : Determination of loading state

The current effective stress state is calculated from the constitutive relation

$$\bar{\sigma}^{(n)} = \sigma_o + C_o : \epsilon^{e(n)}. \tag{134}$$

The principal values of the effective stress ($\bar{\sigma}_1 \leq \bar{\sigma}_2 \leq \bar{\sigma}_3$) are obtained from the eigenvalues of $\bar{\sigma}$. The maximum and minimum principal stresses are identified as σ_{max} and σ_{min}. In the three-dimensional case, the principal stresses are denoted as

$$\bar{\sigma}_{max} = \bar{\sigma}_1, \quad \bar{\sigma}_{min} = \bar{\sigma}_3. \tag{135}$$

In plane strain, however, the requirement of ensuring that the damage only occurs in the plane of loading is equivalent to taking only the principal stresses in the plane into account. Thus, with the convention that $\bar{\sigma}_{33}$ is the out-of-plane stress, the following associations are made

$$\text{if} \quad \begin{cases} \bar{\sigma}_1 = \bar{\sigma}_{33} & \Rightarrow \bar{\sigma}_{max} = \bar{\sigma}_2, \quad \bar{\sigma}_{min} = \bar{\sigma}_3 \\ \bar{\sigma}_2 = \bar{\sigma}_{33} & \Rightarrow \bar{\sigma}_{max} = \bar{\sigma}_1, \quad \bar{\sigma}_{min} = \bar{\sigma}_3 \\ \bar{\sigma}_3 = \bar{\sigma}_{33} & \Rightarrow \bar{\sigma}_{max} = \bar{\sigma}_1, \quad \bar{\sigma}_{min} = \bar{\sigma}_2 \end{cases} . \tag{136}$$

The effective shear and effective normal stresses can be calculated according to equation (75) as

$$\bar{\tau}^{(n)} = 0.5 * \sqrt{(\bar{\sigma}_{max}{}^{(n)} - \bar{\sigma}_{min}{}^{(n)})^2} \quad \text{and} \quad \bar{\sigma}_n{}^{(n)} = 0.5 * (\bar{\sigma}_{max}{}^{(n)} + \bar{\sigma}_{min}{}^{(n)}), \tag{137}$$

from which the changes in the effective shear stress and effective normal stresses

$$d\bar{\tau}^{(n)} = \bar{\tau}^{(n)} - \bar{\tau}^{(n-1)} \quad \text{and} \quad d\bar{\sigma}_n{}^{(n)} = \bar{\sigma}_n{}^{(n)} - \bar{\sigma}_n{}^{(n-1)} \tag{138}$$

are calculated. Then, the damage loading criterion

$$\Gamma^{(n)} = \bar{\tau}^{(n)} - \mu_0 \bar{\sigma}_n{}^{(n)} - \bar{\tau}_o{}^{(n)} \tag{139}$$

is evaluated and the maximum and minimum values are obtained as

$$\Gamma_{max} = \max\{\Gamma^{(n)}, \Gamma_{max}{}^{(n)}\} \quad \text{and} \quad \Gamma_{min} = \min\{\Gamma^{(n)}, \Gamma_{min}{}^{(n)}\}. \tag{140}$$

The current state of damage can be determined by checking Γ, and the following conditions apply

$$\text{if} \quad \begin{cases} d_{cm}{}^{(n)} = 0 & \text{and} \quad \Gamma \leq 0 \quad \rightarrow \quad \text{no damage} \\ d_{cm}{}^{(n)} > 0 & \text{and} \quad \Gamma > 0 \quad \rightarrow \quad \text{damage proceeds.} \end{cases} \tag{141}$$

The residual and 'crack' strains must be updated which depend on the current effective stress state. Thus, one of the following conditions applies :

$$\text{if} \quad \begin{cases} \Gamma^{(n)} > \Gamma_{max}{}^{(n-1)} & \rightarrow \text{loading} \\ \text{otherwise.} & \rightarrow \text{un/reloading.} \end{cases} \tag{142}$$

If the material is in the process of being un/reloaded, it is necessary to determine whether the response is calculated based on a damaged or undamaged stiffness. Thus,

- in mode m=I
    - if $\Gamma^{(n)} > 0 \longrightarrow$ damaged
    - if $\Gamma^{(n)} \leq 0 \longrightarrow$ undamaged

- in mode m = II
  - if $\bar{\tau}^{(n)} > \Lambda^{(n-1)} \rightarrow$ undamaged
  - if $\bar{\tau}^{(n)} \leq \Lambda^{(n-1)} \rightarrow$ damaged
  - if $\left|\bar{\tau}^{(n)} - \bar{\tau}^{(n-1)}\right| < tol$ and $\bar{\tau}^{(n-1)} > \Lambda^{(n-1)} \rightarrow$ damaged

where *tol* is a small value set to prevent unstable oscillations between damaged and undamaged unloading. The update of the residual and 'crack' strains, the stiffness and the stress during each of these conditions is detailed in the following sections.

4.8.4 Evaluation of residual and damaged states

1. *undamaged response :*

   The residual strain is updated since there is no 'crack' strain. Thus,

   $$\epsilon^e_R = \epsilon^e, \quad \epsilon^e_c = \epsilon^e - \epsilon^e_R = 0. \tag{143}$$

2. *anisotropic damaged :*

   (a) *loading with damage*

   If anisotropic damage occurs, then $\Gamma^{(n)} > {\Gamma_{max}}^{(n-1)}$. When the previous maximum of Γ is exceeded, it is necessary to calculate changes in the residual stresses. This is done by assuming a linear change over the increment. Thus,

   $$\text{if} \quad \begin{cases} \Gamma^{(n-1)} < {\Gamma_{max}}^{(n-1)} & \rightarrow \gamma = \left|\frac{\Gamma^{(n)} - {\Gamma_{max}}^{(n-1)}}{\Gamma^{(n)} - \Gamma^{(n-1)}}\right| \\ \text{otherwise} & \rightarrow \gamma = 1. \end{cases} \tag{144}$$

   The residual stresses and strains are updated and the 'crack' strains can be calculated as

   $$\begin{aligned} {\bar{\sigma}_{nR}}^{(n)} &= {\bar{\sigma}_{nR}}^{(n-1)} + (1-\gamma) d{\bar{\sigma}_n}^{(n)} \\ {\bar{\tau}_R}^{(n)} &= {\bar{\tau}_R}^{(n-1)} + (1-\gamma) d\bar{\tau}^{(n)} \\ {\epsilon^e_R}^{(n)} &= \epsilon^{e(n-1)} + (1-\gamma) d\epsilon^{e(n)} \\ \epsilon^{e(n)}_c &= \epsilon^{e(n)} - {\epsilon^e_R}^{(n)}. \end{aligned} \tag{145}$$

   In the increment in which $\Gamma^{(n)} > 0$ the damage mode is defined by Υ. Thus, mode I occurs if $\Upsilon > 0$ and mode II if $\Upsilon \leq 0$. The new position of the unloading surface becomes

   $$\Lambda^{(n)} = \Lambda^{(n-1)} + (\Gamma^{(n)} - {\Gamma_{max}}^{(n-1)}) - \mu_o \gamma \, d{\bar{\sigma}_n}^{(n)}. \tag{146}$$

   (b) *un/reloading*

i. *damaged un/reloading response*

Usually only the 'crack' strain must be updated. However, the change in the residual stresses must be calculated during the first increment of unloading. This is done by again assuming a linear change over the increment. The maximum of the loading surface must be updated as

$$\Gamma_{max}{}^{(n)} = \Gamma_{max}{}^{(n-1)} + (d\bar{\tau})^{(n)} \tag{147}$$

and the elastic unloading surface becomes

$$\Lambda^{(n)} = \Lambda^{(n-1)} + (\Gamma^{(n)} - \Gamma^{(n-1)}) - \mu_o \gamma \, d\bar{\sigma}_n{}^{(n)}. \tag{148}$$

Then, the 'crack' strains can be calculated from

$$\epsilon_c{}^{(n-1)} \;=\; \epsilon_e{}^{(n)} - \epsilon_R{}^{(n)}. \tag{149}$$

ii. *undamaged un/reloading response*

In this case, the residual strains and stresses are updated. Changes in the 'crack' strain occur only when elastic unloading first begins in mode I. In mode II, the initial increment of unloading is entirely elastic because the stress state moves directly off the loading surface into the undamaged domain. The maximum of the loading surface $\Gamma_{max}{}^{(n)}$ and the unloading surface $\Lambda^{(n)}$ remain fixed.

Then, the residual stresses can be calculated as:

$$\begin{aligned} \bar{\sigma}_{nR}{}^{(n)} &= \bar{\sigma}_{nR}{}^{(n-1)} + (1-\gamma) d\bar{\sigma}_n{}^{(n)} \\ \bar{\tau}_R{}^{(n)} &= \bar{\tau}_R{}^{(n-1)} + (1-\gamma) d\bar{\tau}^{(n)} \end{aligned} \tag{150}$$

and the residual and 'crack' strains become

$$\begin{aligned} \epsilon_R^{e\,(n)} &= \epsilon_R^{e\,(n-1)} + (1-\gamma) d\epsilon^{e(n)} \\ \epsilon_c^{e(n)} &= \epsilon^{e(n)} - \epsilon_R^{e\,(n)}. \end{aligned} \tag{151}$$

4.8.5 Update of damaged stiffness and stress

Once the residual and 'crack' strain in the respective loading modes have been determined, the stress update can proceed. For each increment, the positive part of the predicted 'crack' strain is calculated as

$$\epsilon_c^{e+(n)} = \mathbf{P}^{+(n)} \epsilon_c^{e(n)}. \tag{152}$$

The undamaged energy norm of the positive part of the 'crack' strain is evaluated according to equation (94) as

$$\xi_c{}^{(n)} = \epsilon_c^{e+(n)} : \boldsymbol{C}_o : \epsilon_c^{e+(n)}. \tag{153}$$

The confinement is evaluated using the stress from the previous load increment. In mode I, this is

$$\zeta^{(n)} = \|(\boldsymbol{I} - \mathbf{P}^{+}{}_{\epsilon}{}^{(n)}) : \boldsymbol{\sigma}^{(n-1)}\|, \tag{154}$$

and in mode II

$$\zeta^{(n)} = \|\mathbf{P}^{+}{}_{\epsilon}{}^{(n)} : \boldsymbol{\sigma}^{(n-1)}\|. \tag{155}$$

Then, the parameters of the evolution law are determined for $m = \mathrm{I}$ or II as

$$\begin{aligned} \beta_m{}^{(n)} &= \beta_{0m} + \beta_{1m}\zeta^{(n)} \\ \theta_m{}^{(n)} &= \theta_{0m} + \theta_{1m}\zeta^{(n)} \end{aligned} \tag{156}$$

If the 'crack' strain has one or more positive eigenvalues (i.e. $\epsilon_{ci}^{+} > 0$ for any $i = 1, 2, 3$) the change in the stiffness can be determined from

$$\Delta \boldsymbol{C}_c{}^{(n)} = \begin{cases} 0 & \text{if} \quad \tilde{G}(\xi_c{}^{(n)}, \zeta^{(n)}) - r_{cm}{}^{(n-1)} < 0 \\ \Delta \boldsymbol{C}_{cm}{}^{(n)} & \text{if} \quad \tilde{G}(\xi_c{}^{(n)}, \zeta^{(n)}) - r_{cm}{}^{(n-1)} \geq 0 \end{cases}, \tag{157}$$

where

$$\Delta \boldsymbol{C}_{cm}{}^{(n)} = -(\xi_c{}^{(n)} - \xi_c{}^{(n-1)})\tilde{H}_{cm}{}^{(n)}\mathbf{P}^{+(n)} : \boldsymbol{C}_o : \mathbf{P}^{+(n)} \tag{158}$$

and

$$\tilde{H}_{cm} = \frac{d\hat{G}_m^d}{\xi_c} = \frac{\beta_m}{\theta_m}\left[\frac{\xi_c}{\theta_m}\right]^{(\beta_m - 1)} \exp\left[-(\frac{\xi_c}{\theta_m})^{\beta_m}\right]. \tag{159}$$

Otherwise, if there are no positive eigenvalues of the 'crack' strain, $\epsilon_{ci}^{+} \leq 0$ for any $i = 1, 2, 3$, there is no damage. In this case, the stiffness tensor is the same as the one from the previous increment and

$$\Delta \boldsymbol{C}_c{}^{(n)} = 0. \tag{160}$$

The total contribution to the anisotropic damaged secant stiffness can be calculated by integrating the change in stiffness as

$$\boldsymbol{C}_c{}^{(n)} = \boldsymbol{C}_c{}^{(n-1)} + \Delta \boldsymbol{C}_c{}^{(n)}. \tag{161}$$

The total stress can then be calculated from the constitutive relation direction tensor as a function of the eigenvectors of the 'crack' strain, which are known for a particular load path, and measuring the damage magnitude in terms of the scalar undamaged energy norm of the 'crack' strain. The induced anisotropy is therefore path dependent.

The damage evolution is assumed to occur in two modes, depending on the state of the effective stress acting on the plane of maximum shear. The extension mode (mode I) occurs when the effective normal stress is decreasing, and the compression mode (mode II) is defined by constant or increasing effective normal stress. The mode II is more stable than mode I and thus damage evolves in a more stable fashion as the load increases. The phenomenological evolution laws are derived from the Weibull probability density function, and have parameters which can be readily evaluated. The damage evolution is assumed to be a linear function of the confinement.

Loading and unloading can also be defined in terms of the sliding crack analogy. In mode I, unloading results in closure of the directional damage. The stress - strain response on unloading is determined by the anisotropic, damaged stiffness until the effective stress state re-enters the initial undamaged domain. In mode II, the direction of damage is orthogonal to the loading direction and the frictional resistance on the plane of maximum shear must be overcome prior to sliding. The selection of the appropriate unloading and reloading stiffness tensors is achieved by a translation of the undamaged domain in the effective stress states during loading with damage. The material initially unloads with the initial elastic response, and then experiences damaged unloading once the frictional resistance is overcome. On reversal of the load direction, the immediate material response occurs with the undamaged properties, and becomes damaged once the effective stress state exceeds the loading criterion. Additional damage will only occur once the undamaged energy norm exceeds the previous maximum values, expressed by the radius of the damage surface.

The formulation is implemented into a nonlinear finite element program with a Newton-Raphson solution scheme. A predictor - corrector scheme is presented for updating the constitutive equations at the material point level. A strain increment is predicted using the initial elastic modulus, and a corrector scheme determines the current residual and 'crack' strains, evaluates the increment in damage, updates the damage internal variable, and calculates the stress for each iteration.

Chapter 5 Parametric Studies of Damage Model

5.1 Introduction

The calibration of a constitutive model for a particular material requires the identification of the material parameters and a procedure for their determination based on appropriate laboratory tests. The evaluation of the parameters of the damage model and the types of test required to generate the data are described in the first section of this chapter. The 'size' and the 'shape' parameters of the evolution law are investigated in a sensitivity study in the subsequent section. Of particular interest is the ability to accommodate the typical features of dilatancy and induced anisotropy.

The specific application of the calibration procedure to Witwatersrand Quartzite is described in the third section of the chapter. The Quartzite was chosen for two reasons. Firstly, the rock is found in the Hangingwall strata of the deep level gold mines in the main reef group in South Africa. The prediction of reliable stress-strain behaviour and damage in this rock is therefore of great importance to the South African mining industry. Secondly, a large number of locally undertaken laboratory tests were readily available for this research work (Stavropoulou, 1982; TerraTek, 1981; Briggs, 1982; Briggs and Vieler, 1984; Briggs, 1991).

Backpredictions of the stress - strain behaviour and ultimate failure of Quartzite in the triaxial compression and extension tests, considered in the calibration procedure, is then undertaken. Finally, the stress - strain response of a selected number of stress path tests not used in the calibration is predicted to demonstrate other aspects of the model.

5.2 Procedure for calibration of the anisotropic damage model

The model parameters defined in the anisotropic damage model and the laboratory tests required for their evaluation are tabulated in Table 1. These can be any type of triaxial test, conventional triaxial compression and reduced triaxial extension tests. However, in principle, the only data required for evaluation of these parameters are the stress - strain curves from three conventional triaxial compression (CTC) and three reduced triaxial extension (RTE) tests. It should be noted that all the parameters are determined from conventional rock mechanics tests.

A point within the specimen subjected to these test procedures is characterised by the axi-symmetric principal stress state and the corresponding strain state which are expressed as

$$\sigma = \left\{ \begin{array}{c} \sigma_a \\ \sigma_r \\ \sigma_r \end{array} \right\} \quad \text{and} \quad \epsilon = \left\{ \begin{array}{c} \epsilon_a \\ \epsilon_r \\ \epsilon_r \end{array} \right\} \tag{164}$$

with the convention that tension is positive. The CTC test (with an increasing axial stress

Purpose	Parameter	Symbol	Test Required
Elastic constants	Young's modulus Poisson's ratio	E ν	1 or more triaxial tests
Initiation criterion	coefficient of friction effective shear resistance	μ_o $\bar{\tau}_0$	3 or more triaxial tests
Damage evolution	Mode I shape parameters Mode I size parameters	β_{0I} and β_{1I} θ_{0I} and θ_{1I}	3 or more RTE tests
	Mode II shape parameters Mode II size parameters	β_{0II} and β_{1II} θ_{0II} and θ_{1II}	3 or more CTC tests

Table 1: Summary of parameters of anisotropic damage model

σ_a) and the RTE test (with decreasing σ_a) are of particular interest in the determination of the constants of the model, because in both tests the radial stress σ_r (confinement) remains constant. The calibration procedures described below consider only these two standard test conditions.

5.2.1 Elastic constants and damage initiation parameters

The elastic constants, E and ν are obtained from the initial portion of the stress - strain relationship prior to the onset of dilation and can be calculated in a number of ways. With regard to the results of CTC or RTE tests, during the deviatoric loading stage, the relationships are as follows

$$\nu = -\frac{\epsilon_r - \epsilon_h}{\epsilon_a - \epsilon_h} \quad \text{then} \quad E = \frac{\sigma_d(1+\nu)(1-2\nu)}{(1-\nu-2\nu^2)(\epsilon_r - \epsilon_h)}, \tag{165}$$

where ϵ_h is the strain due to the initial hydrostatic loading and σ_d is the deviatoric stress. If a number of tests are available, the calculation of averaged values of E and ν is recommended.

Evaluation of the parameters μ_o and $\bar{\tau}_0$ describing the damage initation surface requires the determination of the stress state at the onset of dilation. This can be achieved using the C' method, determining the onset of nonlinearity of the stress - strain curves, the onset of significant acoustic emission or the onset of an increase in ultrasonic wave travel time (as described in Section 4.3). The axial stress $\bar{\sigma}_{Ra}$ and radial stress $\bar{\sigma}_{Rr}$ states at damage initiation are equal to the effective residual stresses $\bar{\sigma}_{Ra}$ and $\bar{\sigma}_{Rr}$, respectively. Likewise, the strain states at damage initiation define the residual axial and radial strains, ϵ_{Ra} and ϵ_{Rr}. The effective shear stress $\bar{\tau}_R = 0.5 * \sqrt{(\bar{\sigma}_{Ra} - \bar{\sigma}_{Rr})^2}$ and the effective normal stress $\bar{\sigma}_{nR} = 0.5 * (\bar{\sigma}_{Ra} + \bar{\sigma}_{Rr})$ are determined for at least three tests with different confinements. A straight line is fitted to the experimental results (plotted in the $\bar{\tau} - \bar{\sigma}_n$ plane) by linear regression. The slope of the best fit line represents the coefficient of friction μ_o, and the $\bar{\tau}$-intercept defines the initial effective shear resistance $\bar{\tau}_0$.

5.2.2 Parameters of the evolution law

The damage evolution parameters are evaluated once the evolution law, based on the Weibull probability density function (in equation (108)), is integrated to obtain the cumulative distribution function (Nelson, 1982). For a constant stress path, the total damage d_{cm} for any value of the scalar undamaged norm ξ_c is expressed as

$$d_{cm} = 1 - \exp(-(\frac{\xi_c}{\theta_{om} + \zeta_p \theta_{1m}})^{(\beta_{om}+\zeta_p \beta_{1m})}. \tag{166}$$

The values of d_{cm} and ξ_c are calculated for a number of points along the stress-strain curve of each experiment as described below. The values of the Weibull parameters corresponding to the specific experiment can be obtained from a regression analysis of equation (166). Representative values for the evolution of damage over a range of confining pressures are found by linear regression of the parameters evaluated from a series of tests conducted at different confinements.

In mode I, the evolution is determined from stress - strain curves from reduced triaxial extension tests. The material responds in a linear elastic manner up to the residual stress state after which the stress - strain relationship for the damaged material can be considered as a linear, anisotropic elastic reponse. In any RTE test, the radial stress (confining pressure) is controlled and the corresponding axial stress $\sigma_a = \bar{\sigma}_{Ra}$ must be calculated based on the damage initiation criterion. Rearranging equation (68) gives

$$\bar{\sigma}_{Ra} = \frac{(1-\mu_o)\bar{\sigma}_{Rr} + 2\bar{\tau}_0}{(1+\mu_o)}. \tag{167}$$

The 'crack' strain subdomain must be determined as $\epsilon_c^e = \epsilon^e - \epsilon_R^e$ and thus, the axial and radial components of the 'crack' strain tensor are

$$\epsilon_{ca} = \epsilon_a - \epsilon_{Ra} \quad \text{and} \quad \epsilon_{cr} = \epsilon_r - \epsilon_{Rr}, \tag{168}$$

respectively. In the RTE test, only the axial component of the 'crack' subdomain is positive, and therefore

$$\mathbf{P}^+\epsilon_c^e \equiv \left\{ \begin{matrix} \epsilon_{ca} \\ 0 \\ 0 \end{matrix} \right\} \tag{169}$$

and the action of the positive projection operator on the stiffness tensor will identify the damaged components. Thus, the damaged stiffness matrix becomes

$$\mathbf{P}^+ C_o \mathbf{P}^+ \equiv \begin{bmatrix} a_1 & 0 & 0 \\ 0 & 0 & 0 \\ 0 & 0 & 0 \end{bmatrix} \tag{170}$$

in the principal stress co-ordinate system. The model predicts that microcracks will extend perpendicular to the sample axis and the material will become planar transversely isotropic (see equation (14)). This is also in agreement with the findings of Briggs and Vieler (1984) (as described in Section 2.2.2). As in equation (107), stress can be subdivided into residual, effective and positive parts as

$$\sigma = \bar{\sigma}_R + \bar{\sigma}_{cI} - d_{cI}\sigma^+_{cI}. \tag{171}$$

In this particular situation, these terms are then

$$\begin{Bmatrix} \sigma_a \\ \sigma_r \\ \sigma_r \end{Bmatrix} = \begin{bmatrix} a_1 & a_2 & a_2 \\ a_2 & a_1 & a_2 \\ a_2 & a_2 & a_1 \end{bmatrix} \begin{Bmatrix} \epsilon_{Ra} \\ \epsilon_{Rr} \\ \epsilon_{Rr} \end{Bmatrix} + \begin{bmatrix} a_1 & a_2 & a_2 \\ a_2 & a_1 & a_2 \\ a_2 & a_2 & a_1 \end{bmatrix} \begin{Bmatrix} \epsilon_{ca} \\ 0 \\ 0 \end{Bmatrix} - d_{cI} \begin{bmatrix} a_1 & 0 & 0 \\ 0 & 0 & 0 \\ 0 & 0 & 0 \end{bmatrix} \begin{Bmatrix} \epsilon_{ca} \\ 0 \\ 0 \end{Bmatrix}, \tag{172}$$

where the components a_1 and a_2 of the stiffness matrices are calculated using the standard linear elastic constitutive relations. Thus, for axisymmetric loading the components are

$$a_1 = \frac{E(1-\nu)}{(1+\nu)(1-2\nu)} \quad \text{and} \quad a_2 = \frac{E\nu}{(1+\nu)(1-2\nu)}. \tag{173}$$

The damage parameter d_{cI} for the stress state σ is determined by solving equation (172). The damage at any particular stress state is given by

$$d_{cI} = -\frac{\sigma^+_{cI} : (\sigma - \bar{\sigma}_R - \bar{\sigma}_{cI})}{\sigma^+_{cI} : \sigma^+_{cI}}, \tag{174}$$

which can be expressed as

$$d_{cI} = -\frac{\sigma_r - a_1\epsilon_a - 2a_2\epsilon_r}{a_1\epsilon_{ca}}, \tag{175}$$

noting that the total strain is $\epsilon = \epsilon^e_R + \epsilon^e_c$, assuming no plastic strain. The undamaged energy norm associated with the positive projection of the 'crack' strain ϵ^+_c is determined from

$$\begin{aligned} \xi_c &= \tfrac{1}{2}\begin{Bmatrix} \epsilon_{ca} & 0 & 0 \end{Bmatrix} \begin{bmatrix} a_1 & a_2 & a_2 \\ a_2 & a_1 & a_2 \\ a_2 & a_2 & a_1 \end{bmatrix} \begin{Bmatrix} \epsilon_{ca} \\ 0 \\ 0 \end{Bmatrix} \\ &= \tfrac{1}{2}a_1(\epsilon_{ca})^2. \end{aligned} \tag{176}$$

In mode II,the evolution functions can be determined by means of a similar procedure using the CTC test data. In this case, for any given confining pressure $\sigma_r = \bar{\sigma}_{Rr}$, the residual axial stress is

$$\bar{\sigma}_{Ra} = -(|\bar{\sigma}_{Rr}| + \frac{2(\mu_o|\bar{\sigma}_{Rr}| + \bar{\tau}_0)}{(1-\mu_o)}). \tag{177}$$

and the 'crack' strains are again

$$\epsilon_{ca} = \epsilon_a - \epsilon_{Ra} \quad \text{and} \quad \epsilon_{cr} = \epsilon_r - \epsilon_{Rr}. \tag{178}$$

The radial component of the 'crack' strain is positive and so

$$\mathbf{P}^+\epsilon^e_c \equiv \left\{ \begin{array}{c} 0 \\ \epsilon_{cr} \\ \epsilon_{cr} \end{array} \right\}. \tag{179}$$

Applying equation (106), the damaged stiffness matrix is expressed as

$$\mathbf{P}^+ C_o \mathbf{P}^+ \equiv \begin{bmatrix} 0 & 0 & 0 \\ 0 & a_2 & a_2 \\ 0 & a_2 & a_2 \end{bmatrix}. \tag{180}$$

The damage acts in the radial directions and thus results in cylindrical transverse isotropy of the stiffness (see equation (15)). The initial axisymmetry is preserved, assuming the material to be initially isotropic. The microcracks, however, extend along the axis of the specimen (as described in Section 2.2.2). The stress becomes

$$\sigma = \bar{\sigma}_R + \bar{\sigma}_{cII} - d_{cII}\sigma^+_{cII} \tag{181}$$

or,

$$\left\{ \begin{array}{c} \sigma_a \\ \sigma_r \\ \sigma_r \end{array} \right\} = \begin{bmatrix} a_1 & a_2 & a_2 \\ a_2 & a_1 & a_2 \\ a_2 & a_2 & a_1 \end{bmatrix} \left\{ \begin{array}{c} \epsilon_{Ra} \\ \epsilon_{Rr} \\ \epsilon_{Rr} \end{array} \right\} + \begin{bmatrix} a_1 & a_2 & a_2 \\ a_2 & a_1 & a_2 \\ a_2 & a_2 & a_1 \end{bmatrix} \left\{ \begin{array}{c} \epsilon_{ca} \\ \epsilon_{cr} \\ \epsilon_{cr} \end{array} \right\} - d_{cII} \begin{bmatrix} 0 & 0 & 0 \\ 0 & a_1 & a_2 \\ 0 & a_2 & a_1 \end{bmatrix} \left\{ \begin{array}{c} \epsilon_{ca} \\ \epsilon_{cr} \\ \epsilon_{cr} \end{array} \right\}. \tag{182}$$

Solving equation (182) for the damage parameter gives

$$d_{cII} = -\frac{\sigma^+_{cII} : (\sigma - \bar{\sigma}_R - \bar{\sigma}_{cII})}{\sigma^+_{cII} : \sigma^+_{cII}}, \tag{183}$$

which can be expressed in terms of the stress and strains at a point on the stress - strain curve as

$$d_{cII} = -\frac{\sigma_r - a_2\epsilon_a - (a_1 + a_2)\epsilon_r}{(a_1 + a_2)\epsilon_{cr}}. \tag{184}$$

The undamaged energy norm now becomes

$$\begin{aligned} \xi_c &= \tfrac{1}{2}\left\{ \begin{matrix} 0 & \epsilon_{cr} & \epsilon_{cr} \end{matrix} \right\} \begin{bmatrix} a_1 & a_2 & a_2 \\ a_2 & a_1 & a_2 \\ a_2 & a_2 & a_1 \end{bmatrix} \left\{ \begin{matrix} 0 \\ \epsilon_{cr} \\ \epsilon_{cr} \end{matrix} \right\} \\ &= (a_1 + a_2)(\epsilon_{cr})^2. \end{aligned} \tag{185}$$

The parameters from the evolution curve can be obtained by linear regression once the damage parameter d_{cII} and the undamaged energy norm ξ_c are determined for more than three points along the stress - strain curves. By taking the natural logarithm of each side of equation (166), a linear relation can be found as

$$\log d_{cm} = \log \beta_m + \frac{1}{\theta_m} \log[-\ln(1 - \xi_c)] \tag{186}$$

to relate the damage magnitude and the undamaged energy norm. These values of d_{cm} and ξ_c are obtained for a number of points along the stress - strain curve. Again, a linear regression of the $\log d_{cm}$ - $\log[-\ln(1 - \xi_c)]$ diagram will provide the representative values of θ_m and β_m for the specific test where β_m is the intercept along the $\log d_{cm}$-axis, and $\frac{1}{\theta_m}$ is the slope of the regression line.

Finally, the values for θ_{0m} , β_{0m} θ_{1m} and β_{1m} must be obtained from a regression analysis over the expected range of confining stresses. The confinements are evaluated, as given in equations (112) and (113), by

$$\zeta = \sigma_r \tag{187}$$

in both, the conventional triaxial compression and reduced triaxial extension tests.

Unless an extensive test program has been undertaken on a particular rock type, only the ultimate strength data and the elastic constants are usually available in engineering practice. Thus, stress - strain results are seldom available for determination of the material parameters and therefore the evaluation of induced anisotropy is not possible. However, the model parameters may be estimated for any particular rock from an unconfined (uniaxial) compression test stress - strain curve and the failure envelope if a complete set of triaxial test stress - strain results is unavailable. In such a situation, the values of θ_{0II} and β_{0II} (mode II) can be calculated from the uniaxial test. Assuming that the shape of the damage accumulation curve is independent of the confinement, $\beta_{1II} = 0$, and the parameter θ_{1II} is determined by fitting the failure envelope in a trial and error procedure. The mode I parameters can be estimated by considering the uniaxial tensile strength to be some fraction of the unconfined compression strength, and once again applying a trial and error method to determine the respective parameters.

5.3 Parametric study of evolution parameters

As described in Section 4.3, the evolution law is based on the Weibull probability density function. Two parameters need to be evaluated, each of which is assumed to be a linear function of the confinement. To gauge the magnitudes and changes of these two material constants with respect to the material behaviour, it is most convenient to consider the deviatoric stress q - volumetric strain v and the axial strain - radial strain graphs. The deviatoric stress is defined in terms of the deviatoric part of the stress tensor s_{ij} as

$$q = \sqrt{\frac{3}{2} s_{ij} s_{ij}}. \tag{188}$$

The von Mises equivalent stress q represents the axial loading in a triaxial test. The volumetric strain v is defined to be positive for compression and is calculated as

$$\mathrm{v} = -\frac{1}{3}\epsilon_{kk}. \tag{189}$$

The deviatoric stress - volumetric strain relation shows the development of dilatancy with increasing load. The extent of the induced anisotropy is reflected in the degree of nonlinearity of the axial strain - radial strain response.

5.3.1 Investigation of the effect of finite element discretization

The damage model is implemented in the ABAQUS finite element package (Hibbitt, 1994), and in a single material point program based on the finite element code by Owen and Hinton (1980). The Newton-Raphson solution procedure was applied in both cases. The effect of the finite element discretization was investigated by analysing simple test situations, namely the triaxial compression and reduced triaxial extension test with the ABAQUS program, and comparing these with the results obtained using the single material point program.

One-element tests were performed with four-node and eight-node quadrilateral elements to model a quarter of the axisymmetric test specimen. Both, full and reduced integration schemes were considered. Other tests were performed with multi-element meshes. Three alternative mesh geometries were considered, namely 5x10 (width by height), 10x20, and 20x40, to investigate the model response for a range of element sizes.

These single and multi-element tests were performed with load increments of 10 MPa. The results were almost identical. The finite element results were also in close agreement with results from the single material point analysis.

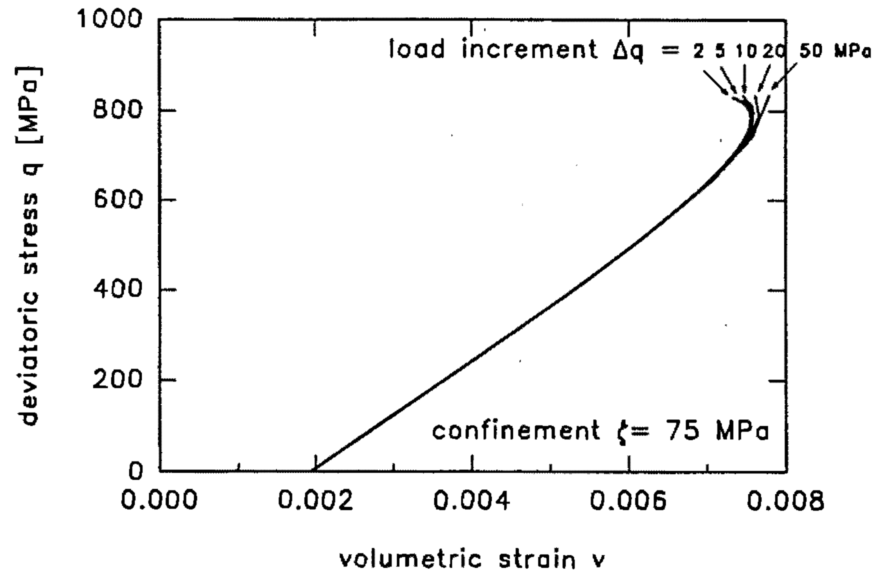

Figure 22: Effect of load increment on the volumetric stress - deviatoric strain response of Quartzite

The damage model is path dependent and therefore alteration of the load increment changes the stress - strain response. The volumetric strain-shear stress curve for triaxial compression of Quartzite is shown in Figure 22. The confinement of 75 MPa represents a typical value considered in the available experimental results. Assuming that the in-situ horizontal and vertical stresses are equal at great depths (Brady and Brown, 1993), this confinement corresponds approximately to the in-situ stress in a 3000m deep mine.

Six different load increment sizes were investigated, these being 1 MPa, 2 MPa, 5 MPa, 10 MPa, 20 MPa and 50 MPa. The loading is stress controlled and the ultimate load is defined by the nonconvergence of the solution scheme after 50 iterations. The magnitudes of the ultimate stress determined from each analysis are in agreement to within the magnitude of the respective stress increment. Due to the path dependence the dilatancy increases as more load increments are taken, which is as expected. Convergence to a single path, on the scale of the figure, is achieved for load increments less than 2 MPa.

The sensitivity studies, which are presented in the following sections, were performed with load increments of 1 MPa.

5.3.2 Size and shape parameter for triaxial compression

The 'size' parameters θ_I and θ_{II} determine the range of the undamaged energy norm over which the damage acts. The data of the conventional triaxial compression (CTC) test, which represent the mode II behaviour, is used to illustrate the effect of different values of the evolution parameters.

The 'size' parameter in mode II is defined as $\theta_{II} = \theta_{0II} + \theta_{1II}\zeta$ and the effect of the magnitude of the parameter on the stress - strain response is shown in Figure 23. Each curve represents the deviatoric stress - volumetric strain response of a predicted CTC test. For the purposes of comparison, the magnitude of the 'shape' parameter β_{II} and the confinement ζ are kept constant. The solid dark lines show the effect of the material constant θ_{0II}, since θ_{1II} was set to zero. The analyses depicted by lines with markers include the effect of the material constant θ_{1II}.

In all cases, the response in the initial hydrostatic compression stage of loading is linear elastic and the volumetric strain increases as the sample is compressed. Before damage initiation, the application of deviatoric stress results in continued elastic compression showing a linear relation between the deviatoric stress and the volumetric strain. After damage initiation, the material dilates. The dilatancy increases rapidly as the stress state approaches failure.

At the lowest value of θ_{0II} (in Figure 23), there is no significant deviation from the linear response up to the point of failure. An increase in θ_{0II}, equivalent to a larger θ_{II}, causes the damage to evolve over a wider range of ξ_c and results in more dilatancy and a higher strength at failure.

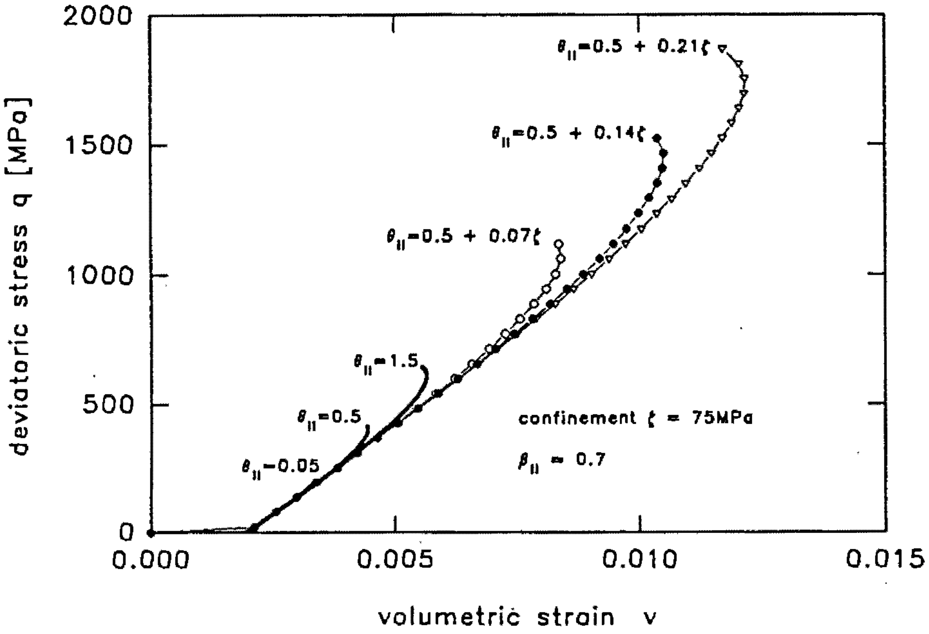

Figure 23: Effect of the 'size' parameter θ_{II} on the volumetric strain - deviatoric stress response in conventional triaxial compression

The material constant θ_{1II} allows the 'size' parameter to be expressed as a function of the confinement. Thus, for any CTC test with a particular confinement ζ an increase in θ_{1II} results in an increase in the total value of θ_{II}. The effect on the stress - strain response for four typical values of θ_{1II}, namely 0.0, 0.07, 0.14 and 0.21 , is shown in Figure 23. As the total value of θ_{II} increases, the magnitude of the dilatancy increases and the material exhibits a higher ultimate strength.

In the axial strain - radial strain graphs, shown in Figure 24, the initial hydrostatic loading is

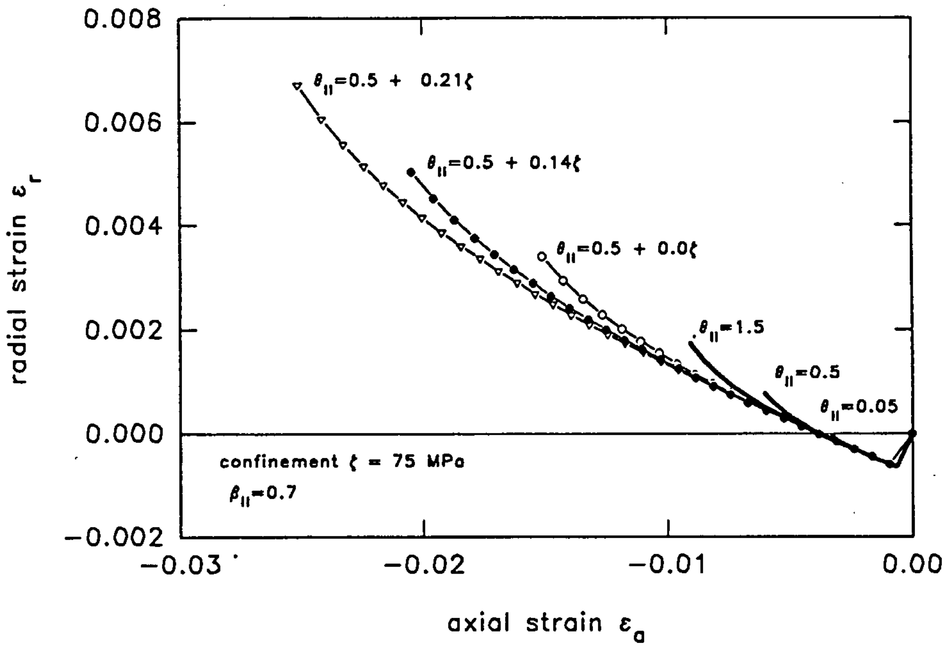

Figure 24: Effect of the 'size' parameter θ_{II} on the axial strain - radial strain response in conventional triaxial compression

reflected by both, axial and radial strains being reduced. During deviatoric loading, the axial strain remains negative, however, the radial strain becomes positive and the material expands. The ratio of the change in radial strain to the change in axial strain is the tangent Poisson's ratio $\nu_t = -\frac{\Delta\epsilon_r}{\Delta\epsilon_a}$. During the initial stages of deviatoric loading, the axial strain - radial strain response is linear and the tangent Poisson's ratio is equal to the elastic value of 0.2. After damage initiation, the radial strain increases relative to the axial strain. Thus, ν_t increases due to damage occurring perpendicular to the axial loading. The axial strain - radial strain response becomes nonlinear as the damage induced anisotropy develops.

The solid lines of the axial strain - radial strain graph in Figure 24 show that for an increase in the value of the size parameter θ_{II} (with $\theta_{1II} = 0$), there is a corresponding increase in the nonlinearity resulting from the anisotropic damage. The maximum values of the axial and radial strain are greater for the higher values of θ_{II}. For non-zero θ_{1II}, the confining pressure comes into effect. As θ_{1II} is increased, θ_{II} corresponding to the selected confinement also increases. The anisotropy develops over a larger range of strain causing an increase in the magnitude of the axial and radial strains at failure. Thus, dilatancy and ultimate strength increase with and increase in θ_{II} i.e. confinement.

The effect of θ_{II} on the damage accumulation d_{II} with respect to the deviatoric stress is shown in Figure 25a. Low values of θ_{II} simulate a steep increase of damage over a small range of deviatoric stress, hence the sudden failure and lack of dilatancy. As the magnitude of θ_{II} increases, the damage evolves less rapidly corresponding to an increased dilatancy and ultimate strength.

In mode II, the magnitude of the dilatancy is strongly affected by the 'shape' parameter β_{II}.

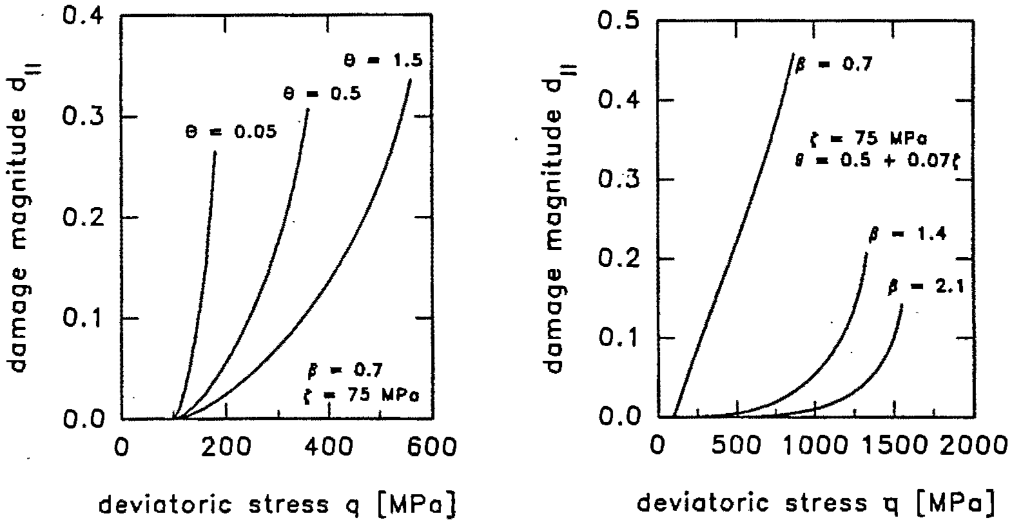

a) b)

Figure 25: Evolution of damage magnitude d_{II} with deviatoric stress a: influence of 'size' parameter θ_{II} and b: influence of 'shape' parameter β_{II}

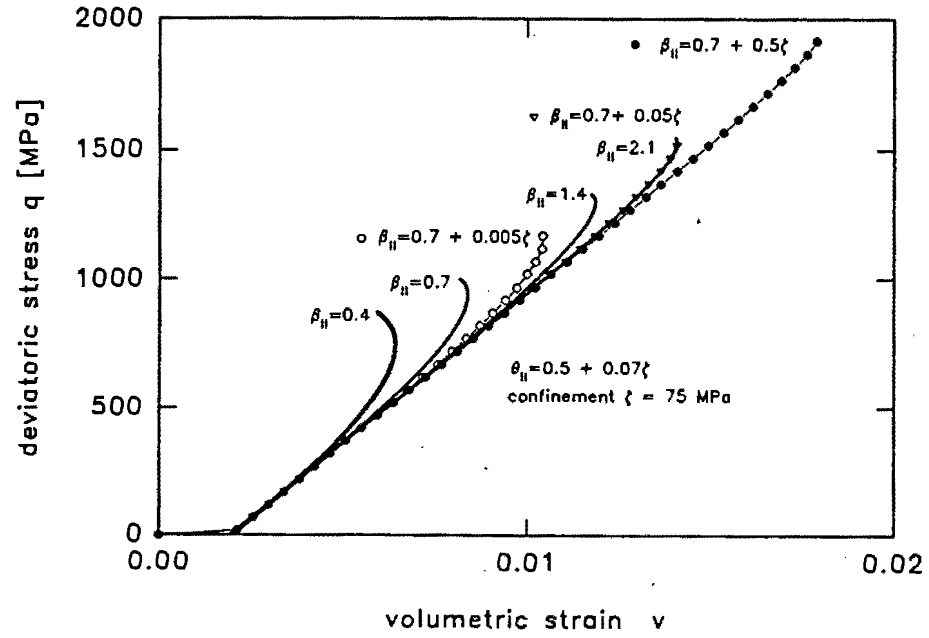

Figure 26: Effect of the 'shape' parameter β_{II} on the volumetric strain - deviatoric stress response in conventional triaxial compression

The parameter is also a function of the confinement as $\beta_{II} = \beta_{0II} + \beta_{1II}\zeta$. In Figure 26 the results of the analyses with $\beta_{1II} = 0$ are depicted as solid lines, while θ_{II} and ζ are kept constant. A range of typical values of β_{0II} from 0.4 to 2.1 is considered. In all cases, the damage initates at the same deviatoric stress, defined by the damage initiation surface. For higher β_{0II}, and thus β_{II}, the dilatancy decreases, however the ultimate strength increases.

Consideration of the rate of damage accumulation with deviatoric stress, as shown in Figure 25b, confirms that an increase in β_{II} reduces the damage at failure. The graph also demonstrates the main effect of β_{II} on the damage evolution, which is to alter the rate of damage accumulation with respect to the load increase. For low values of β_{II}, the damage increase is almost proportional to the increase in deviatoric stress. At higher values of β_{II}, the damage accumulation begins gradually and increases exponentially as the load increases. The sensitivity of the damage evolution to the magnitude of β_{II} is the reason for denoting β_{II} as the 'shape' parameter.

It is suggested that lower values of β_{0II} are suitable for the representation of weak, soft rock types in which the damage initiates at a low deviatoric stress and grows steadily throughout the loading sequence causing considerable dilatancy. Higher values of the constant β_{0II} represent the behaviour of very strong, brittle rocks. These rocks experience a sudden, rapid increase of damage leading to instantaneous failure with little dilatancy.

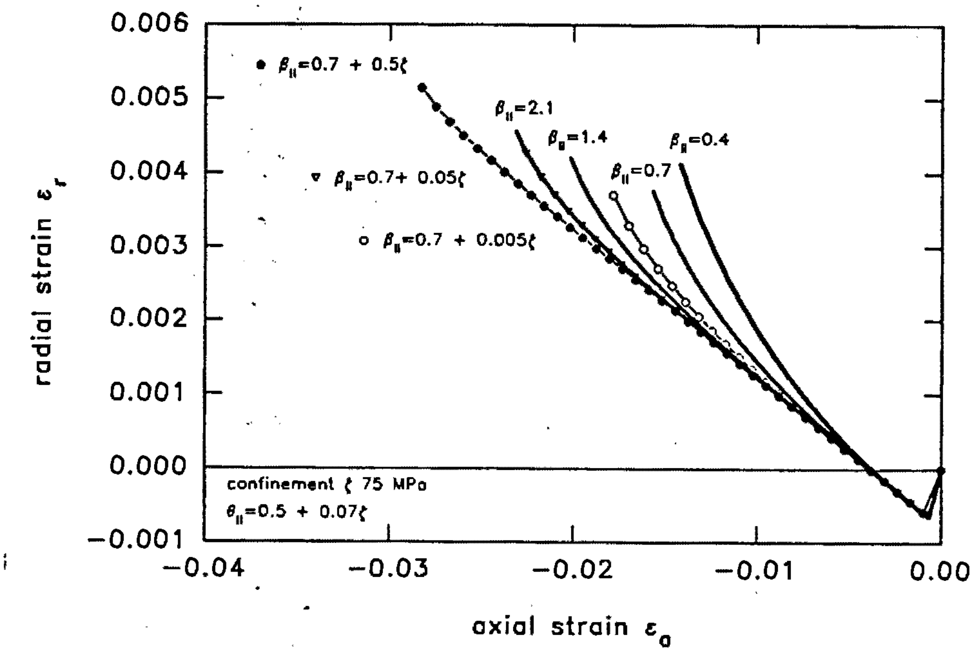

Figure 27: Effect of the 'shape' parameter β_{II} on the axial strain - radial strain response in conventional triaxial compression

The evolution of anisotropy associated with the dilatant volumetric strain is shown in the axial strain - radial strain curves depicted in Figure 27. The continual increase in damage with loading, at low values of β_{II}, is reflected in the considerable deviation from linearity of the axial strain - radial strain response. For example, in the case of $\beta_{0II} = 0.4$, the tangent Poisson's ratio increases from the elastic value of 0.2 to 0.7 at failure. The magnitude of the radial strain is also affected by the 'shape' parameter, but does not increase monotonically with an increase of β_{II}. The radial strain at failure tends to initially reduce, then increase for larger values of β_{II}. Inclusion of the parameter β_{1II} increases the value of β_{II} for a particular confinement. Larger values of β_{II} cause a reduction in dilatancy, however, a higher ultimate strength is simulated with higher confinement.

5.3.3 Failure envelope in triaxial compression

In this damage model formulation, the state of stress at failure is not specified as is the case for constitutive models based on the theory of plasticity. Instead, the damage causes a continual reduction in stiffness during loading until, at some stage, the material can no longer sustain a further increase in deviatoric stress and failure occurs. In real materials, failure would correspond to the localisation of the damage in a macroscopic crack. The failure envelope can be determined numerically from a series of analyses of different stress path tests. Under stress controlled loading, failure is considered to occur when the solution algorithm no longer converges in a specified number of iterations. The point of failure is therefore sensitive to the size of the stress increment applied in the analysis, and the maximum number of iterations that are allowed.

The objective of this study is to determine the effect of the damage evolution parameters on the failure envelope in conventional triaxial compression. A deviatoric stress increment of 1MPa was used and failure was considered to have occurred if the solution did not converge in 50 iterations. Five different confinements were considered from the range of confining pressures applied in the experimental data which were available.

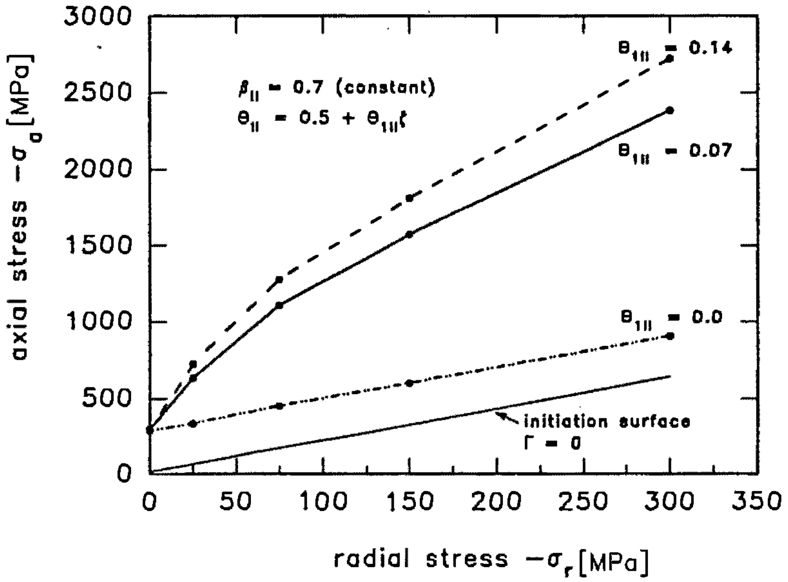

Figure 28: Failure envelopes calculated with different values of θ_{II}

The axial stress σ_a at failure resulting from analyses with various θ_{II} for a constant shape parameter β_{II} are presented in Figure 28. The effect of the confinement is introduced into the 'size' parameter θ_{II} through the material constant θ_{1II}. Thus, for non-zero θ_{1II}, the failure envelope is also a function of confinement. Although θ_{II} depends linearly on the confinement parameter ζ, the failure envelope is characterised by a non-linear curve in the axial stress - radial stress space, resulting in higher ultimate strengths at higher confining pressures. The strength increases more rapidly with an increase in confinement at the lower regions of confining stress. The rate of increase is less at higher confining pressures, giving rise to a convex failure envelope. The shape of the failure surface is similar to the well known Hoek-Brown failure envelope that has been shown to represent the failure states of a number of rocks (Hoek and Brown, 1980). Also shown is the damage initiation surface for Quartzite $\Gamma \equiv \bar{\tau} - 0.35\bar{\sigma}_n - 6.0 = 0$, which was applied in all the parametric studies (to be discussed in Section 5.4).

All the envelopes coincide at zero confinement for a particular value of θ_{0II}, which defines the unconfined (uniaxial) compressive strength (i.e. $\zeta = 0$). When the parameter θ_{1II} is set equal to zero, the deviatoric stress at failure is independent of the confining pressure, in analogy to the von Mises yield surface. As the value of θ_{1II} is increased, the ultimate strength for any confinement is also increased.

The failure envelope for the size parameter $\theta_{II} = 0.5 + 0.07\zeta$, shown as a solid line in Figure 28, is retained for the study of the influence of β_{1II} on the ultimate strength. In Figure 29, the values of β_{II} are varied resulting in the failure envelopes changing in size, although their shapes remain similar. As the magnitude of β_{1II} increases, so the ultimate strength increases.

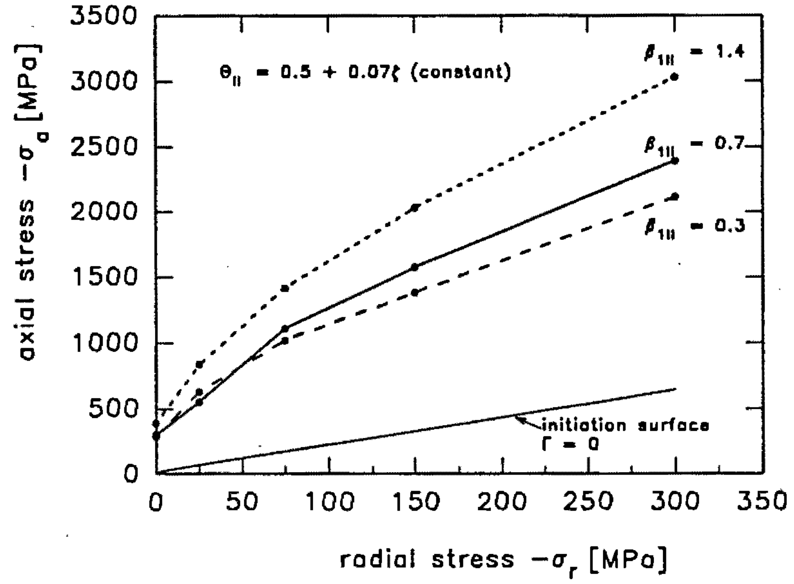

Figure 29: Failure envelopes calculated with different values of β_{II}

5.3.4 Size and shape parameters for reduced triaxial extension

In reduced triaxial extension, the damage behaviour of the material is determined by the mode I parameters θ_I and β_I. In this case, the anisotropy induced in the stiffness occurs in the direction of the axial strain, and does not manifest itself as a change in the Poisson's ratio. The axial strain - radial strain graph is therefore not of interest. The dilatant effect of the damage can, however, still be demonstrated in a volumetric strain - deviatoric stress representation, which is shown in Figure 30 for constant β_I and a confinement ζ of 75 MPa.

The volumetric strain decreases on application of the hydrostatic stress. The subsequent reduction of the axial load leads to linear elastic volumetric increase. Once the damage initiates, the response becomes nonlinear and the dilatancy grows rapidly with increasing deviatoric stress.

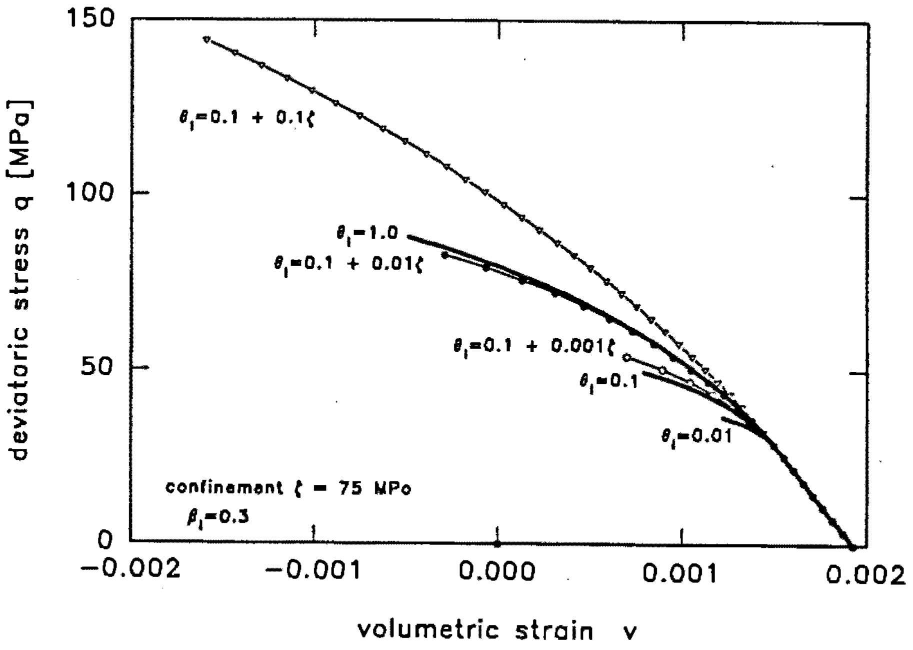

Figure 30: Effect of the 'size' parameter θ_I on the volumetric strain - deviatoric stress response in reduced triaxial extension

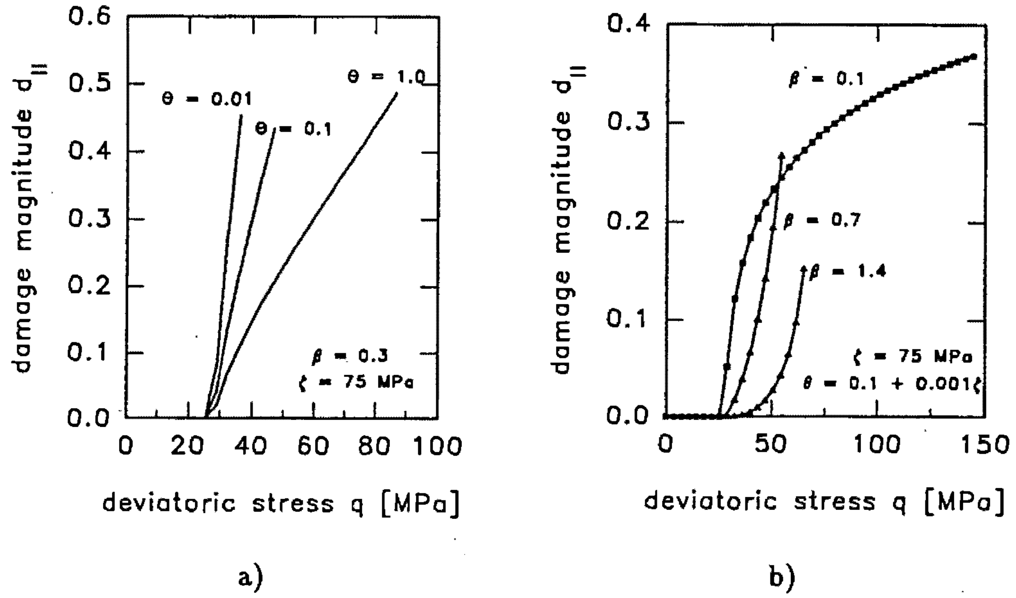

a) b)

Figure 31: Evolution of damage magnitude d_I with deviatoric stress a: influence of 'size' parameter θ_{II} and b: influence of 'shape' parameter β_{II}

The amount of dilatancy is increased for larger values of θ_I. As θ_I is increased, the damage evolution occurs more gradually to an increasingly higher ultimate strength, as shown in Figure 31a.

The effect of changes in β_I on the damage evolution with deviatoric stress is shown in Figure 31b.

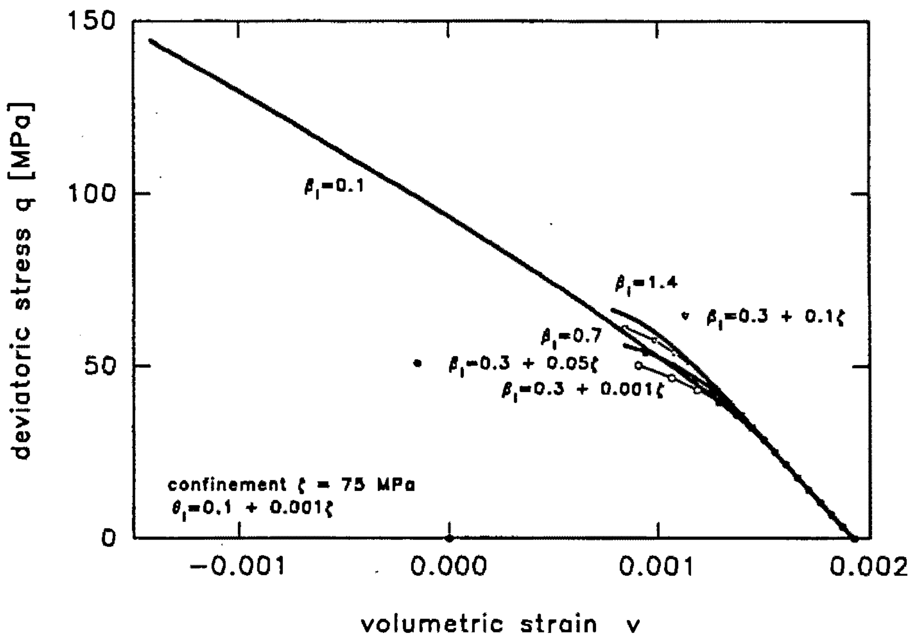

Figure 32: Effect of the 'shape' parameter β_I on the volumetric strain - deviatoric stress response in reduced triaxial extension

At very low values of β_{1I}, the damage shows a rapid increase after initiation, and the rate gradually decreases. The rate of damage changes very gradually and a considerable deviatoric strength is attained prior to failure. This results in the deviatoric stress - volumetric strain response as shown in Figure 32 (for $\beta_{1I} = 0.1$). At higher values of β_I, the trends become more regular with an increase in β_I causing a continuously steeper damage accumulation. Dilatancy and ultimate strength increase for higher values of β_I although the variation is not significant.

5.4 Calibration of damage model for Witwatersrand Quartzite

The calibration procedure, as described in Section 5.2, was applied to Witwatersrand Quartzite. The rock occurs in the hangingwall strata of South African mines and is described by Briggs and Vieler (1984) as being a metamorphosed mature sandstone with a quartz content of between 89 and 94 percent. Approximately 87 to 93 percent of the quartz is contained in the grains which are about 0.5 mm in size. The remaining quartz is distributed within the surrounding matrix material. The grains are generally fused together, but can be separated by argillaceous material derived from clay remnants consisting of grains of sericite and chlorite minerals. Thus, some variation in the engineering properties and behaviour is expected.

The damage model calibration was performed using seven conventional triaxial compression tests and three reduced triaxial extension tests. The data was provided in the form of deviatoric stress - deviatoric strain and hydrostatic stress - volumetric strain relationships.

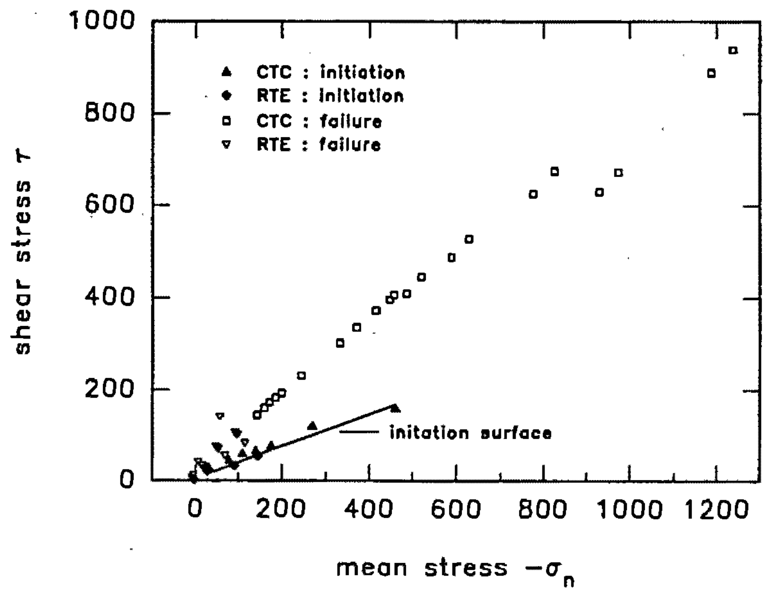

Figure 33: Damage initiation and failure surfaces for Witwatersrand Quartzite

The Young's modulus and Poisson's ratio were obtained from a regression analysis based on the CTC test data from Briggs and Vieler (1984). The damage initiation points and failure stresses determined from the experiments were plotted in the stress space, as shown in Figure 33, and the initiation surface was established. Damage initiation was considered to occur in the CTC test when the radial strain became nonlinear. In the RTE test, the nonlinearity of the axial stress - strain curve was considered to be the onset of damage. There appears to be little difference in the damage initiation surfaces for RTE and CTC tests, however, damage is found to occur at slightly lower stresses in the RTE test. Since a variation in the stress at damage initiation has a greater influence on the mode I behaviour, the final initiation surface was found by a linear regression of the RTE data. The difference of 10 MPa in deviatoric stress at damage initiation between the CTC and the RTE damage surfaces is an insignificant 0.03% of the unconfined compressive strength (mode II behaviour), but is about 60% of the uniaxial tensile strength (mode I behaviour). The damage initiation material constants obtained for the anisotropic damage model based on the regression analysis are $\bar{\tau}_0 = 6\text{MPa}$ and $\mu_o = 0.35$.

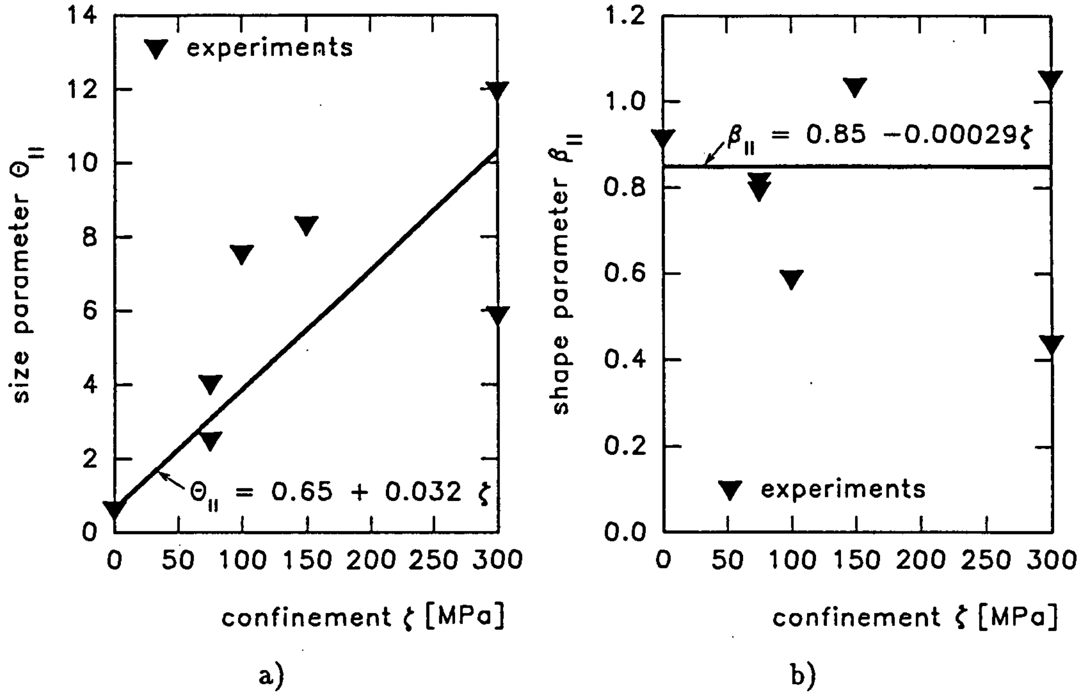

Figure 34: Evolution parameters θ_{II} and β_{II} with respect to confinement for Witwatersrand Quartzite

Using a spreadsheet program, the values of θ_I, β_I, θ_{II} and β_{II} were obtained from linear regression of $\log d_{cm}$ against $\log[-\ln(1-\xi_c)]$ as specified in equation (186). The resulting values of θ_{II} and β_{II} for the seven CTC tests are shown in Figure 34a and Figure 34b, respectively. The variability of the stress - strain response of the Quartzite is reflected in the range of the parameters. A linear regression analysis was applied to select the constants θ_{0II}, θ_{1II}, β_{0II} and β_{1II} to represent the overall response. The value of $\theta_{0II} = 0.65$ was obtained from the unconfined compression test and $\theta_{1II} = 0.032$ was determined from a regression analysis as depicted in Figure 34a. Regression of the shape parameter resulted in $\beta_{0II} = 0.85$ and $\beta_{1II} = -0.00029$. Thus, a shape parameter of $\beta_I = \beta_{0II} = 0.85$ is suggested. The regression lines are included in Figure 34 and demonstrate that the fit is less than perfect due to the variability of the Quartzite.

In reduced triaxial extension, the stress - strain results from the experiments are extremely variable, mainly due to the strong influence of flaws contained in the Quartzite samples. A wide range of parameters was obtained and a linear regression could not be reasonably applied. The parameters were estimated by extrapolating from values obtained in a uniaxial tensile test, and in a RTE test at 125 MPa confinement. Both θ_I and β_I are found to depend on the confinement. The selected values of the parameters are $\theta_{0I} = 0.1$, $\theta_{1I} = 0.004$, $\beta_{0I} = 0.2682$ and $\beta_{1I} = 0.00216$.

To summarise, the expressions for the size and shape parameters of Witwatersrand Quartzite are

$$\begin{array}{lll} \text{in mode I:} & \theta_I = 0.1 + 0.004\zeta, & \beta_I = 0.2682 + 0.00216\zeta. \\ \text{in mode II:} & \theta_{II} = 0.65 + 0.032\zeta, & \beta_{II} = 0.85, \end{array} \tag{190}$$

Assessment of the evaluated parameters can be undertaken by comparing the backpredictions of the stress - strain curves with the original data which is discussed in the following section.

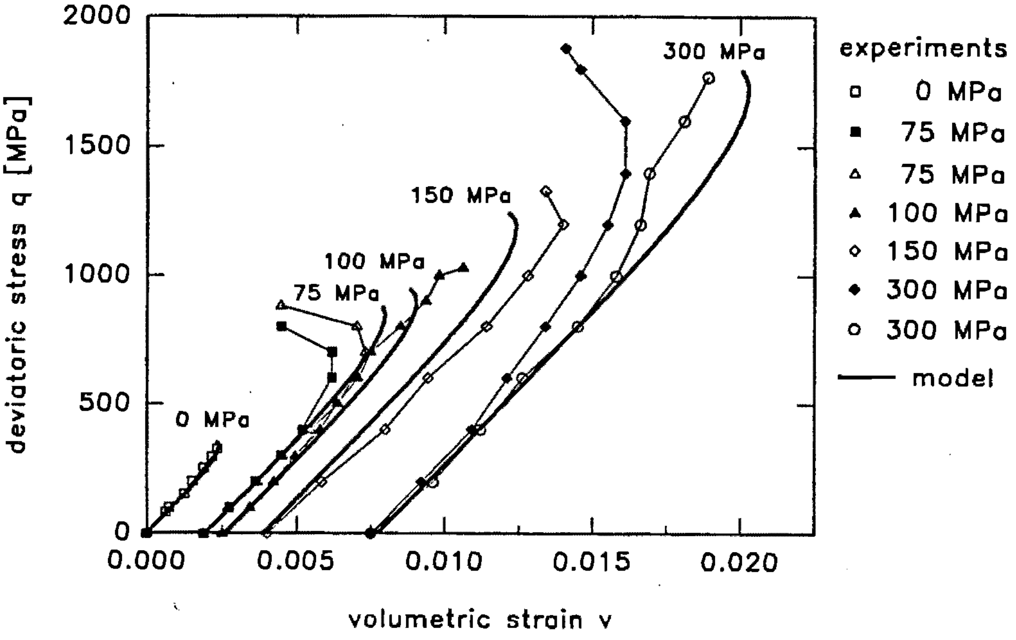

Figure 35: Comparison of backpredicted and experimental volumetric strain - deviatoric stress response in conventional triaxial compression

5.5 Backprediction of conventional triaxial compression and reduced triaxial extension tests

5.5.1 Dilatancy and induced anisotropy

The volumetric strain - deviatoric stress relationships obtained in experiments and their backpredictions using the anisotropic damage model are shown in Figure 35. The backpredicted unconfined (uniaxial) compression results compares well with the data derived from the experiments, due to the material parameters being well matched by the linear regression analysis. However, the deviations between the test data and the computed results become more pronounced, particularly at deviatoric stress levels near failure. In general, the set of parameters evaluated in the calibration procedure underestimates the dilatancy and the ultimate strength of the Witwatersrand Quartzite.

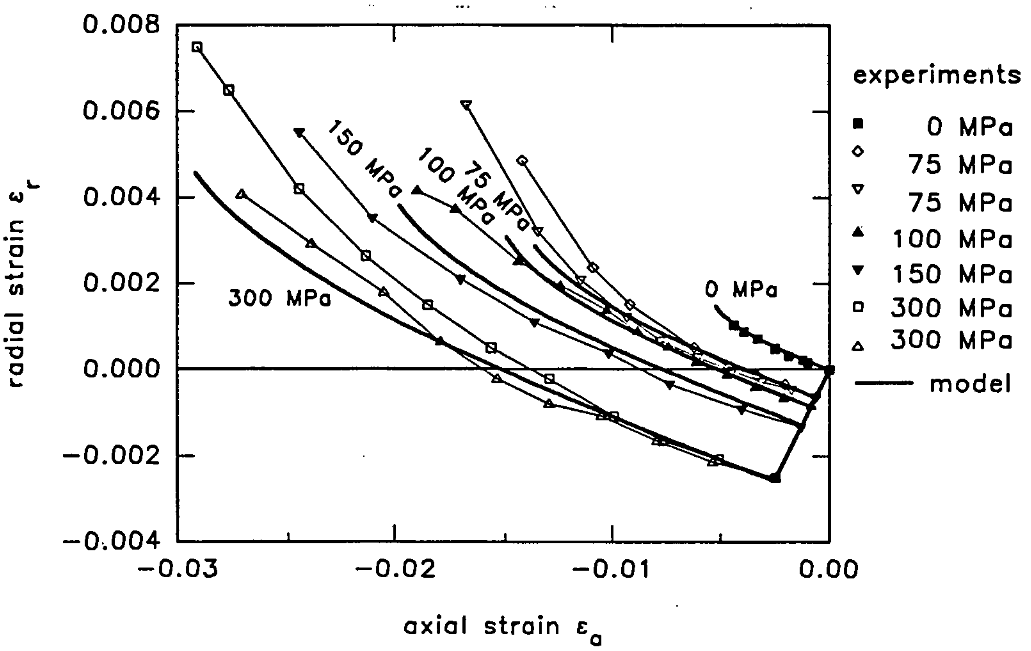

Figure 36: Comparison of the experimental and backpredicted axial strain - radial strain response in conventional triaxial compression

The backprediction of the strain paths, as shown in Figure 36, suggests that the initial elastic behaviour and the simulation of the induced anisotropy is in good agreement with the data. However, since the rock exhibits a wide variation of response in the experiments, there appears to be no clear relationship between the strains at failure and the confining pressure. In general, however, the model attains the objective of providing a very good backprediction of the trends as well as a quantitative agreement with the observed material behaviour in conventional triaxial compression.

The volumetric strain - deviatoric stress results obtained from backpredictions of RTE tests at four different confining pressures are given in Figure 37. The backpredicted tests are in close agreement with the experimental data. The predictions of the magnitudes of the ultimate strength and final volumetric strain agree closely.

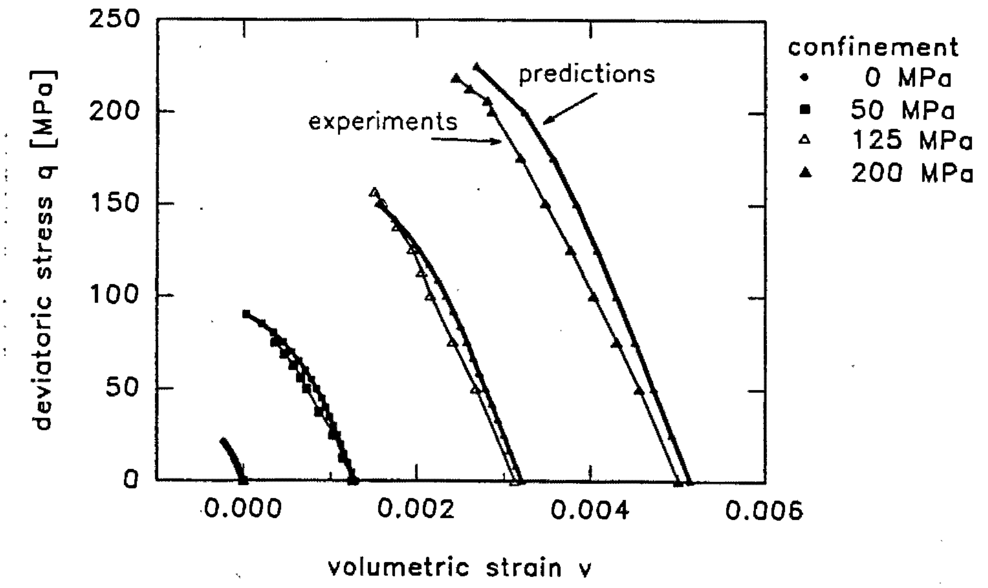

Figure 37: Comparison of backpredicted and experimental volumetric strain - deviatoric stress response in reduced triaxial extension

A difference between the backpredictions of the RTE tests and the experimental data becomes evident in the radial strain - axial strain curves, shown in Figure 38. The ratio of the radial strain to the axial strain during deviatoric loading (equivalent to the tangent Poisson's ratio) measured in the tests has an average value of 0.11 which is significantly lower than the value of 0.2 backpredicted by the damage model. The Witwatersrand Quartzite exhibits different values of Poisson's ratio in triaxial compression and extension. The initial Poisson's ratio of 0.2, applied in the model, is obtained from conventional triaxial compression tests results which does not reflect the RTE response. (The high value of $\nu_t = 0.2$ applied in the analysis of the triaxial extension tests is the cause of the difference between the backpredicted and the experimental volumetric strains, as shown in Figure 37.)

5.5.2 Ultimate strength

Another assessment of the damage model can be obtained by consideration of the predicted failure envelope. Many more experimental results are available since tests in rock engineering are generally focussed on the determination of the ultimate strength. Again, failure was obtained in the numerical simulation, if the solution did not converge within 50 iterations, and a load increment of 1 MPa was applied. The results are shown in the principal stress space in Figure 39.

In the CTC test, with principal stresses $\sigma_1 = \sigma_a$ and $\sigma_3 = \sigma_r$, the deviatoric stress path is a vertical line. The principal stresses of an RTE test are $\sigma_1 = \sigma_r$ and $\sigma_3 = \sigma_a$ and therefore the loading path is a horizontal line.

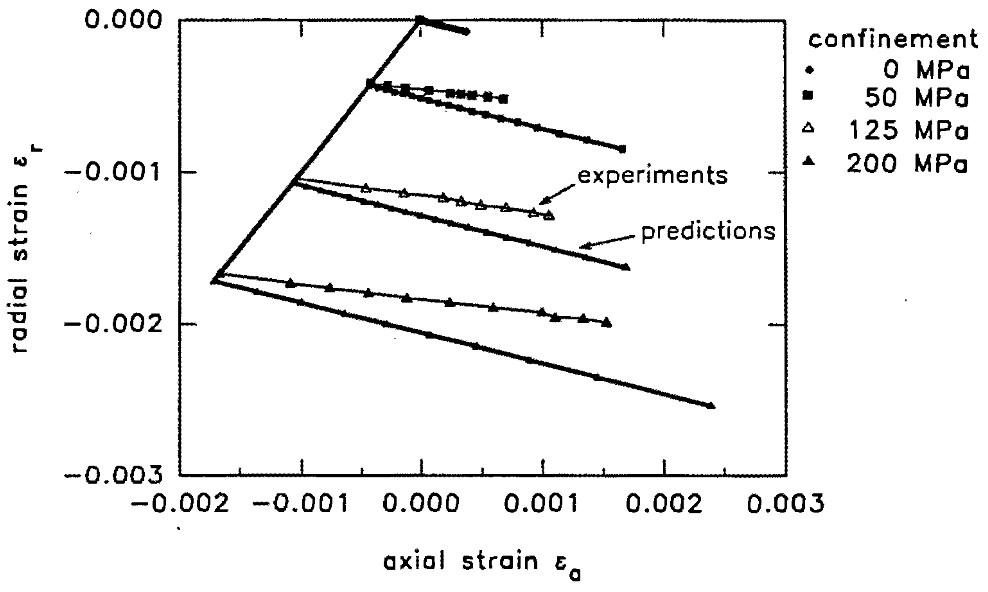

Figure 38: Comparison of the experimental and predicted axial strain - radial strain response in reduced triaxial extension

The envelope of failure points defined by the simulated results is in good agreement with the experimental data, denoted by open circles. The envelope enclosing the RTE results is also within the range of the experimental results, denoted by open square markers. The model predictions tend to overestimate the ultimate strength of the Witwatersrand Quartzite in reduced triaxial extension.

The failure predictions following three other stress paths are shown in Figure 39, each having a different ratio of the principal stresses. For each path, an initial hydrostatic compression of 50 MPa is applied. The first path, is an extension test with a ratio of the principal stress increments $k = \frac{d\sigma_3}{d\sigma_1} = -0.4$. The predicted ultimate strength is slightly outside the envelope defined by the CTC and RTE tests. In the second path, a compression test in which the principal increment ratio is $k = \frac{d\sigma_3}{d\sigma_1} = 0.4$. The stress path intersects the damage initiation surface in the effective stress space. However, there are no positive principal values in the 'crack' strain subdomain and thus, no damage develops. The material response remains linear elastic, corresponding to experimental observations (Bieniawski, 1967; Schock et al., 1973) as discussed in Section 2.2.1. The third path combines the previous two paths up to an initial compression of $\sigma_3 = 450$ MPa with $k = 0.4$, then follows an extension loading path of $k = -0.4$. Damage initiates during the extension loading, once there is a positive principal strain in the 'crack' strain subdomain. Failure occurs at a slightly lower stress state than the triaxial compression envelope indicates. The finite element implementation of the damage model therefore has the ability to represent the behaviour of the rock even if non-standard loading paths are followed.

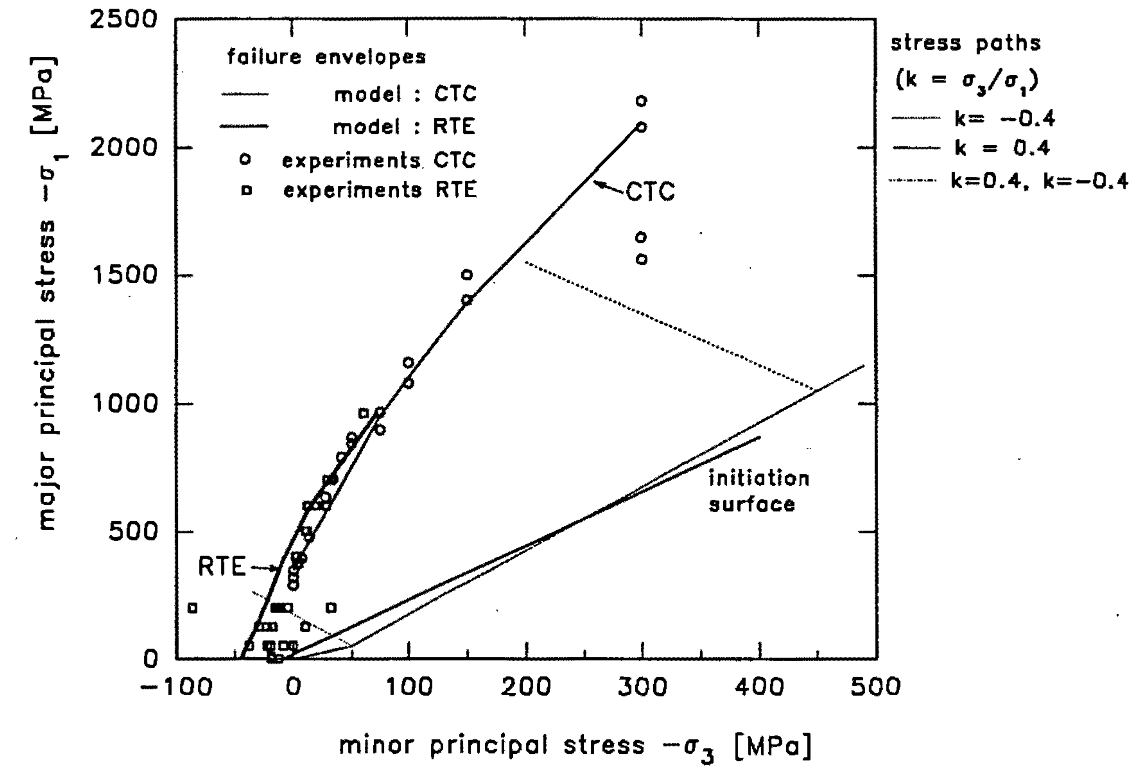

Figure 39: Predicted and experimental failure envelopes for conventional triaxial compression and reduced triaxial extension and selected load path predictions

5.6 Predictions of stress - strain response for specific load paths

5.6.1 Un/reloading in triaxial compression and extension

The predicted stress - strain behaviour for loading, un- and reloading in triaxial compression are shown in Figure 40. The material is loaded to 75 MPa in hydrostatic compression. The subsequent deviatoric loading to 800 MPa was followed by unloading to 200 MPa and reloading to failure. During the unloading/reloading cycle, little nonlinearity is evident in the axial stress-axial strain response. The greater nonlinearity of the axial stress - radial strain response is evidence of the damage induced anisotropy in the radial direction.

The axial stress - radial strain curve is magnified in Figure 40b to demonstrate the predicted unloading and reloading behaviour. The material response is initially undamaged, indicated by the linear stress - strain response. Damage occurs with further loading and the stress - strain curve becomes nonlinear. Unloading initially occurs with the linear, undamaged material response. Further unloading occurs with the lower, damaged stiffness. On reloading, the initial response is again undamaged. At higher deviatoric stress levels, the reloading occurs with the damaged stiffness, and the stress - strain reponse exhibits hystereses. Once the previous maximum stress (800 MPa) is attained, the anisotropic damage process commences again.

The damage formulation is thus, capable of predicting a material response which includes hysteresis of the un/re loading stress - strain response and has a 'memory' of previous maximum

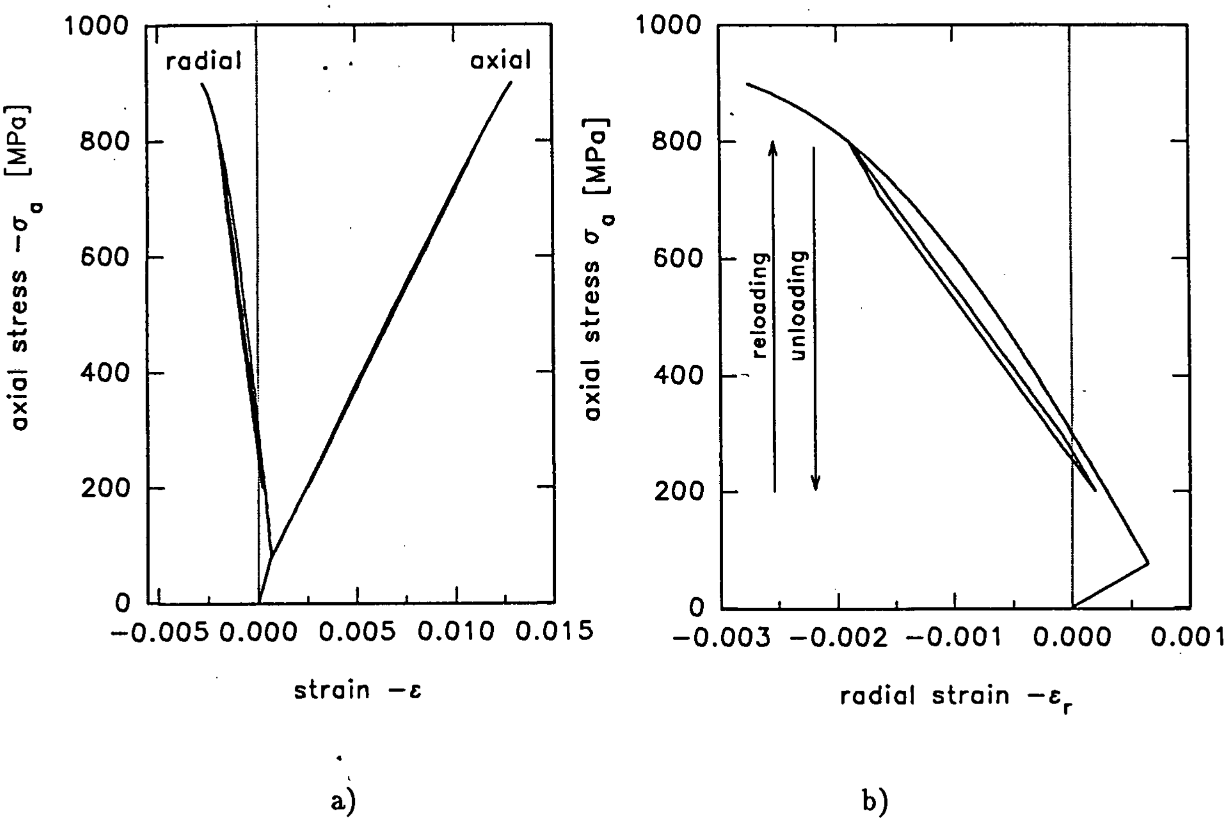

Figure 40: Model simulation of un/reloading behaviour in conventional triaxial compression

loads. The predicted behaviour is in qualitative agreement with the experimental data of Scholz and Kovacs (1974), Holcomb (1981), Zoback and Byerlee (1975) as discussed in Section 2.5. There are no experimental results available for un/reloading of Witwatersrand Quartzite for quantitative comparison.

The model simulation of the stress - strain behaviour in reduced triaxial extension is shown in Figure 41. The predicted axial strains and radial strains become compressive during the hydrostatic loading to 600 MPa confining pressure. As the axial load is reduced and the stress - strain response is initially linear. Damage initiation occurs just prior to the axial strain becoming positive and is evident as nonlinearity in the axial stress - axial strain curve. This is consistent with the damage direction being perpendicular to the axial loading in reduced triaxial extension. The axial stress is reduced to 25 MPa and then re-applied reducing the deviatoric stress, until a hydrostatic stress state is achieved again. As the axial stress is applied, the cracks close first, and thus the 'unloading' occurs at the damaged stiffness. Once the effective stress state re-enters the initial elastic domain, the material becomes completely elastic. The axial stress - axial strain response determined from an experiment on Witwatersrand Quartzite is shown in Figure 41. The predicted response compares well with the test data for most of the load path. The damage model overpredicts the strength of the Quartzite and therefore the nonlinearity of the stress -

strain reponse is less at the maximum stress level.

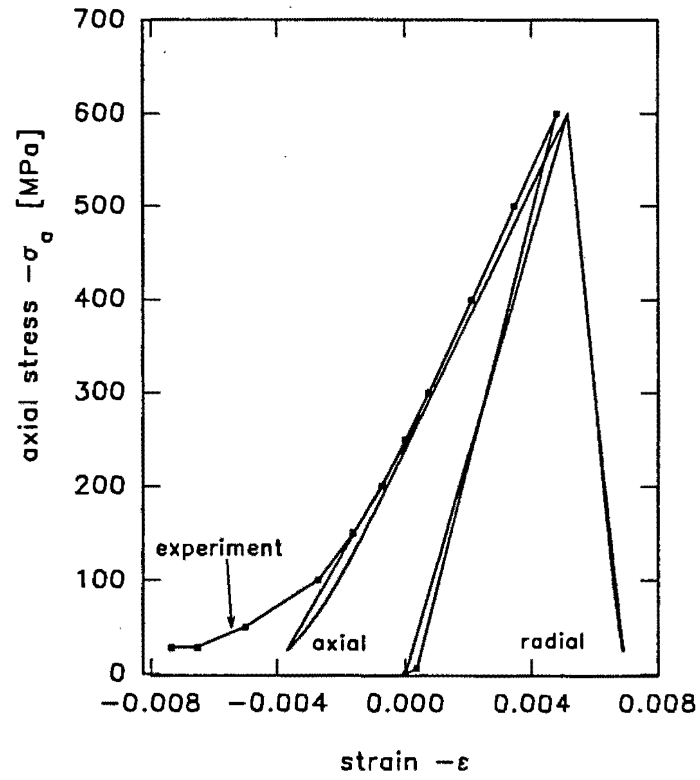

Figure 41: Experimental (after Briggs, 1991) and predicted stress - strain behaviour in reduced triaxial extension

Path dependence of the damage model can be investigated by comparing the analysis of a two-way loading, from compression to tension, with the results from a load path in tension only. The stress - strain response from a two-way loading consisting of unconfined compression to 300 MPa, followed by unconfined tension as shown in Figure 42. The compression part of the cycle exhibits similar loading and unloading behaviour as described for the triaxial compression path.

The stress - strain response under tensile loading is the same for both analyses up to the point of damage initiation. After damage initiation, however, the damage which evolves in the two-way loading analysis is in addition to the anisotropic damage previously induced by the compressive loading. Thus, the stiffness is damaged to a higher degree than in the case of the pure tensile loading, resulting in larger strains and a lower ultimate tensile strength.

5.6.2 Uniaxial loading in plane strain

Many geotechnical applications in engineering practice are modelled in plane strain and therefore the stress - strain curves for an unconfined compression (axisymmetric) test and the equivalent plane strain test with uniaxial loading are investigated. The results are shown in Figure 43.

There is no experimental data of plane strain loading of Witwatersrand Quartzite. For compar-

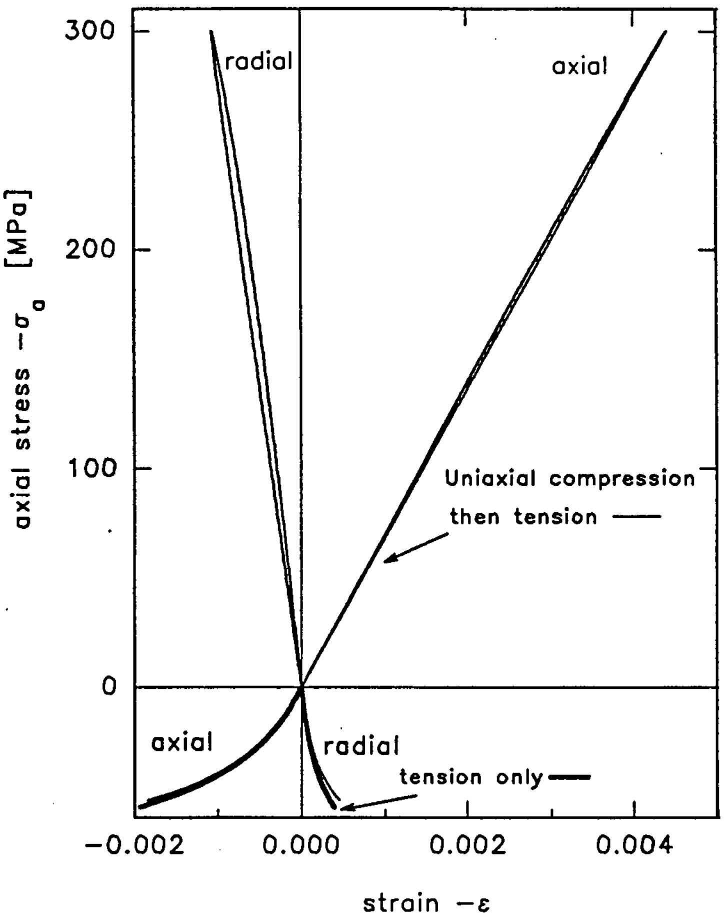

Figure 42: Stress - strain response on two-way loading, unconfined compression and unconfined tension, and on one-way tension loading

ative studies, consideration of the behaviour of other rock types is required. The higher strength and larger strains predicted for the plane strain condition in comparison to the axisymmetric case are in qualitative agreement with test data for Karoo Sandstone (Stavropoulou, 1982). In particular, the ratio of plane strain strength to uniaxial strength determined for the Sandstone is 1.51. The ratio evaluated from the predicted responses for the Quartzite is 1.43. Thus, the damage model predicts that the intermediate principal stress increases the ultimate strength which corresponds to the experimental observations of the failure of a variety of rock types by Mogi (1972). This suggests that the anisotropic damage model, with material parameters fitted from axisymmetric, conventional triaxial compression and reduced triaxial extension data, is successful in predicting the experimentally observed difference in the ultimate strength. It can be assumed therefore that reasonable results can be obtained in plane strain analyses.

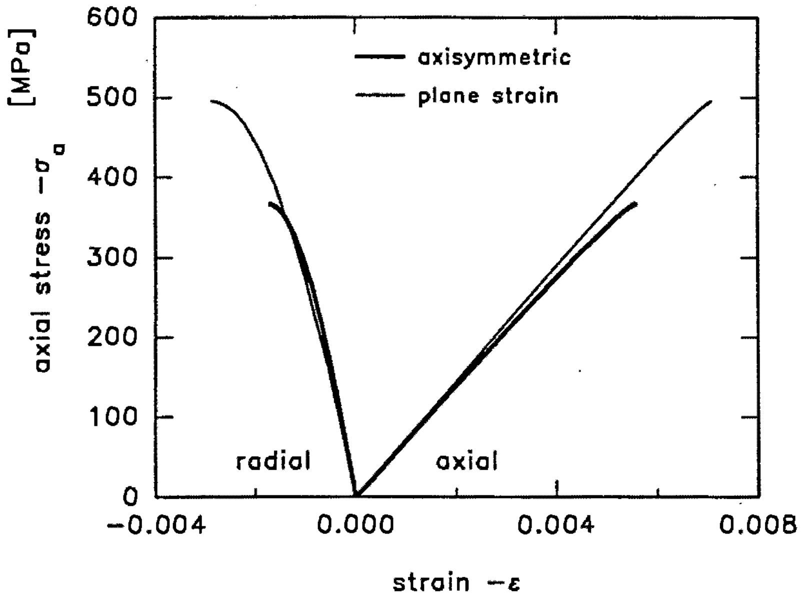

Figure 43: Prediction of stress - strain response in axisymmetric, unconfined compression and plane strain

5.7 Conclusions

A calibration procedure has been developed for the anisotropic damage model, which relies only on conventional triaxial compression and reduced triaxial extension test data. The dependence of the evolution law parameters on the confinement are determined from test results at different confining pressures by a regression analysis.

The damage model has been implemented into a single point numerical solution procedure, and the ABAQUS finite element program. Finite element analyses of a triaxial test specimen were performed with 1, 50, 200, and 800 element meshes, with a variety of element types. The choice of the type of finite element does not alter the stress -strain response. The model is path dependent and thus, smaller load increments result in increased dilatancy.

The investigation of the influence of the evolution parameters on the material behaviour in triaxial compression and extension showed that an increase in the 'size' parameter θ_m causes greater dilatancy and higher ultimate strength. The 'shape' parameter β_m alters the rate of the damage accumulation. At low values of β_m, the damage shows a continually increasing rate of growth. Higher values simulate sudden, rapid damage. Increasing β_m increases the ultimate strength and decreases the dilatancy.

The damage model was calibrated for Witwatersrand Quartzite. The rock exhibits a variable response in terms of the magnitude of dilatancy and ultimate strength. Backprediction of the triaxial compression and tension tests demonstrated that the anisotropic damage model predictions are in good agreement with the Quartzite stress-strain response, within the spread of the test data. The rock samples tested in the reduced triaxial extension and conventional triaxial compression tests showed different initial Poisson's ratios. It is therefore recommended that the calibration of the material parameters be undertaken in accordance with the intended application of the model.

The failure envelope predicted by the model corresponds closely to the envelope defined by 45 triaxial tests. The envelope predicted for extension tests lie somewhat outside of the triaxial compression envelope. Predictions following other stress paths shows that the failure points are all in good agreement with the triaxial compression test data.

The stress - strain response for tests consisting of sequences of loading, unloading and reloading correspond well to experimental evidence. Exact comparisons are prevented by the lack of adequate tests on Quartzite. The investigation into the simulation of unconfined (axisymmetric) and plane strain conditions showed that the model is able to predict the difference in the material behaviour which exists for plane strain and axisymmetric loading.

Chapter 6 Modelling of Damage due to an Excavation in a Quartzite Block

6.1 Introduction

The objective of the development of the anisotropic damage model is to create a numerical tool which will contribute to the study of the deformation and fracturing of the rockmass around a deep level gold mining stope. In the first stage of evaluation of the finite element implementation of the anisotropic damage model, simple test problems subjected to straightforward stress paths were analysed (in Chapter 5). It is now necessary to validate the constitutive model in test situations which incorporate features such as non-uniform stress states, and loading with both, compression and extension modes of damage before the model can be applied to full scale engineering problems.

Many geotechnical and mining engineering problems involve sequential excavations in rock. Therefore, the stability of the numerical scheme must be investigated in analyses which include the removal of elements under stress. The rock surrounding the excavation experiences redistribution of stress i.e. loading and unloading, and the simulation of these processes is considered to be a stringent test of the capabilities of the damage model. Verification of the anisotropic damage model should address whether

- there is any significant deformation due to damage induced anisotropy,
- the predicted microfracturing initiates at the expected location and at the appropriate loading state (excavation stage),
- the predicted directions of fracture growth are as observed.

A suitable problem is provided by a series of experiments which simulate the excavation sequence of deep level mining in small blocks of Sandstone and Quartzite, undertaken at the University of the Witwatersrand by Gay (1976). The objective was to study the fracturing around excavations at a laboratory scale and thus obtain insight into the formation of the fracture patterns in the highly stressed environment around tabular excavations in deep mines. These tests are similar in terms of the excavation sequence to the mining problem, yet are on a much smaller scale with respect to geometry and magnitude. Sufficient strain measurements have been undertaken on the specimens so that verification of the damage model predictions can be undertaken.

Blocks of Quartzite and Sandstone, 100mm in width and height, and 75mm in thickness were tested. Two situations were considered in the experiments. Static tests were undertaken by making an initial hole in the blocks in an unstressed state. The blocks were subsequently loaded to failure by the application of horizontal and vertical stresses. Various stress ratios were applied in the tests to examine the effect of the confinement. The second test series simulated a longwall mining sequence by applying a selected horizontal and vertical stress state to the block, containing a central hole, which was sequentially enlarged towards the edges of the block.

Quantitative comparison of the finite element results with the experiments is made possible, because strain gauges were located at two points on the surface of the block, near the excavation, for the purposes of determining the magnitude and direction of the principal strains. Detailed maps of the mining induced fracturing can be used to evaluate the predictions of the extent and direction of the damage. In previous theoretical analyses of the problem, the material was considered to be linear elastic. The strains induced in the rock by the excavation were analysed by Gay (1976). The fracture patterns resulting from the static loading were studied with a displacement discontinuity approach by Napier and Hilyard (1992). The anisotropic damage model allows the prediction of both, the strain distribution and fracture pattern during the sequential excavation sequence which is analysed in this chapter.

6.2 Material parameters and finite element discretization

The material parameters for the Witwatersrand Quartzite, determined as described in Section 5.4, are used in these analyses. The magnitudes of the parameters are listed in Table 2.

	Parameter	Symbol	Value
Elastic constants	Young's modulus	E	70 GPa
	Poisson's ratio	ν	0.2
Damage initiation	coefficient of friction	μ_o	0.35
	effective shear resistance	$\bar{\tau}_o$	6.0 MPa
Damage evolution	Mode I shape parameters	β_{0I} and β_{1I}	0.2682, 0.00216
	Mode I size parameters	θ_{0I} and θ_{1I}	0.1 MPa, 0.004 MPa
	Mode II shape parameters	β_{0II} and β_{1II}	0.85 , 0.0
	Mode II size parameters	θ_{0II} and θ_{1II}	0.65 MPa , 0.032 MPa

Table 2: Damage model parameters for Witwatersrand Quartzite

Two different types of Quartzite were used in the block experiments (Gay, 1976), each having somewhat different properties to the Quartzite which was used in the calibration studies (Briggs and Vieler, 1982). The material properties of the rocks used in the experiments are listed in Table 3. Comparing the three sets of elastic properties, it is obvious shows that the elastic constants evaluated for the damage model correspond to the ones determined for the footwall (F.W.) Quartzite. The ultimate strength (see Figure 39), however, corresponds to the strength of the hangingwall (H.W.) Quartzite. In addition, the type of Quartzite of each block specimen used in the experiments cannot be established.

The faces of the blocks which contain the excavation are 100mm square, and the blocks are 75mm thick. Thus, the size of the blocks is in the same order of magnitude as the triaxial test

Rock Type	Young's Modulus	Poisson's Ratio	Unconfined compression strength
F.W. Quartzite	70 GPa	0.2	200 MPa
H.W. Quartzite	86 GPa	0.1	350 MPa

Table 3: Material properties of Quartzite blocks

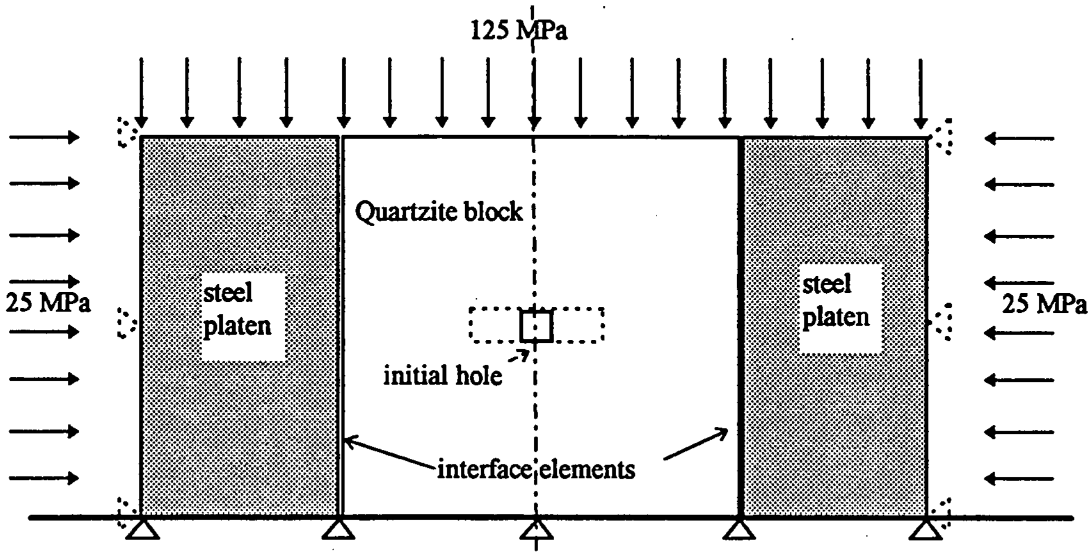

Figure 44: Schematic of the block experiment with loading and boundary conditions for the finite element model

specimens used to determine the model parameters. Therefore, there is no need to investigate any scale effects of the rock (Pinto da Cunha, 1990).

Two investigations were undertaken involving different meshes and loading conditions. Firstly, a coarse, square mesh with simple boundary conditions was used to test the stability of the numerical scheme during element removal. As discussed in the following section, it was found that the boundary conditions need to be accurately modelled and the excavated area for each removal step needs to be discretized by at least four elements. A second investigation was therefore performed with a refined mesh to produce a better simulation of the exact loading conditions and achieve a higher resolution in terms of the stresses, strains and the damage. The block is approximated as a plane strain analysis which implies that the development of damage is independent of the out-of-plane direction.

In the final finite element mesh, only one half of the block is modelled considering the symmetry of the system about the centreline. A schematic diagram of the experimental set-up is shown in Figure 44. The rock is modelled with 840 four-noded plane strain elements in a regular grid, 21 elements wide by 40 elements high. Only reduced integration was considered. The 2.5mm square elements provide an improved approximation of the edges of the excavation. Elements along the centreline are 1.25mm long and 2.5 mm high.

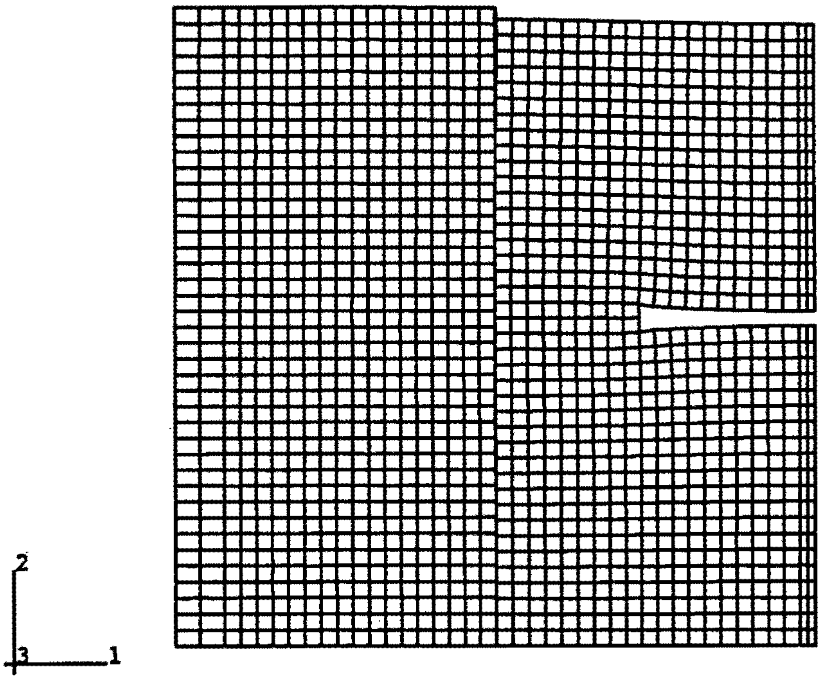

Figure 45: Displaced shape of the finite element mesh of the block and the loading platen

In the experiments, a horizontal pressure of 25 MPa was applied by stiff steel loading platens which were locked in place once the desired horizontal loading was achieved. The steel platen is modelled by 760, four-noded, plane strain elements; 19 elements wide by 40 high. A vertical line of 40 interface elements divides the load platen from the rock. The symmetry axis is constrained to allow vertical movement only, and the lower edges of the platen and rock are prevented from vertical movements. The vertical loading of 125 MPa was applied to the block with a compression testing machine and was modelled by a distributed load. The free edge of the steel platen was fixed in the horizontal direction once the distributed load had been applied. This simulates the locking of the loading device in the horizontal direction in the experiments.

In the finite element analysis, each excavation step consists of the removal of a 5mm square region comprising four elements, starting at the centre and progressing towards the edges of the block. The geometry of the mesh is shown in Figure 45 in a displaced configuration after removal of a of sequence six 'mining' steps.

6.3 Comparison of experimental and finite element results

6.3.1 Principal strains

The principal strain magnitudes and directions measured in one of the tests (C18) provide quantitative evidence of the behaviour of Quartzite in the mined block experiment. The strain measurements were taken at two points on the block surface. One gauge was positioned at a

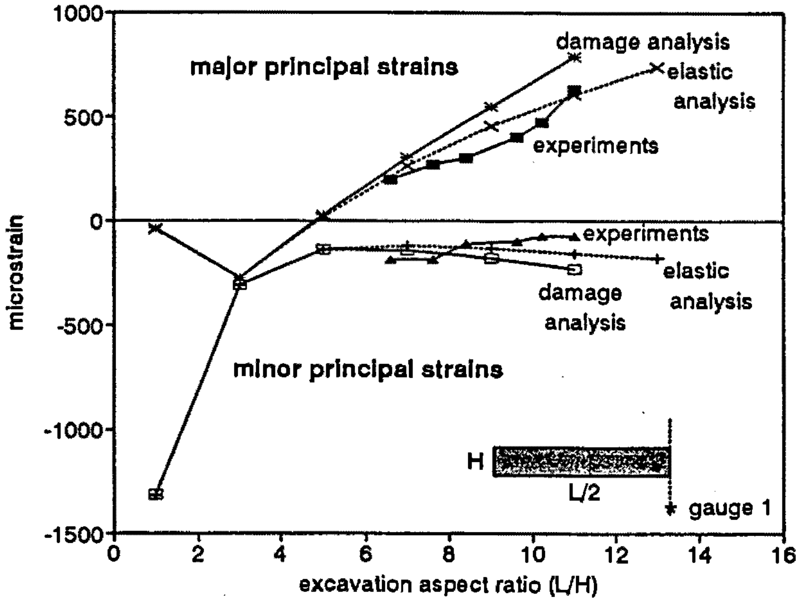

Figure 46: Predictions and experimental data (Gay, 1976) of principal strains with aspect ratio of excavation at gauge position 1

point 10mm below the centre of the initial hole along the symmetry axis (gauge position 1), and the other was located 10 mm ahead of and 5mm above the initial hole (gauge position 2). Strains computed at the integration point closest to these measuring points were considered in comparative studies.

The variation in the principal strains at gauge position 1, 10mm below the centre of the excavated region, is shown in Figure 46. The trend of the predicted major principal strains is similar to the experimental results. An initial compression occurs as a result of the applied loading. As the excavation progresses, the strains become positive and gradually reduce. In the experiments, a rapid increase in strain is observed as the maximimum excavated span length of 55mm (aspect ratio L/H = 11) is approached. The finite element simulation does not show the same increase in strains. A smaller excavation step size is required in the finite element analysis for a better representation of the deformations when the block specimen is close to failure. The measured and predicted minor principal strains are similar in magnitude although the trends are opposite with increasing aspect ratio.

A question that must be addressed is whether the inclusion of anisotropic damage in the formulation has any significant effect on the deformation. Therefore, a linear elastic analysis was undertaken for comparison. The general trend of the results of both analyses are similar, which is expected, since in the damage analysis the material is initially elastic and the influence of the damage affects only a small region of the mesh. The major and minor principal strains are initially identical for both elastic and damage analyses, however begin to diverge when the span reaches 25mm (excavation aspect ratio of 5). The anisotropic damage model results in higher values of the major principal strains relative to the elastic analysis. The difference between the strains predicted in the two analyses increases as the removal of elements progresses, indicating

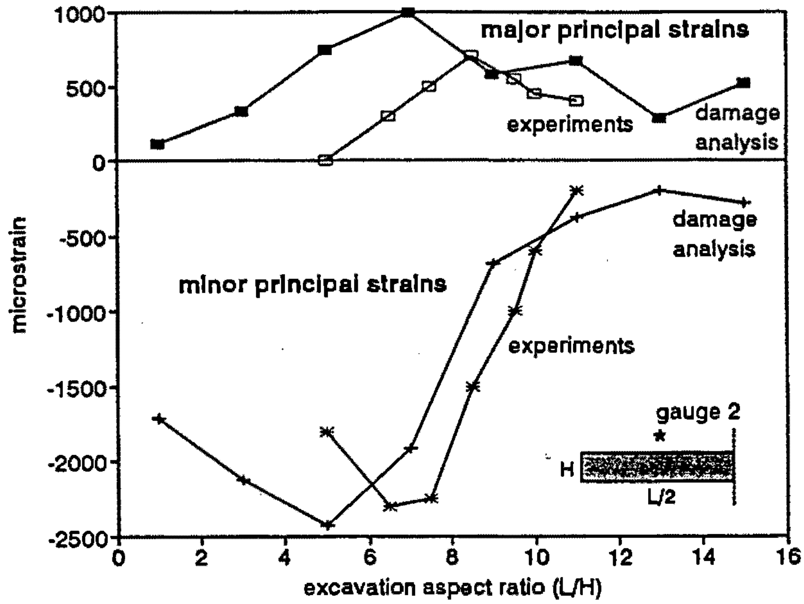

Figure 47: Predictions and experimental data (Gay, 1976) of change of principal strains with excavation aspect ratio at gauge position 2

the evolution of the damage. The development of damage at the location of strain gauge 1 corresponds to the experimental observation of a vertical fracture which grows outwards from the initial hole along the central axis of the excavation, as shown in Figure 51. The damage analysis predicts failure of the specimen at an excavated span of 55mm which agrees exactly with the observations. Failure cannot be detected in the elastic analysis.

The prediction of the results for the second strain gauge position, ahead of and above the initial excavation, are shown in Figure 47. The trend shows an increase in the magnitude of both, the major and minor principal strains as the "stope face" approaches the position of measurement. The strains reduce once the excavation has passed the gauge. The measured strains demonstrate a very similar trend, but the predictions of the maximum of the strains occurs slightly before the strains measured in the experiments. This is due to the offset of the integration point at which the analysis results are derived which is 1.25mm before and below the actual strain gauge location. The effect of the damage associated with the passing of the stope face is measured at a slightly earlier stage in the mining sequence.

Another comparison that is relevant is the consideration of the angle of the principal strain to the long axis of the excavation which was measured in the experiments. The predicted and measured values of this angle at the strain gauge location below the centreline of the excavation (measured manually from plots of the principal strain vectors) are shown in Figure 48. The model predicts a rapid increase in the angle which occurs during the initial phases of the excavation process. At a span of 35mm (aspect ratio L/H = 7), the angle reaches a maximum and then decreases with further excavation. This final decrease occurs over a similar range of excavation aspect ratios and thus, corresponds fairly well to the trends exhibited by the measured data.

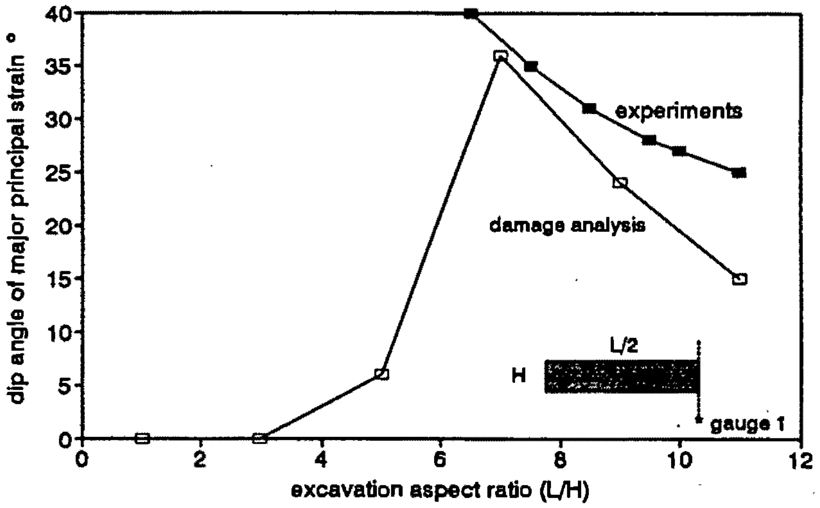

Figure 48: Predictions and experimental data (Gay, 1976) of change of dip angle of major principal strain with aspect ratio

6.3.2 Total damage magnitude and direction

The most interesting findings of the application of the anisotropic damage model to this excavation problem concern the development of the damage in the block. However, the tensor nature of the damage internal variable complicates the presentation of the results. The damage is presented in two plots, one showing the magnitude and the other showing the direction. The magnitude of damage is given in the contour plots of the total accumulated scalar damage magnitude $d = \int_0^t d_I dt + \int_0^t d_{II} dt$. The current damage direction is shown by a plot of the vectors of the positive part of the 'crack' strain tensor (ϵ_c^{e+}). The vectors are scaled according to the magnitude of ϵ_c^{e+} and depict the strain due to microcrack opening. Each vector indicates the direction normal to the growth of microcracking at the integration point; the lengths are some measure of the crack opening, however they do not represent the relative amounts of damage. Therefore, it is imperative that the contour and vector plots are viewed together for a complete evaluation of the extent of damage in the block.

The contours of the total accumulated damage magnitude d for four of the excavation steps are shown in Figure 49. In each plot, the extent of the completely undamaged areas is defined by the minimum damage contour level (darkest blue region). The maximum contour level (red region) is set at $d = 0.1$ for each plot. This value of d is selected to demonstrate the evolution of damage as excavation progresses.

The mode and direction of damage can be determined from the corresponding vector plots in Figure 50. Each vector is scaled to the magnitude of the maximum positive 'crack' strain and centred at the relevant integration point. Thick line vectors denote mode I behaviour, and the thin line vectors represent mode II.

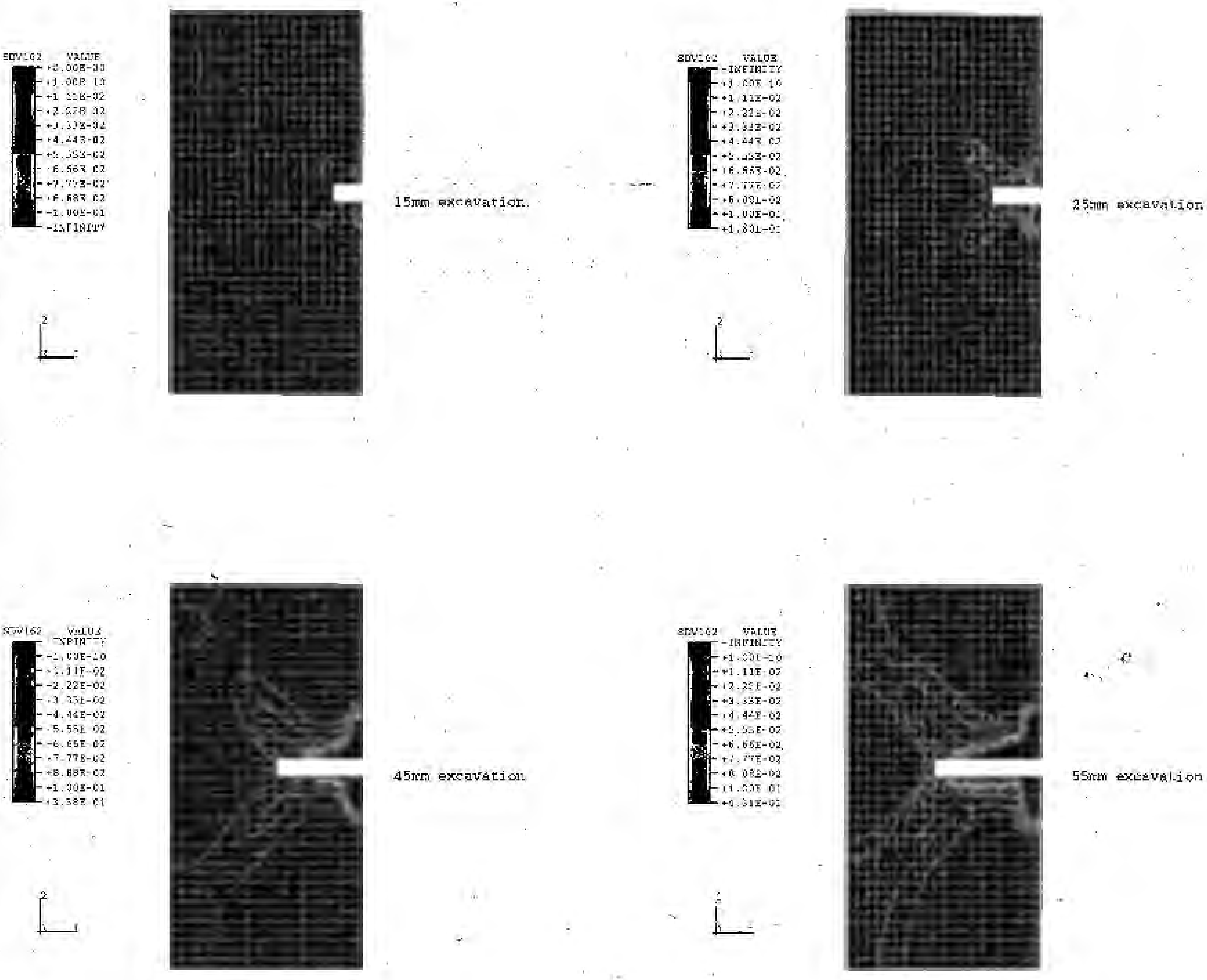

15mm excavation

25mm excavation

45mm excavation

55mm excavation

Figure 49: Contours of total damage d for excavated spans of 15mm, 25mm, 45mm, 55mm

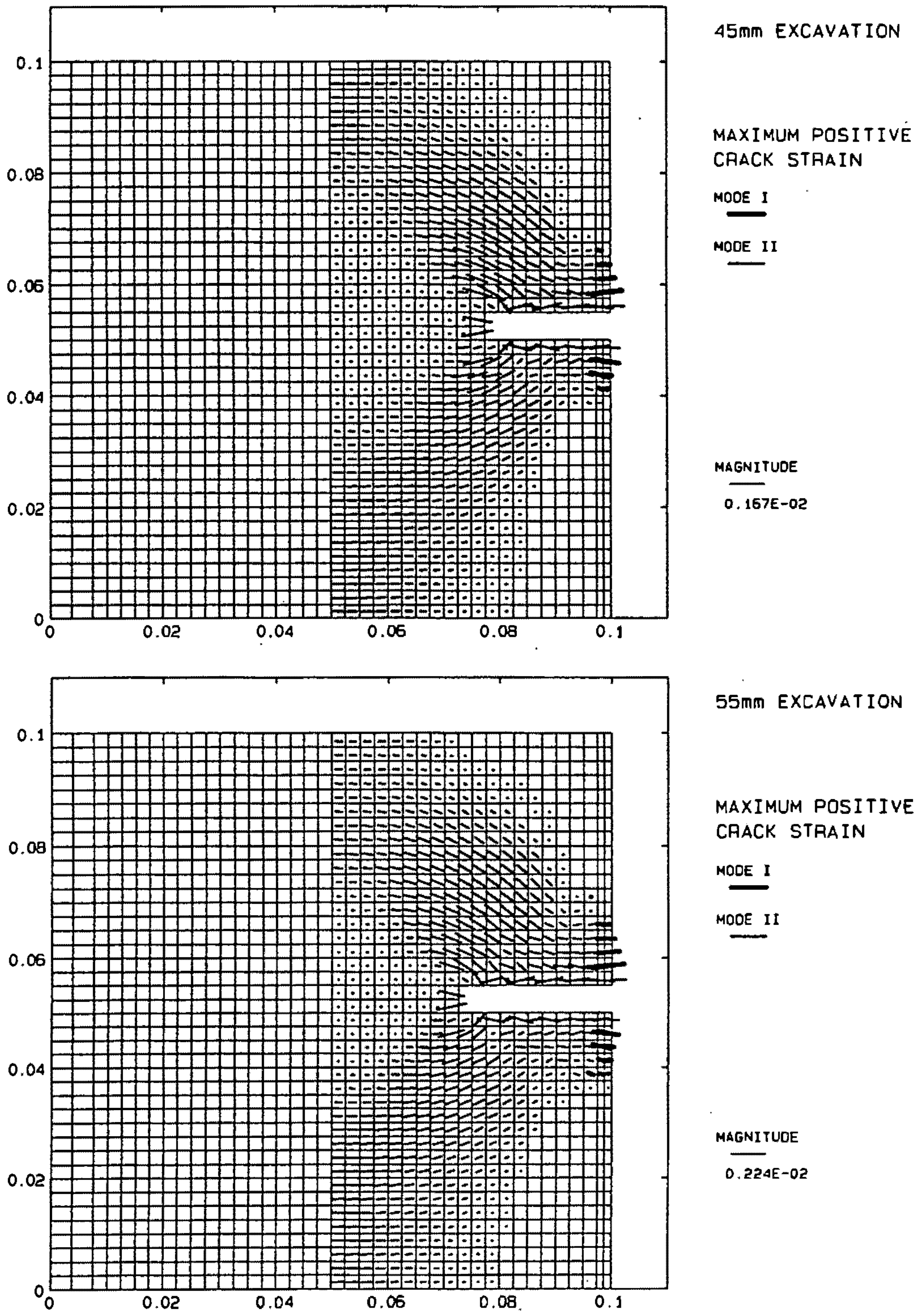

Figure 50: Vectors of positive 'crack' strain for excavated spans of a: 45mm and b: 55mm

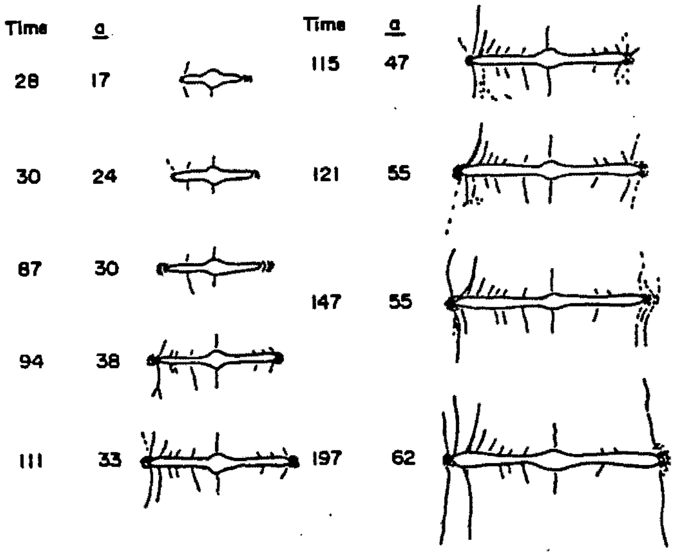

Figure 51: Typical sequence of fracturing in experiments (Gay, 1976)

The damage only becomes significant after an excavation of 25mm. Three main area of damage can be identified. The first being the regions of highest damage above and below the centreline of the excavation. The corresponding vector plot shows that these are extension damage regions. The 'crack' strain vectors are subparallel to the long axis of the excavation and reduce in magnitude with distance into the rock. This represents a central crack growing vertically out from the excavation into the rock hanging and footwalls.

The second region consists of "wings" of damage extending from the edges of the excavation towards the corners of the block. The damage normals shown in the vector plot suggest that the microcracks develop along a curved arch, starting near the excavation corner and extending into the rock above the mined-out region.

A third significant zone of damage develops at the stope face as the rock ahead of the excavation tends to bulge into the mined region. The damage normals show that the microcracking is subvertical, corresponding to slabbing behaviour of the rock generally observed at the face and sidewalls of underground excavations.

Each of these regions of damage expand as the excavation progresses. The vertical cracking at the centre extends slightly further outwards. The region of highest damage extends in two narrow bands along the hangingwall and footwall of the excavation. The microcracking tends to be subvertical and evolves in compression (mode II). The development of vertical cracking above the stope is evident in the sketches of the crack growth from the experiments as shown in Figure 51. It is also a commonly observed feature of large scale mining excavations (Brummer, 1987).

The damage in the second zone, arching above and below the stope, extends considerably as the mining progresses. The third damage zone ahead of the stope also intensifies and develops into

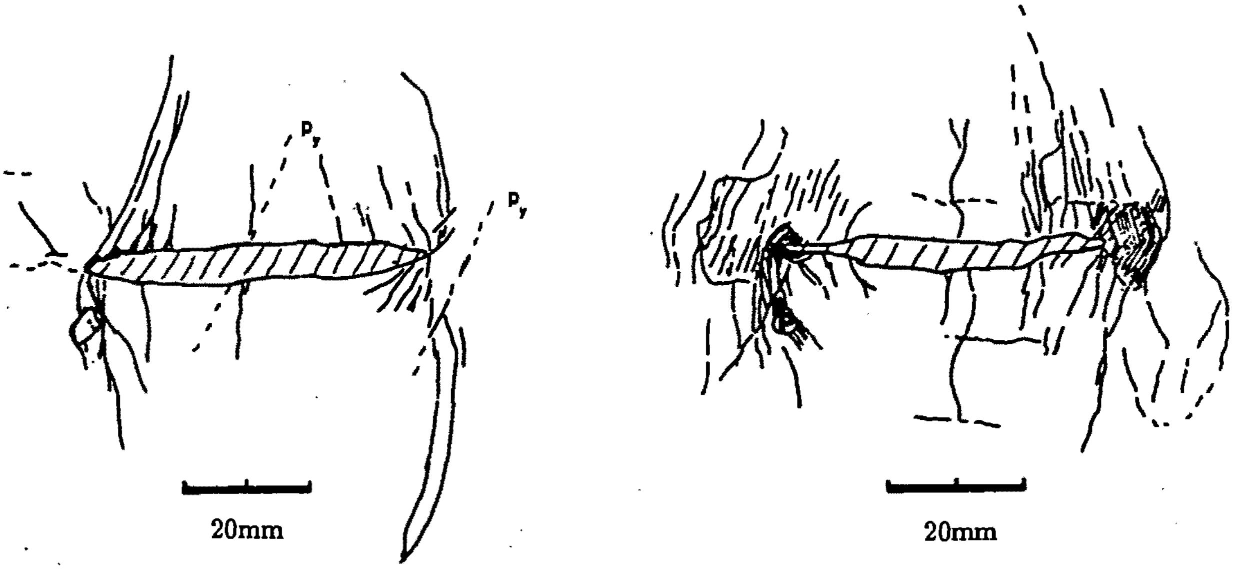

Figure 52: Fracture map of the front and back faces of a Quartzite block (Gay, 1976)

the rock. The position and direction of the microcracks at the 55mm span compare well with the fracture map obtained in the experiments, as shown in Figure 52. Collapse of the Quartzite specimens was observed to occur when shear type fractures initiated in the fracture zones and propagate diagonally across the block towards the boundaries. This pattern of behaviour is strongly suggested by the damage contours which extend toward the corners of the block as the span increases.

A small amount of damage occurs at the corners of the block due to interaction with the loading platen. The removal of elements is achieved up to a final span of 55mm. Failure of the numerical scheme occurs due to the development of very high damage ($d = 0.43$) along the centreline of the mesh, above and below the stope. Thus, a macro fracture will eventually develop along this line which cannot be predicted in this analysis. The damage material model becomes invalid as soon as the microcracks localize into macroscopic fractures.

6.4 Conclusions

The damage model has proved to be successful in modelling a complex situation involving biaxial loading of a plane strain block and the removal of elements to simulate an excavation sequence. The magnitudes and trends of the predicted strains at two points near the excavation agree with strain gauge measurements, providing quantitative and qualitative verification of the model. The predictions of the angle between the maximum principal strain direction and a horizontal plane correspond closely to the measured values. The comparison with the elastic analysis shows that significant strains develop due to the formation of anisotropic damage as the excavation sequence proceeds.

Damage is predicted in the elements around the excavation as the initial stress state changes.

The removal of elements results in a redistribution of stress around the opening, changing the distribution of damage in the remaining material. At all stages of the mining simulation, the damage corresponds closely to the fracture patterns observed in the experiments. A region of extension (mode I) damage extends outwards along centreline of the excavation corresponding to microcracks growing vertically along the centreline. The compression (mode II) damage predicts that microcracking will arch over the excavation. A region of microcracking parallel to the free face is predicted ahead of the excavation.

The analysis remains stable during the removal of the elements which is a stringent test of the finite element implementation of the damage model. The analysis only fails to converge at a span of 55mm due to the high degree of damage at the centreline of the block. A macroscopic crack should form at this location which cannot be predicted in the damage analysis. The maximum span is the same as observed in the tests on the Quartzite blocks, proving further confirmation that the model can predict the complete range of material response from an initial undamaged state up to failure.

Thus, the good agreement of the anisotropic damage predictions with the simulation of 'mining' in laboratory size specimens suggests that the model has the potential to capture the fracture patterns characteristic of full scale mining applications. However, the finite element implementation should be extended to include the material response due to the development localized fracturing when the damage causes the material to reach a state of failure.

Chapter 7 Simulation of Damage in Experiments on Indiana Limestone

7.1 Introduction

Although the damage model has the potential to describe the behaviour of any brittle rock, the analyses presented in the preceding chapters have only considered the hard, brittle Witwatersrand Quartzite. In this chapter, the investigation of the response of the damage formulation is undertaken with a completely different set of material parameters, namely those typical for a relatively soft rock, the Indiana Limestone. The rock consists of loosely cemented, calciferous grains of up to 1mm in diameter and has a high porosity of about 10% to 12%. The material properties are reported to vary over a wide range depending on the origin of the samples (Zheng, 1989). The high porosity of the material has a significant effect on the initial compressibility and some adaptions to the formulation of the model are required.

The finite element analysis of two demanding, non-uniform loading paths is performed to further establish the applicability and adequacy of the anisotropic damage model. Firstly, by simulating of diametral compression (or splitting tensile) tests on specimens of Indiana Limestone, the damage model is tested in a compression-tension stress field. Secondly, a non-standard indirect tensile test, the three point compression test, was analysed to investigate the damage model simulations in another, non-uniform state of stress. Experimental verification is obtained using results from an independently undertaken rock testing program in which the mechanisms of rock fracture were studied (Scheele et al., 1994). In these tests, the accumulated acoustic emission (AE) from the rock was measured in relation to the magnitude of the applied load. Acoustic-emission energy is released during fracturing processes resulting from deformation of the specimen. The amount of acoustic energy released is proportional to the internal structural changes (Lockner et al., 1991) and hence is a quantitative measure of the accumulation of damage. This allows comparison of the theoretical and experimental measures of damage and thus, the evaluation of the finite element analyses need not be limited to the consideration of the generally available stress and strain results.

7.2 Modification of damage model for porous rock

The constitutive relations for the damage model have been based on the assumption that a linear elastic material provides a reasonable approximation of the initial undamaged material response. However, in a porous material, the closure of pores during loading in compression results in a highly non-linear constitutive behaviour as the material compresses (Walsh, 1965). To account for the stiffening of the material during pore closure, a quasi-linear model (Desai and Siriwardane, 1984) was implemented for compressive stress states (i.e. mean pressure $\frac{1}{3}\sigma_{kk} < 0$).

The following modifications are proposed in this approach. The bulk and shear moduli of the material initially have low values appropriate to the highly porous material. Upon loading, the magnitude of the stiffness increases rapidly. Once damage initiation occurs, the components of the stiffness tensor are reduced due to the anisotropic stiffness loss resulting from directional microcrack formation. The tangent bulk modulus K_t increases continuously with increasing volumetric strain $\epsilon_v = \epsilon_{kk}$ and is defined (Janbu, 1963) as

$$K_t = \exp(a)(b-1)(-\epsilon_{kk})^b, \tag{191}$$

where a and b are material parameters. The tangent shear modulus G_t is calculated from the standard relation

$$G_t = K_t \frac{3(1-2\nu)}{2(1+\nu)}, \tag{192}$$

assuming a constant Poisson's ratio. Pore closure therefore results in an increase of both the bulk and shear moduli. For a loading path in compression, the two conflicting processes of stiffening due to pore closure, and softening due to microcrack opening are possible when the quasi-linear model is combined with the damage model.

The undamaged material response is expressed in terms of the residual strain subdomain $\boldsymbol{\epsilon}^e_R$ as expressed in Section 4.3. The constitutive equations for the residual stress, given in equation (73), are now expressed in incremental form as

$$d\sigma_{(ij)R} = \frac{K_t}{3} d\epsilon^e_{(kk)R} + 2G_t de^e_{(ij)R} \tag{193}$$

where $d\epsilon^e_{(kk)R}$ and $de^e_{(ij)R}$ are the increments of the residual volumetric and residual deviatoric strains, respectively. The residual stress σ_R is updated during undamaged loading and thus the complete constitutive relationship, equivalent to equation (85), is given by

$$\boldsymbol{\sigma} = \boldsymbol{\sigma}_o + \boldsymbol{\sigma}_R + \boldsymbol{C}_c : \boldsymbol{\epsilon}^e_c = \boldsymbol{\sigma}_o + \boldsymbol{\sigma}_R + \boldsymbol{\sigma}_c. \tag{194}$$

The scalar undamaged norm is now defined in terms of the elastic constitutive tensor at the point of damage $\boldsymbol{C}_{oR}(\epsilon_{(kk)R})$ thus,

$$\xi_c = \frac{1}{2}\boldsymbol{\epsilon}^e_c : \boldsymbol{C}_{oR}(\epsilon_{(kk)R}) : \boldsymbol{\epsilon}^e_c. \tag{195}$$

The tensile behaviour (for$\frac{1}{3}\sigma_{kk} > 0$) is considered to be modelled by the anisotropic damage model with linear elastic undamaged material. Thus, the material would exhibit a discontinuous stress - strain response during a change from compression to tension loading.

To reduce the computational effort, the tangent bulk modulus K_t is assumed to reach a limiting value $K_{t\max}$. The magnitude of $K_{t\max}$ is determined as the bulk modulus from the linear, central portion of the stress - strain relationship. Also, unloading and reloading in modes I and II is charcaterized by the damaged modulus of the material, whenever the effective stress

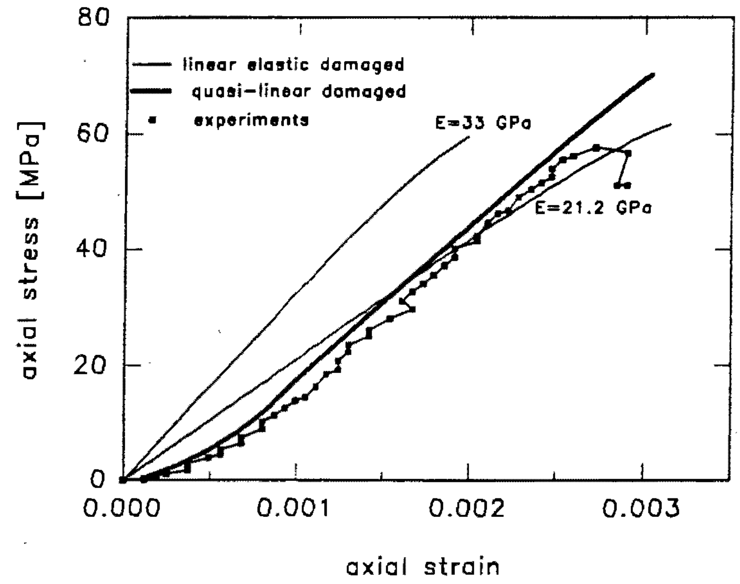

Figure 53: Unconfined compression test results on Indiana Limestone (Scheele et al., 1993) and backpredictions using various initial moduli

state exceeds the initial damage criterion and is less than the previous maximum of the loading criterion. This is equivalent to the un/reloading procedure in mode I as detailed in Section 4.7. The elastic domain does not translate and if the effective stress is less than the damage initiation surface, the material response reverts to the quasi-linear model.

7.3 Experimental procedure and model calibration

The experimental series which are used in this study consisted of both, diametral and unconfined compression tests. The tests were conducted in a stiff load frame which was connected to a closed-loop, servo-controlled testing machine (Scheele et. al., 1993). All tests were carried out in accordance with the Rock Testing Handbook (1990). The cores of Indiana Limestone, 5.08cm and 10.16cm in diameter, were cut to a length equal to half the diameter and all specimens were ovendried prior to testing. The diametral compression tests were undertaken at strain rates of $5.0\text{x}10^{-5}$, $1.0\text{x}10^{-5}$ and $1.0\text{x}10^{-6}$ per second and the strains measured in the direction of the load application. The acoustic emission was monitored by means of a piezoelectric transducer bonded to the centre of the flat surfaces of the disc.

The acoustic emission was converted into a voltage signal by the transducer. Any voltage peak exceeding a predetermined threshold voltage, sufficient to mask the background noise, is counted as an event. The total number of counts as well as load and deformation was recorded at one second intervals from the beginning of the test until failure and rupture of the specimen.

The calibration of the parameters of the anisotropic damage model is based on a variety of tests on Indiana Limestone from different sources, because a complete set of tests on exactly the same material, undertaken by the same experimenter, was not available. The data available consisted of unconfined compression tests (Zheng, 1989; Scheele, 1993), conventional triaxial compression tests (Friedel and Thill, 1990) and direct tension tests (Hawkes et al., 1973). Uniaxial compression tests carried out in the experimental program were the main component of the model calibration. A typical stress - strain relationship from these experiments, shown in Figure 53, demonstrates the S - shaped response characteristic of porous rock in compression (Brace, 1965). The diametral test results were not used in the calibration process.

The initial Young's modulus of the linear elastic undamaged material can be selected either as the intrinsic modulus E = 33 GPa or as an average modulus E = 21.2 GPa. The intrinsic modulus corresponds to the central, linear portion of the uniaxial stress - strain response. The material parameters in the tangent bulk modulus expression (as in equation (191)) were calibrated from the mean stress - volumetric strain values for the initial portion of the curve. The values of all the material constants are given in Table 4.

Elastic constants	Young's modulus	E	21.2GPa
	Poisson's ratio	ν	0.24
Damage initiation	coefficient of friction	μ_o	0.434
	effective shear resistance	$\bar{\tau}_0$	1.37 MPa
Damage evolution	Mode I shape parameters	β_{I0} and β_{I1}	0.863, 0.0
	Mode I size parameters	θ_{I0} and θ_{I1}	0.02 MPa, 0.0 MPa
	Mode II shape parameters	β_{II0} and β_{II1}	0.9 , 0.0
	Mode II size parameters	θ_{II0} and θ_{II1}	0.1 MPa, 0.0035 MPa
Porous material	Bulk modulus parameters	a and b	14.811 , 1.78
	Maximum bulk modulus	$K_{t\max}$	16.0 GPa

Table 4: Damage model parameters for Indiana Limestone

Comparison of the predicted and experimental stress - strain curves for unconfined compression are shown in Figure 53. Two simulations with the linear elastic - damage model are presented for E = 33 GPa, and E = 21.2 GPa. The axial stress - strain response for the analysis with the linear elastic material using the intrinsic Young' modulus results in an unacceptably low prediction of the ultimate strain. Close agreement with the predicted ultimate strength and strain are obtained when the average Young's modulus is applied. However, the strain observed in the initial stages of the test during pore closure is underpredicted. The average value of E = 21.2 GPa was selected for the analysis of the diametral compression and three point tests with the linear elastic - damage model.

The quasi-linear damage model predictions correspond closely to the observed results over the entire test. In general, the behaviour predicted by the model is slightly stiffer than the experimental response. The predicted ultimate strength is 72 MPa, which is greater than the ultimate strength determined in this unconfined compression test. However, this maximum value is in the same range as unconfined compression strengths reported for other tests. The failure strain for the model predictions corresponds well to the test result.

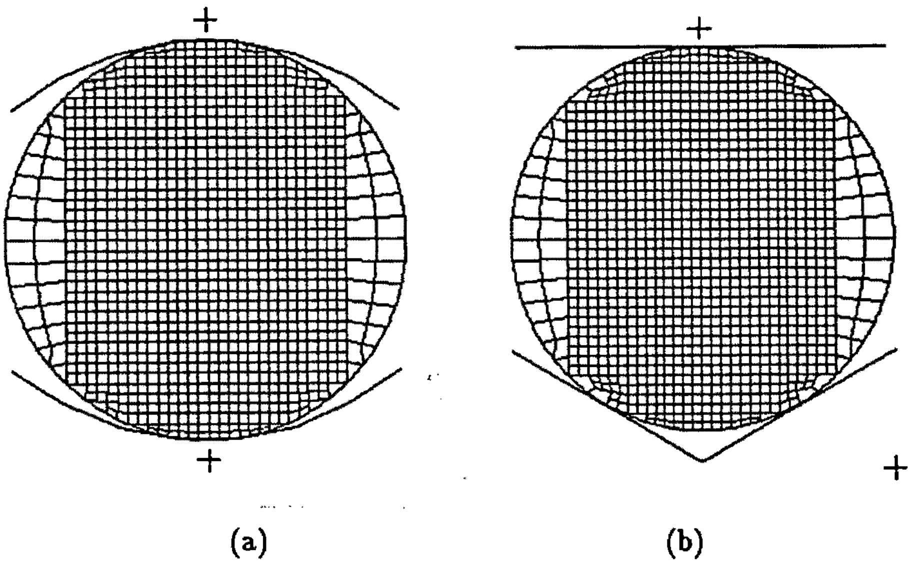

Figure 54: Schematic of test specimens with mesh discretization of a: diametral compression test and b: three point test

7.4 Modelling of experiments

The analysis of the diametral compression, and three point tests was performed using the ABAQUS finite element program (Hibbitt et al., 1993). The incremental solution technique employed was a modified Newton-Raphson scheme with an initial stiffness approach. Failure of the specimen was obtained when convergence of the solution could not be achieved. Post failure material response was allowed by applying the Riks solution algorithm.

In the analysis of the diametral compression test the cross-sectional area of the rock specimen was discretized in 1072 plane strain elements. The mesh configuration is shown in Figure 54a. The inner region of the model was discretized with a regular mesh of square, four-noded elements. Two different analyses were performed using reduced integration as well as incompatible mode elements. The outer boundary was modelled with six- and eight-noded, quadratic interpolation elements in order to preserve the circular shape. Reduced integration was applied in these elements. A block of elements, consisting of 6 rows of 10 elements situated adjacent to the contact points of the loading platens, was converted to eight-noded, quadrilateral, reduced integration elements to improve the modelling of the high stress gradients in the contact region. These blocks were constrained to the surrounding four-noded elements with multipoint constraints.

The loading platens were modelled by two curved rigid surfaces. To make provision for a wide contact zone, 12 contact elements were placed on the upper and lower regions of the specimen boundary, symmetric to the contact points. Load application was simulated by applying a controlled vertical displacement to the upper rigid surface, keeping the lower rigid surface fixed in the horizontal and vertical directions. The horizontal degrees of freedom of the nodes at the

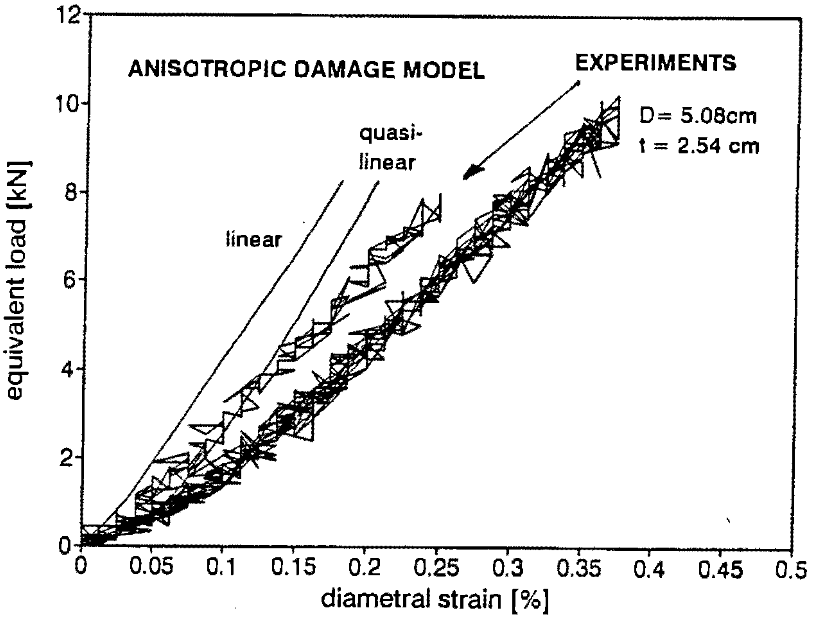

Figure 55: Load - diametral strain relationships of experiments and predictions

top and bottom of the loaded diameter were constrained in the horizontal direction.

In the three point compression test, the specimen was compressed vertically between a flat and a V-shaped loading platen as shown in Figure 54b. These platens were modelled as rigid surfaces; the lower V shaped platen consisting of two planes with an interior angle of 120°. The finite element mesh layout for the rock specimen was essentially the same as the configuration in the diametral compression test with 1072 elements. The only difference was the replacement of the six-noded elements in the contact regions of the V-shaped loading platen by eight-node quadrilateral elements with reduced integration. Due to the additional contact regions, the number of contact elements along the corresponding boundary was increased from 12 to 20.

7.5 Results and discussion

In the case of the diametral compression test, a convenient way of comparing the finite element results with those of the experiments is to examine the overall response in terms of the load applied versus diametral strain. The load-strain relationships of three diametral compression tests on specimens of Indiana Limestone of 5.08cm diameter are shown in Figure 55. On the same graph the finite element predictions are illustrated using the anisotropic damage material model. The initial undamaged behaviour was modelled as linear elastic and as a quasi-linear material. In both experiments and analyses, the same general pattern of gradually stiffening response until failure is demonstrated. The predictions of the ultimate loads are in good agreement with the observations.

The initial change of gradient observed in the load-diametral strain curves can be attributed to the change of the loading conditions due to widening of the contact zone between the platens and the specimen as the load increases. The linear elastic material is not suited for modelling

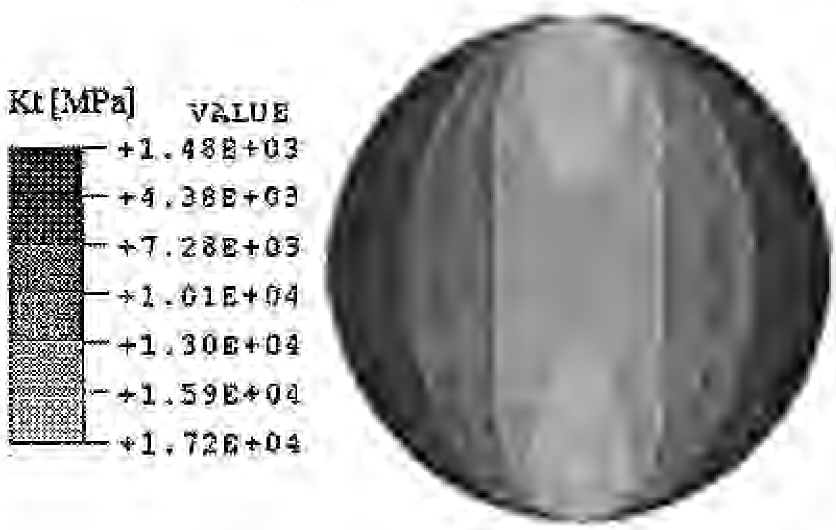

Figure 56: Predicted contours of tangent bulk modulus at failure in diametral compression with quasi-linear damage model

the Indiana Limestone in diametral compression, since pore closure causes a highly nonlinear increase in diametral strain during loading. The elastic modulus, calculated as an averaged term from the unconfined compression test data, is not representative of the overall material behaviour in the non-uniform stress state caused by the diametral compression. However, the effect of pore closure is well modelled with the quasi-linear material parameters. The load strain response is in very good agreement with the test results during the initial part of the test, and the material tends to get stiffer with increasing load. Thus, the quasi-linear damage model is able to model the complex interactions resulting from the simultaneous closure of pre-exisiting flaws and development of microcracking which occur under non-uniform stress states.

The contours of the tangent bulk modulus, K_t shown in Figure 56, depict the regions where the volume of voids has changed. The highest moduli, corresponding to stiffening and pore closure, are located in a bulb shaped area below the loading platens. The magnitude of the stiffness at failure reduces with increasing distance from the loaded diameter. The region of the highest tangent bulk modulus contains the damage initiation zone, which is shown in the contour plot of the total damage in Figure 57a. It is a compression (mode II) type of damage. The direction of the positive 'crack' strain vectors (not shown here) is aligned perpendicular to the loaded diameter and the cracking spreads from the two points of damage concentration towards the centre of the specimen.

The predictions appear to be in good agreement with results obtained by Falls et al. (1989) investigating the location of cracking events by means of the acoustic emission (AE) source localization technique. In Figure 57a, the distribution of acoustic events at 90% of the failure load and the final crack pattern are shown. The acoustic events, designated by circular markers, are clustered near to the edge of the specimen. This is in contrast to the conventional interpretation

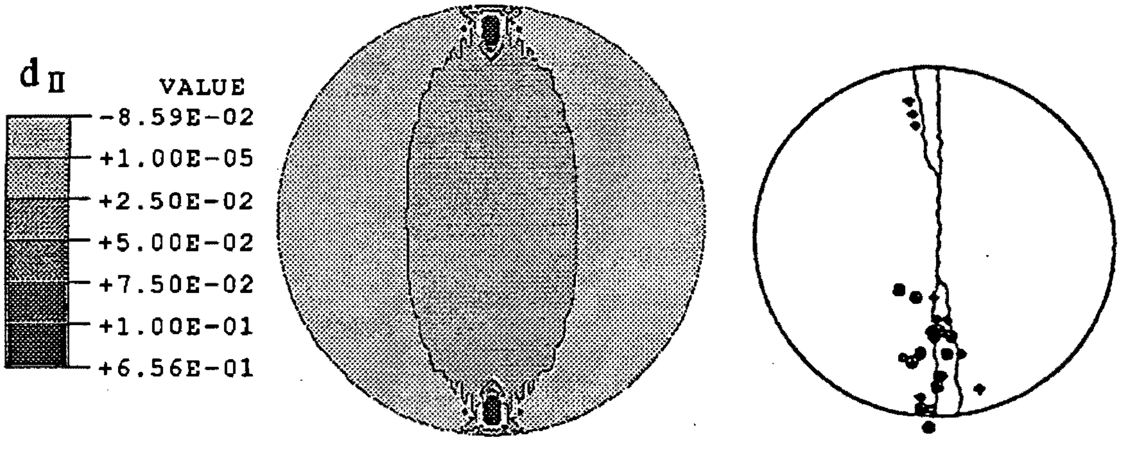

a) b)

Figure 57: Damage at failure a: contours of damage predicted with quasi-linear damage model and b: origins of acoustic events and crack pattern at failure (after Falls et al., 1989)

of the diametral compression test (Jaeger, 1967), which suggests that cracking starts in the centre of the disc.

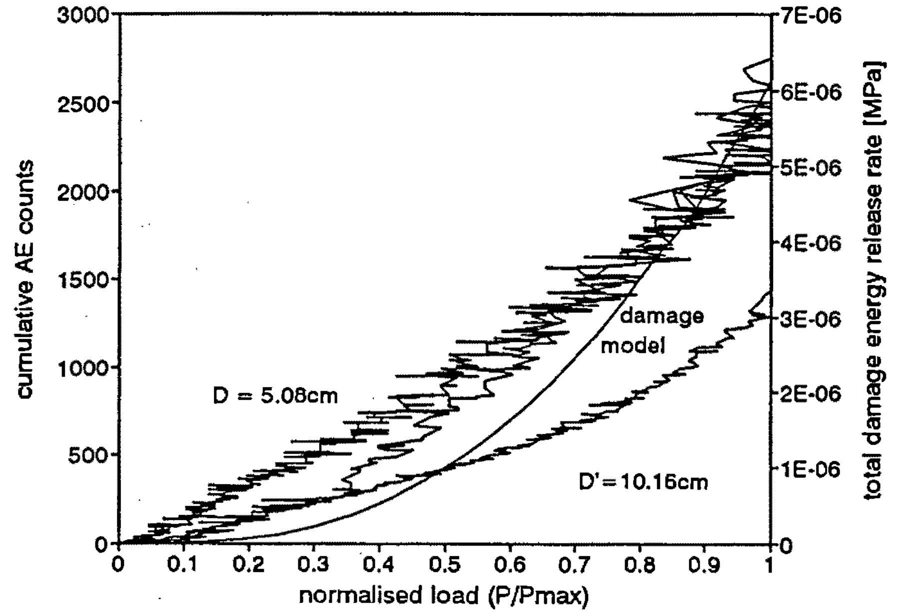

Figure 58: Increase of cumulative acoustic emission and total damage energy release rate with normalised load

In Figure 58, the AE responses of the same experiments (see Figure 55) are shown as a function of the normalised load applied. The cumulative AE counts increase consistently during the strain controlled tests which is not in agreement with Mogi's AE signatures established for unconfined

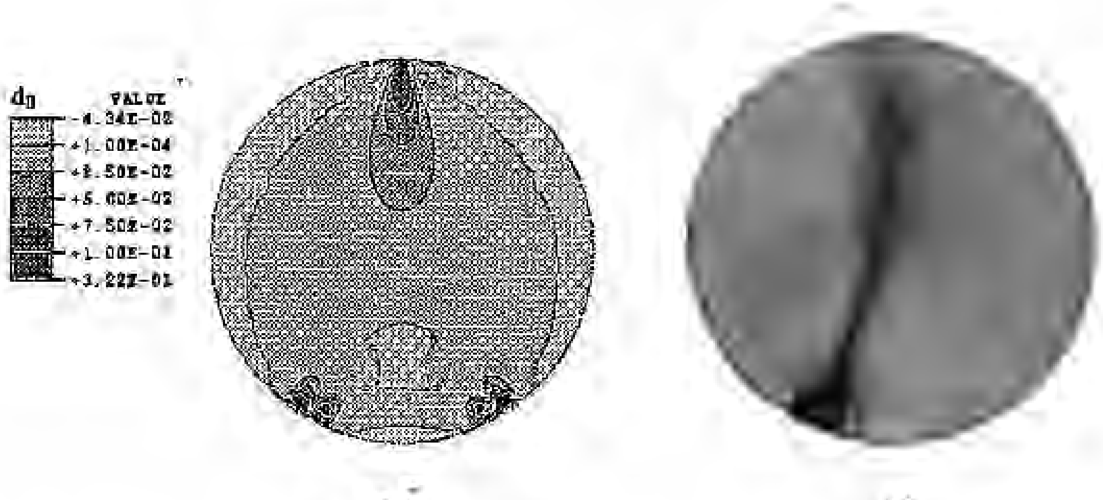

(a) (b)

Figure 59: Three-point loading tests a: damage contours within specimen prior to failure b: scanned photograph of a three-point test specimen at failure (Jaeger, 1967)

compression tests (Mogi, 1962). There is no interruption in AE energy being released during the tests indicating that there is continuous fracturing taking place. The increase in the total positive damage energy release rate for the whole finite element mesh with respect to the normalised applied load is also shown in Figure 58. The finite element analysis using the linear elastic damage model (shown in graph) and the quasi-linear damage model provide very similar trends. The increase in energy release measured in terms of AE in the experiments is in good agreement with the calculated energy release and demonstrates the equivalence between microcracking and damage.

The three-point test investigation concentrates only on the distribution of damage within the specimen close to failure as predicted by the anisotropic damage model. No experimental data was available to compare the load deformation responses. A damage contour representation is shown in Figure 59a. In this case, three concentrations of damage develop in the sample close to the loading points. The distribution of damage is symmetric to the vertical axis suggesting that the final crack pattern consists of two separate cracks joining at the upper damage concentration. The photograph (see Figure 59b) of a failed three-point test specimen of Marble (Jaeger, 1967) shows that in this particular specimen only one crack eventually developed due to inhomogeneities in the rock material. Three-point tests on Limestone are reported to fail in a similar manner (Jaeger, 1967).

7.6 Conclusions

The behaviour of Indiana Limestone, a relatively weak and highly porous rock, is modelled using the anisotropic damage model. The model is extended to incorporate a quasi-linear constitutive relationship to account for the nonlinear increase in bulk stiffness resulting from closure of pores under compression. Under a general stress path, stiffening due to pore closure and softening as a result of damage evolution may occur simultaneously.

The unconfined compression behaviour of the material can be represented by the linear - elastic damage model with an average value for the Young's Modulus. The quasi-linear damage model provides a good agreement with the entire stress - strain reponse of the unconfined compression test.

Application of the linear elastic damage model to the splitting tensile tests results in an underprediction of the strain at failure. The quasi-linear damage model is able to closely predict the load - deformation response. The damage initiates at a point immediately below the platen, which correponds to experimental observations of the location of acoustic emission events. The development of the total damage energy release as a function of the loading is in good agreement with the cumulative acoustic emission count which is further evidence of the representative selection of the evolution laws.

The three point test was modelled using the linear elastic damage model, and the predictions of the damage initiation zones agrees with the location of the final fracture pattern determined in experiments on a similar material.

Chapter 8 Analysis of Cavern Excavation

8.1 Introduction

At this stage, the anisotropic damage model has been applied to small scale, laboratory test problems. In the following section, the analysis of a major civil engineering project is presented to demonstrate the potential for the prediction of microcracking and damage in an in-situ scale application. A trial enlargement excavated during construction of the Dinorwig Hydroelectric Power Station in North Wales, United Kingdom is considered as a case study. Detailed description and discussion of the project design is given in Baines et al. (1983 & 1986), and the construction procedure is detailed in Jones et al. (1983). Preliminary studies were initiated in 1970, construction began in 1974 and the station was completed in 1983. The intention of this study is to demonstrate how the anisotropic damage model can be applied to assist in the design of such a structure. No attempt is made to re-evaluate the design assumptions of the Dinorwig cavern.

The Dinorwig power station consists of nine main caverns and numerous tunnels, as shown in a schematic in Figure 60. The largest cavern, the machine hall, is 24.5m wide, 180.3 m long and has a height of 59.7 m high. The rock, in which the caverns are located, is a Cambrian slate. The rock mass is traversed by subvertical Dolerite dykes and contains a series of clay filled faults (Whittle, 1977; Douglas et. al., 1983). A trial enlargement was performed in the beginning of 1976, prior to the commencement of the excavation of the machine hall, to provide experience of the excavation and to finalise the design of the support (Douglas et. al., 1983; Douglas, 1994). Extensive instrumentation was installed to ascertain the initial stress conditions and to obtain in-situ measurements of the rockmass behaviour under the construction sequence. The location of the trial enlargement relative to the machine hall and the other caverns is shown in Figure 60.

The trial enlargement was excavated in three main stages as indicated by the dashed lines in the cross-section of the excavation in Figure 61. Rock bolts and anchors were installed and tensioned to the design loads at the completion of each stage. Once the enlargement was complete, the support loads in the central region were gradually reduced to study the effects of the excavation on the rock, and to test the actual support requirements for the design of the excavations. During this process the deformations in the rock around the trail excavation were measured by means of a series of multiple-point borehole extensometers and by precise levelling.

A two-dimensional finite element analysis of the trial enlargement is performed simulating the same sequence of excavation and support installation. The section is intersected by a Dolerite dyke, which extends along the length of the machine hall. The theoretical investigation is not limited to the initial test sections and the analysis is, in fact, extended to include the excavation of the machine hall cavern and the adjacent main inlet valve gallery. The objective of the study is to examine the development of damage as a result of each stage of excavation and to compare the resulting displacements with the in-situ measurements.

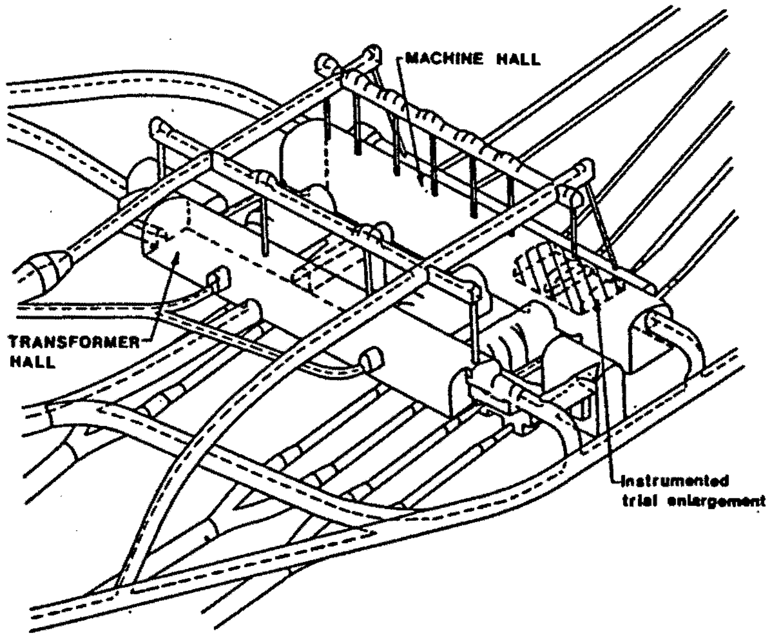

Figure 60: Layout of underground caverns at Dinorwig Power Station (Douglas et al., 1984)

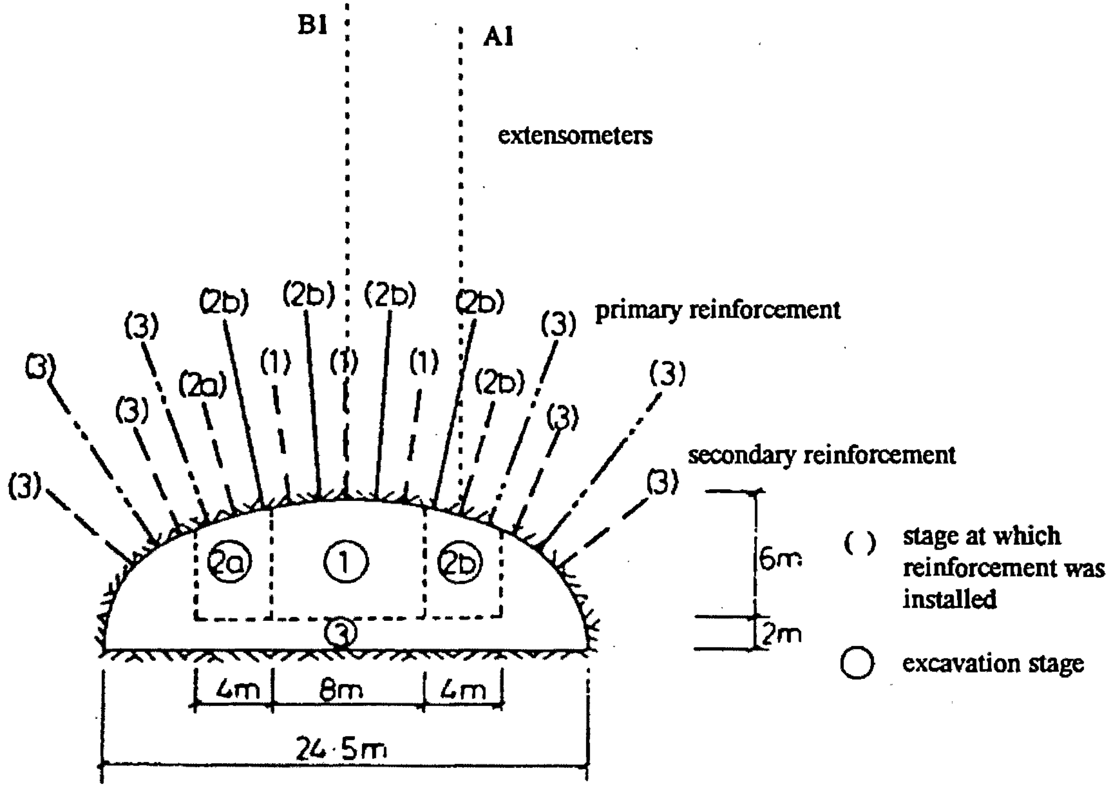

Figure 61: Cross-section of the trial enlargement showing the excavation sequence, the rock reinforcement and the extensometer positions (after Douglas et al., 1983)

8.2 Finite element model and parameters

The cross-section of the trial enlargement is shown in Figure 61. The dimensions of the trial enlargement and the position of the Dolerite dyke which intersects the excavation on the downstream side correspond to the layout in the instrumented section (Douglas et al., 1983). The

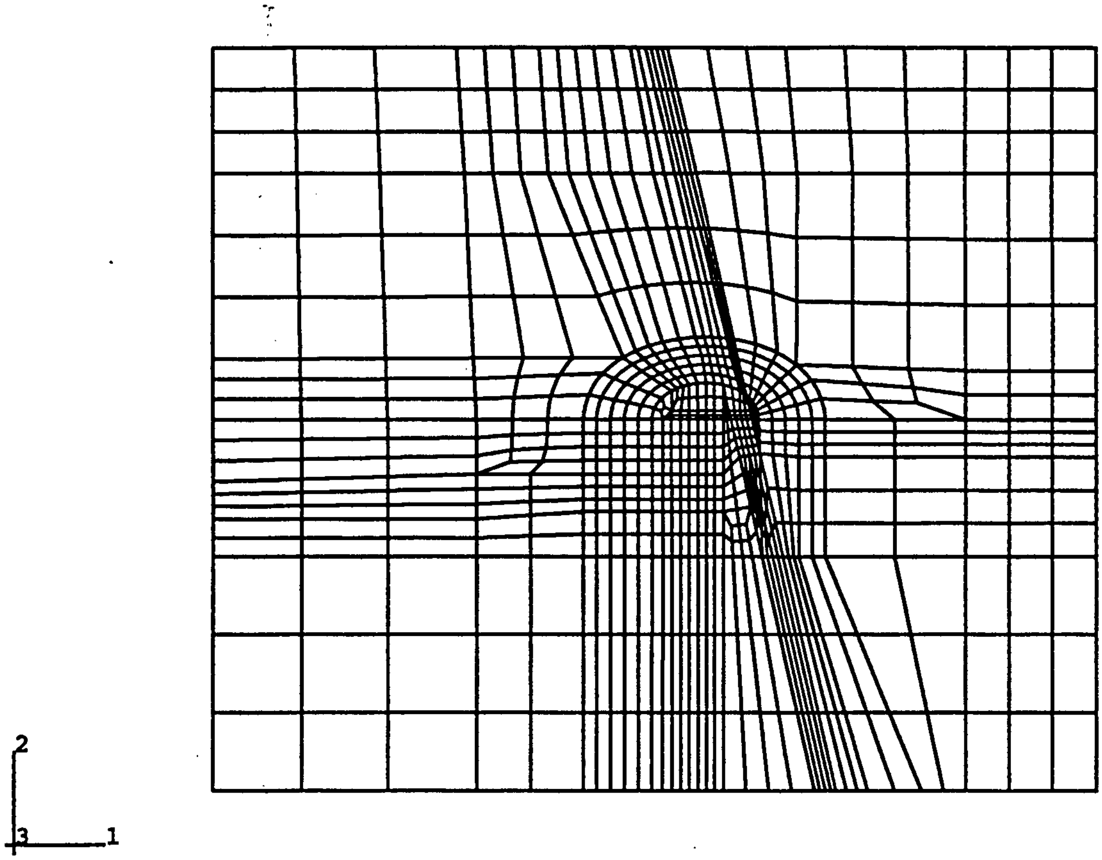

Figure 62: Finite element mesh for Dinorwig cavern analysis

base of the section is 24.5m wide and the excavation is 8m high at the centre. The machine hall, below the trial enlargement, is modelled as a rectangular section, 30m in height. The valve gallery has a cross-section of 15m by 14 m and is positioned at a distance of 16m from the upstream wall of the machine hall. The complete finite element mesh, shown in Figure 62, covers an extent of 203m in width by 172 m in height to reduce any interaction between the region of interest and the boundary conditions. The mesh consists of 736 plane strain elements. A combination of eight-node quadrilateral elements with quadratic displacement interpolation and reduced integration and six-node, quadratic interpolation triangular elements is required to discretize the sharp angled intersections between the Dolerite dyke and the excavation. The Dolerite dyke is 5m thick. The dyke is divided into four elements across the thickness. The outer two elements are assumed to have a lower stiffness to model the softer material in the dyke margins.

The boundaries of the model are constrained against vertical movement along the lower boundary. However, vertical displacement is permitted along both sides of the mesh whilst horizontal displacement is prevented. The measured in-situ stress states consist of 9 MPa in the vertical direction, an 8 MPa horizontal stress, and a 15 MPa out-of-plane stress. The overburden is simulated by the application of 9 MPa vertical pressure to the upper, free, surface of the mesh. Gravity loading due to self-weight is also applied. The specific gravity of the rock is 2.8.

The primary support which was installed consisted of 10m long rock anchors loaded to 600kN, at 3m centres, as shown in Figure 61. Rock bolts, 6m long and 3m apart, tensioned to 100kN comprise the secondary reinforcement. The rock bolts and anchors are approximated in the finite element analysis by the application of vertical concentrated forces at corresponding nodes in the roof of the excavation.

In the analysis, the same sequence of construction was followed to simulate the trial excavation as indicated Figure 61. The in-situ stress state was established in the initial loading step. The subsequent analysis steps are

- stage 1 : excavation of 8m span and installation of secondary support,
- stage 2a : 4m enlargement upstream,
- stage 2b : 4m enlargement downstream and installation of secondary support,
- stage 3 : enlargement to 24.5m span and installation of primary and secondary support.

After completion, the primary support elements were unloaded in a controlled fashion. The simulation of the destressing of these supports is performed by reducing the equivalent force to 150kN. In another step, the supports were restressed to the initial loads. The machine hall construction was simulated in six intermediate excavation steps (stage 6 to stage 11). The valve inlet gallery was excavated in the final step.

During stage 1 of the trial enlargement a series of extensometers were installed in the roof of the excavation. The deformation measurements relevant to this study were taken at the extensometers, A1 and B1, extending 25m into the rock as shown in Figure 61. The predicted deformation of the finite element analysis with the anisotropic damage material is calculated as the difference in the displacements of the nodes at the locations corresponding to the upper and lower ends of the extensometer.

The engineering properties of the Slate and Dolerite were evaluated in a series of laboratory and field tests (Douglas et al., 1977). The design considered only linear elastic material behaviour and therefore only the elastic constants and the uniaxial compressive strengths were determined. The Slate is an anisotropic material and the elastic moduli and the compressive strength vary with the cleavage plane angle β. The lower bound expressions for the Young's modulus E and ultimate compressive strength σ of the Slate are given (Douglas et al., 1977) by

$$\begin{aligned} E &= 91 - 66\cos 2(\beta - 40) \quad [\mathrm{GPa}] \\ \sigma &= 148 - 108\cos 2(\beta - 40) \quad [\mathrm{MPa}]. \end{aligned} \tag{196}$$

In-situ testing suggested that the jointed rockmass could be approximated as an isotropic linear elastic material with values of 50 GPa for the Young's modulus and 0.2 for the Poisson's ratio. These values were used in the original design. The Dolerite was found to be isotropic and has a Young's modulus of 86 GPa ±14 GPa, and an uniaxial compressive strength between 80 and 180 MPa.

No stress - strain relationships or failure envelopes for the Slate are available for the calibration of the damage model. The parameters were estimated by considering slates of various origins (Anderson, 1974; Kulhawy, 1975; Lama and Vutukuri, 1978; Brady and Brown, 1993). The slate is regarded as a material with a transversely anisotropic initial stiffness tensor $\boldsymbol{C}_o$. However, due to the lack of stress - strain data for the material, the slate is assumed in this study to be initally isotropic with the elastic constants $E = 50$ GPa and $\nu = 0.2$ (as in the original design). The damage evolution parameters were estimated using the trial and error procedure, described in Chapter 5, until a failure envelope was obtained which appeared to be representative for the rock. The material parameters of the anisotropic damage model evaluated for the Slate are given in Table 5.

The predicted stress-strain response for the Dinorwig Slate in unconfined compression is shown in Figure 63a. The predicted failure envelopes for conventional triaxial compression and reduced triaxial extension are shown in Figure 63b in terms of the major and minor principal stresses. The failure strengths for a representative slate, the Welsh Slate (Anderson, 1974) are included in the stress diagram to show the appropriateness of the selected model parameters. Also plotted is the Hoek-Brown failure criterion (Hoek and Brown, 1980) using the material constants $m = 10$ and $s = 1$ which are typical for slate (Brady and Brown, 1993).

	Parameter	Symbol	Value
Elastic constants	Young's modulus	E	50 GPa
	Poisson's ratio	ν	0.2
Damage initation	coefficient of friction	μ_o	0.4
	effective shear resistance	$\bar{\tau}_o$	2.0 MPa
Damage evolution	Mode I shape parameters	β_{0I} and β_{1I}	0.7, 0.0
	Mode I size parameters	θ_{0I} and θ_{1I}	0.008 MPa, 0.03 MPa
	Mode II shape parameters	β_{0II} and β_{1II}	0.5 , 0.0
	Mode II size parameters	θ_{0II} and θ_{1II}	0.07MPa , 0.004 MPa
Dolerite dyke	Young's modulus	E	50 GPa
	Poisson's ratio	ν	0.2
Dyke margin	Young's modulus	E	5 GPa
	Poisson's ratio	ν	0.2

Table 5: Material parameters for Slate rockmass, Dolerite dyke and the dyke margins

The Dolerite dyke is modelled as a linear elastic material with the reduced, in-situ modulus $E = 50$ GPa and Poisson's ratio $\nu = 0.2$. The dyke margins are considered to be softer than the surrounding rock, and are assumed to be linear elastic material with a Young's modulus selected to be 10% of the solid rock (i.e. $E = 5$ GPa), with the same Poisson's ratio of $\nu = 0.2$.

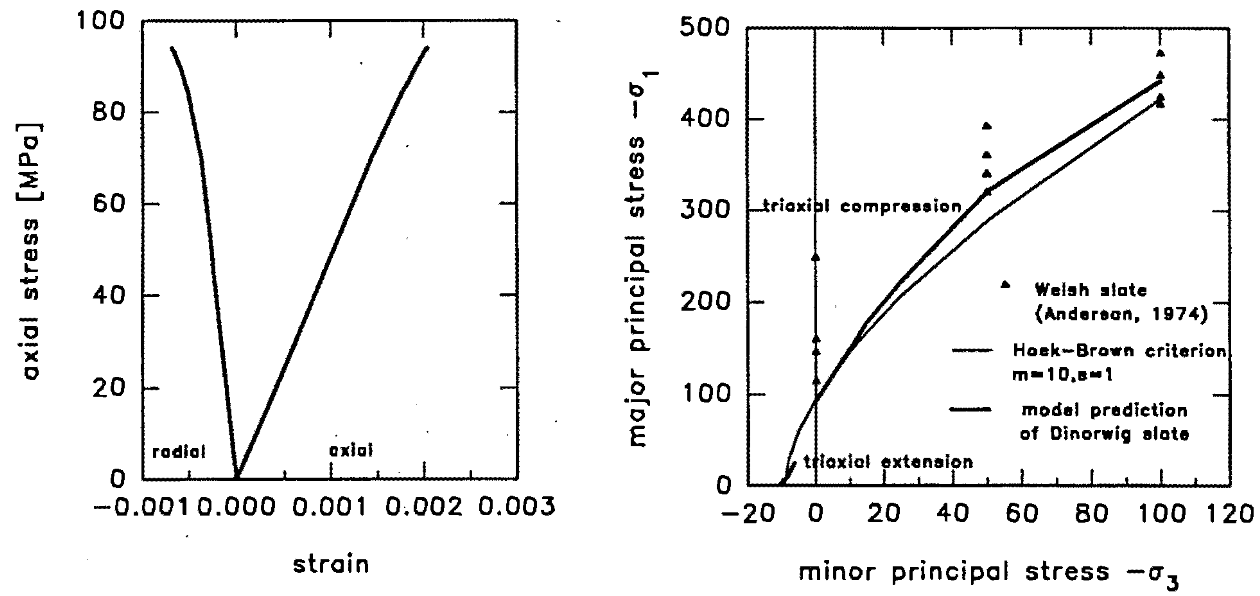

Figure 63: Finite element simulation of Dinorwig Slate (a) uniaxial stress - strain response (b) failure envelope

8.3 Prediction of damage and deformations due to sequential excavation

The contours of total damage for some selected excavation steps are shown in Figure 64 a,b,c,d and Figure 66 a,b,c,d. For the purposes of comparison, the minimum and maximum total damage contours in all plots are set to $d = 0$ and $d = 0.05$, respectively. Thus, as before, the lower limit (darkest blue) indicated regions which are completely undamaged, and the upper limit (in red) displays the areas in which damage is most developed. Again, there is no particular physical meaning attached to this choice of the damage magnitudes. The vector plots shown in Figure 65a and 65b are given for stage 1 and stage 3 of the trial enlargement. Vector plots for the final cavern excavation and the main inlet valve gallery excavation are presented in Figure 67a and 67b.

After the first stage of the excavation a very low measure of damage is predicted that extends into the rockmass surrounding the cavity, as shown in Figure 64a. The positive damage strain vectors on the wall of the excavation bordering the Dolerite dyke are approximately normal to the face of the excavation, suggesting that microcracks grow sub-parallel to the free faces (see Figure 65a). The presence of the linear elastic material of the Dolerite dyke causes a rotation of the damage vectors in the region of the dyke. Thus, the direction of the microcrack growth in the roof and floor of the excavation is generally parallel to the free edges. The triangular shaped region between the face of the excavation and the elastic dyke exhibits the highest damage because the softer material in the dyke margins tends to deform towards the excavated region. The 'crack' strain vectors appear to be inclined perpendicular to the dyke.

With the excavation of stage 2a the damage in the rock triangle adjacent to the dyke increases further (see Figure 64b). Removal of the rock material on the downstream side of the initial

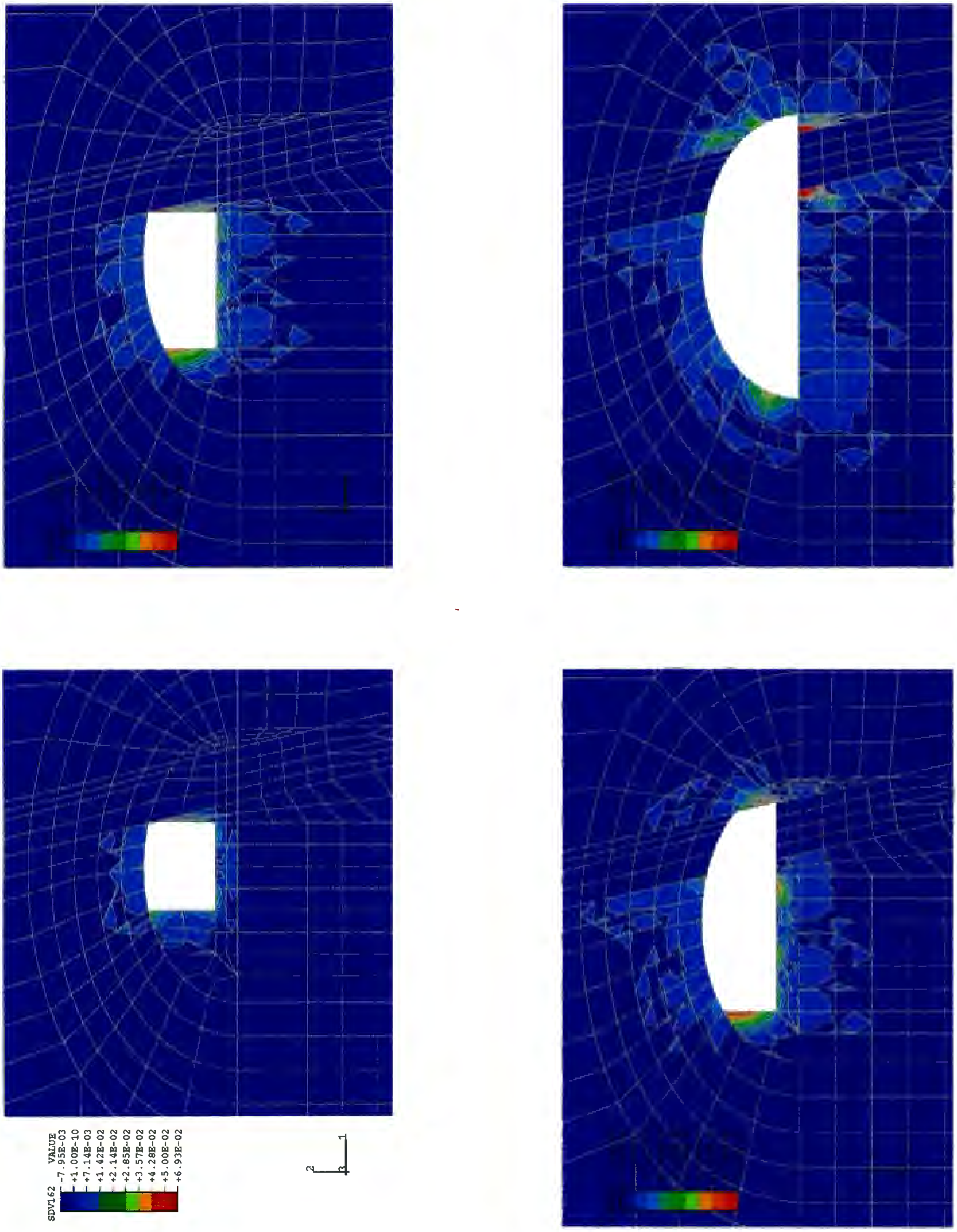

Figure 64: Damage contours at trial excavation steps: stage 1, stage 2a, stage 2b, stage 3

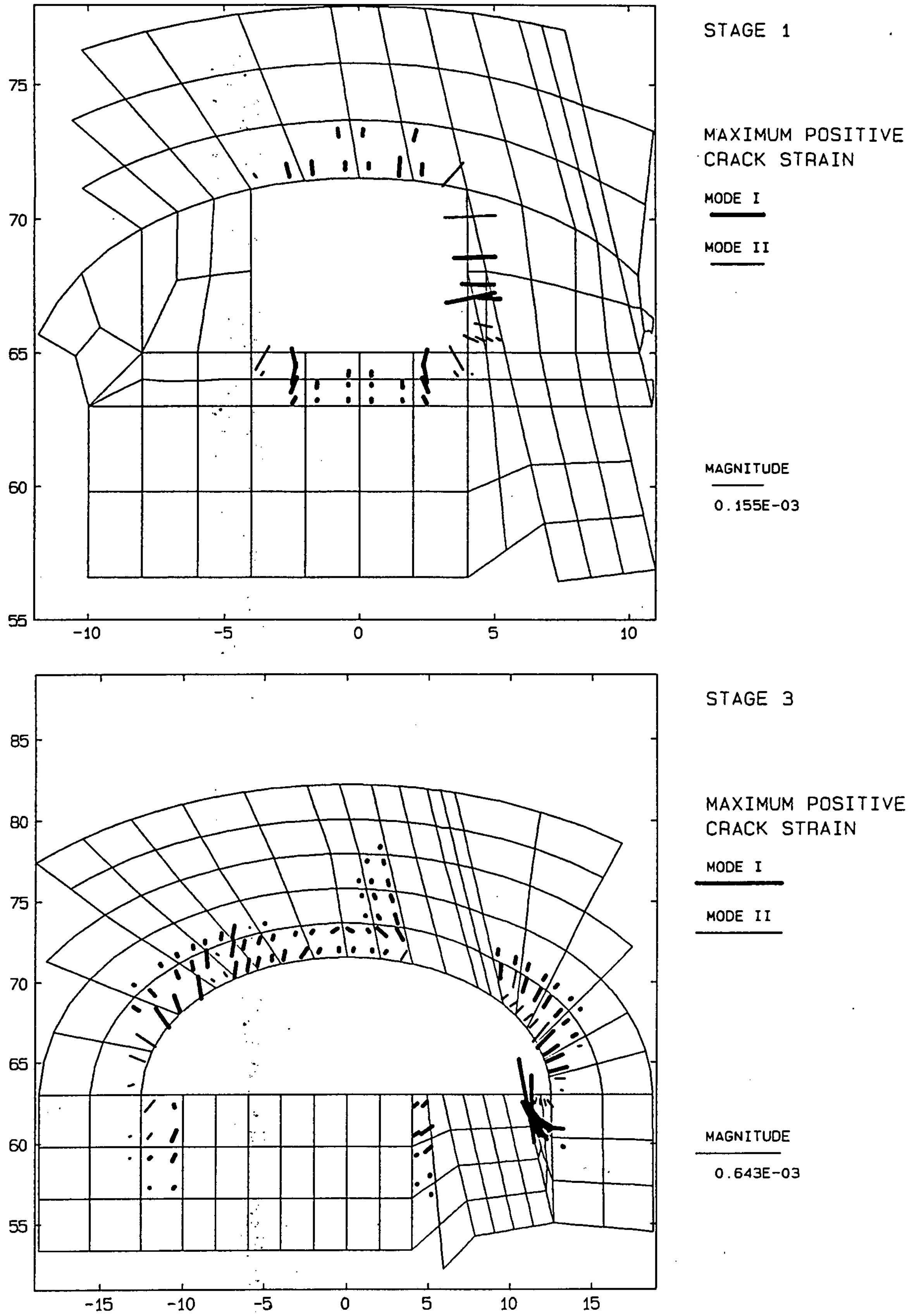

Figure 65: Damage vectors after excavation a: stage 1 b: stage 3

Figure 66: Damage contours at various stage of excavation: stage 6, stage 7, complete machine hall, main inlet valve gallery

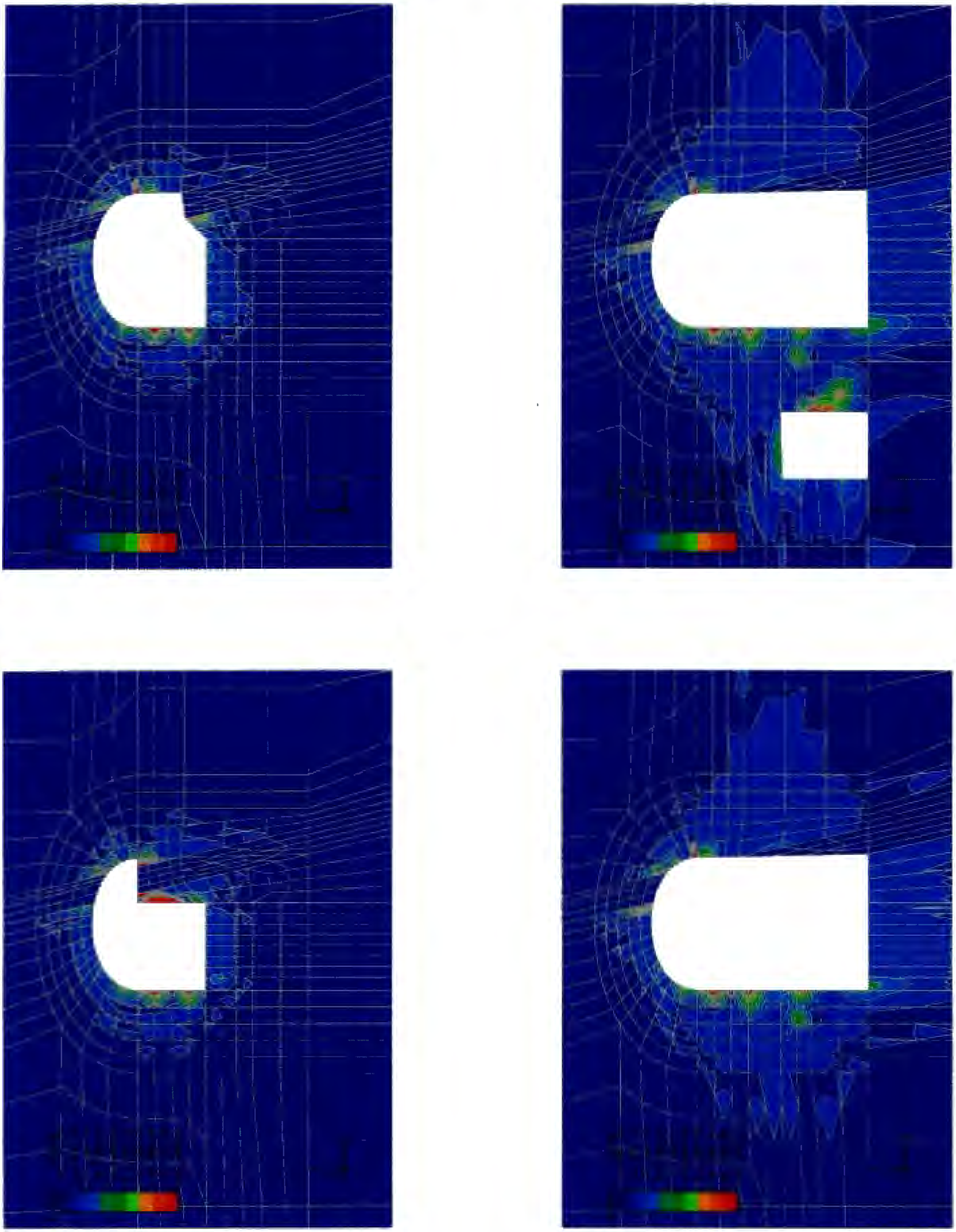

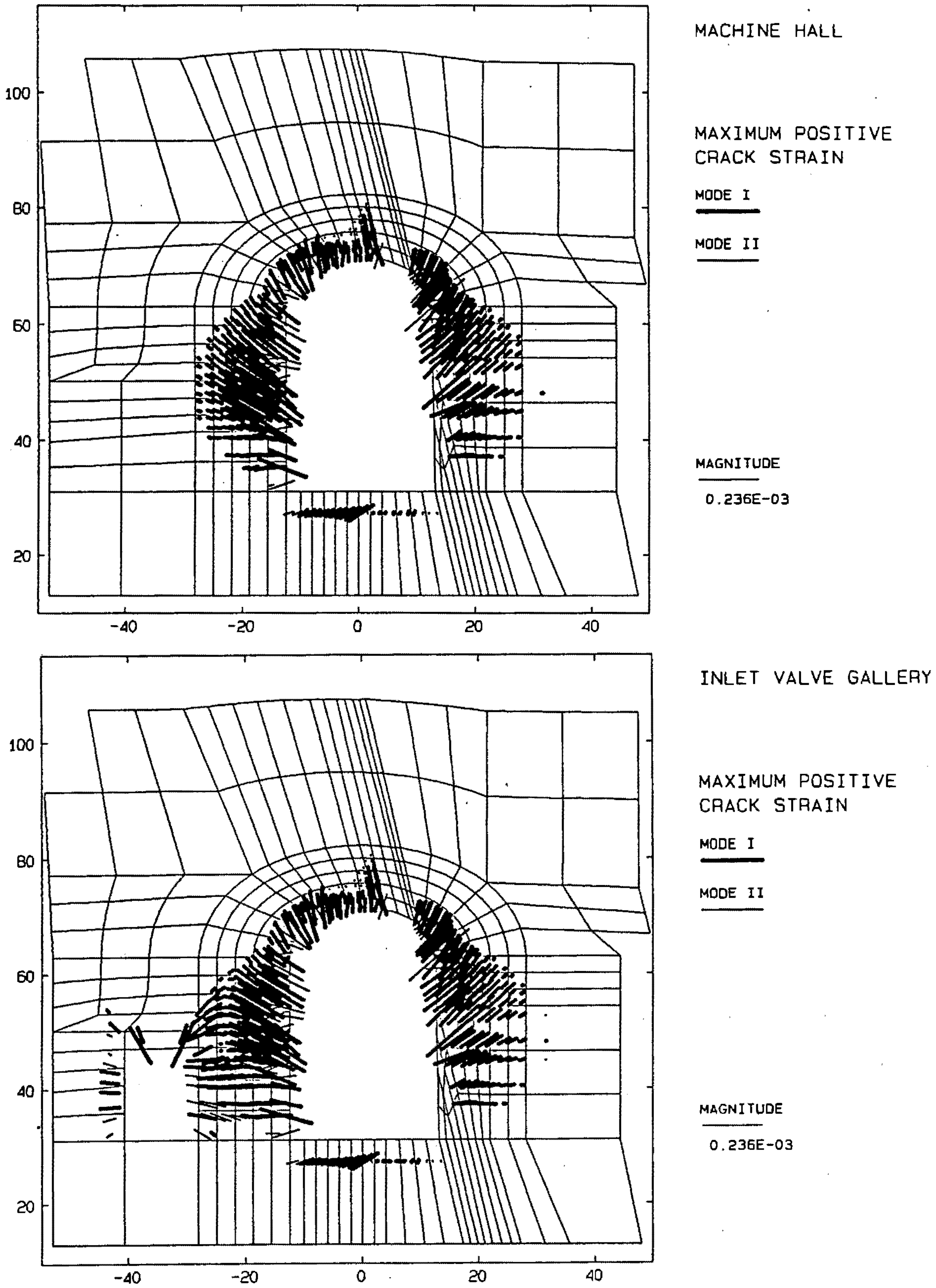

Figure 67: Damage vectors after excavation of a: machine hall b: machine hall and valve gallery

enlargement causes additional damage in the corner of the roof. The excavation of stage 2b extends to the edge of the dyke causing damage deep into the roof and in the side-wall which overhangs the excavation (see Figure 64c).

The full trial enlargement to an excavated width of 24.5m is achieved in stage 3. The curved roof of the cavern is now completely formed and due to the elliptical shape only a small amount of damage develops and is induced in the surrounding rock (see Figure 64d). The majority of this damage occurs in mode I i.e. extension cracking. The 'crack' strain vectors are normal to the free edges of the cavern (see Figure 65b) suggesting that the microcracking tends to be paralled to the face of the excavation. Interaction of the soft margin of the Dolerite dyke with the surrounding Slate causes the 'crack' strain vectors at the sides of the dyke to rotate so that they are directed parallel to the dyke. Thus, microcracks will extend perpendicular to the dyke.

The trial excavation procedures are completed with the destressing of the supports. The removal of support does not affect the stability of the roof, since only a slight increase of damage was predicted as was determined in the in-situ experiments (Douglas et al., 1983). After restressing of the supports to the design loads, simulated in the analysis as a single load step, the excavation of the main cavern was advanced in six further construction steps, i.e. load increments.

Excavation of the next step (stage 6) into the floor of the trial enlargement leaves a highly damaged region of rock adjacent to the Dolerite dyke (see Figure 66a). Microcracking is found to occur parallel to the face, which favours spalling of the rock into the excavation. Regions of increased damage develop on the opposite side of the cavern, as the side walls deform towards the excavated region. The predicted direction of crack growth is approximately parallel to the side walls. Upon removal of the highly damaged region, a relatively low state of damage remains in the rockmass surrounding the excavation as shown in Figure 66b.

Simulation of the construction is continued in several intermediate steps (contour plots not shown) until the main cavern excavation is completed. At this stage an extensive region around the cavern is damaged as shown in Figure 66c. Small pockets of highly damaged material exist where the sharp corners of the previous excavations were located. The corresponding 'crack' strain vectors are shown in Figure 67a. Vectors in the roof of the cavern are aligned normal to the free edge, except near the dyke. The vectors along the side walls of the cavern dip at about 20 to 30 degrees to the horizontal. This suggests that rock bolts should be installed upwards, inclined in the same direction as the 'crack' strain vectors in order to limit the dilatancy due to the fracturing.

The main inlet valve gallery is excavated upstream of the machine hall by the removal of four elements in one step. Greatest damage is exhibited in the region between the existing machine hall cavern and the newly formed opening. The 'crack' strain vectors in this case are shown in Figure 67b. Damage in the 'pillar' between the two openings is directed so that microcracks will be aligned sub-parallel to the free face. The longest vectors are situated well within the rock mass between the caverns. The confinement in this region acts to restrict the formation of damage. The highest damage occurs near the free surfaces where there is no confinement. At

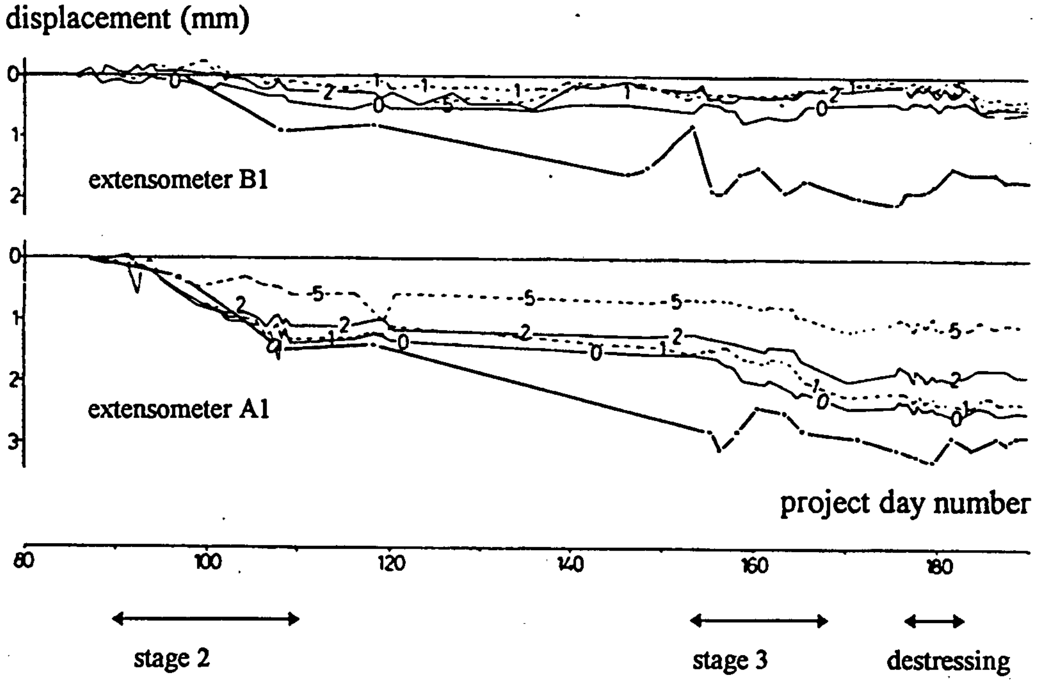

Figure 68: Measurement of in-situ deformations at extensometers A1 and B1

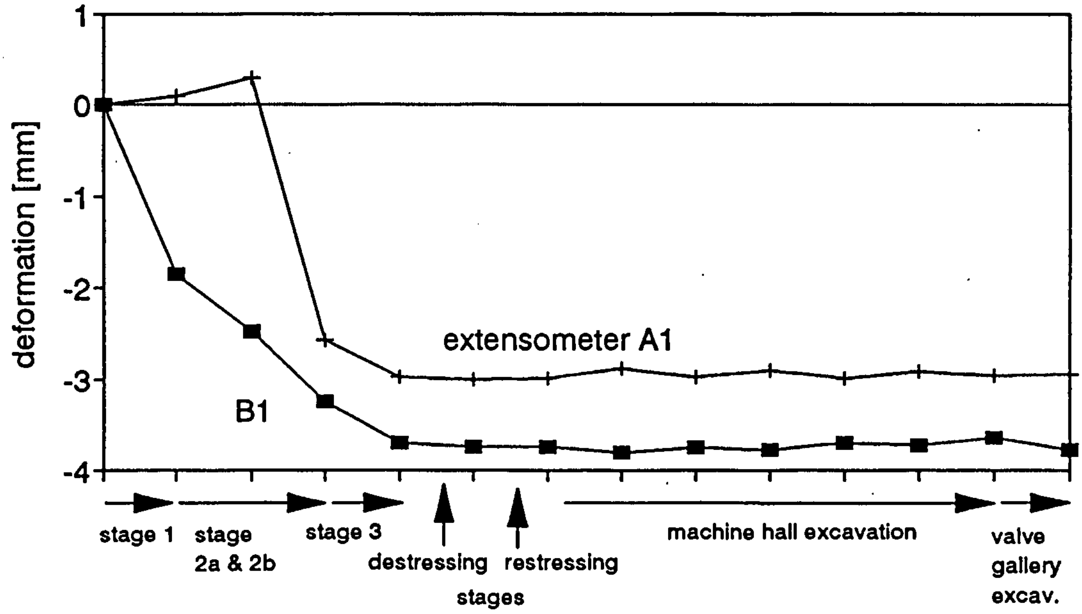

Figure 69: Extensometer deformations predicted for the Dinorwig cavern analysis

the base of the 'pillar' there is some indication of maximum positive 'crack' strains in mode II.

The deformations of the extensometers predicted in the finite element analysis for the entire sequence of excavation are shown in Figure 69. The finite element predictions show an initial increase in deformations as the rock below the extensometer positions is excavated. The general trend of the deformations during the trial enlargement sequence agrees with the corresponding in-situ measurements, as shown in Figure 68. The in-situ measurements were recorded for stage 2 and stage 3, during excavation of the trial enlargement, and during the destressing and restressing of the support. The graphs show the readings at four points along the extensometer (labeled 0,1,2,5) and the deformations from precise levelling (thick line). The extensometer at the centreline (B1) shows less than 1mm deformation over the trial enlargement sequence. The predicted deformations are in agreement with the levelling measurements. The magnitudes of the deformations, at the location A1, after stage 3 are of the order of 2.5mm. These correspond to the extensometer readings and the levelling results. The analysis and in-situ measurements show that only a small amount of deformation results from destressing of the support which is recovered during the reloading of the reinforcement. Insignificant changes in deformation are predicted during the cavern construction sequence.

8.4 Conclusions

In a complex case study, the anisotropic damage model has been applied to re-analyse the sequential excavation of the Dinorwig Hydoelectric power station cavern in Wales. The analysis consisted of the numerical simulation of a number of construction stages and included the effect of the initial in-situ stress state, different rock types, loading and unloading of rock reinforcement and the interaction between two adjacent openings. The Slate rockmass is intersected by a Dolerite dyke, which results in a complicated finite element discretization. A series of in-situ measurements is available for comparison with the the model predictions.

Due to insufficient stress path testing and insufficient material properties, the evaluation of the anisotropic damage material constants for the Dinorwig Slate had to be based on the elastic constants and ultimate strength. The material parameters are therefore estimated from similar slates for this backanalysis.

The damage is presented in contour and vector diagrams. The contour plots clearly demonstrate the evoltuion of damage during each construction stage, depending on the shape of the excavation and also the interaction between the Slate rockmass, the Dolerite dykes and the softer dyke margins. In the analysis of the instrumented trial enlargement, no significant damage was predicted. The subsequent excavation of the main cavern resulted in more damage, particularly in the regions adjacent to the Dolerite dyke. An important feature of the application of the anisotropic damage model is the ability to predict the changes in the rock behaviour due to the stress redistribution resulting from the construction sequence and to identify how the geometry of each excavation influences the final distribution of fracturing around the excavation.

The diagrams of the 'crack' strain vectors depict the direction of the damage. The model predicts that the microcracking is aligned approximately parallel to the face of the excavation. The interaction between the rockmass and the dolerite dyke is indicated by the rotation of the damage direction to become orthogonal to the dyke.

Comparison of the predicted deformation of the cavern roof with in-situ extensometer measurements shows that the finite element analysis predicts the trends in deformation resulting from the excavation sequence. The magnitudes of the deformations are in reasonable agreement with the in-situ observations.

Chapter 9 Conclusions

A constitutive model has been proposed to model the development of anisotropic damage in brittle rock. In general, microcracking causes a reduction in the stiffness of a material. In a continuum damage mechanics theory, the elastic stiffness is modified by a set of internal variables which measure the extent of the stiffness change. Thus, the fundamental problem in the development of a damage model is the identification of the internal variables, and the manner in which they alter the components of the stiffness tensor as a result of damage growth.

The majority of damage formulations are intended to model the growth of microcracking due to the application of tensile stresses to the material. The literature investigation of the behaviour of rock in triaxial, plane strain and multiaxial laboratory experiments showed that microcracking develops in rock under both, compressive and tensile states of stress. The dilatancy associated with the preferentially orientated microcracking characterises the stress - strain response of the material. When rock is loaded in compression, the preexisting fractures tend to close. New microcracks develop as the deviatoric stress increases. These fractures are, in general, aligned towards the major principal compressive stress.

The evolution of the damage can be measured in terms of fracture density counts, the inelastic volumetric strain, the increase of acoustic emission and the decrease of compression wave travel times. All these methods show an exponential increase in fracturing as the loading increases. The continued growth of microcracks is reflected as nonlinearity of the stress - strain response. Consideration of the stress - strain behaviour in different directions shows that the stiffness becomes anisotropic as the material damage forms. This is confirmed by indirect techniques such as ultrasonic compression wave velocity measurements.

Micromechanical models indicate that tensile cracks induce anisotropy and cause an increase in the compliance of the material. The type of anisotropy depends on the distribution of the cracking within the material. A number of micromechanical concepts are able to explain the initiation of directional cracking in compression stress states. Of these, the sliding crack model is able to account for most of the observed stress - strain behaviour, and has been extensively analysed in micromechanical models. The sliding crack concept suggests that directional microcracking is initiated at the edges of an inclined flaw when the flaw surfaces slide relative to each other once the applied loading has overcome the shear resistance. A population of these sliding crack mechanisms causes the compliance tensor to become fully anisotropic.

The components of the damage model are developed in analogy to the sliding flaw concept. The undamaged material is assumed to be elastic and the Coulomb friction law defines a damage initiation criterion in the effective stress space. The stress and strain state at damage initiation are defined as the residual stresses and strains, respectively. The special feature of this formulation is that the damage is only induced in a subdomain of the strain, the 'crack' strain subdomain, defined by the difference between the total and the residual strain states. The internal variable, which represents the history of damage, is the secant stiffness of the 'crack' subdomain. The stiffness becomes anisotropic as its components are reduced due to damage.

Evolution of the damage causes the effective stress acting on the undamaged material to increase relative to the applied, Cauchy stress. The effective normal stress acting on the plane of maximum shear determines the mode of damage growth. When the effective normal stress increases relative to the residual normal stress, the material is in extension and the damage growth is defined by the 'unstable' mode I evolution function, otherwise the material is in compression and the damage is described by the 'stable', mode II evolution.

The growth of the directional damage is governed by the principle of maximum damage dissipation, and depends on the 'crack' strain through the conjugate thermodynamic force which is the damage energy release rate. The damage surface is expressed as a function of a scalar variable, the undamaged energy norm of the positive part of the 'crack' strain tensor. The magnitude of the damage depends on the positive eigenvalues of the 'crack' strain tensor. The direction of the damage is calculated from the corresponding eigenvectors of the 'crack' strain tensor by means of the positive projection operator.

Evolution laws for the damage are developed in terms of the undamaged energy norm and depend on the confining pressure. A versatile expression, based on the Weibull probability density function, is proposed to describe the evolution of the damage over a wide range of confining pressure. Loading and unloading criteria have been developed which are consistent with the sliding flaw analogy. In extension, mode I, unloading occurs with the damaged modulus. Once the effective stress state returns to the initial elastic domain the material behaviour is determined by the undamaged stiffness. During loading and unloading in compression, mode II, the elastic domain is assumed to translate in the effective stress space. The material response upon unloading is initially characterised by the undamaged stiffness which is followed by unloading with the damaged stiffness. The hysteresis observed in the stress - strain response of rock during a cycle of unloading and reloading is sucessfully modelled. Accumulation of damage due to cyclic loading is not considered at this stage.

A simple and straightforward procedure is described for the determination of the material constants of the anisotropic damage model. Three conventional triaxial compression and three reduced triaxial extension tests are required to evaluate the elastic constants, the initiation surface and the evolution laws for mode I and mode II. The sensitivity study of a range of material constants in the evolution laws demonstrates that the 'size' parameter θ has a significant effect on the simulation of the magnitude of the dilatancy and the ultimate strength of the material. The 'shape' parameter β governs rate of accumulation of damage with loading. The clear physical interpretation of the parameters is evidence of the suitability of the proposed evolution function for modelling damage in different rock types.

The direction of damage predicted by the anisotropic damage model agrees with the experimental observations for a range of stress path tests. In conventional triaxial compression, the damage forms orthogonal to the loading leading to an increase in the radial strain relative to the axial strain and hence an increase in the tangent Poisson's ratio. In reduced triaxial extension, the damage forms in the axial direction and there is not much change in the Poisson's ratio. This corresponds to the experimental observations that the microcracks grow orthogonal to the loading in extension. Thus, the damage is predicted to grow in the direction of the maximum compressive principal stress under both, compression and extension stress paths.

The model is implemented into a nonlinear finite element program and is verified by application to a series of practical problems beginning with simple stress path tests, then considering selected laboratory experiments with nonuniform stress states and sequences of element removal, and then analysing a large scale problem involving the construction of an underground cavern.

The material parameters are evaluated for Witwatersrand Quartzite which is found above the gold bearing reef and is of particular interest to the South African mining industry. The engineering properties of the material show significant variation making calibration difficult. The selection of the material parameters is verified by backprediction of conventional triaxial compression and reduced triaxial extension tests. In all cases, the predictions of the anisotropy and dilatancy of the rock are in very good agreement with the experimental data over a realistic range of confining pressures. The failure strength increases at higher confining pressures, and the failure envelope agree with the ultimate strengths from published data of triaxial compression and extension test. The ultimate strains predicted by the model are also in good agreement with the experimental results.

The modelling of a sequential excavation is undertaken at a small scale by the finite element analysis of a mining simulation in 100mm square Quartzite blocks with the anisotropic damage model as the material description. The initiation of damage occurs at locations which correspond closely to fracture patterns derived from the experiments. The damage directions are depicted in terms of the vectors of the positive 'crack' strain. Three regions of damage are present. A narrow zone of extension damage extends along the centreline of the model, outwards from the excavation. An area of compression damage arches over the excavated region, and further damage occurs ahead of the the face of the excavation. These patterns are in agreement with the observations from the experiments, and are also very similar to in-situ observations in mining and tunnelling.

The finite element analysis of diametral compression tests on the weak, porous Indiana Limestone emphasised the importance of correctly modelling the co-existing micromechanical processes of crack closure due to applied compression and crack growth resulting from deviatoric stresses in the rock. The linear - elastic damage model was calibrated for an average stress - strain response during uniaxial compression. The ultimate strength and strain were closely modelled. The deformation in the nonuniform diametral compression test was, however, considerably underpredicted. A quasi-linear constitutive relation was adapted to model the increase of stiffness during the initial compression of the highly porous rock. The bulk modulus increases as a power law function of the volumetric strain during pore closure which significantly improved the predictions of the deformation under diametral compression. The location of the damage is in good agreement with experimental observations for both, the splitting tensile test, and the three-point test. The increase of the total damage energy release rate with load corresponds to the cumulative acoustic emission from microcrackimg events, and suggests a physical meaning for the damage energy release.

The application of the anisotropic damage model on an engineering scale is considered in the analysis of the Dinowing power station. The case study provides a sophisticated finite element mesh involving a solid Slate rockmass intersected by a Dolerite dyke, in-situ pressures corresponding to low depth, a construction sequence consisting of a number of excavations of different shapes, and the installation of support. The damage model is calibrated based on a limited amount of test data and back predictions of triaxial tests suggest that the failure envelope is in good agreement with the data for other Welsh slates. The potential for modelling a large scale excavation sequence, is demonstrated by the quantitative agreement of the predicted deformations with measured values. Relatively little damage is predicted, as was observed during the construction of the power station. The main advantage of the model which is highlighted by this study is the ability to predict the evolution of the damage magnitude and direction during a complex excavation and construction sequence.

Although significant progress has been made in the computational modelling of cracking and fracturing of a rock, it is apparent that further advancements are needed. The analysis of mining excavations requires large, complicated finite element meshes, suggesting the need for improvement of the rate of convergence of the Newton-Raphson solution procedure, and for the consideration of the material behaviour once the deformations have localised into macroscopic shear or extension fractures. In addition, the potential of the damage model to include the influence of initial anisotropy in layered rock, the brittle-ductile transition at high confinements, the accumulation of damage due to cyclic loading, and the extension to rate dependent behaviour have not yet been investigated due to the shortage of experimental data.

The anisotropic damage model represents a major step in the constitutive modelling of the fracture processes in rock. The theoretical framework is formulated to represent the micromechanics of the initiation, and evolution of the fractures under general loading. The parameters can be determined from standard tests. The stress - strain response resulting from the induced anisotropy provides good agreement with observations for a variety of loading paths including compression and extension behaviour, uniform and nonuniform stress states, loading, unloading and reloading. The benefit of the finite element implementation is that relatively minor modifications of the program input allow for evaluation of the influence of the in-situ stress state, the geometry of the opening, the interaction between the rockmass and other geological features, and the amount of support on the direction and magnitude of fracturing, and the deformation of the rock, at each stage of the construction or mining procedure.

Chapter 10 References

Abdel-Gawad, M., Bulau, J. & Tittmann, B. (1987) Quantitative characterization of microcracks at elevated pressure. *J. Geophys. Res.* **92**: 12911-12916.

Adams, M. & Sines, G. (1978) Crack extension from flaws in a brittle material subjected to compression. *Tectonophysics* **49**: 97-118.

Anderson, T. B. (1974) The relationship between kink-bands and shear fractures in the experimental deformation of slate. J. Geol. Soc. Lond. **130**: 367-382.

Baines, J.A., Newman, V.G., Hanna, I.W., Douglas, T.H., Caryle, W. Jones, I.L., Eaton, D.M., & Zeronian, G. (1986) Discussion: Dinorwig pumped storage scheme. *Proc. Instn Civ. Enginrs. Part 1,* **80**: 493-536.

Baines, J.A., Newman, V.G., Hanna, I.W., Douglas, T.H. & Caryle, W. (1983) Dinorwig pumped storage scheme, Part 1: Design. *Proc. Instn Civ. Enginrs. Part 1,* **74**: 635-680.

Baste, S., Guerjouma, R.E. & Audoin, B. (1992) Effect of microcracking on the macroscopic behaviour of ceramic matrix composites : Ultrasonic evaluation of anisotropic damage. *Mechanics of Materials* **14**: 15-31.

Baste, S. & Audoin, B. (1991) On internal variables in anisotropic damage. *Eur. J. Mech., A/Solids* **10**: 587-606.

Batzle, M.L., Simmons, G. & Siegfried, R.W. (1980) Microcrack closure in rocks under stress: Direct observation. *J. Geophys. Res.* **85**: 7072- 7090.

Bieniawski, Z.T. (1967) Mechanism of brittle fracture of rock. Part 1 - theory of the fracture process. *Int. J. Rock Mech. Min. Sci.* **4**: 395- 406.

Brace, W.F. & Bombolakis, E.G. (1963) A note on brittle crack growth in compression. *J. Geophys. Res.* **68**: 3709-3713.

Brace, W.F. (1965) Some new measurements of linear compressibility of rocks. *J. Geophys. Res.* **70**: 391-398.

Brace, W.F. (1965) The effect of cracks on the uniaxial elastic compression of rocks. *J. Geophys. Res.* **70**: 399-411.

Brace, W.F., Paulding, Jr., B.W. & Scholz, C. (1966) Dilatancy in the fracture of crystalline rocks. *J. Geophys. Res.* **71**: 3939-3953.

Brady, B.H.G. & Brown E.T. (1993) *Rock Mechanics for underground mining.* Chapman and Hall, London.

Breysse, D. (1990) Probabilistic formulation of damage-evolution law of cementitious composites. *J. Engng Mechs Div. ASCE,* **116**: 1489-1510.

Briggs, D.J. (1982) Mechanical properties of quartzites and associated rock types, *Research Report No. 13/83*, Chamber of Mines of South Africa Research Organization.

Briggs, D.J. & Vieler, J.D.S. (1984) Micro-fracture studies of quartzite in triaxial extension, *Research Report No. 12/84*, Chamber of Mines of South Africa Research Organization.

Brummer, R.K. (1987) *Fracturing and deformation at the edges of tabular gold mining excavations and the development of a numerical model describing such phenomena*, PhD. Thesis, Rand Afrikaans University, Johannesburg.

Budiansky, B. & O'Connell, R.J. (1976) Elastic moduli of a cracked isotropic solid. *Int. J. Solids Structures* **12**: 81-97.

Burger, B.B. & Resende, L. (1987) Localised failure in brittle materials. *UCT/CSIR Applied Mechanics Research Unit, Report No. 96.*

Byerlee, J.D. (1968) Brittle-ductile transition in rocks. *J. Geophys. Res.* **73**: 4741-4750.

Chaboche, J.L. (1988) Continuum damage mechanics: Part I and Part II. *J. Appl. Mechs.* **55**: 59-72.

Chaboche, J.L. (1984) Anisotropic creep damage in the framework of continuum damage mechanics. *Nuclear Engng. Des.* **79**: 309-319.

Chaboche, J.L. (1992) Damage induced anisotropy : On the difficulties associated with the active/passive condition. *Int. J. of Damage Mechanics* **1**: 148-171.

Chow, C.L. & Wang, J. (1987) An anisotropic theory of elasticity for continuum damage mechanics. *Int. J. of Fracture* **33**: 3-16.

Chow, C.L. & Lu, T.J. (1989) On evolution laws of anisotropic damage. *Eng. Frac. Mechs* **34**: 679-701.

Coleman, B.C. & Gurtin, M. (1967) Thermodynamics with internal state variables. *J. of Chemical Physics* **47**: 597-613.

Costin, L.S. (1983) A microcrack model for the deformation and failure of brittle rock. *J. Geophys. Res.* **88**: 9485-9492.

Dengler, L. (1976) Microcracks in crystalline rocks. *Electron microscopy in minerology*, in Wenk, H.R. (ed.), Springer, Berlin, 550-556.

Desai, C.S. & Siriwardane, H.J. (1984) *Constitutive equations for engineering materials with emphasis on geological materials.* Prentice Hall, New Jersey.

Dey, T.N. & Wang, C-Y. (1981) Some mechanisms of microcrack growth and interaction in compressive rock failure. *Int. J. Rock Mech. Min. Sci. & Geomech. Abstr.* **18**: 119-209.

Dougill, J.W. & Rida, A.M. (1980) Further consideration of progressively fracturing solids. *J. Engng Mechs Div. ASCE,* **106**: 1021-1038.

Douglas, T.H., Richards, L.R. & Arthur, L.J. (1983) Trial excavation for underground caverns at Dinorwig power station. *Geotechnique* **33**: 407-431.

Douglas, T.H., Richards, L.R.& Arthur, L.J. (1977) Site investigation for main underground complex - Dinorwig power station. *International Symposium: Field measurements in rock mechanics,* Zurich, Preprint, 1-17.

Douglas, T.H., Richards, L.R., Arthur, L.J. (1984) Dinorwig power station : Rock support of the underground caverns. *ISRM Symposium: Design and performance of underground excavations*, Cambridge, U.K., 361-369.

Douglas, T.H. (1994) *Personal Communication.*

Dragon, A. (1976) On phenomenological description of rock-like materials with account for kinetics of brittle fracture. *Archives of Mechs.* **28**: 13-30.

Dragon, A. & Mroz, Z. (1979) A model for plastic creep of rock- like materials accounting for the kinetics of fracture, *Int. J. Rock Mech. Min. Sci.* **16**: 253-259.

Dyskin, A.V., Germanovich, L.N., Lee, K.K., Ring, L.M. & Ingraffea, A.R. (1994) Modelling of crack propagation in compression. *Rock Mechanics : models and measurements, challenges from the industry.* in Nelson P. & Laubach, S. E. (eds) Balkema, Rotterdam 451-462

Falls, S.D., Young, R.P., Chow, T. & Hutchins, D.A. (1989) Acoustic emission analyses and tomographic velocity imaging in the study of failure in Brazilian disk tests. *Rock mechanics as a guide for efficient utilization of natural resources.* in Khair (ed), Rotterdam, Balkema. 647-654.

Fanella, D. & Krajcinovic, D. (1988) A micromechanical model for concrete in compression. *Eng. Frac. Mechs* **29**: 49-66.

Farmer, I. (1983) *Engineering behaviour of rocks.* Chapman and Hall, London.

Feves, M. & Simmons, G. (1976) Effects of stress on cracks in Westerly Granite. *Bull. Seism. Soc. Am.* **66**: 1755-1765.

Friedel, M.J. & Thill, R.E. (1990) *Stress determination in rock using the Kaiser effect.* US Bureau of Mines, Ri 9286.

Friedman, M. & Logan, J.M. (1970) Influence of residual elastic strain on the orientation of experimental fractures in three quartzose sandstones. *J. Geophys. Res.* **75**: 387-405.

Friedman, M. (1972) Residual elastic strain in rocks. *Tectonophysics* **15**: 297-330.

Gambarotta, L. & Lagomarisino, S. (1993) A microcrack damage model for brittle materials *Int. J. Solids Structures* **25**: 803-833.

Gay, N.C. (1976) Fracture growth around openings in large blocks of rock subjected to uniaxial and biaxial compression. Int. J. Rock. Mech. Min. Sci. & Geomech. Abstr. **13**: 231-243.

Germain, P., Nguyen, Q.S., Suquet, P. (1983) Continuum thermodynamics. *Trans. A.S.M.E. J. of Applied Mechanics* **50**: 1010-1020.

Gupta, I.N. (1973) Seismic velocities in rock subjected to axial loading up to shear fracture. *J. Geophys. Res.* **78**: 6936-6943.

Hadley, K. (1976) The effect of cyclic stress on dilatancy : Another look. *J. Geophys. Res.* **81**: 2471-2474.

Hallbauer, D.K., Wagner, H. & Cook, N.G.W. (1973) Some observations concerning the microscopic and mechanical behaviour of quartzite specimens in stiff, triaxial compression tests. *Int. J. Rock Mech. Min. Sci. & Geomech. Abstr.* **10**: 713-726.

Hawkes, I., Mellor, M. & Gariepy, S. (1973) Deformation of rocks under uniaxial tension. *Int. J. Rock Mech. Min. Sci. & Geomech. Abstr.* **10**: 493-507.

Hibbitt, Karlsson & Sorensen, Inc. (1993) ABAQUS User Manual.

Hoek, E. & Brown, E.T. (1980) Empirical strength criterion for rock masses. *J. Geotech. Engng Div. ASCE* **106**: 1013-1035.

Hoenig A. (1978) The behaviour of a flat elliptical crack in an anisotropic body. *Int. J. Solids Structures*, **14**: 925.

Hoenig, A. (1979) Elastic moduli of a non-randomly cracked body. *Int. J. Solids Structures* **15**: 137-154.

Holcomb, D.J. (1978) A quantitative model of dilatancy in dry rock and its application to Westerly Granite. *J. Geophys. Res.* **83**: 4941-4950.

Holcomb, D.J. (1981) Memory, relaxation, and microfracturing in dilatant rock. *J. Geophys. Res.* **86**: 6235-6248.

Holcomb, D.J. & Stevens, J.L. (1980) The reversible Griffith crack: A viable model for dilatancy. *J. Geophys. Res.* **85**: 7101-7107.

Holcomb, D.J. & Costin, L.S. (1986) Detecting damage surfaces in brittle materials using acoustic emission. *J. Appl. Mechs.* **53**: 536-544.

Homand, F., Morel, E., Henry, J.P., Cuxac, P. & Hammade, E. (1993) Characterization of the moduli of elasticity of an anisotropic rock using dynamic and static methods. *Int. J. Rock Mech. Min. Sci. & Geomech. Abstr.* **30**: 527-535.

Horii, H. & Nemat-Nasser, S. (1986) Brittle failure in compression : Splitting, faulting and brittle-ductile transition. *Phil. Trans. R. Soc. Lond.* **319**: 337-374.

Horii, H. & Nemat-Nasser, S. (1983) Overall moduli of solids with microcracks : Load-induced anisotropy. *J. Mech. Phys. Solids* **31**: 155-171.

Hult, J. (1987) Introduction and general overview. *Continuum damage mechanics; theory and applications.* in Krajcinovic, D. and Lemaitre, J. (eds), Springer, Wien, 1-36.

Ilankamban, R. & Krajcinovic, D. (1987) A constitutive theory for progressively deteriorating brittle solids. *Int. J. Solids Structures* **23**: 1521-1534.

Jaeger, J.C. (1967) Failure of rocks under tensile conditions. *Int. J. Rock Mech. Min. Sci.* **4**: 219-227.

Jaeger, J.C. & Cook, N.G. W. (1979) *Fundamentals of rock mechanics*, Chapman and Hall, London.

Janbu, N. (1963) Soil compressibility as determined by oedometer and triaxial tests. *Proc. Eur. Conf. Soil Mech. Found. Eng.*, Wiesbaden, **1**: 19-25.

Jones, I.L., Eaton, D.M., Zeronian, G. (1983) Dinorwig pumped storage scheme, Part 2: Construction. *Proc. Instn Civ. Enginrs. Part 1*, **74**: 681-718.

Ju, J.W. (1989) On energy-based coupled elastoplastic damage theories: Constitutive modeling and computational aspects. *Int. J. Solids Structures* **25**: 803-833.

Ju, J.W. (1990) Isotropic and anisotropic damage variables in continuum damage mechanics. *J. Engng Mechs Div. ASCE*, **116**: 2764-2770.

Ju, J.W. (1990) On two-dimensional micromechanical damage models for brittle solids with interacting microcracks. *Damage mechanics in engineering materials.* Ju, J.W., Krajcinovic, D., Schryer, H.L. (eds), ASME, **AMD-109**: 17-26.

Ju, J.W. & Lee. X. (1991) Micromechanical damage models for brittle solids. I : Tensile loadings. *J. Engng Mechs. Div. ASCE,* **117**: 1495-1536.

Kachanov, L.M. (1958) On the creep rupture time. *Izv. AN SSSR, Otd. Tekhn. Nauk.* **8**: 26.

Kachanov, M. (1980) Continuum model of medium with cracks. *J. Engng Mechs. Div. ASCE.* **106**: 1039-1051.

Kachanov, M.L. (1982) A microcrack model of rock inelasticity. Parts I and II. *Mechanics of Materials* **1**: 19-27.

Kachanov, L.M. (1986) *Introduction to continuum damage mechanics.* Martinus Nijhoff, Dordrecht.

Kawamoto, T., Ichikawa, I. & Kyoya, T. (1988) Deformation and fracturing behaviour of discontinuous rock mass and damage mechanics theory. *Int. J. Numer. Anal. Methods Geomech.* **12**: 1-31.

Kemeny, J.M. & Cook, N.G.W. (1987) Crack models for the failure of rocks in compression. *Constitutive laws for engineering materials: Theory and applications.* C.S. Desai et al. (eds.) Elsevier, New York, 879-888

Krajcinovic, D. (1983) Constitutive equations for damaging materials. *J. Appl. Mechs.* **50**: 355-360.

Krajcinovic, D. (1985) Continuous damage mechanics revisited : Basic concepts and definitions. *J. Appl. Mechs.* **52**: 829-834.

Krajcinovic, D. & Fonseka, G.U. (1981) The continuous damage mechanics of brittle materials. Parts 1 and 2. *J. Appl. Mechs.* **48**: 809-824.

Krajcinovic, D. (1984) Continuum damage mechanics. *Appl. Mechs. Rev.* **37**: 1-6.

Krajcinovic, D. (1987) Micromechanical basis of phenomenological models. *Continuum damage mechanics; theory and applications.* Krajcinovic, D. and Lemaitre, J. (eds), Springer, Wien, 195-206.

Krajcinovic, D. (1989) Damage mechanics. *Mechanics of Materials* **8**: 117-197.

Kranz, R.L. (1979) Crack-crack and crack-pore interactions in stressed granite. *Int. J. Rock Mech. Min. Sci. & Geomech. Abstr.* **16**: 37- 47.

Kranz, R.L. (1983) Microcracks in rocks : A review. *Tectonophysics* **100**: 449-480.

Kulhawy, F.H. (1975) Stress deformation properties of rock and rock discontinuities. *Engineering Geology* **9**: 327-350.

Lawn, B.R. & Wilshaw, T.R. (1975) *Fracture of brittle solids.* Cambridge University Press, Cambridge.

Lee, X., Ju, J.W. (1991) Micromechanical damage models for brittle solids, II : compressive loadings, *J. Engng Mechs Div. ASCE,* **117**: 1515-1536.

Lama, R.D., Vutukuri, V.S. (1977) Handbook on mechanical properties of rocks. Trans Tech, Clausthal.

Lemaitre, J. (1984) How to use damage mechanics. *Nuclear Engng. Des.* **80**: 233-245.

Lemaitre, J. (1985) Coupled elasto-plasticity and damage constitutive equations. *Computer Methods in Appl. Mechs. and Engng.* **51**: 31-49.

Lemaitre, J. (1987) Formulation and identification of damage kinetic constitutive equations, *Continuum damage mechanics; theory and applications.* Krajcinovic, D. and Lemaitre, J. (eds), Springer-Verlag, Wien, 37-90.

Lemaitre, J. & Chaboche, J.L. (1990) *Mechanics of solid materials.* Cambridge University Press.

Lockner, D.A., Byerlee, J.D., Kuksenko, V., Ponomarev, A. & Sidorin A. (1991) Quasi-static fault growth and shear fracture energy in granite. *Nature.* **350**: 39-42.

Love, A. (1937) *A treatise on the mathematical theory of elasticity.* Cambridge University Press, Cambridge.

Lubliner, J., Oliver, J., Oller, S. & Onate, E. (1989) A plastic-damage model for concrete. *Int. J. Solids Structures* **25**: 299-326.

Lubliner, J. (1990) *Plasticity Theory,* MacMillan, New York.

Malvern, L.E. (1969) Introduction to the mechanics of a continuum. Prentice Hall, New Jersey.

Margolin, L.G. (1984) A generalized griffith criterion for crack propagation. *Eng. Frac. Mechs.* **19**: 539-543.

Martin, J.B. (1976) *Plasticity; fundamentals and general results.* M.I.T. Press, Cambridge, Mass.

Mazars, J. & Pijaudier-Cabot, G. (1989) Continuum damage theory - application to concrete. J. Engng Mechs Div. ASCE **115**: 345-365

Mitchell, G.P. (1990) *Topics in the numerical analysis of solids.* PhD. Thesis, University of Wales, Swansea.

Mroz, Z. (1973) *Mathematical models of inelastic behaviour.* University of Waterloo, Waterloo, Ont.

Mogi, K. (1962) Study of elastic shocks caused by the fracture of heterogeneous materials and its relations to earthquake phenomena. *Bulletin of the Earthquake Research Institute*, University of Tokyo, **40**: 126-173.

Mogi, K. (1967) Effect of the intermediate principal stress on rock failure. *J. Geophys. Res.* **72**: 5117-5131.

Murakami, S. (1987) Progress of continuum damage mechanics. *JSME Int. J.* **30**: 701-710.

Murakami, S. (1987) Anisotropic aspects of material damage and application of continuum damage mechanics. *Continuum damage mechanics: theory and applications.* Krajcinovic, D. & Lemaitre, J. (eds), Springer, Wien, 91-134.

Murakami, S. (1988) Mechanical modeling of material damage. *J. Appl. Mechs.* **55**: 280-286.

Murakami, S. & Ohno, N. (1981) A continuum theory of creep and damage. *Creep of Structures*, Ponter A. (ed.), IUTAM symposium, Springer, Berlin.

Nelson, W. (1982) *Applied Life Data Analysis.* John Wiley and Sons, New York.

Napier J.A.L. & Hildyard M.W. (1992) Simulation of fracture growth around openings in highly stressed brittle rock. *J. S. Afr. Inst. Min. Metall.* **92**: 159-168.

Nemat-Nasser, S. & Horii, H. (1982) Compression-induced non-planar crack extension with application to splitting, exfoliation and rockburst. *J. Geophys. Res.* **87**: 6805-6821.

Nemat-Nasser, S. (1983) On finite plastic flow of crystalline solids and geomaterials. *J. Appl. Mechs.* **50**: 1114-1126.

Nemat-Nasser, S. & Obata, M. (1988) A microcrack model of dilatancy in brittle materials. *J. Appl. Mechs.* **55**: 24-35.

Nur, A. & Simmons, G. (1969) Stress-induced velocity anisotropy in rock : an experimental study. *J. Geophys. Res.* **77**: 6667-6674.

Onat, E.T. & Leckie, F.A. (1988) Representation of mechanical behaviour in the presence of changing internal structure. *J. Appl. Mechs.* **55**: 1-10.

Ortiz, M. & Martin, J.B. (1988) Symmetry preserving return mapping algorithms and incrementally extremal paths : a unification of concepts. *Applied Mechanics Research Unit Report No. 114*, University of Cape Town.

Ortiz, M., Popov, E. (1982) Plain concrete as a composite material. *Mechanics of Materials* **1**: 139-150.

Ortiz, M., Popov, E.P. (1982) A physical model for the inelasticity of concrete, *Proc. Royal Soc.* London, **A.383**: 101-125.

Ortiz, M. (1985) A constitutive theory for the inelastic behaviour of concrete. *Mechanics of Materials* **4**: 67-93.

Ortiz, M. (1987) An analytical study of the localised failure modes of concrete. *Mechanics of Materials.* **6**: 159-164.

Owen, D.R.J. & Hinton, E. (1980) *Finite elements in plasticity.* Pineridge Press Ltd, Swansea.

Pinto da Cunha, A. (1990) *Scale effects in rock masses.* Balkema, Rotterdam.

Rabotnov, Y.N. (1969) *Creep problems in structural mechanics.* North Holland, Amsterdam.

Resende, L. (1984) *Constitutive modelling and finite element analysis in geomechanics.* PhD. Thesis. University of Cape Town.

Resende, L. & Martin, J.B. (1984) A progressive damage continuum model for granular materials. *Composite Meth. Appl. Mech. Eng.* **42**: 1-18.

Resende, L. & Martin, J.B. (1988) Parameter identification in a damage model for rock mechanics. *Int. J. Numer. Methods Geomechs.* **12**: 79-97.

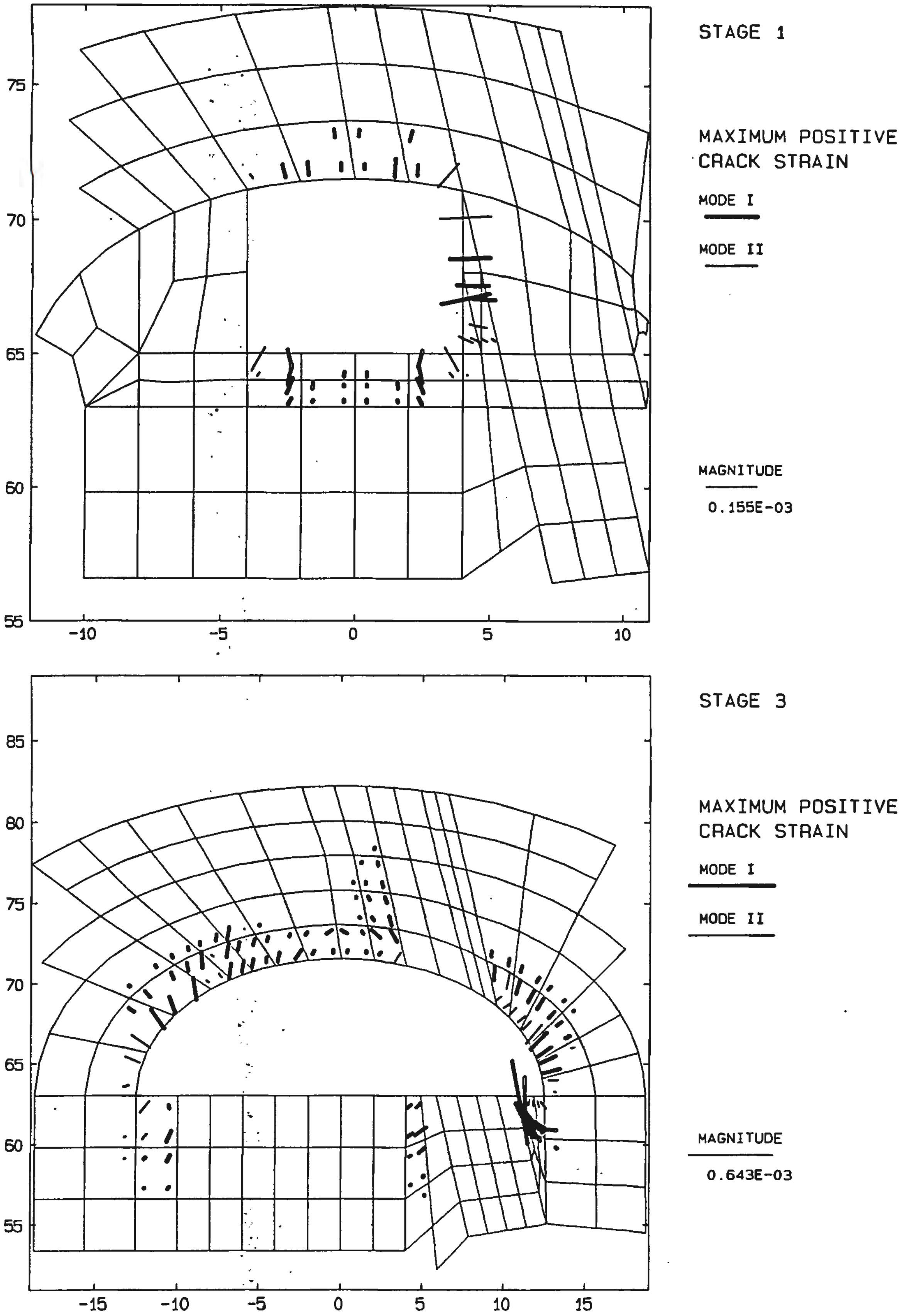

Figure 65: Damage vectors after excavation a: stage 1 b: stage 3

Rock Testing Handbook (1990) Techn. Info. Centre, US Army Engineer Waterways Experiment Station, Vicksburg.

Sayers, C.M. (1988) Stress-induced ultrasonic wave velocity anisotropy in fractured rock. *Ultrasonics* **26**: 311-317.

Sayers, C.M. (1988) Inversion of ultrasonic wave velocity measurements to obtain the microcrack orientation distribution function in rocks. *Ultrasonics* **26**: 73-77.

Sayers, C.M., Van Munster, J.G. & King, M.S. (1990) Stress-induced ultrasonic anisotropy in Berea Sandstone. *Int. J. Rock Mech. Min. Sci. & Geomech. Abstr.* **27**: 429-436.

Sayers, C.M. (1993) Comment on "Crack models for a transversely isotropic medium" by C. H. Cheng. *J. Geophys. Res.* **98**: 14211-14213.

Scheele, F., (1994) Cracking and failure of Indiana Limestone discs in diametral compression *WES Res. Report,* Vicksburg, (in preparation).

Scheele, F., Miller, W.O. & Banks, D. (1993) Acoustic emission during diametral and uniaxial compression of Indiana Limestone. *Geotechnical Engineering Report No. 9*, University of Cape Town.

Schock, R.N., Heard, H.C. & Stephens, D.R. (1973) Stress-strain behaviour of a Granodiorite and two greywackes on compression to 20 kilobars. *J. Geophys. Res.* **78**: 5922-5941.

Scholz, C.H. & Kranz, R. (1974) Notes on dilatancy recovery. *J. Geophys. Res.* **79**: 2132-2135.

Scholz, C.H. & Koczynski, T.A. (1979) Dilatancy anisotropy and the response of rock to large cyclic loads. *J. Geophys. Res.* **84** : 5525-5534.

Scholz, C.H. (1968) Microfracturing and the inelastic deformation of rock in compression. *J. Geophys. Res.* **73**: 1417-1432.

Scholz, C.H. (1968) Experimental study of the fracturing process in brittle rock. *J. Geophys. Res.* **73**: 1447-1454.

Sellers, E. & Scheele, F. (1993) Considerations of microcrack induced anisotropy in the modelling of selected rock tests. *F.E.M.S.A.*, University of Pretoria.

Simmons, G., Siegfried II, R.W. & Feves, M. (1974) Differential strain analysis : A new method for examining cracks in rocks. *J. Geophys. Res.* **79**: 4383-4385.

Simmons, G. and Richter, D. (1976) Microcracks in rocks. *The physics & chemistry of minerals and rocks.* Strens, R.G.J. (ed.) Wiley & Sons, London.

Simo, J.C. & Ju, J.W. (1987) Strain- and stress-based continuum damage models, I - formulation, II - computational aspects. *Int. J. Solids Structures.* **23**: 821-840 and **23**: 841-869.

Singh, U.K. & Digby, P.J. (1989) A continuum damage model for simulation of the progressive failure of brittle rocks. *Int. J. Solids Structures.* **25**: 647-663.

Stavropoulou, V. (1982) *Consitutive laws for brittle rocks*, PhD. Thesis, University of the Witwatersrand, Johannesburg.

Steif, P.S. (1984) Crack extension under compressive loading. *Eng. Frac. Mechs.* **20**: 463-473.

Stevens, J. & Holcomb, D.J. (1980) A theoretical investigation of the sliding crack model of dilatancy. *J. Geophys. Res.* **85**: 7091-7100.

Stumvoll, M., Kyoya, T., Ichikawa, Y. & Swoboda, G. (1991) A damage model for discontinuous rock based on thermodynamic principles. *Computer methods and advances in geomechanics.* Beer G., Booker, J.R. & Carter, J.P. (eds.) Rotterdam. Balkema. 1679- 1691.

Stumvoll, M. & Swoboda, G. (1993) Deformation behaviour of ductile solids containing anisotropic damage. *J. Eng. Mechs.* **119**: 1331-1352.

Sumarac, D. & Krajcinovic, D. (1987) A self-consistent model for microcrack-weakened solids. *Mechanics of Materials* **6**: 39-52.

Swoboda, G. (1990) Numerical Modelling of Tunnels. *Numerical methods and constitutive modelling in geomechanics.* in Desai, C.S. & Gioda, G. (eds), Springer-Verlag, Wien.

Swoboda, G. & Beichuan, H. (1991) Impact of numerical models on the development of new tunnelling methods. *Computer methods and advances in geomechanics.* Beer, G., Booker, J.R. & Carter, J.P. (eds), Rotterdam, Balkema 1679-1691.

Swoboda, G. & Ito, F. (1993). Two dimensional damage failure propogation model of jointed rock mass. *Assessment and prevention of failure phenomena in rock engineering.* Pasamehmetoglu, A.G., Kawamoto, T., Whittaker, B. N. & Aydan, O. (eds), Rotterdam, Balkema 53-59.

Swoboda, G. Stumvoll, M., & Beichuan, H. (1990) Damage tensor theory and its application to tunnelling. *Mechanics of Jointed and Faulted Rock.* Rossmanith, H.P. (ed.), Rotterdam, Balkema 51-58.

Talreja, R. (1985) A continuum mechanics characterization of damage in composite materials. *Proc. R. Soc. Lond.* **399**: 195-216.

Tapponnier, P. & Brace, W.F. (1976) Development of stress-induced microcracks in Westerly Granite. *Int. J. Rock Mech. Min. Sci. & Geomech. Abstr.* **13**: 103-112.

TerraTek, Inc., (1981) Mechanical properties of precambrian quartzite from South Africa. *Report TR 81-65*, Salt Lake City, Utah.

Valliappan, S., Murti, V. & Wohua, Z. (1990) Finite element analysis of anisotropic damage mechanics problems. *Eng. Frac. Mechs.* **35**: 1061-1071.

Walsh, J.B. (1965) The effect of cracks on the uniaxial elastic compression of rocks. *J. Geophys. Res.* **70**: 399-411.

Walsh, J.B. (1965) The effect of cracks on the compressibility of rock. *J. Geophys. Res.* **70**: 381-389.

Walsh, J.B. (1980) Static deformation of rock. *J. Engng Mechs. Div. ASCE* **106**: 1005-1019.

Walsh, J.B. & Grosenbaugh, M.A. (1979) A new model for analyzing the effect of fractures on compressibility. *J. Geophys. Res.* **84**: 3532-3536.

Whittle, R. A. (1977) Geotechnical aspects of the tunnel construction for the Dinorwig power station. *Ground Engineering.* 15-20.

Wiebols, G.A. & Cook, N.G.W. (1968) An energy criterion for the strength of rock in polyaxial compression. *Int. J. Rock Mech. Min. Sci.* **5**: 529-549.

Wong, T., Fredrich, J.T. & Gwanmesia, G.D. (1989) Crack aperture statistics and pore space fractal geometry of Westerly Granite and Rutland Quartzite : Implications for an elastic contact model of rock compressibility. *J. Geophys. Res.* **94**: 10267-10278.

Yazdani S., Schreyer H.L. (1990) Combined plasticity and damage mechanics model for plain concrete. *J. Engng Mech. Div. ASCE,* **116**: 1435-1450.

Yazdani S., Schreyer H.L. (1988) An anisotropic damage model with dilation for concrete. *Mechanics of Materials* **7**: 231-244.

Yazdani, S. (1993) On a class of continuum damage mechanics theories. *Int. J. of Damage Mechanics* **2**: 162-176.

Zheng, Z. (1989) Compressive stress-induced microcracks in rocks and applications to seismic anisotropy and borehole stability. *PhD. Thesis,* Univ. of California, Berkeley.

Zoback, M.D. & Byerlee, J.D. (1975) The effect of microcrack dilatancy on the permeability of Westerly Granite. *J. Geophys. Res.* **80**: 752-755.

Zoback, M.D. & Byerlee, J.D. (1975) The effect of cyclic differential stress on dilatancy in Westerly Granite under uniaxial and triaxial conditions. *J. Geophys. Res.* **80**: 1526-1530.

Zhang, W., Murti, V. & Valliappan, S. (1990) *Effects of matrix symmetrization in anisotropic damage models.* UNICIV Report No. R-273, University of New South Wales, Australia.

Zhang, W. & Valliappan, S. (1990) Analysis of random anisotropic damage mechanics problems of rock mass. Parts I and II. *Rock Mechanics and Rock Engineering* **23**: 91-112 and **23**: 241-249.